Electronic Thesis and Dissertation Repository

4-5-2024 1:30 PM

Bioactive and Electrically Conductive Nanocomposite Bone Biomaterials

Rebeca A. Arambula-Maldonado,

Supervisor: Mequanint, Kibret, *The University of Western Ontario*
A thesis submitted in partial fulfillment of the requirements for the Doctor of Philosophy degree in Biomedical Engineering
© Rebeca A. Arambula-Maldonado 2024

Follow this and additional works at: https://ir.lib.uwo.ca/etd

Part of the Biomaterials Commons, and the Molecular, Cellular, and Tissue Engineering Commons

Abstract

Electrically conductive carbon-based materials are emerging as potential biomaterials for bone tissue engineering. Their incorporation into organic-inorganic nanocomposites mimics the structural composition and electrically conductive nature of bone.

The aim of this research was to design bone biomaterials from gelatin-based polymers, tertiary bioactive glasses (BG) via a sol-gel method, and multiwall carbon nanotubes (MWCNT). The incorporation of calcium into organic-inorganic nanocomposites plays an essential role in the development of bioactive bone biomaterials. Calcium chloride and calcium ethoxide were investigated as calcium sources in gelatin-BG-MWCNT nanocomposites. The resulting surface elemental distribution was homogeneous, but the swelling, degradation and porosity properties of nanocomposites differed due to the fate of calcium ions within the organic-inorganic network. Mineralization on the surfaces of nanocomposites was observed after treatment in simulated body fluid. Favorable cell adhesion, spreading, and viability were observed on nanocomposites, with calcium ethoxide having more advantageous properties. Furthermore, an alternative synthesis strategy comprising gelatin methacryloyl (GelMA), sol-gel derived tertiary BG containing calcium ethoxide as calcium source, and MWCNT was developed to create nanocomposite organic-inorganic hydrogels. Using this strategy, biomaterials possessed mechanical and electrically conductive properties as a function of MWCNT loading. In addition, suitable electro-mechanical responses similar to that found in endogenous bone were observed without affecting their bioactive and biocompatibility properties. Nanocomposite hydrogels also supported mouse embryo multipotent mesenchymal progenitor (10T1/2) cells and drove differentiation into an osteogenic lineage.

Mesenchymal stem cells derived from human-induced pluripotent stem cells (iMSCs) were also able to attach to GelMA-BG-MWCNT nanocomposite hydrogels. Cell adhesion onto the surfaces of nanocomposite was improved when hydrogels were coated with fibronectin and seeding pre-differentiated iMSCs. Increased osteogenic differentiation and the formation of mature mineral deposition were observed in hydrogels with increasing MWCNT concentration. Overall, the data presented in this thesis demonstrated that nanocomposites containing MWCNT could potentially become promising bioactive biomaterials for bone repair and regeneration applications.

Summary for Lay Audience

Bone loss is clinically defined as a defect in the bone structure that is caused either by external factors or deformation of existing bone, causing structural deterioration. The repair of bone fractures and reconstruction of critical-size bone defects that exceed the healing capacity of the human body represent a significant challenge. Currently, treatment for cases of orthopedic intervention involves a grafting procedure that replaces the defected bone with autograft or allograft sources as well as xenograft or synthetic bone substitutes, however, these procedures often lead to complications causing hemorrhage and vascular lesions, limited quality of harvested bone as well as risk of disease transmission and immune response. In addition, patients display limited anatomical and functional recovery demonstrating the requirement for an alternative therapeutic solution that would ideally degrade at a similar rate to the formation of new tissue to maintain the integrity of the repaired region of bone. Although several materials such as organic polymers, inorganic phosphates, and organic-inorganic hybrids have been extensively studied for bone tissue engineering solutions, new generation of biomaterials that better mimic the bone's natural electrically conductive property may have significant advantages.

In this research, nanocomposite biomaterials comprised of gelatin, bioactive glass (BG) and multiwall carbon nanotubes (MWCNT) were developed to establish a favorable approach that incorporates all three components for the development of a bone biomaterial. Comparison of the role of different calcium sources in the gelatin-BG-MWCNT were evaluated. An improved strategy was further developed to prepare bioactive nanocomposite hydrogels composed of gelatin methacryloyl (GelMA), BG and MWCNT containing tunable electro-mechanical responses similar to those found in endogenous bone during its regeneration and healing. The nanocomposite hydrogels were able to induce osteogenic differentiation in mouse- and human-derived stem cells and enhanced protein expression and mineralization in pre-differentiation human-derived stem cells.

In conclusion, organic-inorganic nanocomposite biomaterials containing an electrically conductive component mimic the natural structural composition and electrical conductive properties of bone, and may be good candidates for bone tissue engineering.

Co-Authorship Statement

Chapter 1: Rebeca Arambula-Maldonado – author; Dr. Kibret Mequanint – guidance and manuscript revision.

Chapter 2: Rebeca Arambula-Maldonado – author; Dr. Kibret Mequanint – guidance and manuscript revision.

Chapter 3: Rebeca Arambula-Maldonado – experimental setup, data collection, author; Dr. Kibret Mequanint – guidance and manuscript revision.

Chatper 4: Rebeca Arambula-Maldonado – experimental setup, data collection, author; Drs. Yuqing Liu and Malcolm Xing – provided support on the electrical and electro-mechanical studies; Dr. Kibret Mequanint – guidance and manuscript revision.

Chapter 5: Rebeca Arambula-Maldonado – material synthesis, cell culture experimental setup, data collection, author; Dr. Kibret Mequanint – guidance and chapter revision.

Chapter 6: Rebeca Arambula-Maldonado – author; Dr. Kibret Mequanint – guidance and chapter revision.

This work is dedicated to my father, mother, and brother.

Thank you for being my rock, for supporting me, and always being by my side.

Thank you, God, for the many blessings in my life… and the many blessings yet to come.

Acknowledgments

First and foremost, I am truly grateful for the support of my supervisor, Dr. Kibret Mequanint, for giving me the opportunity to work under his guidance. Dr. Mequanint was always there whenever I ran into difficulties and provided valuable advice and insightful discussions to help me achieve my goals. I am thankful that he has believed in me since the very beginning of my PhD journey, even as I hurdled different obstacles during my research. His knowledge and experience guided me every step of the way and allowed me to gain independence and develop critical thinking for the successful completion of this research work.

I would also like to extend my appreciation to my advisory committee members, Drs. Aaron Price and Amin Rizkalla. I could not have undertaken this journey without their valuable expertise and generous knowledge during my PhD studies. Thank you for your mentorship and for providing me with valuable comments on this work.

I am thankful to my current and previous lab members for their help and encouragement. Specifically, I would also like to give an extra thank you to Drs. Neda Aslankoohi, Kalin Penev, and Meng Wang for their constructive feedback. Another sincere thank you to Dr. Shigang Lin for his valuable suggestions and insightful comments on cell culture experiments.

Last but not least, I would like to express my gratitude to my family and friends. Thank you for your emotional support and encouraging me to keep moving forward.

I will forever be grateful for this opportunity, which allowed me to grow both professionally and personally. It has been an incredible journey that I will always cherish when I look back at this time.

Table of Contents

ix

List of Tables

List of Figures

List of Schemes

Appendix

List of Abbreviations

3D	Three dimensional
Alp	Alkaline phosphatase
ANOVA	Analysis of variance
ATR-FTIR	Attenuated Total Reflectance Fourier Transform Infrared Spectroscopy
BG	Bioactive glass
BSA	Bovine serum albumin
$CaCl_2$	Calcium chloride
$Ca(OEt)_2$	Calcium ethoxide
cDNA	Complementary Deoxyribonucleic acid
Col1	Collagen type I
DAPI	$4',6$-diamidino-2-phenylindole
DMEM	Dulbecco's modified Eagle's medium
DNA	Deoxyribonucleic acid
ECM	Extracellular matrix
EDX	Energy-dispersive X-ray spectroscopy
EtOH	Ethanol
FBS	Fetal bovine serum
FITC	Fluorescein isothiocyanate
FTIR	Fourier transform infrared
GAPDH	Glyceraldehyde 3-phosphate dehydrogenase
HA	Hydroxyapatite
HCA	Hydroxycarbonate apatite
HBSS	Hanks' balanced salt solution
HCl	Hydrochloric acid
iMSC	Mesenchymal stem cells derived from human induced pluripotent stem cells
MSC	Mesenchymal stem cell
NMR	Nuclear magnetic resonance
OCN	Osteocalcin
OPN	Osteopontin
PBS	Phosphate-buffered saline
PFA	Paraformaldehyde
qRT-PCR	Quantitative real-time polymerase chain reaction
RNA	Ribonucleic acid
RT	Room Temperature
SBF	Simulated body fluid
SD	Standard deviations
SEM	Scanning electron microscopy
TCP	Tissue culture plate
TEOS	Tetraethyl orthosilicate
TEP	Triethyl phosphate
XRD	X-ray diffraction

Chapter 1

1. Introduction*[1]

1.1. Overview

By 2025, there will be over 3 million cases of bone fractures in the United States that require clinical intervention, creating an increased medical system cost of $25 billion per year.[1]   In Canada, the healthcare system already faces an overall yearly cost of $2.3 billion for the treatment of osteoporosis and osteoporosis-related fractures,[2,3] and as the aging segment of the population increases, an ever-increasing financial burden will be imposed on the healthcare system. Repair of bone fractures and reconstruction of critical-size bone defects that exceed the natural healing ability of the human body thus represents a significant challenge.[4]

Bone defects are caused by either external factors or deformation of existing bone, resulting in structural deterioration.[5] Current intervention strategies to treat bone defects involve the replacement of the damaged region with donor bone either from autograft, allograft, or xenogeneic sources. However, the use of donor bone sources possesses significant risks, including donor-site morbidity, hemorrhaging, and an elevated risk of disease transmission.[6] Of greater concern is their limited availability, with autografts already in short supply and therefore unable to meet the increased demand for our aging population. For these reasons, synthetic bone graft substitutes have received significant attention.

Synthetic materials were first prepared as bone graft substitutes with the design purpose of matching the physical properties present in natural bone, with minimal adverse response to the host.[7] Sustained research in this field developed biomaterials that could create a favorable interface between the implanted material and the host tissue, promoting positive responses in the surrounding tissues within the body.[8] One of the most studied bone biomaterials is bioactive glass (BG), originally the 45S5 BG invented by Hench,[9] which has gained great attention due to its ability to bond to bone through

---

*[1] Part of this chapter has been published. Reprinted with permission from Arambula-Maldonado, R., Mequanint, K.; Carbon-based electrically conductive materials for bone repair and regeneration; *Materials Advances* 2022, 3 (13), p.5186-5526.

the formation of hydroxyapatite layers on its surface within a physiological environment. However, the processing of synthetic bone graft substitutes into porous complex scaffolds for load-bearing implantation sites can become challenging due to their brittle and stiff nature. In addition, patients treated with scaffolds made entirely of BG displayed limited anatomical and functional recovery, demonstrating the requirement for an alternative intervention solution.[10] The new solution would integrate natural or synthetic polymers to create a hybrid tissue-engineered bone that would ideally degrade at a similar rate to the formation of new tissue to maintain the integrity of the repaired region of bone which can physiologically and mechanically adapt to the natural environment, and local load within the body.[11]

Although several materials such as organic polymers, inorganic phosphates, and organic-inorganic hybrids have been extensively studied for bone repair and regeneration,[12–15] new-generation biomaterials that provide additional functionality for bone scaffolds such as conductivity,[16-18] fluorescence property, and drug delivery[19] are active areas of research being applied for bone tissue engineering solutions. The native bone possesses endogenous conductive properties[20,21] and the incorporation of a conductive element into a bone biomaterial could better mimic the bone natural electrical conductivity, providing significant advantages at a physiological level.[22] Carbon-based conductive materials have specifically been incorporated into polymer-based bone biomaterials as a reinforcement element and as a component that can deliver electrical cues through the application of electrical stimulation for the maturation of osteoblasts and promotion of the repair and regeneration of bone defects (**Fig. 1.1**).

The overall objective of this work is to design and synthesize organic-inorganic biomaterials for bone tissue engineering with the attempt to provide several of the above-mentioned features in a single structure.
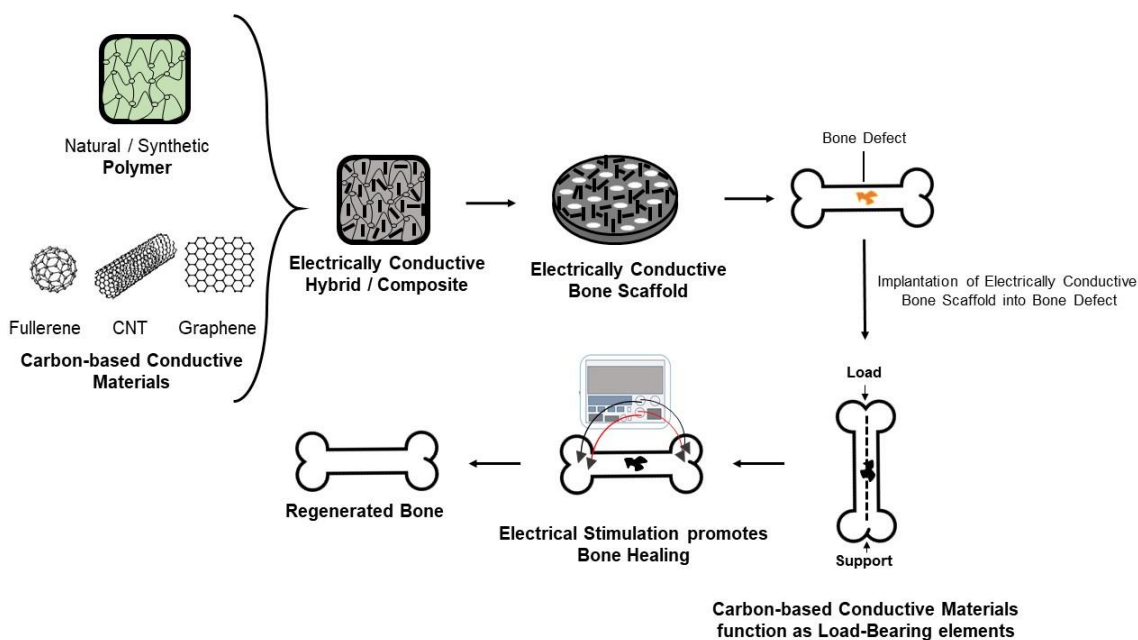
Figure 1.1. Application of carbon-based conductive materials for bone repair and regeneration. Electrically conductive bone scaffolds are developed through the incorporation of carbon-based conductive materials into natural/synthetic polymers, creating a tissue-engineered bone that can be implanted into regions of bone defects. The aim of the implanted electrically conductive tissue-engineered bone is to degrade at a similar rate to the formation of new tissue to maintain the integrity of the repaired region while acting as a load-bearing element until the scaffold is completely remodeled and matches the original tissue's mechanical strength. Electrical stimulation can be delivered to the implanted conductive bone scaffold to promote cell proliferation, migration, and maturation of bone.[23]

1.2. Thesis Outline

This thesis is divided into 6 chapters. Chapter 2 presents a thorough literature review on the principle of bone tissue engineering, the electrically conductive nature of endogenous bone and the importance of incorporating carbon-based conductive materials into organic-inorganic composites to develop bioactive biomaterials that mimic the structural composition and electrical properties of endogenous bone. In addition, the preparation strategies of different types of carbon-based conductive materials are presented, focusing on their properties, applications, and physiological responses for bone tissue engineering. Hypothesis and objectives are provided at the end of this chapter. Furthermore, chapter 3 describes exploratory experiments on the preparation and characterization of gelatin-BG-MWCNT biomaterial to establish the best approach to incorporate all three components for the development of a bone biomaterial. Following the conditions assessed in the exploratory experiments, chapter 4

presents an efficient approach that incorporates GelMA, tertiary BG, and uniformly dispersed MWCNT to create nanocomposite hydrogels. This chapter assesses the physicochemical, structural, mechanical, and electrical characterizations of GelMA-BG-MWCNT hydrogels, as well as their biological evaluation. Chapter 5 evaluates the osteogenic differentiation of iMSCs on nanocomposite hydrogels with the presence of electrical stimulation and their potential application in *in vivo* models. Finally, the significance, limitations, and future directions of this research are defined in chapter 6.

1.3. References

[1]   R. Burge, B. Dawson-Hughes, D.H. Solomon, J.B. Wong, A. King, A. Tosteson, Incidence and Economic Burden of Osteoporosis-Related Fractures in the United States, 2005-2025, J. Bone Miner. Res. 22 (2007) 465–475. https://doi.org/10.1359/jbmr.061113.

[2]   J.-E. Tarride, R.B. Hopkins, W.D. Leslie, S. Morin, J.D. Adachi, A. Papaioannou, L. Bessette, J.P. Brown, R. Goeree, The burden of illness of osteoporosis in Canada, Osteoporos. Int. 23 (2012) 2591–2600. https://doi.org/10.1007/s00198-012-1931-z.

[3]   R.B. Hopkins, N. Burke, C. Von Keyserlingk, W.D. Leslie, S.N. Morin, J.D. Adachi, A. Papaioannou, L. Bessette, J.P. Brown, L. Pericleous, J. Tarride, The current economic burden of illness of osteoporosis in Canada, Osteoporos. Int. 27 (2016) 3023–3032. https://doi.org/10.1007/s00198-016-3631-6.

[4]   T.-M. De Witte, L.E. Fratila-Apachitei, A.A. Zadpoor, N.A. Peppas, Bone tissue engineering via growth factor delivery: from scaffolds to complex matrices, Regen. Biomater. 5 (2018) 197–211. https://doi.org/10.1093/rb/rby013.

[5]   A. Wiese, H.C. Pape, Bone Defects Caused by High-energy Injuries, Bone Loss, Infected Nonunions, and Nonunions, Orthop. Clin. North Am. 41 (2010) 1–4. https://doi.org/10.1016/j.ocl.2009.07.003.

[6]   J.-H. Zeng, S.-W. Liu, L. Xiong, P. Qiu, L.-H. Ding, S.-L. Xiong, J.-T. Li, X.-G. Liao, Z.-M. Tang, Scaffolds for the repair of bone defects in clinical studies: a systematic review, J. Orthop. Surg. 13 (2018) 33. https://doi.org/10.1186/s13018-018-0724-2.

[7]   L.L. Hench, Biomaterials, Science. 208 (1980) 826–831. https://doi.org/10.1126/science.6246576.

[8]   R. Arambula-Maldonado, A. Geraili, M. Xing, K. Mequanint, Tissue engineering and regenerative therapeutics: The nexus of chemical engineering and translational medicine, Can. J. Chem. Eng. (2021) cjce.24094. https://doi.org/10.1002/cjce.24094.

[9]   L.L. Hench, Bioceramics: From Concept to Clinic, J. Am. Ceram. Soc. 74 (1991) 1487–1510. https://doi.org/10.1111/j.1151-2916.1991.tb07132.x.

[10]   Q. Fu, M.N. Rahaman, B.S. Bal, R.F. Brown, Preparation and in vitro evaluation of bioactive glass (13-93) scaffolds with oriented microstructures for repair and regeneration of load-bearing bones: Preparation and in Vitro Evaluation of Bioactive Glass Scaffolds, J. Biomed. Mater. Res. A. 93A (2010) 1380–1390. https://doi.org/10.1002/jbm.a.32637.

[11]   B.A. Allo, A.S. Rizkalla, K. Mequanint, Hydroxyapatite Formation on Sol–Gel Derived Poly(ε-Caprolactone)/Bioactive Glass Hybrid Biomaterials, ACS Appl. Mater. Interfaces. 4 (2012) 3148–3156. https://doi.org/10.1021/am300487c.

[12]   B.A. Allo, S. Lin, K. Mequanint, A.S. Rizkalla, Role of Bioactive 3D Hybrid Fibrous Scaffolds on Mechanical Behavior and Spatiotemporal Osteoblast Gene Expression, ACS Appl. Mater. Interfaces. 5 (2013) 7574–7583. https://doi.org/10.1021/am401861w.

[13]   D. Mondal, S. Lin, A.S. Rizkalla, K. Mequanint, Porous and biodegradable polycaprolactone-borophosphosilicate hybrid scaffolds for osteoblast infiltration and stem cell differentiation, J. Mech. Behav. Biomed. Mater. 92 (2019) 162–171. https://doi.org/10.1016/j.jmbbm.2019.01.011.

[14]   D. Mondal, S.J. Dixon, K. Mequanint, A.S. Rizkalla, Mechanically-competent and cytocompatible polycaprolactone-borophosphosilicate hybrid biomaterials, J. Mech. Behav. Biomed. Mater. 75 (2017) 180–189. https://doi.org/10.1016/j.jmbbm.2017.07.010.

[15]   N. Aslankoohi, D. Mondal, A.S. Rizkalla, K. Mequanint, Bone Repair and Regenerative Biomaterials: Towards Recapitulating the Microenvironment, Polymers. 11 (2019) 1437. https://doi.org/10.3390/polym11091437.

[16]   A.G. Guex, J.L. Puetzer, A. Armgarth, E. Littmann, E. Stavrinidou, E.P. Giannelis, G.G. Malliaras, M.M. Stevens, Highly porous scaffolds of PEDOT:PSS for bone tissue engineering, Acta Biomater. 62 (2017) 91–101. https://doi.org/10.1016/j.actbio.2017.08.045.

[17]   S. Shokri, B. Movahedi, M. Rafieinia, H. Salehi, A new approach to fabrication of Cs/BG/CNT nanocomposite scaffold towards bone tissue engineering and evaluation of its properties, Appl. Surf. Sci. 357 (2015) 1758–1764. https://doi.org/10.1016/j.apsusc.2015.10.048.

[18]   J.H. Lee, Y.C. Shin, S.-M. Lee, O.S. Jin, S.H. Kang, S.W. Hong, C.-M. Jeong, J.B. Huh, D.-W. Han, Enhanced Osteogenesis by Reduced Graphene Oxide/Hydroxyapatite Nanocomposites, Sci. Rep. 5 (2015) 18833. https://doi.org/10.1038/srep18833.

[19]   N. Aslankoohi, K. Mequanint, Intrinsically fluorescent bioactive glass-poly(ester amide) hybrid microparticles for dual drug delivery and bone repair, Mater. Sci. Eng. C. 128 (2021) 112288. https://doi.org/10.1016/j.msec.2021.112288.

[20]   E. Fukada, I. Yasuda, On the Piezoelectric Effect of Bone, J. Phys. Soc. Jpn. 12 (1957) 1158–1162. https://doi.org/10.1143/JPSJ.12.1158.

[21]   The classic: Fundamental aspects of fracture treatment by Iwao Yasuda, reprinted from J. Kyoto Med. Soc., 4:395-406, 1953, Clin. Orthop. (1977) 5–8.

[22]   T.W. Balmer, S. Vesztergom, P. Broekmann, A. Stahel, P. Büchler, Characterization of the electrical conductivity of bone and its correlation to osseous structure, Sci. Rep. 8 (2018) 8601. https://doi.org/10.1038/s41598-018-26836-0.

[23]   R. Arambula-Maldonado, K. Mequanint, Carbon-based electrically conductive materials for bone repair and regeneration, Mater. Adv. (2022) 10.1039.D2MA00001F. https://doi.org/10.1039/D2MA00001F.

Chapter 2

2. Literature Review*²

Overview: This chapter provides background information on the current clinical strategies for the repair of bone defects, emphasizing on the importance of bone tissue engineering strategies leading to the types of synthetic bone biomaterials and the importance of sol-gel-derived organic-inorganic bone biomaterials. The chapter subsequently discusses the electrically conductive nature of bone and the properties and characterizations of different carbon-based electrically conductive materials that are used as bone biomaterials for their applications in bone tissue engineering solutions. At the end of the chapter, an outline of the scope of this work and the objectives are provided.

2.1. The need for bone tissue engineering

Bone is a complex organic-inorganic composite tissue composed of 30 wt.% collagen and 70 wt.% hydroxycarbonate apatite (HCA) [1] where collagen fibers provide a framework in which the HCA nucleates and grows.[2] As a mineralized connective organ, bone undergoes natural tension and compressive forces that provide structural support while protecting vital organs, serving as a mineral reservoir that produces blood cells in our body.[3]

Global statistics have shown that bone is one of the organs in the human body that has frequently required repairing. Yearly cases of approximately 2.2 million bone graft procedures have been reported, with the number of interventions estimated to increase by approximately 13% annually.[4,5] Such bone graft procedures involve the replacement of the damaged region with donor's bone either from autograft, allograft, or xenogeneic sources. Bone graft interventions are performed on critical-size bone defects that are caused by the removal of osseous tumors,[6] fracture regenerations[7] and the repair of natural structural deteriorations, such as osteoporosis or birth defects.[8] However, grafting procedures often lead to complications causing hemorrhage and vascular lesions, limited quality of harvested bone, as well as risk of disease transmission and immune response.[9] The limited

---

availability of natural bone grafts is a cause of great concern since they cannot meet the increased demand of our aging population. Therefore, the field of bone tissue engineering has been noticeably developing bone biomaterials for the healing and regeneration of bone defects.

The aim of bone tissue engineering is to create biomaterials for critical-size bone defects that cannot heal naturally.[10] Pre-osteoblasts and mesenchymal stem cells (MSC) are examples of cells that have been previously used because they can readily differentiate to an osseous lineage.[10,11] Bioactive molecules also play a crucial role to direct regeneration of osseous tissue. The *in vivo* microenvironment surrounding a cell is rich in biomolecular signals from other cells and the extracellular matrix (ECM). Such biomolecular signals can be autocrine, which affects the same cell that released the molecule, paracrine signals that affect proximal cells, or endocrine signals which affects remote targets.[12] Bioactive molecules can be growth factors, cytokines, hormones or transcription factors and thus can be introduced onto three-dimensional (3D) scaffolds to direct the regeneration of skeletal tissues and interact with and modulate the activity of various bone cell populations (**Fig. 2.1**).[13] Moreover, scaffolds are critically important providing a temporary mechanical support and act as a temporal and spatial guide to promote cell attachment, migration, proliferation, and differentiation during the development of new bone tissue.[14] Bone repair materials should preferably be osteoinductive, osteoconductive, and capable of osseointegration.[15] Ideally, to maintain the integrity of the repaired region of bone, the biomaterials within the scaffold would be resorbed and replaced over time and in tune with the body's own newly regenerated biological tissue.[15,16]
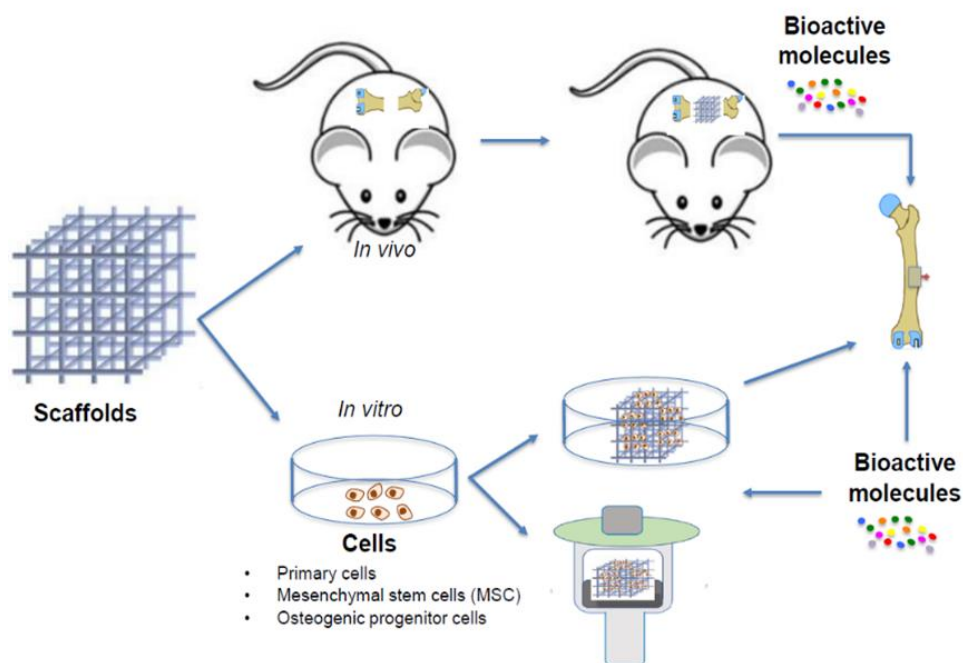
Figure 2.1. Tissue engineering components. The building blocks for bone tissue engineering comprise functionally active osteoblastic cells to secrete new bone matrix (osteogenesis), bioactive molecules (growth factors) to drive the regeneration process (osteoinduction), and scaffolds upon which cells attach and signaling molecules can be delivered to the bone site to be regenerated (osteoconduction) either *in vitro* or *in vivo*.[11]

2.2. Types of inorganic synthetic bone biomaterials

2.2.1. Calcium phosphate crystalline ceramics

Calcium phosphates (CaP), specifically hydroxyapatite (HA) ($Ca_{10}(PO_4)_6(OH)_2$), β-tricalcium phosphate (β-TCP) ($Ca_3(PO_4)_2$) and a combination of both producing biphasic CaP (BCP) ceramic are accounted as the most widely used ceramic-based bone graft substitutes due to their osteoconductive and bioresorbable properties.[17–20] The chemical composition of calcium ceramics is similar to the inorganic phase of natural bone, which is composed of CaP in the form of carbonate apatite nanocrystals.[21,22] Crystalline ceramics can be synthesized through solid-state reactions, thermal conversion or direct precipitation,[23–25] in an attempt to mimic the natural nanocrystals. Furthermore, dense CaP can be produced through sintering, a process in which ceramics in the form of powder go through a thermal treatment at temperatures of 1000°C and above, to induce a three-dimensional porous structure through ion diffusion at the grain boundaries.[26] However, the main property that is considered to determine the mechanical strength of ceramics is the Ca/P molar ratio, which is related

to the degree of crystallinity.[27,28] Metastable intermediate precursors are formed during the crystallization process of CaP as follows.[28]

i)   Amorphous CaP

ii)   Brushite ($CaHPO_4 \cdot 2H_2O$)

iii)   Octacalcium phosphate ($Ca_8(HPO_4)_2(PO_4)_4 \cdot 5H_2O$)

iv)   Tricalcium phosphate ($\alpha(\beta)\text{-}Ca_3(PO_4)_2$)

v)   HA ($Ca_{10}(PO_4)_6(OH)_2$)

Furthermore, Ca/P molar ratios also determine the rate at which the ceramics are reabsorbed; a high crystallization delays the resorption rate, whereas amorphous or low crystallization ceramics have higher relative solubilities.[29] HA is the most crystalline ceramic with a Ca/P molar ratio of 1.67,[30] it is, therefore, very stable when implanted into damaged bone sites but possesses a very slow rate of reabsorption. In contrast, β-TCP is a less crystalline ceramic with a Ca/P molar ratio of 1.5 than HA and, therefore, reabsorbs more rapidly in the human body.[29,31] As β-TCP degrades, there is an increased concentration of calcium and phosphate on the surface of the ceramic which enhances the mineralization and formation of bone. However, the mechanical strength of β-TCP is lower due to the rapid resorption in the body, compromising the intrinsic strength of the repairing bone at the site of implantation. The high crystalline form of β-TCP can be achieved by sintering to obtain a mechanically stronger ceramic; however, their reabsorption rate would become very slow, preventing bone repair.

2.2.2. Non-crystalline bioactive glasses

BGs are amorphous, silicate-based materials that are based on a covalent random network of corner-sharing silica tetrahedra containing Si-O-Si bridging bonds.[8] The original BG (46.1%, SiO_2, 24.4%, Na_2O, 26.9% CaO, and 2.6% P_2O_5, in mol%), 45S5 Bioglass®, was developed by Hench and his colleagues.[32] Bioglass® was first produced through melt-quenching processing which involved melting the oxide components in platinum crucibles at a temperature of 1370°C, followed by pouring into a preheated mold or pouring the melt into water to quench, creating a powder or frit.[32,33] BG can also be synthesized via the sol-gel process. The sol-gel process is a technique in which BGs are

produced at room temperature. The process involves the synthesis of BGs where colloidal suspensions (sol) of glass precursors undergo a series of hydrolysis and polycondensation reactions to form a gel, an inorganic network composed of the glass elements forming covalent bonds.[34] Glass precursors are present in the form of metal alkoxides with the structure of M-(OR)x, where a central metallic ion, such as silicon (Si) is bound to functional organic groups (R) through oxygen linkage (O).[34,35] Common glass network formers used are metal alkoxides that can readily react with water, such as tetraethyl orthosilicate (TEOS) and triethyl phosphate (TEP) and are used as silica and phosphate precursors respectively (Equation 2.1).[35] Sources of calcium can also be incorporated during the sol-gel process in the form of calcium salt precursors, which act as network modifiers by breaking down the glass network through the creation of non-bridging bonds. A gel is formed by polycondensation of the silica species in the sol (Equation 2.2), forming a network of silica (Si-O-Si bridging bonds) that subsequently goes through a heat treatment to remove the condensation by-products and remove the nitrates in cases where calcium nitrate salt is used, due to the cytotoxic nature of nitrate.[8,36] In addition, different drying techniques for wet gels result in porous, structured materials known as aerogels and xerogels.[36] Aerogels are low-density gels that are produced by the removal of liquid from the interconnected pore network as a gas phase under supercritical drying; whereas xerogels, generically called gels, are the resulting product from drying at or near ambient conditions by thermal evaporation.[36,37]

$$\text{Hydrolysis: } Si\text{-}(OC_2H_5)_4 + 4H_2O \rightarrow Si(OH)_4 + 4C_2H_5\text{-}OH \qquad (2.1)$$

$$\text{Self-condensation: } Si(OH_4) \rightarrow SiO_2 + 2H_2O \qquad (2.2)$$
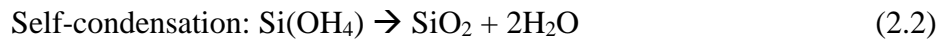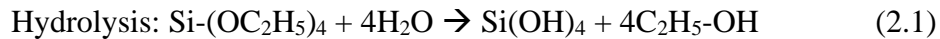
Further self-condensation →
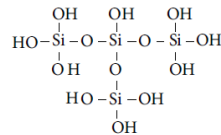
$$
\begin{array}{ccccc}
OH & & OH & & OH \\
| & & | & & | \\
HO-Si & -O- & Si & -O- & Si-OH \\
| & & | & & | \\
OH & & O & & OH \\
& & | & & \\
& & HO-Si-OH & & \\
& & | & & \\
& & OH & &
\end{array}
$$

The advantage of sol-gel-derived over melt-quenching-derived BGs is the generation of different gel products, such as aerogels and gels, that can be characterized for their applications as potential bioactive bone biomaterials.[38,39] One of the possible ways bone bonds to BG is through the formation of a hydroxycarbonate apatite (HCA) layer on the surface of the glasses in contact with body fluid,

similar to the apatite in bone, that would facilitate the formation of a strong bond through the plausible interaction of collagen fibrils from the host bone and the HCA nodules forming on the glass.[32] This process occurs through the release of soluble ionic species from the glass to form a high-surface-area hydrated silica and polycrystalline HCA bilayer on the glass surface.[33] The formation of HCA layer on the surfaces of glasses and bondage to bone can be achieved with compositions of 90 mol% silica in the sol-gel method, whereas osteoconduction and osteoinduction property is achieved at a silica content of 60 mol% or less in melt-derived BGs.[40] The increased bioactivity of sol-gel-derived BGs is due to its enhanced surface area as a result of its nanoporous network, compared to the dense melt-derived BGs, causing an increased rate of dissolution of the soluble ionic species of the BG composition. [41,42]

BGs prepared through the sol-gel method have been widely used for bone repair and regeneration applications.[43–45] The application of BG as a component to develop bone biomaterials has been of great interest due to their biocompatibility, osteoconductivity, biodegradability, and ability to form bone-mimetic mineral phases at their interfaces in physiological conditions.[34,35] BGs are, however, brittle and require the incorporation of a polymer to induce toughness. In addition, an ideal bone biomaterial should mimic the organic-inorganic composition of bone. Therefore, development of sol-gel-derived organic-inorganic bone biomaterials have potential applications in the field of bone tissue engineering.

2.3. Development of sol-gel-derived organic-inorganic bone biomaterials

The use of a degradable polymer and BG together mimic the organic (collagen-rich ECM) and the inorganic (hydroxyapatite) components of bone, respectively.[16] The development of sol-gel-derived organic-inorganic bone biomaterials has gained much attention because of the advantages of combining their properties while achieving bioactive features.[46] In addition, tunable degradation behavior and mechanical properties can be achieved by tailoring the concentrations of organic and inorganic elements.[47]

A common approach in preparing sol-gel-derived organic-inorganic bone biomaterials is by using polymers as matrix and BGs as filler.[48,49] This method can also allow the modulation of the degradation rate of the biomaterial by preparing various concentrations of the polymer and the inorganic component.[48] In addition to preparing tunable biodegradable biomaterials, the preparation of different concentrations of the organic and inorganic elements allows for determining the most

similar composition to bone. Additionally, the mechanical properties can be evaluated as a function of the organic-inorganic ratio to investigate the effects of the prepared compositions.

Among the polymers that can be incorporated into the BG system, synthetic polymers offer increased mechanical strength compared to natural polymers.[45,50] However, natural polymers are preferred because they possess macromolecules that the biological environment recognizes and metabolizes.[51,52] These recognizable macromolecules allow favorable interactions between cells and the ECM which are regulated by an arginine-glycine-aspartic acid (RGD) sequence present within the natural polymer structure, which also functions as a specific integrin recognition site that promotes cell adhesion, preventing cells from apoptosis as well as accelerating tissue regeneration and therefore functioning as a biomimetic peptide.[48,53] Therefore, combining both a natural polymer and sol-gel-derived BG would create a biomaterial that mimics the hierarchical organic-inorganic structure of bone that could potentially improve the mechanical and bioactive response of the biomaterial, as well as its ability to support mineralization and the proliferation of cells.[54]

2.3.1. Incorporation of calcium in sol-gel-derived organic-inorganic bone biomaterials

Calcium is fundamental to the bioactivity of sol-gel tertiary BGs and a key component of osteogenesis that could mimic bone's natural inorganic composition.[55,56] Calcium ions are introduced to the silicate network as a network modifier. The incorporation of calcium ions to the silicate network occurs through ionic bonds with two non-bonding oxygens (NBO). Consequently, their incorporation reduces the network connectivity of the silicate glass. Calcium nitrate has been conventionally used as a calcium source to prepare BGs; however, its use has some disadvantages. The heterogeneity caused by calcium-rich regions and thermal treatments (>400°C) to incorporate calcium ions into the silicate glass network are some of the drawbacks.[57–60] However, its major limitation comes from its incompatibility to incorporate a polymer component for the preparation of organic-inorganic biomaterials at room temperature because of the high-temperature treatment needed to thermally decompose the nitrate.[61,62]

Different calcium precursors that can be used at lower temperatures are required for the synthesis of sol-gel-derived organic-inorganic biomaterials. The use of calcium chloride, a calcium salt, entraps calcium ions in the silicate network. However, the calcium ions are physically entrapped in the glass network and can diffuse upon contact with water or biological fluids. The burst release of ions could cause a change in ionic strength leading to an abrupt change in pH that could cause cytotoxicity.[63]

Calcium alkoxides are another alternative of calcium sources that are used for the preparation of sol-gel-derived organic-inorganic biomaterials.[44,64] Some examples of typical calcium alkoxides used in the sol-gel method are calcium ethoxide and calcium methoxyethoxide. Calcium alkoxides readily hydrolyze alongside other alkoxide precursors, such as silicon alkoxide and phosphorous alkoxide. However, it is necessary to control the rate of the sol-gel reaction when using calcium alkoxides by minimizing the amount of water used which could otherwise cause an uncontrollable hydrolysis reaction resulting in inhomogeneous phases.[65] The main advantage of using calcium alkoxides is that the calcium ions can be incorporated into the silicate network at room temperature, which favors the addition of a polymer for the preparation of organic-inorganic biomaterials.[55,61,66].

2.4. Fourth generation of bone biomaterials

Synthetic bone biomaterials have been evolving throughout the years until obtaining a bone biomaterial that can mimic bone's endogenous microenvironments. Starting with the first generation of biomaterials, which were developed with the purpose to develop a bone substitute with physical properties that matched that of natural bone and were biologically inert inside the human body.[67] The second generation of biomaterials was characterized by their bioactive and resorbable properties, followed by the third generation of biomaterials which stimulated cellular responses through the use of immobilized biomolecules onto the materials and dissolution products from bioactive materials.[33,67,68] The fourth generation of biomaterials are becoming more attractive because they are able to mimic the electrical properties and natural environments in living organisms.[69] Development of electrically conductive bone biomaterials could potentially become a fundamental step for the repair and regeneration of bone.

2.5. Electrical conductivity of native bone

The electrical conductivity of bone was discovered in the 1950s when Fukada and Yasuda observed that by applying mechanical stress to the bone in different directions, electrical signals were generated within the bone and produced an endogenous electric field that supported osteogenic cell proliferation.[70–72] Since then, it has been suggested that stress on the crystalline components of bone produces current to flow and triggers healing and that electrical signals similar to those generated by mechanical stress can enhance fracture-healing.[73,74]

The endogenous electric field is generated by an applied mechanical load on the bone which creates strain gradients, and these strain gradients produce pressure gradients which in turn allow interstitial fluid to flow through small channels known as caniculae within the bone structure. Fluid flows from areas of compression to areas of tension within the stressed bone, and as a result, electrical potentials are generated (**Fig. 2.2**).[75] Electronegative potentials are developed upon compression, producing bone formation, whereas electropositive potentials are produced when bone is under tension, causing bone resorption.[75,76] Therefore, administration of exogenous electrical stimulation at the site of a bone defect can be applied as a way to mimic the normal formation of electrical potentials generated on bone upon application of mechanical loads.

Since the discovery of electrically conductive properties of bone, various methods have been investigated clinically to deliver electrical stimulation in an attempt to aid bone healing ranging from treatment of non-union,[77–79] bone fractures,[80,81] delayed unions,[82–84] osteotomies,[85,86] bone grafts with electrical stimulation,[87–89] and aiding of osteonecrosis.[90,91] Exogenous stimulation of bone healing can be delivered electrically through three main methods. The first approach is an invasive direct electrical current technique to stimulate bone whereby one or multiple cathodes are implanted onto the site of injury and an anode is implanted on soft tissue to permit current flow.[77,92,93] However, this technique carries a significant risk of infection and tissue reaction due to a lack of biocompatibility from the electrodes. Therefore, the two other alternative non-invasive techniques, namely, capacitive coupling and inductive coupling, have received significantly more attention in promoting bone healing. Capacitive coupling uses two electrodes that are placed onto the skin between the bone defects. The electrodes generate an alternating electric field which is delivered to the damaged site.[94,95] However, the need for a high voltage power source in this method is a major limitation since the energy dissipated from the electric field decreases quickly. In the alternative, inductive coupling uses non-invasive electromagnetic field stimulation.[96–98] In this method, one or two current-carrying coils are placed onto the skin, through which pulsed or sinusoidal electromagnetic fields are delivered that subsequently induce an electrical field in the damaged area.[99] Amongst these three techniques, inductive coupling best mimics the natural strain-generated potentials found in bone for its repair.[100,101] However, the principle behind all three techniques has made possible the development of medical devices that have received FDA approval[102,103] to stimulate bone electrically for its healing.[104,105]
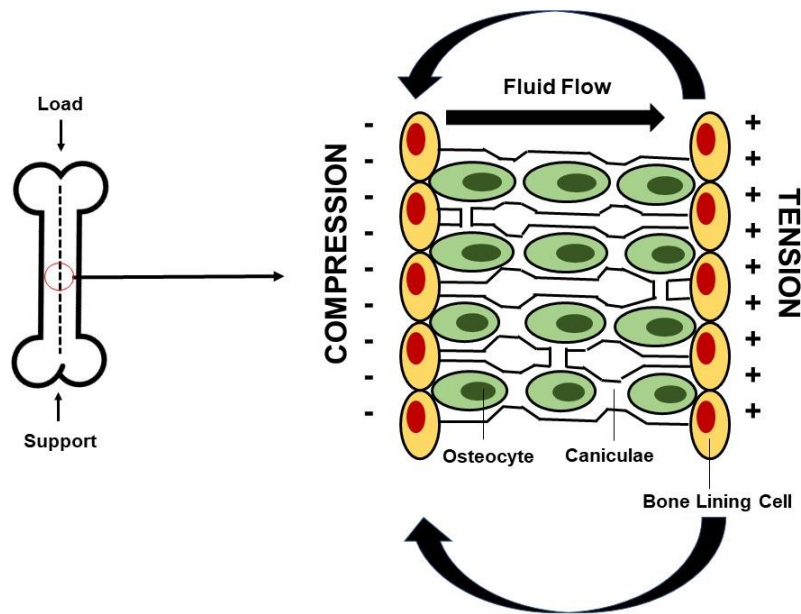
Figure 2.2. Generation of electrical potentials through mechanotransduction in bone. Endogenous electrical potentials are generated in bone through the application of mechanical strain, during which interstitial fluid flows through the caniculae canals from areas of compression, generating electronegative potentials, to areas of tension, producing electropositive potentials. Bone formation is induced upon compression. Adapted from Duncan and Turner.[75] (Used with permission).

Although electrical activity on bone defects promotes accelerated healing, there are some drawbacks, as mentioned above, related to the use of electrodes or the amount of energy required to promote bone regeneration. However, incorporating a conductive material directly onto a polymer scaffold could potentially eliminate the requirement for electrodes and could allow the effects of electrical stimulation on bone regeneration to be explored. Electrically conductive materials are thus emerging for bone tissue engineering due to the natural conductive properties of bone. Although conducting polymers, such as polyaniline (PANI), polypyrrole (PPY), and polythiophene and their derivatives have also been used for bone tissue engineering applications,[106,107] carbon nanotubes (CNTs), graphene, and reduced graphene oxide (rGO) have received the greatest attention for application in bone tissue engineering solutions as they possess different geometrical and morphological structures that can alter their physiological responses and thus enhance their potential to function and treat bone defects.

2.6. Types of carbon-based conductive materials and their preparation strategies

Carbon-based conductive materials are divided into zero-dimensional buckminsterfullerene (C_{60}), one-dimensional carbon nanotubes (CNTs), and two-dimensional graphene sheets. Buckminsterfullerene (C_{60}), also known as fullerene or buckyball, are hollow spheres typically composed of 60 carbon atoms formed through a layer of stacked sp^2 hybridized carbon sheets arranged in hexagonal rings.[108] Buckyballs can exist in other forms and structures, such as ellipsoids or buckytubes, which are also known as carbon nanotubes (CNTs). CNTs are made from single atoms of sp^2 hybridized hexagonal carbon, a single atomic layer of graphitic sheet can be rolled up into a single hollow cylinder creating a structure commonly referred to as single-wall CNT (SWCNT) with typical diameters ranging between 0.5 to 1.5 nm.[109] Alternatively, between 2 - 50 graphitic sheets can be rolled up into a coaxial tube with an outer diameter ranging between 2 and 100 nm forming multi-wall CNT (MWCNT).[109] A major feature of CNTs, is that they possess unique mechanical, chemical, and electrical properties that resulted from their tubular shape and sp^2 hybridized C-C bonds.[110] Lastly, two-dimensional graphene is composed of a two-dimensional monolayer sheet of carbon in which the carbon atoms are sp^2 hybridized, containing σ bonds that create a lattice structure and conjugated π orbitals that form a delocalized electron network providing excellent conductive properties.[111,112]

Carbon-based conductive materials can be produced predominantly based on a technique in which gaseous carbon feedstock reacts in the presence of catalysts to form different shapes of carbon allotropes.[108,113] An example of this is buckyballs, which were first produced through laser ablation[114] and the process later adapted for the synthesis of MWCNTs and SWCNTs in the presence of metal catalyst particles.[115-117] However, MWCNTs were first produced using arc discharge fullerene reactors,[118,119] and were later applied for the synthesis of SWCNTs.[120] Currently, the most affordable and scalable technique to produce CNTs is using chemical vapor deposition (CVD), during which a gaseous carbon precursor is thermally decomposed under the presence of metal catalysts and subsequently deposited inside a nanostructured tubing.[121,122] The scalability of this approach ensures the use of carbon-based materials remains an attractive avenue in clinical-scale production. However, it is not the only method through which CNTs can be produced. CNTs and graphene can also be synthesized either using bottom-up or top-down approaches.[123] Bottom-up techniques include epitaxial growth,[124] pyrolysis,[125,126] and CVD[127] and operate based on the principle of depositing gaseous precursors, typically graphite, onto a substrate. Top-down approaches, however, involve

breaking down graphitic layers until obtaining graphene, and common techniques use exfoliation and reduction processes.[123,128,129]

Another set of popular graphene-based materials includes graphene oxide (GO) and its reduced form, reduced graphene oxide (rGO). GO is synthesized using Hummer's method, in which pristine graphene is first oxidized and then exfoliated to obtain graphene oxide (GO).[130-132] The resulting GO has many oxygen-containing functional groups bound to sp^3 carbons, thus containing both sp^2 and sp^3 hybridization.[133] The change in hybridization reduces the electrical conductivity of GO via disrupting the conjugated structure, in turn blocking conductive connecting pathways between the sp^2 domains.[133] GO can be subsequently reduced to rGO via many different processes, including thermal annealing, electrochemical reduction, or chemical reduction. The reduction process removes oxygen-containing functional groups, resulting in a higher conductivity than GO but lower conductivity than pristine graphene due to remaining oxygen groups.[134]

The different preparation strategies of zero-dimensional fullerene, one-dimensional CNT, and two-dimensional graphene sheets allowed the development of various carbon-based conductive materials that can be incorporated into different biomaterial systems to fabricate bone tissue engineering scaffolds. Their applications in bone repair and regeneration bring significant advantages, leading to the design of novel biomaterials that overcome some of the drawbacks of current bone repair materials (**Table 2.1**).

Table 2.1. Types of carbon-based conductive materials and their role in bone tissue engineering.

Type of Carbon-based Conductive Material	Biomaterials System	Role in Bone Tissue Engineering
Fullerene	- Polyhydroxylated Fullerene (fullerol)[135] - Polyethylene glycol (PEG)-functionalized C_{60} fullerene derivative[136] - Aligned fullerene C60 nanowhiskers[137] - GelMA-fullerol microspheres and bone marrow-derived mesenchymal stem cells	- Antioxidative capacity promotes osteogenic differentiation and mineralization[135] - Good biocompatibility and enhanced osteoblast proliferation[136] - Good osteoblast adherence, aligned oriented cell growth, low toxicity[137] - Antioxidant activity is able to quench intra- and extracellular reactive oxygen species (ROS), promotion of osteogenic stem cell differentiation *in vitro* and bone healing in rat calvarial

	(BMSCs)-laden GelMA-fullerol microspheres[138]	defects via modulating the ROS microenvironment[138]
SWCNT/MWCNT	• CNT-hydroxyapatite (HA) based nanocomposite[139] • Functionalization of 3D-printed poly(propylene fumarate) (PPF) scaffolds with single-stranded deoxyribonucleic acid (ssDNA) bound CNTs[140] • SWCNT gel scaffold with nanofibrous architecture via pairing of heparin functionalized nucleobases[141] • MWCNT compacts[142] • MWCNT-COOH reinforced borosilicate BG scaffolds[143] • Chitosan-hydroxyapatite MWCNT nanocomposite films[144] • Polycaprolactone (PCL)/MWCNT scaffolds[145] • MWCNT reinforced polyvinyl alcohol/Biphasic calcium phosphate (PVA/BCP) scaffold[146] • Bionic mineralized MWCNT scaffold[147]	• Good biocompatibility[139] • Improved cell adhesion, proliferation, and differentiation of preosteoblast cells enabling modulation of cell behavior through electrical stimulation[140] • Targeted drug delivery, increased mechanical properties, improved osteogenic properties through the application of electrical stimulation[141] • Induction of osteogenic gene expression, increased protein adsorption and mineralization, influence of ectopic bone formation[142] • Enhanced mechanical properties, bioactive behavior promoting hydroxyapatite formation, good cell viability, osteogenic initiation[143] • Biocompatible, electrically conductive, and good mechanical properties[144] • Promotion of thick bone tissue formation *in vivo*, increased angiogenesis and mineralization of bone through electrical stimulation *in vivo*, activation of ostoeclastogenesis through electrical stimulation for bone remodeling[145] • Increased mechanical properties, high interconnectivity, good biocompatibility[146] • Improved mechanical properties, enhanced cell growth *in vitro* and *in vivo*, increased osteogenic differentiation and promotion of bone defect repair *in vivo* [147]
Graphene/GO/rGO	• Hyaluronic acid-chitosan with simvastatin[148] • rGO coated collagen scaffolds[149] • Graphene hydrogel membrane[150] • Gelatin methacrylate, acryloyl-β-cyclodextrin, and β-cyclodextrin-functionalized rGO	• Biocompatible and bioactive 3D scaffold with improved osteogenic properties[148] • Enhanced mechanical properties, good biocompatibility, and proliferation of human bone marrow-derived mesenchymal stem cells (hBMSCs), increased bone formation after implantation into cranial bone defects in animal model[149]

• nanocomposite hydrogel patch[151] • Vascularized GO-collagen chamber model[152] • GO-modified silk fibroin/nanohydroxyapatite scaffold loaded with urine-derived stem cells (SCs)[153] • Polylactic acid (PLA)/GO nanocomposite 3D scaffold[154] • Graphene/hydroxyapatite nanoparticle composite hydrogels[155] • Collagen-rGO coated scaffolds[156] • rGO-coated titanium substrates[157] • 3D-printed β-tricalcium phosphate (TCP)-based scaffolds filled with freeze-dried gelatin/rGO-magnesium-arginine matrix[158]	• Guided bone tissue regeneration in rat calvarial model, diffusion of proteins and nutrients, promotion of early osteogenesis and mineralization to induce mature bone formation *in vivo* [150] • Improved mechanical strength, increased conductivity, good biocompatibility, promotion of cell proliferation and osteogenic differentiation, enhanced *in vivo* bone defect repair in rat skull model[151] • Improved bone regeneration *in vivo*, osteoinductive properties and anti-fibrosis effects in animal model, improved angiogenic, mineralization and osteogenic differentiation of BMSCs[152] • Immunomodulation and promotion of bone regeneration *in vivo*, enhanced mechanical properties[153] • Enhanced mechanical properties, good biocompatibility and promotion of cell proliferation and mineralization[154] • Mechanically strong, electrically conductive, and biocompatible[155] • Improved mechanical properties, enhanced osteogenic capability[156] • Promotion of osteogenic differentiation of hMSCs, increased calcium phosphate deposition and osteogenic potential[157] • Enhanced mechanical properties, improved cell proliferation and osteogenic differentiation[158]

2.7. Relevant properties of carbon-based conductive materials for bone tissue engineering

2.7.1. Physico-chemical properties of carbon-based conductive materials

An interesting feature of carbon-based conductive materials is their ability to strongly adsorb most organic compounds.[159] Incorporating carbon-based conductive materials into polymers or ceramics is thus beneficial in bone tissue engineering as carbon-based biomaterials have highly delocalized π-bonds on their surfaces and can adsorb proteins.[160] The addition of carbon-based conductive materials is an important factor in fabricating a tissue-engineered bone since the grafted scaffold can

interact with the host tissue through the materials' protein absorption properties, permitting osteogenic progenitor cells to adhere, implant, and begin to lay down their extracellular matrix (ECM).[161] The establishment of a new ECM is the critical first step in scaffold remodeling and bone tissue regeneration. Adsorption of proteins onto CNTs and graphene surfaces is mediated by several different variables, including the geometry of carbon-based conductive materials and the formation of non-covalent interactions.[160,162] The non-covalent interactions or physical adsorption of proteins with carbon-based conductive materials involves the presence of different binding selectivity, which is governed by the formation of hydrophobic interactions, π-π stacking interactions (van der Waals forces and dispersion forces), electrostatic interactions, and H−π bonds.[160,163,164]

Hydrophobic interactions occur due to the great affinity of the hydrophobic regions of cell-binding proteins with the hydrophobic carbon lattices present in the conductive material.[165] Protein adsorption on CNTs and graphene surfaces strongly depends on the electron density and geometry of protein molecules.[166] In the case of π-π stacking interactions, binding interactions occur when the aromatic side chains of amino acids are oriented parallel with the plane of the carbon-based conductive materials at different charged states.[162,167] Peptides possess different aromatic side chains, resulting in different polarizability properties, which, in turn, influence the strength of binding with carbon-based conductive materials. In general, the higher the polarizability of the protein aromatic side chains, the greater the binding strength. Polarizability of aromatic protein side chains is in increasing order of His<Phe<Tyr<Tryp.[168–170]

Another non-covalent interaction is electrostatic binding, which forms in the presence of different charges between cellular proteins and carbon-based conductive materials. Surface charges vary in carbon-based conductive materials due to the type of product synthesized and the variation of preparation procedures. As an example, GO is a material with a surface rich in negatively charged oxygenated functional groups. The strong negative charge generated by these groups facilitates GO binding with proteins that have either negatively or positively charged surfaces, resulting in electrostatic interactions with various degrees of stability.[160] The importance of material surface structure and functionalization was demonstrated in a study by Chong et al.,[171] in which the strength of protein interactions with various carbon-based conductive materials was assessed.[171] The study revealed that GO and rGO have an increased ability to adsorb proteins compared to SWCNT because it is easier for proteins to bind onto the planar surfaces of graphene compared to the curved surfaces of CNT.[171]

Incorporation of a carbon-based conductive material into a bone tissue engineering scaffold could be beneficial for bone defect treatments since their ability to adsorb proteins allows osteoblasts to attach to the bone scaffold. This step appeared to be crucial for the remodeling and regeneration of bone tissue and as demonstrated in the following studies. Taale et al.[172] developed bioactive carbon-based hybrid 3D scaffolds composed of either CNT-bioactive glass nanoparticles (BGN) or CNT-hydroxyapatite (HA) nanoparticles to assess their protein adsorption capacity using bovine serum albumin (BSA) as a model protein.[172] This study revealed that CNT-BGN had a higher protein adsorption ability than CNT-HA scaffolds due to a plausible electrostatic interaction between the high polarity of BSA and the BGN surface etching/sintering process to remove a sacrificial ZnO template.[172] Similarly, Fu et al.[173] incorporated GO into poly (L-lactic-co-glycolic acid) (PLGA)/HA nanofiber scaffolds and observed that the addition of the carbon-based conductive material significantly increased protein adsorption (**Fig. 2.3A**).[173] PLGA/GO/HA nanofibrous matrices obtained the highest protein adsorption rate of nearly 1.46 and 1.25 times that of PLGA/HA and PLGA/GO nanofibrous matrices, respectively, since the addition of GO and HA improved surface properties resulting in higher specific surface areas.[173] Using materials that increase protein adsorption can therefore promote cell adhesion and proliferation of preosteoblasts, enhancing bone maturation and mineral deposition.[173] Du et al.[174] compared the osteogenic ability of MWCNTs and nanohydroxyapatite (nHA), the main inorganic component of bone, and showed that MWCNTs are more effective materials for the promotion of bone formation.[174] Results showed that MWCNT compacts possessed a higher ability to adsorb fetal bovine serum (FBS) proteins than nHA (**Fig. 2.3B**). High protein adsorption ability had a positive effect in further *in vitro* studies revealing that human adipose-derived mesenchymal stem cells cultured on MWCNT compacts possessed a higher cell attachment strength and proliferation than nHA specimens.[174] In addition, MWCNTs could induce osteogenic differentiation better than nHA since an increased protein concentration modulates the conformation of the adsorbed proteins driving differentiation of cells toward an osteoblastic lineage by the activation of Notch signaling pathways.[174.] Translation of *in vitro* results was further investigated in a rabbit model, where both MWCNTs and nHA compacts were implanted in the dorsal musculatures. Results showed that MWCNT compacts were able to induce ectopic bone formation while nHA did not (**Fig. 2.3C**) as a result of the increased ability of MWCNT compacts to adsorb proteins and drive the formation of new bone tissue.[174]
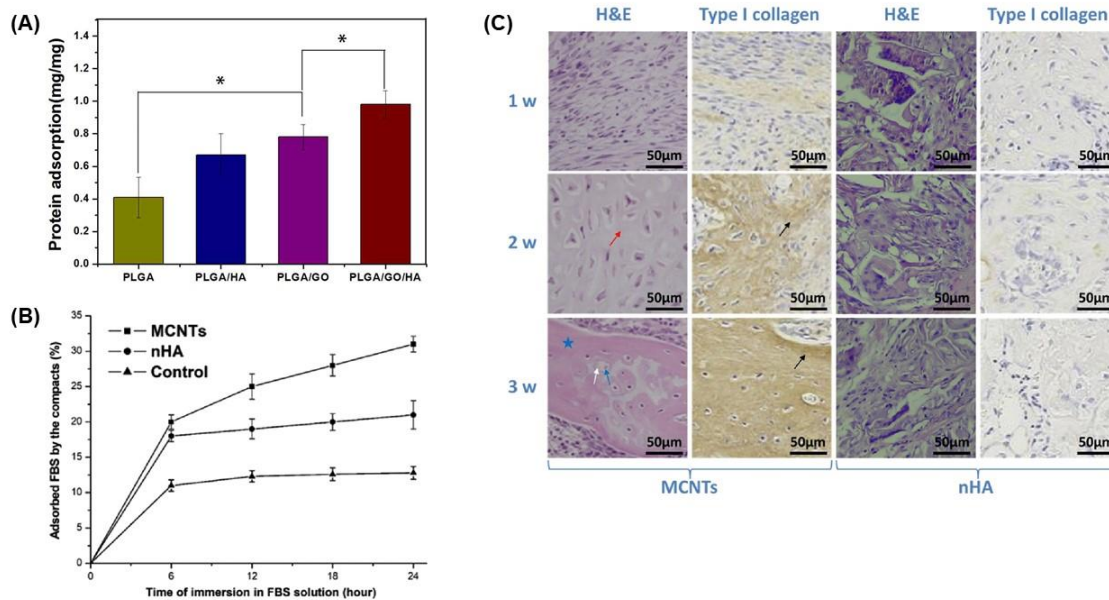
Figure 2.3. Protein adsorption ability of bone tissue engineering scaffolds containing GO and MWCNT promote bone formation. Different carbon-based conductive materials have been incorporated into bone scaffolds to test their protein adsorption efficiencies, which can subsequently drive bone differentiation and maturation. (**A**) Protein adsorption efficiencies of nanofibrous matrices composed of PLGA, GO, and HA were assessed after 24 h using BSA as a model protein. Materials containing GO displayed the highest level of protein adsorption.[173] (**B**) Protein adsorption in compacts composed of either MWCNTs or nHA in an FBS protein model at increasing time points. Compacts containing MWCNT displayed a higher ability to adsorb protein than those composed of nHA.[174]. (**C**) *In vivo*, compacts containing MWCNT implanted into the rabbit dorsal muscle pouch displayed higher levels of new bone and collagen formation as evidenced by hematoxylin and eosin (H&E) and type I collagen staining that is not observed in the nHA compacts.[174] (Used with permission).

2.7.2. Electrical properties of carbon-based conductive materials

Human cortical and cancellous bone have electrical conductivities of 0.02 S/m and 0.07 S/m, respectively.[175] CNTs and graphene are two of the most attractive materials that are being used in scaffolds for bone repair and regeneration applications[143–145,149,151,153,157] as they possess very high electrical conductivities of 10^6-10^7 S/m for pure CNT and 10^8 S/m for pure graphene.[176] Therefore, hybrid bone scaffolds containing a low amount of CNT or graphene can result in a conductivity that recapitulates endogenous bone. The high conductivity of carbon-based conductive materials is a result of their basic microstructural element in which a 2D single-layered graphene sheet is arranged in a honeycomb grid of carbon atoms possessing four electrons in the outer shell, three of them are used

for covalent bonds while the remaining electron is highly mobile promoting electrical conduction.[177] Therefore, the electrical conductivity of bone scaffold composites is more appropriately explained in terms of the percolation threshold.

The percolation threshold is related to the addition of a critical volume fraction of conductive filler within a hybrid material that results in the transition from an insulating state to a significant change of the overall electrical conductivity caused by the formation of a continuous network of conductive particles within the insulating matrix.[178] Percolation threshold is described by an empirical model known as scaling law, expressed as $\sigma(\Phi) = \sigma_0(\Phi - \Phi_c)^t$ where Φc is the percolation threshold concentration and t the critical exponent.[179] Below the critical volume fraction of the percolation threshold, the conductivity of the composite remains electrically insulating since the conductive particles are dispersed into small clusters. Above the critical volume fraction, however, the material no longer behaves as an insulator, and its conductivity increases by many orders of magnitude.[178] The aspect ratio of the conductive fillers determines the percolation threshold value. Graphene and CNT have a length-to-diameter aspect ratio of 0.01 and 100, respectively, which differs due to their different geometrical structures.[176] Therefore, hybrid bone biomaterials containing a low amount of carbon-based conductive materials can significantly increase the overall electrical conductivity, thus requiring a small amount of filler to achieve the percolation threshold.[176]

The advantages of incorporating a carbon-based conductive material directly onto a polymer bone scaffold could, in principle, eliminate the requirement for electrodes that are normally used for the treatment of bone defects since they possess electrically conductive properties (**Fig. 2.4**). Cells are responsive to exogenous electric fields and have been shown to promote key signaling pathways that accelerate osteogenesis and angiogenesis, the main processes for bone regeneration and remodeling, upon application of different field strengths and current densities.[88,180] *In vitro* studies have shown that the application of electrical stimulation through direct, capacitive and inductive coupling induces key molecular pathways at different cellular locations involved in osteogenesis, specifically through the calcium/calmodulin pathway, resulting in minor alternative cellular responses (**Fig. 2.5A**).[88,181] Direct and capacitive coupled stimulation exert their effects on the cell membrane, increasing the intracellular Ca^{2+} concentration and prostaglandin E2 synthesis through calcium translocation via voltage-gated calcium channels.[182] Moreover, inductively coupled stimulation through electromagnetic fields achieves its effects in the cytoplasm where intracellular calcium accumulation is released from reservoirs, such as the endoplasmic reticulum.[183] Application of these exogenous

stimulations results in cellular responses that increase calcium concentration, thus promoting activated calmodulin levels to drive osteoblast cell proliferation, as well as an increased expression of vascular endothelial growth factor (VEGF) and transforming growth factor (TGF)-β1.[181,184,185]
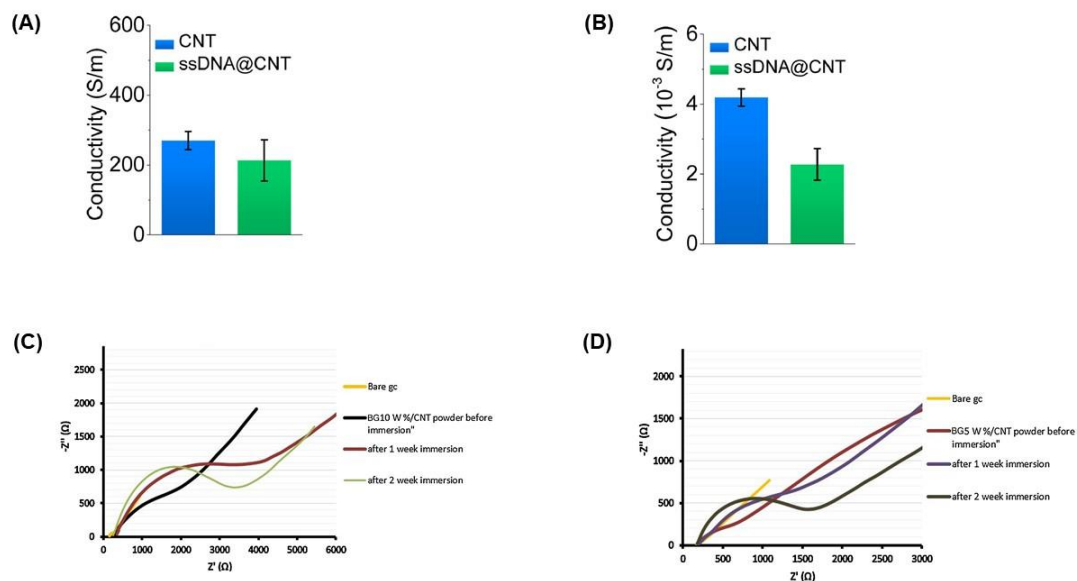
Figure 2.4. Carbon-based conductive materials incorporated into bone tissue engineering scaffolds possess electrically conductive properties, eliminating electrodes in bone healing treatments. Carbon-based conductive materials have been incorporated into bone scaffolds and tested for their electrical properties. Electrical conductivities for CNT and CNT with water-soluble single-stranded deoxyribonucleic acid (ssDNA) (ssDNA@CNT complex) were tested both in solution at a concentration of 0.5 mg/ml (**A**) and in solid-state in the form of pellets (**B**).[140] Electrochemical impedance of (**C**) BG/10 wt.% CNT and (**D**) BG/5 wt.% CNT powders before and after immersion in simulated body fluid (SBF) for one and 2 weeks were measured.[186] (Used with permission).

The addition of carbon-based conductive materials into bone tissue engineering scaffolds improves the effects of bone regeneration rate through electrical stimulation.[141,154,187,188] Injectable conductive hydrogels have gained significant attention in bone tissue engineering since they can be delivered into irregular bone tissue defects while guiding new bone formation.[189–191] As demonstrated in a study by Liu et al.,[192] an injectable conductive hydrogel, BP-CNTpega-gel, composed of CNT-poly(ethylene glycol)-acrylate (CNTpega) with black phosphorous (BP) was developed to support bone regeneration.[192] The inclusion of CNT as the conductive component in the hydrogel allowed BP-CNTpega-gel to possess electrically conductive properties. The highest conductivity value

reported was 0.008 S/m at a CNTpega concentration of 16 mg/ml and a BP nanosheet concentration of 0.8 mg/ml.[192] Furthermore, *in vitro* studies showed that hydrogels with CNTpega effectively respond to exogenous electrical stimulation resulting in increased cell proliferation and ALP activity, as well as an upregulation of osteogenic genes and bone mineralization markers (**Fig. 2.5B-E**).[192] In another study, 3D conductive scaffolds composed of polycaprolactone (PCL) and MWCNTs (0.75 wt.% and 3 wt.%) were developed by e Silva et al.[145] to treat large calvarial bone defects in rats. [145] Conductive scaffolds were produced through extrusion-based additive manufacturing and cut to fit the bone defect in animal skull models (**Fig. 2.5F**).[145] The authors applied non-invasive electrical stimulation to the grafted region for 5 min at 10 µA intensity twice a week for a 60 or 120 day period. Prolonged stimulation at this frequency was considered appropriate for future clinical trials in potential long-term treatment patients.[145] Histomorphometry results from the study showed that thicker tissue formation was present in treatment groups that contained scaffolds than the untreated groups. Furthermore, groups treated with PCL scaffolds containing 3 wt.% MWCNT and additionally underwent electrical stimulation showed elevated connective and denser bone tissue formation (**Fig. 2.5G**).[145] Therefore, incorporating MWCNT into PCL scaffolds and applying electrical stimulation significantly promoted angiogenesis and mineralized bone tissue formation.[145] Similar findings have also been reported in 3D printed PCL/graphene scaffolds in rat calvarial bone defect model.[193] New bone tissue formation was most effective with scaffolds containing graphene and electrical stimulation *in vivo*, leading to organized tissue deposition and bone remodeling.[193] Collectively, these studies demonstrate the translational potential for clinical approaches combining conductive materials into bone scaffolds and electrical stimulation for accelerated repair and regeneration of bone defects.
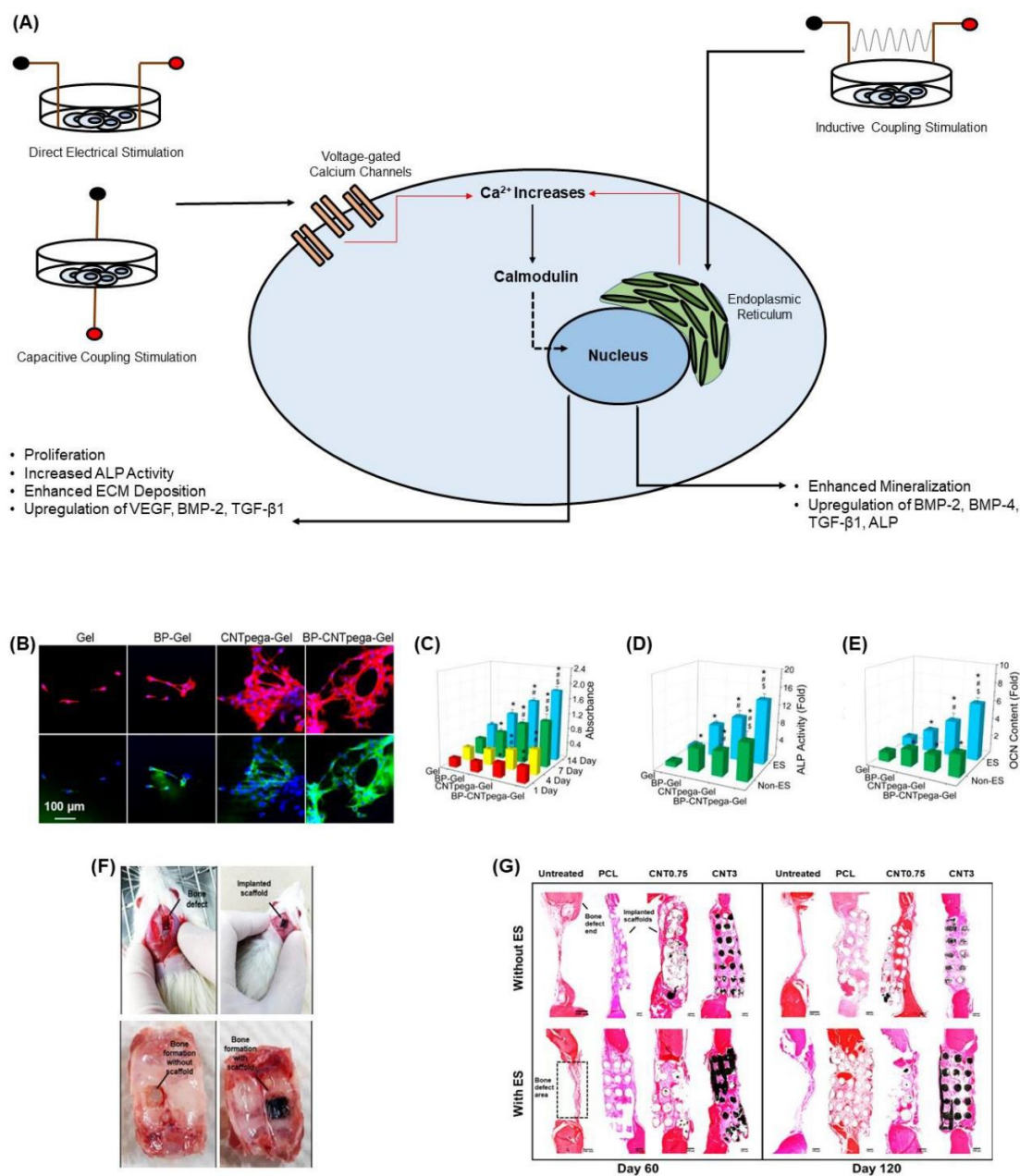
Figure 2.5. Incorporation of carbon-based conductive materials into bone tissue engineering scaffolds promote osteogenesis and *in vivo* bone formation. (**A**) Cellular response of different electrical stimulation techniques promotes osteogenesis through the activation of the calcium/calmodulin pathway.[181] (**B**) Immunofluorescence staining images on MC3T3-E1 preosteoblasts show a cellular response upon the application of electrical stimulation after 7 days post-seeding. Cells were largely elongated and stretched in cell shape.[192] (**C**) Cell proliferation under electrical stimulation was evaluated on the hydrogels at 1, 4, 7, and 14 days post-seeding. At days 1 and 4, CNTpega-gel and BP-CNTpega-gels showed significantly higher cell numbers than BP-gel and oligo(poly(ethylene glycol) fumarate) (OPF) as the control.[192] BP-gel, CNTpega-gel and BPCNTpega-gel showed significantly higher cell numbers than OPF at day 7. However, BP-CNTpega-gel had the highest cell density.[192] (**D**) Intracellular ALP activity was assessed in cells

grown on hydrogels with or without electrical stimulation after 14 days of culture. Cells growing on BP-CNTpega-gel possessed the highest ALP activity.[192] After treatment with electrical stimulation, ALP activities increased for all hydrogels; however, the highest increase in ALP activity was shown in cells growing on BP-CNTpega-gel.[192] (**E**) Determination of osteocalcin (OCN) content in cell culture media after 21 days of culture with and without electrical stimulation. OCN was significantly higher in cells grown on BP-CNTpega-gel under the presence of exogenous stimulation, indicating potential mineralization enhancement.[192] (**F**) Image of bone defect in calvarial animal model as well as the implanted PCL/MWCNT scaffold. Subsequent bone tissue formation with and without scaffold was obtained at day 60 post-implantation.[145] (**G**) The cross-sections of bone tissue regeneration at the bone defect for untreated, PCL and PCL/MWCNT (0.75 wt.% and 3 wt.%) groups after 60 days and 120 days post-operation.[145] PCL/MWCNT 3 wt.% submitted to electrical stimulation formed the highest connective and bone tissues at days 60 and 120.[145] (Used with permission).

2.7.3. Mechanical properties of carbon-based conductive materials

The mechanical properties of carbon-based conductive materials can greatly influence their application and function in different types of biomaterials. CNTs and pristine graphene have different mechanical properties (**Table 2.2**) due to their varied morphological and geometrical structures but possess excellent mechanical strength of approximately 100 times greater than that of steel, but with an extremely low density ($1.3\text{-}2.0$ g/cm^3) compared to metals or ceramics (>2.0 g/cm^3).[194] The high mechanical and tensile strength of CNTs set them apart from other carbon-based materials. In comparison to GO and rGO, both CNTs and graphene possess mechanical strengths greater than that of GO and rGO. GO and rGO monolayers possess a Young's modulus of 207.6 ± 23.4 GPa and 250 ± 150 GPa, respectively.[195,196] The lower strength of GO and rGO is predominantly due to the chemical processes used in their production which decrease their stability originating from the sp2 bond that forms the hexagonal lattice.[197] Mechanical strength is considered one of the most crucial properties in the preparation of a scaffold for bone tissue engineering applications. It is imperative that an implanted scaffold is strong enough to initially withstand the load that the bone tissue would have carried, but it gradually decreases as it is being remodeled by new tissue that eventually takes over the load. Therefore, it is important to know the mechanical properties of different types of bone (**Table 2.2**) in order to establish what concentration of carbon-based conductive material is necessary to design a bone substitute that can support the natural mechanical strength of the defective bone region prior to its regeneration.

Table 2.2. Comparison between the mechanical properties of carbon nanotube and pristine graphene monolayer, cortical and cancellous bone.

Carbon Nanotube	Tensile Strength	10-200 GPa[198-200]
	Compressive Strength	~1 GPa[201]
	Young's modulus	0.27-1.47 TPa[200,202]
	Surface Area	50-1,315 m^2/g[194]
Pristine Graphene Monolayer	Tensile Strength	130.5 GPa[203]
	Compressive Strength	~416 MPa[204]
	Young's modulus	1 TPa[205]
	Surface Area	2,391-2,630 m^2/g[206]
Cortical Bone	Tensile Strength	50 -150 MPa[207]
	Compressive Strength	100 -230 MPa[207]
	Young's modulus	7-30 GPa[207]
Cancellous Bone	Tensile Strength	10-20 MPa[207]
	Compressive Strength	2-12 MPa[207]
	Young's modulus	0.5-0.05 GPa[207]

Carbon-based conductive materials can be used by themselves, but given their overall higher mechanical properties, stress shielding will likely cause bone resorption. Instead, they are incorporated into polymers as secondary structural reinforcing agents to increase the mechanical properties of two- and three-dimensional polymeric bone scaffolds. The unique structures and properties of carbon-based conductive materials provide an ideal solution for creating a bone scaffold that better matches the mechanical properties of natural bone tissue compared to previously explored polymeric-based scaffolds.[208–211]

In a study by Lu et al.[150], a multilayered graphene hydrogel (MGH) membrane was developed to investigate whether the biomaterial possessed the ability to guide bone tissue regeneration in rat calvarial model.[150] Within the regenerating region, diffusion of proteins and nutrients took place through the selective permeability of the MGH membranes promoting early osteogenesis and mineralization which resulted in the formation of mature bone structure surrounded by external and internal cortical bone after eight weeks of implantation.[150] Although MGH membranes are very flexible, they maintain a mechanical strength similar to that of rat braincase with a tensile modulus of 69 ± 5 MPa.[150]

The mechanical strength of a biomaterial can be modulated by altering the proportion of carbon-based material in the final composition. This principle was demonstrated in a study by Belaid et al.[154] which investigated biocompatible polylactic acid (PLA)-based scaffolds produced by 3D printing and the effect of incorporating different concentrations of GO (0.1, 0.2, and 0.3 wt.%) as a reinforcement element for bone healing applications. [154] Pure PLA scaffolds presented a Young's modulus of 2 GPa, but this was significantly increased to 2.6 GPa upon the addition of 0.3 wt.% GO (**Fig. 2.6A**).[154] In addition, materials containing 0.3 wt.% GO presented the highest tensile strength with a value of 39 MPa, whereas pure PLA presented the lowest tensile strength of 34 MPa (**Fig. 2.6B**).[154] However, GO concentrations of 0.1 and 0.2 wt.% showed a decreased tensile strength compared to 0.3 wt.% GO since a lower filler concentration induced flaws at a local scale resulting in a weaker material.[154] Therefore, at higher GO concentrations, the filler is intrinsically stronger than PLA, resulting in a stronger material.[154]

Qian et al.[141] developed a CNT gel scaffold that contained functionalized nucleobase pairing for targeted drug delivery and *in vitro* osteogenesis.[141] The conductive gel scaffold was prepared by functionalizing heparin (HP) with adenine (HP-A) and thymine (HP-T) which were subsequently grafted to aminated CNTs forming CNT-HP-A and CNT-HP-T precursors.[141] The mixture of these precursors resulted in a nucleobase paired CNT gel network. Dynamic time sweep rheological tests were performed in order to investigate the gel network evolution during the gelation process at 37°C. Results showed that CNT-HP-A/CNT-HP-T mixture formed a dynamic network within less than 5 min which was shown by the crossover of storage modulus (G') and loss modulus (G") (**Fig. 2.6C**).[141] In addition, after 14 min a structurally stable network was formed for both CNT and control (HP-A/HP-T) gels, reaching a G' value of around 100 Pa which could translate to the successful development of gels capable of maintaining their 3D shape for therapeutic drug loading purposes.[141] The structural integrity of the scaffold gels were also evaluated through compressive tests, and results were compared before and after loading with bone morphogenetic protein 2 (BMP-2) as a potential osteogenic drug loading model.[141] The compressive modulus of scaffold gels containing CNTs was significantly higher (256 kPa) than that of HP-A/HP-T gels (83 kPa).[141] Loading of gels with 50 ng/ml BMP-2 did not affect the overall compressive strength of the gels, but CNT-containing scaffolds presented a final modulus value of 264 kPa (**Fig. 2.6D**).[141] Furthermore, Bahrami et al.[149] prepared rGO coated collagen (Col-rGO) scaffolds by chemical crosslinking and freeze-drying method to assess their mechanical strength for implantation into rabbit cranial bone defects.[149] Compressive

tests were performed on collagen and Col-rGO scaffolds to evaluate the elastic modulus of the scaffolds.[149] Col-rGO scaffolds showed an elastic modulus of 325 ± 18 kPa, whereas pure collagen scaffolds presented a modulus of 115 ± 16 kPa, which is not sufficient for rabbit cranial bone structural support.[149] The addition of coated rGO on collagen scaffolds not only increased the mechanical strength of the material but enhanced cell viability and proliferation which translated into increased *in vivo* bone formation after 12 weeks of implantation into rabbit cranial bone defects.[149]
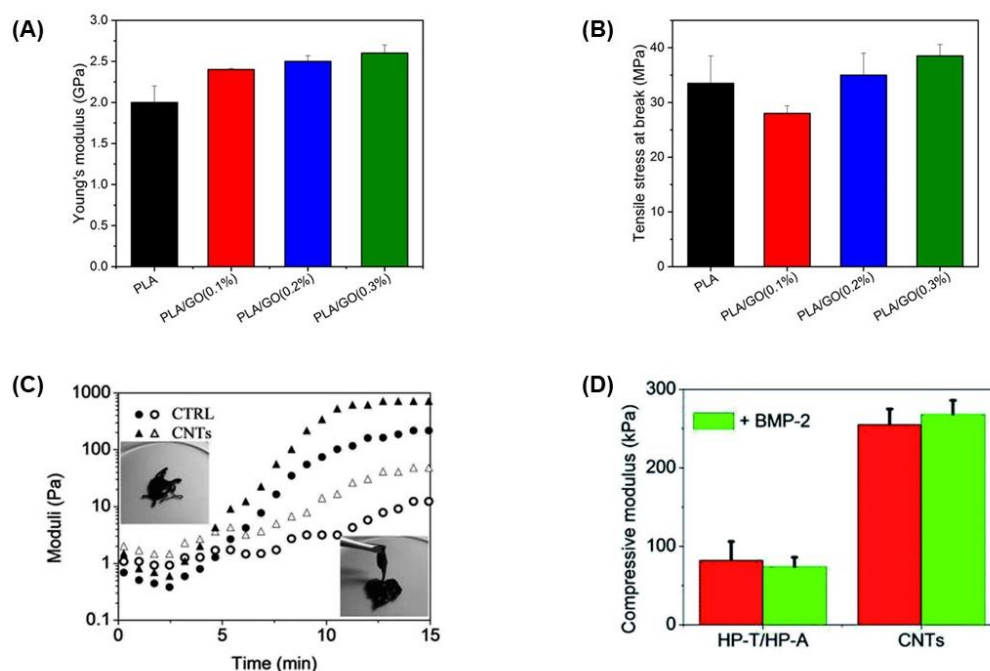
Figure 2.6. Carbon-based conductive materials enhance the mechanical strength of bone tissue engineering scaffolds. (**A**) Young's modulus and (**B**) Tensile strength at break of pure PLA scaffolds and PLA scaffolds containing 0.1, 0.2, and 0.3 wt.% concentrations of GO as a reinforcement filler.[154] Higher concentrations of GO increased the mechanical properties of the PLA-based scaffolds.[154] (**C**) Dynamic time sweep rheological tests were performed to HP-A/HP-T control and CNT-HP-A/CNT-HP-T to assess the gel network evolution at 37°C.[141] A dynamic network was formed in the CNT-HP-A/CNT-HP-T mixture within less than 5 min which was shown by the crossover of storage modulus (G': filled symbols) and loss modulus (G": open symbols).[141] (**D**) Compressive modulus of HP-A/HP-T control and CNT-HP-A/CNT-HP-T with or without BMP-2 loading at 37°C.[141] The compressive modulus of scaffold gels containing CNTs was significantly higher than that of control gels, especially with BMP-2 loading.[141] (Used with permission).

2.8. Cellular processing mechanisms of carbon-based conductive materials

Ideally, bone scaffolds should degrade at a similar rate to the formation of new tissue to maintain the integrity of the repaired region of bone, which can physiologically and mechanically adapt to the natural environment and local load within the body.[43,161] Although carbon-based conductive materials can be degraded through enzymatic oxidation using horseradish peroxidase, or hydrolytically through lipases,[213] the complete degradation and fate of CNTs and graphene-based materials in the body are still relatively unknown. However, *in vitro* and *in vivo* studies have shown that a variety of cell types such as macrophages,[214–216] endothelial cells,[217] pulmonary epithelia,[218,219] intestinal epithelia[220] and neuronal cells[221] can degrade and uptake carbon-based conductive materials. Therefore, understanding how carbon-based conductive materials in bone scaffolds are processed and degraded by the specialized cell types they will interact with will be important for establishing safety in clinical translation.

In vitro studies have shown that carbon-based conductive materials can be internalized by cells; this movement is promoted by the hydrophobic interaction between the material and cell membrane imparted by the phospholipid bi-layer.[222–224] However, cellular internalization is still reliant either on passive or active transport pathways present on the cell membrane. Passive diffusion transport is a non-energy-dependent process in which carbon-based conductive materials land on the surface of cell membranes and penetrate the phospholipid bi-layer, resulting in subsequent transport into the cytoplasm.[224,225] On the other hand, the active pathways are energy-dependent processes and mainly occur through endocytic mechanisms that control the internalization of foreign objects from the cell membrane into cytoplasmic organelles called lysosomes, which can break down extracellular material.[224,226] Although temperature and metabolic inhibitors potentially influence endocytosis, no factors have been identified to date that governs the method or rate at which carbon-based conductive materials are internalized into cells.[224,227] Lacerda et al.[228] investigated the uptake mechanism of functionalized MWCNT (f-MWCNT) with the presence of cell uptake inhibitors at different temperatures and concluded that there was no single mechanism responsible for the transportation of CNTs into cells since 30-50% of f-MWCNT were internalized into cells through an energy-independent pathway, but the remaining f-MWCNT entered cells through endocytosis.[228]

The diameter of the conductive nanomaterial appears to be a critical factor in determining degradation post-internalization. Several studies have reported that small agglomerates of carbon-based

conductive materials are more easily degraded in macrophages through lysosomal and endosomal activity, [223,229,230] in contrast to larger agglomerates of carbon-based conductive materials that are expelled from the cell through exocytosis.[231,232] Once internalized, materials on the nanoscale can migrate to other subcellular organelles.[233,234] This internalization of material into cell and subsequently through the subcellular compartments was first demonstrated by exposure of human monocyte-derived macrophages to SWCNTs ranging from 0.6-3.5 nm in diameter.[233,234] In these studies, SWCNTs were observed to be localized solely within lysosomes two days after exposure, however, after four days, they were observed to have crossed the nuclear membrane, as nanoparticle sizes of less than 40 nm can enter the nuclear pore complex.

In addition to the diameter, the configuration of carbon-based materials can also influence how they are processed cellularly. Work by Mu et al.[235] showed that single MWCNT-COOH and MWCNT-NH2 (20-30 nm diameter and ~1,000 nm average length) were transported into human embryonic kidney epithelial cells (HEK293) through direct passive diffusion, whereas bundled MWCNTs entered cells through endocytosis.[235] The bundled MWCNTs were also subsequently processed and could release single MWCNTs capable of endosomal escape and release into the cytoplasm. Furthermore, those released single MWCNTs of shorter length were also capable of achieving nuclear translocation.[235]

Internalization, degradation, and externalization of carbon-based conductive materials need to be further investigated in osteoblasts and *in vivo* bone defects in order to understand their impact in bone tissue engineering applications and targeted bone drug delivery. In addition, migration of carbon-based conductive materials from bone scaffolds could occur as the scaffold is being remodeled and it is imperative to investigate whether their translocation causes any toxicity and adverse effects.

Processing techniques used to synthesize carbon-based conductive materials influence the physico-chemical properties of the material, causing different potential toxicological interactions.[236] Of key concern within the field is the potential of a carbon-based conductive material to generate reactive oxygen species (ROS), which can cause subcellular damage to organelles and processes, ultimately resulting in cell toxicity.[237] Catalytic metal impurities left over from the material processing are suggested to be one of the main reasons why ROS are formed.[238] The metal catalysts used during synthesis can remain attached to carbon-based conductive materials which can subsequently influence intracellular calcium concentrations, activate transcription factors, and modulate cytokine production

via the generation of free radicals creating ROS and thus inducing acute toxicity.[239] However, carbon-based conductive materials can undergo various treatments to achieve a higher purification to reduce potential metal particles that induce ROS formation. Treatments include; chemical selective oxidations and dissolution of metallic impurities or physical-based purifications that involve the separation of impurities through their physical sizes and aspect ratios.[240]

In addition to impurities, the sizes of carbon-based conductive materials can influence immunological effects in cells. Yoon et al.[241] showed that smaller graphene nanoflakes (30.9 ± 5.4 nm) have a higher uptake affecting cell membrane function, thus inducing apoptosis compared to larger graphene nanoflakes (80.9 ± 5.5 nm) which were shown to be less toxic given that they were mostly aggregated on cell membrane.[241] The effect of length and diameter of CNTs have also been shown to impact toxicity, with shorter CNTs (sub-1 µm) can easily penetrate into cell membranes and internalize accumulating in cell lysosomes,[242] whereas longer CNTs (> 8 µm in length and < 1.25 µm in diameter) are not engulfed into cell membranes and degraded causing acute inflammation increasing the production of ROS and cytokines thus exerting more significant biological effects.[243] However, Zhang et al.[244] showed that larger CNTs were taken up by macrophages and that the rope-like structures of CNTs had similar properties to spherical nanoparticles where cytotoxicity increased upon higher internalization concentration of CNTs causing cell death with levels above 20 pg/cell.[244] Another factor that influences cytotoxicity is the dose of carbon-based conductive materials to cells. The effects of pristine GO concentrations on the viability of bone mesenchymal stem cells (BMSCs) was investigated and showed that high concentrations (10 µg/ml) of GO inhibited proliferation of BMSCs, while low concentrations (0.1 µg/ml) enhanced cell proliferation.[245] Similar behavior was observed in biphasic calcium phosphate (BCP) coated with different concentrations of rGO; osteoblast viability was maintained above 80% at concentrations below 62.5 µg/ml, but significantly decreased at concentrations above 100 µg/ml.[246]

Ultimately, the aim of designing tissue engineering scaffolds containing carbon-based conductive materials is to utilize them for clinical translation. Therefore, understanding the cellular processing mechanisms that one- and two-dimensional carbon-based conductive materials undergo and the factors that influence their performance is important. Preclinical studies have shown that carbon-based conductive materials can be excreted via the kidneys and urinary tract after intravenous injection when graphene sheets are well dispersed and CNTs have a high degree of disaggregation.[247–250] These studies also provided evidence that the excretion of carbon-based conductive materials from the body

is dependent on size and shape. Although CNTs of dimensions over 2000 nm length and over 30 nm diameter, [249] and GO sheets of over 5 nm thickness[250] accumulated in the liver and spleen, they showed very little toxicity *in vivo* and eventually cleared from the body.[249,250] Since incorporating carbon-based conductive materials into bone tissue engineering scaffolds is primarily for implants, they are less likely to enter the bloodstream and translocate to other organs.[251,252] Usui et al.[253] investigated the effects of pure MWCNT, with an average diameter of 80 nm and a length from 10 to 20 µm, in mouse skull and tibial defects to assess their compatibility and influence on bone healing.[253] Results showed that MWCNTs caused a reduced local inflammatory reaction, possessed high bone tissue compatibility and were able to integrate into new bone tissue formation.[253]

Although *in vitro* and *in vivo* research have shown that developing bone scaffolds with CNTs or graphene-based materials has positively influenced cell proliferation, mineralization and bone regeneration with minimal toxicological effects and inflammation,[142,152,251,254] further investigations are still required to better understand their impact in the human body and whether they can be degraded or migrated for their excretion through the kidney and bile ducts for their future use in clinical translation for bone tissue engineering solutions.

2.9. Hypothesis and objectives

Hypothesis: Gelatin-based conductive and bioactive glass nanocomposites promote *in vitro* biomineralization and osteogenic differentiation of stem cells.

Objectives:

(i)   Synthesis and characterizations of calcium chloride- and calcium ethoxide-based organic-inorganic nanocomposites.

(ii)   Preparation and characterization of electrically conductive, bioactive, and biodegradable organic-inorganic nanocomposite biomaterials.

(iii)   Evaluation of *in vitro* cell studies on the effects of electrically conductive and bioactive organic-inorganic nanocomposites to direct osteogenic differentiation on cells.

2.10. References

[1]   T. Wang, X. Yang, X. Qi, C. Jiang, Osteoinduction and proliferation of bone-marrow stromal cells in three-dimensional poly (ε-caprolactone)/ hydroxyapatite/collagen scaffolds, J Transl Med 13 (2015) 152. https://doi.org/10.1186/s12967-015-0499-8.

[2]   M. Tavafoghi, M. Cerruti, The role of amino acids in hydroxyapatite mineralization, J. R. Soc. Interface. 13 (2016) 20160462. https://doi.org/10.1098/rsif.2016.0462.

[3]   N.H. Hart, R.U. Newton, J. Tan, T. Rantalainen, P. Chivers, A. Siafarikas, S. Nimphius, Biological basis of bone strength: anatomy, physiology and measurement, J Musculoskelet Neuronal Interact 20 (2020) 347–371.

[4]   R. Zhao, R. Yang, P.R. Cooper, Z. Khurshid, A. Shavandi, J. Ratnayake, Bone Grafts and Substitutes in Dentistry: A Review of Current Trends and Developments, Molecules 26 (2021) 3007. https://doi.org/10.3390/molecules26103007.

[5]   J.T.B. Ratnayake, M. Mucalo, G.J. Dias, Substituted hydroxyapatites for bone regeneration: A review of current trends: Substituted HA for Bone Regeneration, J. Biomed. Mater. Res. 105 (2017) 1285–1299. https://doi.org/10.1002/jbm.b.33651.

[6]   S.M. Gorski, C. Dong, Andreas.H. Krieg, M. Haug, Vascularized Bone Graft Reconstruction Following Bone Tumor Resection at a Multidisciplinary Sarcoma Center: Outcome Analysis, Anticancer Res 41 (2021) 5015–5023. https://doi.org/10.21873/anticanres.15316.

[7]   C.E. Gillman, A.C. Jayasuriya, FDA-approved bone grafts and bone graft substitute devices in bone regeneration, Materials Science and Engineering: C 130 (2021) 112466. https://doi.org/10.1016/j.msec.2021.112466.

[8]   J.R. Jones, S. Lin, S. Yue, P.D. Lee, J.V. Hanna, M.E. Smith, R.J. Newport, Bioactive glass scaffolds for bone regeneration and their hierarchical characterisation, Proc Inst Mech Eng H 224 (2010) 1373–1387. https://doi.org/10.1243/09544119JEIM836.

[9]   J.-H. Zeng, S.-W. Liu, L. Xiong, P. Qiu, L.-H. Ding, S.-L. Xiong, J.-T. Li, X.-G. Liao, Z.-M. Tang, Scaffolds for the repair of bone defects in clinical studies: a systematic review, J Orthop Surg Res 13 (2018) 33. https://doi.org/10.1186/s13018-018-0724-2.

[10]   M. Orciani, M. Fini, R. Di Primio, M. Mattioli-Belmonte, Biofabrication and Bone Tissue Regeneration: Cell Source, Approaches, and Challenges, Front. Bioeng. Biotechnol. 5 (2017). https://doi.org/10.3389/fbioe.2017.00017.

[11]   E.L. Francois, M.J. Yaszemski, Preclinical Bone Repair Models in Regenerative Medicine, in: Principles of Regenerative Medicine, Elsevier, 2019: pp. 761–767. https://doi.org/10.1016/B978-0-12-809880-6.00043-6.

[12]   D. Gabriel, T. Dvir, D.S. Kohane, Delivering bioactive molecules as instructive cues to engineered tissues, Expert Opinion on Drug Delivery 9 (2012) 473–492. https://doi.org/10.1517/17425247.2012.668521.

[13]   T.A. Holland, A.G. Mikos, Advances in drug delivery for articular cartilage, Journal of Controlled Release 86 (2003) 1–14. https://doi.org/10.1016/S0168-3659(02)00373-5.

[14]   L. Roseti, V. Parisi, M. Petretta, C. Cavallo, G. Desando, I. Bartolotti, B. Grigolo, Scaffolds for Bone Tissue Engineering: State of the art and new perspectives, Materials Science and Engineering: C 78 (2017) 1246–1262. https://doi.org/10.1016/j.msec.2017.05.017.

[15]   M.M. Stevens, Biomaterials for bone tissue engineering, Materials Today 11 (2008) 18–25. https://doi.org/10.1016/S1369-7021(08)70086-5.

[16]   B.A. Allo, Sol-Gel Derived Biodegradable and Bioactive Organic-Inorganic Hybrid Biomaterials for Bone Tissue Engineering, (n.d.) 219.

[17]   C. Mangano, V. Perrotti, J.A. Shibli, F. Mangano, L. Ricci, A. Piattelli, G. Iezzi, Maxillary Sinus Grafting with Biphasic Calcium Phosphate Ceramics: Clinical and Histologic Evaluation in Man, JOMI 28 (2013) 51–56. https://doi.org/10.11607/jomi.2667.

[18]   C. Schwartz, R. Bordei, Biphasic phospho-calcium ceramics used as bone substitutes are efficient in the management of severe acetabular bone loss in revision total hip arthroplasties., Eur J Orthop Surg Traumatol 15 (2005) 191–196. https://doi.org/10.1007/s00590-005-0244-8.

[19]   R.D.A. Gaasbeek, H.G. Toonen, R.J. van Heerwaarden, P. Buma, Mechanism of bone incorporation of β-TCP bone substitute in open wedge tibial osteotomy in patients, Biomaterials 26 (2005) 6713–6719. https://doi.org/10.1016/j.biomaterials.2005.04.056.

[20]   J.H. Scheer, L.E. Adolfsson, Tricalcium phosphate bone substitute in corrective osteotomy of the distal radius, Injury 40 (2009) 262–267. https://doi.org/10.1016/j.injury.2008.08.013.

[21]   S. Zwingenberger, C. Nich, R.D. Valladares, Z. Yao, M. Stiehler, S.B. Goodman, Recommendations and Considerations for the Use of Biologics in Orthopedic Surgery, (2012) 12.

[22]   A.J. Salinas, P. Esbrit, M. Vallet-Regí, A tissue engineering approach based on the use of bioceramics for bone repair, Biomater. Sci. 1 (2013) 40–51. https://doi.org/10.1039/C2BM00071G.

[23]   Y.X. Pang, X. Bao, Influence of temperature, ripening time and calcination on the morphology and crystallinity of hydroxyapatite nanoparticles, Journal of the European Ceramic Society 23 (2003) 1697–1704. https://doi.org/10.1016/S0955-2219(02)00413-2.

[24]   M. Jevtić, M. Mitrić, S. Škapin, B. Jančar, N. Ignjatović, D. Uskoković, Crystal Structure of Hydroxyapatite Nanorods Synthesized by Sonochemical Homogeneous Precipitation, Crystal Growth & Design 8 (2008) 2217–2222. https://doi.org/10.1021/cg7007304.

[25]   R. Enderle, F. Götz-Neunhoeffer, M. Göbbels, F.A. Müller, P. Greil, Influence of magnesium doping on the phase transformation temperature of β-TCP ceramics examined by Rietveld refinement, Biomaterials 26 (2005) 3379–3384. https://doi.org/10.1016/j.biomaterials.2004.09.017.

[26]   D.L. Johnson, New Method of Obtaining Volume, Grain-Boundary, and Surface Diffusion Coefficients from Sintering Data, Journal of Applied Physics 40 (1969) 192–200. https://doi.org/10.1063/1.1657030.

[27]   M.T. Fulmer, I.C. Ison, C.R. Hankermayer, B.R. Constantz, J. Ross, Measurements of the solubilities and dissolution rates of several hydroxyapatites, Biomaterials 23 (2002) 751–755. https://doi.org/10.1016/S0142-9612(01)00180-6.

[28]   L. Wang, J. Lu, F. Xu, F. Zhang, Dynamics of crystallization and dissolution of calcium orthophosphates at the near-molecular level, Chin. Sci. Bull. 56 (2011) 713–721. https://doi.org/10.1007/s11434-010-4184-2.

[29]   M. Nagano, T. Nakamura, T. Kokubo, M. Tanahashi, M. OgawaS, Differences of bone bonding ability and degradation behaviour in tivo between amorphous calcium phosphate and highly crystalline hydroxyapatite coating, 17 (1996) 7.

[30]   A. Ogose, N. Kondo, H. Umezu, T. Hotta, H. Kawashima, K. Tokunaga, T. Ito, N. Kudo, M. Hoshino, W. Gu, Histological assessment in grafts of highly purified beta-tricalcium phosphate (OSferion®) in human bones, Biomaterials 27 (2006) 1542–1549. https://doi.org/10.1016/j.biomaterials.2005.08.034.

[31]   A. Ogose, T. Hotta, H. Kawashima, N. Kondo, W. Gu, T. Kamura, N. Endo, Comparison of hydroxyapatite and beta tricalcium phosphate as bone substitutes after excision of bone tumors, J. Biomed. Mater. Res. 72B (2005) 94–101. https://doi.org/10.1002/jbm.b.30136.

[32]   L.L. Hench, R.J. Splinter, W.C. Allen, T.K. Greenlee, Bonding mechanisms at the interface of ceramic prosthetic materials, J. Biomed. Mater. Res. 5 (1971) 117–141. https://doi.org/10.1002/jbm.820050611.

[33]   J.R. Jones, E. Gentleman, J. Polak, Bioactive Glass Scaffolds for Bone Regeneration, Elements 3 (2007) 393–399. https://doi.org/10.2113/GSELEMENTS.3.6.393.

[34]   N. Aslankoohi, D. Mondal, A.S. Rizkalla, K. Mequanint, Bone Repair and Regenerative Biomaterials: Towards Recapitulating the Microenvironment, Polymers 11 (2019) 1437. https://doi.org/10.3390/polym11091437.

[35]   D. Mondal, S.J. Dixon, K. Mequanint, A.S. Rizkalla, Bioactivity, Degradation, and Mechanical Properties of Poly(vinylpyrrolidone- *co* -triethoxyvinylsilane)/Tertiary Bioactive Glass Hybrids, ACS Appl. Bio Mater. 1 (2018) 1369–1381. https://doi.org/10.1021/acsabm.8b00344.

[36]   L.L. Hench, J.K. West, The sol-gel process, Chem. Rev. 90 (1990) 33–72. https://doi.org/10.1021/cr00099a003.

[37]   W. Sakuma, S. Yamasaki, S. Fujisawa, T. Kodama, J. Shiomi, K. Kanamori, T. Saito, Mechanically Strong, Scalable, Mesoporous Xerogels of Nanocellulose Featuring Light Permeability, Thermal Insulation, and Flame Self-Extinction, ACS Nano 15 (2021) 1436–1444. https://doi.org/10.1021/acsnano.0c08769.

[38]   D. Ksouri, H. Khireddine, A. Aksas, T. Valente, F. Bir, N. Slimani, B. Cabal, R. Torrecillas, J.D. Santos, Synthesis of ternary bioactive glass derived aerogel and xerogel: study of their structure and bioactivity, Nova Biotechnologica et Chimica 17 (2018) 150–159. https://doi.org/10.2478/nbec-2018-0016.

[39]   A. Pérez-Moreno, M. Piñero, R. Fernández-Montesinos, G. Pinaglia-Tobaruela, M.V. Reyes-Peces, M.D.M. Mesa-Díaz, J.I. Vilches-Pérez, L. Esquivias, N. De La Rosa-Fox, M. Salido, Chitosan-Silica Hybrid Biomaterials for Bone Tissue Engineering: A Comparative Study of Xerogels and Aerogels, Gels 9 (2023) 383. https://doi.org/10.3390/gels9050383.

[40]   R. Li, A.E. Clark, L.L. Hench, An investigation of bioactive glass powders by sol-gel processing, J of Applied Biomaterials 2 (1991) 231–239. https://doi.org/10.1002/jab.770020403.

[41]   P. Sepulveda, J.R. Jones, L.L. Hench, Characterization of melt-derived 45S5 and sol-gel-derived 58S bioactive glasses, J. Biomed. Mater. Res. 58 (2001) 734–740. https://doi.org/10.1002/jbm.10026.

[42]   P. Sepulveda, J.R. Jones, L.L. Hench, *In vitro* dissolution of melt-derived 45S5 and sol-gel derived 58S bioactive glasses, J. Biomed. Mater. Res. 61 (2002) 301–311. https://doi.org/10.1002/jbm.10207.

[43]   B.A. Allo, A.S. Rizkalla, K. Mequanint, Hydroxyapatite Formation on Sol–Gel Derived Poly(ε-Caprolactone)/Bioactive Glass Hybrid Biomaterials, ACS Appl. Mater. Interfaces 4 (2012) 3148–3156. https://doi.org/10.1021/am300487c.

[44]   D. Mondal, S. Lin, A.S. Rizkalla, K. Mequanint, Porous and biodegradable polycaprolactone-borophosphosilicate hybrid scaffolds for osteoblast infiltration and stem cell differentiation, Journal of the Mechanical Behavior of Biomedical Materials 92 (2019) 162–171. https://doi.org/10.1016/j.jmbbm.2019.01.011.

[45]   N. Aslankoohi, K. Mequanint, Intrinsically fluorescent bioactive glass-poly(ester amide) hybrid microparticles for dual drug delivery and bone repair, Materials Science and Engineering: C 128 (2021) 112288. https://doi.org/10.1016/j.msec.2021.112288.

[46]   M. Prokopowicz, A. Szewczyk, W. Sawicki, Bioactive monolithic composites of silica/polydimethylsiloxane/calcium phosphate obtained at room temperature in sol–gel micromolding technique, Materials Letters 184 (2016) 239–242. https://doi.org/10.1016/j.matlet.2016.08.063.

[47]   H.H. Lu, S.F. El-Amin, K.D. Scott, C.T. Laurencin, Three-dimensional, bioactive, biodegradable, polymer–bioactive glass composite scaffolds with improved mechanical properties support collagen synthesis and mineralization of human osteoblast-like cells *in vitro*, J Biomedical Materials Res 64A (2003) 465–474. https://doi.org/10.1002/jbm.a.10399.

[48]   R. Arambula-Maldonado, Y. Liu, M. Xing, K. Mequanint, Bioactive and electrically conductive GelMA-BG-MWCNT nanocomposite hydrogel bone biomaterials, Biomaterials Advances 154 (2023) 213616. https://doi.org/10.1016/j.bioadv.2023.213616.

[49]   Y. Li, Y. Guo, W. Niu, M. Chen, Y. Xue, J. Ge, P.X. Ma, B. Lei, Biodegradable Multifunctional Bioactive Glass-Based Nanocomposite Elastomers with Controlled Biomineralization Activity, Real-Time Bioimaging Tracking, and Decreased Inflammatory Response, ACS Appl. Mater. Interfaces 10 (2018) 17722–17731. https://doi.org/10.1021/acsami.8b04856.

[50]   D. Mondal, S.J. Dixon, K. Mequanint, A.S. Rizkalla, Mechanically-competent and cytocompatible polycaprolactone-borophosphosilicate hybrid biomaterials, Journal of the Mechanical Behavior of Biomedical Materials 75 (2017) 180–189. https://doi.org/10.1016/j.jmbbm.2017.07.010.

[51]   P.C. Pires, F. Mascarenhas-Melo, K. Pedrosa, D. Lopes, J. Lopes, A. Macário-Soares, D. Peixoto, P.S. Giram, F. Veiga, A.C. Paiva-Santos, Polymer-based biomaterials for pharmaceutical and biomedical applications: A focus on topical drug administration, European Polymer Journal 187 (2023) 111868. https://doi.org/10.1016/j.eurpolymj.2023.111868.

[52]   J. Hum, A. Boccaccini, Collagen as Coating Material for 45S5 Bioactive Glass-Based Scaffolds for Bone Tissue Engineering, IJMS 19 (2018) 1807. https://doi.org/10.3390/ijms19061807.

[53]   M.C. Echave, P. Sánchez, J.L. Pedraz, G. Orive, Progress of gelatin-based 3D approaches for bone regeneration, Journal of Drug Delivery Science and Technology 42 (2017) 63–74. https://doi.org/10.1016/j.jddst.2017.04.012.

[54]   C. Gao, Q. Gao, Y. Li, M.N. Rahaman, A. Teramoto, K. Abe, *In vitro* evaluation of electrospun gelatin-bioactive glass hybrid scaffolds for bone regeneration, J. Appl. Polym. Sci. 127 (2013) 2588–2599. https://doi.org/10.1002/app.37946.

[55]   B. Yu, C.A. Turdean-Ionescu, R.A. Martin, R.J. Newport, J.V. Hanna, M.E. Smith, J.R. Jones, Effect of Calcium Source on Structure and Properties of Sol–Gel Derived Bioactive Glasses, Langmuir 28 (2012) 17465–17476. https://doi.org/10.1021/la303768b.

[56]   C. Bossard, H. Granel, É. Jallot, V. Montouillout, F. Fayon, J. Soulié, C. Drouet, Y. Wittrant, J. Lao, Mechanism of Calcium Incorporation Inside Sol–Gel Silicate Bioactive Glass and the Advantage of Using Ca(OH)$_2$ over Other Calcium Sources, ACS Biomater. Sci. Eng. 5 (2019) 5906–5915. https://doi.org/10.1021/acsbiomaterials.9b01245.

[57]   B. Yu, G. Poologasundarampillai, C. Turdean-Ionescu, M.E. Smith, J.R. Jones, A New Calcium Source for Bioactive Sol-Gel Hybrids, Bioceram. Dev. Appl. 1 (2011) 1–3. https://doi.org/10.4303/bda/D110178.

[58]   B.A.E. Ben-Arfa, I.E. Palamá, I.M. Miranda Salvado, J.M.F. Ferreira, R.C. Pullar, The role of calcium (source & content) on the in vitro behaviour of sol–gel quaternary glass series, Ceramics International 46 (2020) 1065–1075. https://doi.org/10.1016/j.ceramint.2019.09.073.

[59]   S. Lin, C. Ionescu, S. Baker, M.E. Smith, J.R. Jones, Characterisation of the inhomogeneity of sol–gel-derived SiO2–CaO bioactive glass and a strategy for its improvement, J Sol-Gel Sci Technol 53 (2010) 255–262. https://doi.org/10.1007/s10971-009-2085-0.

[60]   A. Rámila, F. Balas, M. Vallet-Regí, Synthesis Routes for Bioactive Sol−Gel Glasses: Alkoxides versus Nitrates, Chem. Mater. 14 (2002) 542–548. https://doi.org/10.1021/cm0110876.

[61]   N. Aslankoohi, K. Mequanint, Poly(ester amide)–Bioactive Glass Hybrid Biomaterials for Bone Regeneration and Biomolecule Delivery, ACS Appl. Bio Mater. 3 (2020) 3621–3630. https://doi.org/10.1021/acsabm.0c00257.

[62]   J.R. Jones, Review of bioactive glass: From Hench to hybrids, Acta Biomaterialia 9 (2013) 4457–4486. https://doi.org/10.1016/j.actbio.2012.08.023.

[63]   S. Maeno, Y. Niki, H. Matsumoto, H. Morioka, T. Yatabe, A. Funayama, Y. Toyama, T. Taguchi, J. Tanaka, The effect of calcium ion concentration on osteoblast viability, proliferation and differentiation in monolayer and 3D culture, Biomaterials 26 (2005) 4847–4855. https://doi.org/10.1016/j.biomaterials.2005.01.006.

[64]   N. Aslankoohi, K. Mequanint, Poly(ester amide)–Bioactive Glass Hybrid Biomaterials for Bone Regeneration and Biomolecule Delivery, ACS Appl. Bio Mater. 3 (2020) 3621–3630. https://doi.org/10.1021/acsabm.0c00257.

[65]   A. Ruiz-Clavijo, A. Hurt, A. Kotha, N. Coleman, Effect of Calcium Precursor on the Bioactivity and Biocompatibility of Sol-Gel-Derived Glasses, JFB 10 (2019) 13. https://doi.org/10.3390/jfb10010013.

[66]   J. Lao, X. Dieudonné, M. Benbakkar, É. Jallot, Bioactive glass coating on gelatin scaffolds at ambient temperature: easy route to make polymer scaffolds become bioactive, J Mater Sci 52 (2017) 9129–9139. https://doi.org/10.1007/s10853-017-0781-7.

[67]   L.L. Hench, I. Thompson, Twenty-first century challenges for biomaterials, J. R. Soc. Interface 7 (2010). https://doi.org/10.1098/rsif.2010.0151.focus.

[68]   J. Jeong, J.H. Kim, J.H. Shim, N.S. Hwang, C.Y. Heo, Bioactive calcium phosphate materials and applications in bone regeneration, Biomater Res 23 (2019) 4. https://doi.org/10.1186/s40824-018-0149-3.

[69]   G.G. Dos Santos, M.S. Malherbi, N.S. De Souza, G.B. César, T.T. Tominaga, R.Y. Miyahara, P.D.S.B. De Mendonça, D.R. Faria, J.M. Rosso, V.F. Freitas, W.R. Weinand, G.S. Dias, I.A. Santos, L.F. Cotica, T.G.M. Bonadio, 4th Generation Biomaterials Based on PVDF-Hydroxyapatite

Composites Produced by Electrospinning: Processing and Characterization, Polymers 14 (2022) 4190. https://doi.org/10.3390/polym14194190.

[70]   E. Fukada, I. Yasuda, On the Piezoelectric Effect of Bone, J. Phys. Soc. Jpn. 12 (1957) 1158–1162. https://doi.org/10.1143/JPSJ.12.1158.

[71]   The classic: Fundamental aspects of fracture treatment by Iwao Yasuda, reprinted from J. Kyoto Med. Soc., 4:395-406, 1953, Clin Orthop Relat Res (1977) 5–8.

[72]   B. Tandon, J.J. Blaker, S.H. Cartmell, Piezoelectric materials as stimulatory biomedical materials and scaffolds for bone repair, Acta Biomaterialia 73 (2018) 1–20. https://doi.org/10.1016/j.actbio.2018.04.026.

[73]   C.T. Brighton, W. Wang, R. Seldes, G. Zhang, S.R. Pollack, Signal Transduction in Electrically Stimulated Bone Cells:, The Journal of Bone and Joint Surgery-American Volume 83 (2001) 1514–1523. https://doi.org/10.2106/00004623-200110000-00009.

[74]   M. Cerrolaza, V. Duarte, D. Garzón-Alvarado, Analysis of Bone Remodeling Under Piezoelectricity Effects Using Boundary Elements, J Bionic Eng 14 (2017) 659–671. https://doi.org/10.1016/S1672-6529(16)60432-8.

[75]   R.L. Duncan, C.H. Turner, Mechanotransduction and the functional response of bone to mechanical strain, Calcif Tissue Int 57 (1995) 344–358. https://doi.org/10.1007/BF00302070.

[76]   D. Lilly-Masuda, S. Towne, Bioelectricity and Bone Healing, J Orthop Sports Phys Ther 7 (1985) 54–58. https://doi.org/10.2519/jospt.1985.7.2.54.

[77]   R.B. Heppenstall, Constant Direct-current Treatment for Established Nonunion of the Tibia:, Clinical Orthopaedics and Related Research NA; (1983) 179???184. https://doi.org/10.1097/00003086-198309000-00020.

[78]   C.T. Brighton, Treatment of Nonunion of the Tibia with Constant Direct Current (1980 Fitts Lecture, A.A.S.T.):, The Journal of Trauma: Injury, Infection, and Critical Care 21 (1981) 189–195. https://doi.org/10.1097/00005373-198103000-00001.

[79]   I.S. Aleem, I. Aleem, N. Evaniew, J.W. Busse, M. Yaszemski, A. Agarwal, T. Einhorn, M. Bhandari, Efficacy of Electrical Stimulators for Bone Healing: A Meta-Analysis of Randomized Sham-Controlled Trials, Sci Rep 6 (2016) 31724. https://doi.org/10.1038/srep31724.

[80]   C.A. Bassett, S.N. Mitchell, S.R. Gaston, Treatment of ununited tibial diaphyseal fractures with pulsing electromagnetic fields.:, The Journal of Bone & Joint Surgery 63 (1981) 511–523. https://doi.org/10.2106/00004623-198163040-00001.

[81]   M.B. Bhavsar, L. Leppik, K.M.C. Oliveira, J.H. Barker, Electrical stimulation–fracture treatment: new insights into the underlying mechanisms, Bioelectronics in Medicine 2 (2019) 5–7. https://doi.org/10.2217/bem-2019-0010.

[82]   W. Sharrard, A double-blind trial of pulsed electromagnetic fields for delayed union of tibial fractures, The Journal of Bone and Joint Surgery. British Volume 72-B (1990) 347–355. https://doi.org/10.1302/0301-620X.72B3.2187877.

[83]   O. Wahlström, Stimulation of fracture healing with electromagnetic fields of extremely low frequency (EMF of ELF), Clin Orthop Relat Res (1984) 293–301.

[84]   H. Shi, J. Xiong, Y. Chen, J. Wang, X. Qiu, Y. Wang, Y. Qiu, Early application of pulsed electromagnetic field in the treatment of postoperative delayed union of long-bone fractures: a prospective randomized controlled study, BMC Musculoskelet Disord 14 (2013) 35. https://doi.org/10.1186/1471-2474-14-35.

[85]   G. Borsalino, M. Bagnacani, E. Bettati, F. Fornaciari, R. Rocchi, S. Uluhogian, G. Ceccherelli, R. Cadossi, G.C. Traina, Electrical Stimulation of Human Femoral Intertrochanteric Osteotomies: Double-Blind Study, Clinical Orthopaedics and Related Research NA; (1988) 256???263. https://doi.org/10.1097/00003086-198812000-00037.

[86]   X. Tian, X. Li, L. Zhou, J. Zhao, X. Li, Y. Huang, T. Ding, On the Effect of Electroacupuncture in Promoting Healing after High Tibial Osteotomy, Computational and Mathematical Methods in Medicine 2022 (2022) 1–7. https://doi.org/10.1155/2022/6428759.

[87]   C.A.L. Bassett, M.M. Schink, Treatment of Therapeutically Resistant Non-Unions with Bone Grafts and Pulsing Electromagnetic Fields, 64 (1982) 7.

[88]   L. Leppik, K.M.C. Oliveira, M.B. Bhavsar, J.H. Barker, Electrical stimulation in bone tissue engineering treatments, Eur J Trauma Emerg Surg 46 (2020) 231–244. https://doi.org/10.1007/s00068-020-01324-1.

[89]   P.J. Nicksic, D.T. Donnelly, M. Hesse, S. Bedi, N. Verma, A.J. Seitz, A.J. Shoffstall, K.A. Ludwig, A.M. Dingle, S.O. Poore, Electronic Bone Growth Stimulators for Augmentation of Osteogenesis in In Vitro and In Vivo Models: A Narrative Review of Electrical Stimulation Mechanisms and Device Specifications, Front. Bioeng. Biotechnol. 10 (2022) 793945. https://doi.org/10.3389/fbioe.2022.793945.

[90]   M.E. Steinberg, C.T. Brighton, A. Corces, G.D. Hayken, D.R. Steinberg, B. Strafford, S.E. Tooze, M. Fallon, Osteonecrosis of the femoral head. Results of core decompression and grafting with and without electrical stimulation, Clin Orthop Relat Res (1989) 199–208.

[91]   S. Fornell, J. Ribera, M. Mella, A. Carranza, D. Serrano-Toledano, G. Domecq, Effects of electrical stimulation in the treatment of osteonecrosis of the femoral head, HIP International 28 (2018) 434–441. https://doi.org/10.5301/hipint.5000581.

[92]   C.T. Brighton, Z.B. Friedenberg, E.I. Mitchell, R.E. Booth, Treatment of nonunion with constant direct current, Clin Orthop Relat Res (1977) 106–123.

[93]   R.O. Becker, J.A. Spadaro, A.A. Marino, Clinical experiences with low intensity direct current stimulation of bone growth, Clin Orthop Relat Res (1977) 75–83.

[94]   J.C. Gan, D.C. Fredericks, P.A. Glazer, Direct Current and Capacitive Coupling Electrical Stimulation Upregulates Osteopromotive Factors for Spinal Fusions, (n.d.) 4.

[95]   F. Benazzo, M. Mosconi, G. Beccarisi, U. Galli, Use of Capacitive Coupled Electric Fields in Stress Fractures in Athletes:, Clinical Orthopaedics and Related Research NA; (1995) 145???149. https://doi.org/10.1097/00003086-199501000-00023.

[96]   W. Li, W. Liu, W. Wang, J. Wang, T. Ma, J. Chen, H. Wu, C. Liu, Sinusoidal electromagnetic fields accelerate bone regeneration by boosting the multifunctionality of bone marrow mesenchymal stem cells, Stem Cell Res Ther 12 (2021) 234. https://doi.org/10.1186/s13287-021-02302-z.

[97]   L. Peng, C. Fu, F. Xiong, Q. Zhang, Z. Liang, L. Chen, C. He, Q. Wei, Effectiveness of Pulsed Electromagnetic Fields on Bone Healing: A Systematic Review and Meta-Analysis of Randomized Controlled Trials, Bioelectromagnetics 41 (2020) 323–337. https://doi.org/10.1002/bem.22271.

[98]   P.F.W. Hannemann, E.H.H. Mommers, J.P.M. Schots, P.R.G. Brink, M. Poeze, The effects of low-intensity pulsed ultrasound and pulsed electromagnetic fields bone growth stimulation in acute fractures: a systematic review and meta-analysis of randomized controlled trials, Arch Orthop Trauma Surg 134 (2014) 1093–1106. https://doi.org/10.1007/s00402-014-2014-8.

[99]   X. Zhang, J. Zhang, X. Qu, J. Wen, Effects of Different Extremely Low-Frequency Electromagnetic Fields on Osteoblasts, Electromagnetic Biology and Medicine 26 (2007) 167–177. https://doi.org/10.1080/15368370701580756.

[100] H. Murray, B. Pethica, A follow-up study of the in-practice results of pulsed electromagnetic field therapy in the management of nonunion fractures, ORR Volume 8 (2016) 67–72. https://doi.org/10.2147/ORR.S113756.

[101] A.M. Hollenberg, A. Huber, C.O. Smith, R.A. Eliseev, Electromagnetic stimulation increases mitochondrial function in osteogenic cells and promotes bone fracture repair, Sci Rep 11 (2021) 19114. https://doi.org/10.1038/s41598-021-98625-1.

[102] EBI bone healing system, The Case Manager 10 (1999) 37–40. https://doi.org/10.1016/S1061-9259(99)80129-5.

[103] S. Akhter, A.R. Qureshi, I. Aleem, H.A. El-Khechen, S. Khan, O. Sikder, M. Khan, M. Bhandari, I. Aleem, Efficacy of Electrical Stimulation for Spinal Fusion: A Systematic Review and Meta-Analysis of Randomized Controlled Trials, Sci Rep 10 (2020) 4568. https://doi.org/10.1038/s41598-020-61266-x.

[104] E. Kozhevnikov, X. Hou, S. Qiao, Y. Zhao, C. Li, W. Tian, Electrical impedance spectroscopy – a potential method for the study and monitoring of a bone critical-size defect healing process treated with bone tissue engineering and regenerative medicine approaches, J. Mater. Chem. B 4 (2016) 2757–2767. https://doi.org/10.1039/C5TB02707A.

[105] C. Bonifasi-Lista, E. Cherkaev, Electrical impedance spectroscopy as a potential tool for recovering bone porosity, Phys. Med. Biol. 54 (2009) 3063–3082. https://doi.org/10.1088/0031-9155/54/10/007.

[106]   A.G. Guex, J.L. Puetzer, A. Armgarth, E. Littmann, E. Stavrinidou, E.P. Giannelis, G.G. Malliaras, M.M. Stevens, Highly porous scaffolds of PEDOT:PSS for bone tissue engineering, Acta Biomaterialia 62 (2017) 91–101. https://doi.org/10.1016/j.actbio.2017.08.045.

[107]   B. Guo, P.X. Ma, Conducting Polymers for Tissue Engineering, Biomacromolecules 19 (2018) 1764–1782. https://doi.org/10.1021/acs.biomac.8b00276.

[108]   S. Goodarzi, T. Da Ros, J. Conde, F. Sefat, M. Mozafari, Fullerene: biomedical engineers get to revisit an old friend, Materials Today 20 (2017) 460–480. https://doi.org/10.1016/j.mattod.2017.03.017.

[109]   S. Ahadian, R. Obregón, J. Ramón-Azcón, G. Salazar, H. Shiku, M. Ramalingam, T. Matsue, Carbon Nanotubes and Graphene-Based Nanomaterials for Stem Cell Differentiation and Tissue Regeneration, J Nanosci Nanotechnol 16 (2016) 8862–8880. https://doi.org/10.1166/jnn.2016.12729.

[110]   B. Ribeiro, E.C. Botelho, M.L. Costa, C.F. Bandeira, Carbon nanotube buckypaper reinforced polymer composites: a review, Polímeros 27 (2017) 247–255. https://doi.org/10.1590/0104-1428.03916.

[111]   Y. Liu, M. Park, H.K. Shin, B. Pant, J. Choi, Y.W. Park, J.Y. Lee, S.-J. Park, H.-Y. Kim, Facile preparation and characterization of poly(vinyl alcohol)/chitosan/graphene oxide biocomposite nanofibers, Journal of Industrial and Engineering Chemistry 20 (2014) 4415–4420. https://doi.org/10.1016/j.jiec.2014.02.009.

[112]   Y. Zhu, S. Murali, W. Cai, X. Li, J.W. Suk, J.R. Potts, R.S. Ruoff, Graphene and Graphene Oxide: Synthesis, Properties, and Applications, Adv. Mater. 22 (2010) 3906–3924. https://doi.org/10.1002/adma.201001068.

[113]   M.J. Green, N. Behabtu, M. Pasquali, W.W. Adams, Nanotubes as polymers, Polymer 50 (2009) 4979–4997. https://doi.org/10.1016/j.polymer.2009.07.044.

[114]   H.W. Kroto, J.R. Heath, S.C. O'Brien, R.F. Curl, R.E. Smalley, C60: Buckminsterfullerene, Nature 318 (1985) 162–163. https://doi.org/10.1038/318162a0.

[115]   T. Guo, P. Nikolaev, A. Thess, D.T. Colbert, R.E. Smalley, Catalytic growth of single-walled nanotubes by laser vaporization, Chemical Physics Letters (1995) 6.

[116]   A. Thess, R. Lee, P. Nikolaev, H. Dai, P. Petit, J. Robert, C. Xu, Y.H. Lee, S.G. Kim, A.G. Rinzler, D.T. Colbert, G.E. Scuseria, D. Tománek, J.E. Fischer, R.E. Smalley, Crystalline Ropes of Metallic Carbon Nanotubes, Science 273 (1996) 483–487. https://doi.org/10.1126/science.273.5274.483.

[117]   A. Eatemadi, H. Daraee, H. Karimkhanloo, M. Kouhi, N. Zarghami, A. Akbarzadeh, M. Abasi, Y. Hanifehpour, S.W. Joo, Carbon nanotubes: properties, synthesis, purification, and medical applications, Nanoscale Res Lett 9 (2014) 393. https://doi.org/10.1186/1556-276X-9-393.

[118]   S. Iijima, Helical microtubules of graphitic carbon, Nature 354 (1991) 56–58. https://doi.org/10.1038/354056a0.

[119]   T.W. Ebbesen, P.M. Ajayan, Large-scale synthesis of carbon nanotubes, Nature 358 (1992) 220–222. https://doi.org/10.1038/358220a0.

[120]   D.S. Bethune, C.H. Kiang, M.S. de Vries, G. Gorman, R. Savoy, J. Vazquez, R. Beyers, Cobalt-catalysed growth of carbon nanotubes with single-atomic-layer walls, Nature 363 (1993) 605–607. https://doi.org/10.1038/363605a0.

[121]   D. Chauhan, A. Pujari, G. Zhang, K. Dasgupta, V.N. Shanov, M.J. Schulz, Effect of a Metallocene Catalyst Mixture on CNT Yield Using the FC-CVD Process, Catalysts 12 (2022) 287. https://doi.org/10.3390/catal12030287.

[122]   A. Yahyazadeh, B. Khoshandam, Carbon nanotube synthesis via the catalytic chemical vapor deposition of methane in the presence of iron, molybdenum, and iron–molybdenum alloy thin layer catalysts, Results in Physics 7 (2017) 3826–3837. https://doi.org/10.1016/j.rinp.2017.10.001.

[123]   Y. Yan, F.Z. Nashath, S. Chen, S. Manickam, S.S. Lim, H. Zhao, E. Lester, T. Wu, C.H. Pang, Synthesis of graphene: Potential carbon precursors and approaches, Nanotechnology Reviews 9 (2020) 1284–1314. https://doi.org/10.1515/ntrev-2020-0100.

[124]   J. Dong, L. Zhang, X. Dai, F. Ding, The epitaxy of 2D materials growth, Nat Commun 11 (2020) 5862. https://doi.org/10.1038/s41467-020-19752-3.

[125]   N. Hong, W. Yang, C. Bao, S. Jiang, L. Song, Y. Hu, Facile synthesis of graphene by pyrolysis of poly(methyl methacrylate) on nickel particles in the confined microzones, Materials Research Bulletin 47 (2012) 4082–4088. https://doi.org/10.1016/j.materresbull.2012.08.049.

[126]   X. Kong, Y. Zhu, H. Lei, C. Wang, Y. Zhao, E. Huo, X. Lin, Q. Zhang, M. Qian, W. Mateo, R. Zou, Z. Fang, R. Ruan, Synthesis of graphene-like carbon from biomass pyrolysis and its applications, Chemical Engineering Journal 399 (2020) 125808. https://doi.org/10.1016/j.cej.2020.125808.

[127]   Abubakar Yakubu, Kebbi State University of Science and technology, Aliero, Graphene Synthesis by Chemical Vapour Deposition (CVD): A Review on Growth Mechanism and Techniques, IJERT V8 (2019) IJERTV8IS050012. https://doi.org/10.17577/IJERTV8IS050012.

[128]   K.S. Novoselov, Electric Field Effect in Atomically Thin Carbon Films, Science 306 (2004) 666–669. https://doi.org/10.1126/science.1102896.

[129]   E. Andrijanto, S. Shoelarta, G. Subiyanto, S. Rifki, Facile synthesis of graphene from graphite using ascorbic acid as reducing agent, in: Semarang, Indonesia, 2016: p. 020003. https://doi.org/10.1063/1.4945457.

[130]   W.S. Hummers, R.E. Offeman, Preparation of Graphitic Oxide, J. Am. Chem. Soc. 80 (1958) 1339–1339. https://doi.org/10.1021/ja01539a017.

[131]   G. Shao, Y. Lu, F. Wu, C. Yang, F. Zeng, Q. Wu, Graphene oxide: the mechanisms of oxidation and exfoliation, J Mater Sci 47 (2012) 4400–4409. https://doi.org/10.1007/s10853-012-6294-5.

[132] N. Kumar, V.C. Srivastava, Simple Synthesis of Large Graphene Oxide Sheets via Electrochemical Method Coupled with Oxidation Process, ACS Omega 3 (2018) 10233–10242. https://doi.org/10.1021/acsomega.8b01283.

[133] D. Roy Chowdhury, C. Singh, A. Paul, Role of graphite precursor and sodium nitrate in graphite oxide synthesis, RSC Adv. 4 (2014) 15138. https://doi.org/10.1039/c4ra01019a.

[134] S. Pei, H.-M. Cheng, The reduction of graphene oxide, Carbon 50 (2012) 3210–3228. https://doi.org/10.1016/j.carbon.2011.11.010.

[135] X. Yang, E. Li, Y. Wan, P. Smith, G. Shang, Q. Cui, Antioxidative fullerol promotes osteogenesis of human adipose-derived stem cells, IJN (2014) 4023. https://doi.org/10.2147/IJN.S66785.

[136] P. Piotrowski, K. Klimek, G. Ginalska, A. Kaim, Beneficial Influence of Water-Soluble PEG-Functionalized C60 Fullerene on Human Osteoblast Growth In Vitro, Materials 14 (2021) 1566. https://doi.org/10.3390/ma14061566.

[137] V. Krishnan, Y. Kasuya, Q. Ji, M. Sathish, L.K. Shrestha, S. Ishihara, K. Minami, H. Morita, T. Yamazaki, N. Hanagata, K. Miyazawa, S. Acharya, W. Nakanishi, J.P. Hill, K. Ariga, Vortex-Aligned Fullerene Nanowhiskers as a Scaffold for Orienting Cell Growth, ACS Appl. Mater. Interfaces 7 (2015) 15667–15673. https://doi.org/10.1021/acsami.5b04811.

[138] J. Yang, J. Liang, Y. Zhu, M. Hu, L. Deng, W. Cui, X. Xu, Fullerol-hydrogel microfluidic spheres for in situ redox regulation of stem cell fate and refractory bone healing, Bioactive Materials 6 (2021) 4801–4815. https://doi.org/10.1016/j.bioactmat.2021.05.024.

[139] S. Constanda, M.S. Stan, C.S. Ciobanu, M. Motelica-Heino, R. Guégan, K. Lafdi, A. Dinischiotu, D. Predoi, Carbon Nanotubes-Hydroxyapatite Nanocomposites for an Improved Osteoblast Cell Response, Journal of Nanomaterials 2016 (2016) 1–10. https://doi.org/10.1155/2016/3941501.

[140] X. Liu, M.N. George, S. Park, A.L. Miller II, B. Gaihre, L. Li, B.E. Waletzki, A. Terzic, M.J. Yaszemski, L. Lu, 3D-printed scaffolds with carbon nanotubes for bone tissue engineering: Fast and homogeneous one-step functionalization, Acta Biomaterialia 111 (2020) 129–140. https://doi.org/10.1016/j.actbio.2020.04.047.

[141] S. Qian, Z. Yan, Y. Xu, H. Tan, Y. Chen, Z. Ling, X. Niu, Carbon nanotubes as electrophysiological building blocks for a bioactive cell scaffold through biological assembly to induce osteogenesis, RSC Adv. 9 (2019) 12001–12009. https://doi.org/10.1039/C9RA00370C.

[142] X. Li, H. Liu, X. Niu, B. Yu, Y. Fan, Q. Feng, F. Cui, F. Watari, The use of carbon nanotubes to induce osteogenic differentiation of human adipose-derived MSCs in vitro and ectopic bone formation in vivo, Biomaterials 33 (2012) 4818–4827. https://doi.org/10.1016/j.biomaterials.2012.03.045.

[143] K. Dixit, N. Sinha, Additive Manufacturing of Carbon Nanotube Reinforced Bioactive Glass Scaffolds for Bone Tissue Engineering, Journal of Engineering and Science in Medical Diagnostics and Therapy 4 (2021) 041004. https://doi.org/10.1115/1.4051801.

[144]   A.G. Sanchez, E. Prokhorov, G. Luna-Barcenas, J. Hernández-Vargas, R. Román-Doval, S. Mendoza, H. Rojas-Chávez, Chitosan-hydroxyapatite-MWCNTs nanocomposite patch for bone tissue engineering applications, Materials Today Communications 28 (2021) 102615. https://doi.org/10.1016/j.mtcomm.2021.102615.

[145]   E.P. e Silva, B. Huang, J.V. Helaehil, P.R.L. Nalesso, L. Bagne, M.A. de Oliveira, G.C.C. Albiazetti, A. Aldalbahi, M. El-Newehy, M. Santamaria-Jr, F.A.S. Mendonça, P. Bártolo, G.F. Caetano, In vivo study of conductive 3D printed PCL/MWCNTs scaffolds with electrical stimulation for bone tissue engineering, Bio-Des. Manuf. 4 (2021) 190–202. https://doi.org/10.1007/s42242-020-00116-1.

[146]   W. Lan, X. Zhang, M. Xu, L. Zhao, D. Huang, X. Wei, W. Chen, Carbon nanotube reinforced polyvinyl alcohol/biphasic calcium phosphate scaffold for bone tissue engineering, RSC Adv. 9 (2019) 38998–39010. https://doi.org/10.1039/C9RA08569F.

[147]   L. Liu, B. Yang, L.-Q. Wang, J.-P. Huang, W.-Y. Chen, Q. Ban, Y. Zhang, R. You, L. Yin, Y.-Q. Guan, Biomimetic bone tissue engineering hydrogel scaffolds constructed using ordered CNTs and HA induce the proliferation and differentiation of BMSCs, J. Mater. Chem. B 8 (2020) 558–567. https://doi.org/10.1039/C9TB01804B.

[148]   A. Rajan Unnithan, A. Ramachandra Kurup Sasikala, C.H. Park, C.S. Kim, A unique scaffold for bone tissue engineering: An osteogenic combination of graphene oxide–hyaluronic acid–chitosan with simvastatin, Journal of Industrial and Engineering Chemistry 46 (2017) 182–191. https://doi.org/10.1016/j.jiec.2016.10.029.

[149]   S. Bahrami, N. Baheiraei, M. Shahrezaee, Biomimetic reduced graphene oxide coated collagen scaffold for in situ bone regeneration, Sci Rep 11 (2021) 16783. https://doi.org/10.1038/s41598-021-96271-1.

[150]   J. Lu, C. Cheng, Y.-S. He, C. Lyu, Y. Wang, J. Yu, L. Qiu, D. Zou, D. Li, Multilayered Graphene Hydrogel Membranes for Guided Bone Regeneration, Advanced Materials 28 (2016) 4025–4031. https://doi.org/10.1002/adma.201505375.

[151]   Y. Li, J. He, J. Zhou, Z. Li, L. Liu, S. Hu, B. Guo, W. Wang, A conductive photothermal non-swelling nanocomposite hydrogel patch accelerating bone defect repair, Biomater. Sci. 10 (2022) 1326–1341. https://doi.org/10.1039/D1BM01937F.

[152]   H. Fang, C. Luo, S. Liu, M. Zhou, Y. Zeng, J. Hou, L. Chen, S. Mou, J. Sun, Z. Wang, A biocompatible vascularized graphene oxide (GO)-collagen chamber with osteoinductive and anti-fibrosis effects promotes bone regeneration *in vivo*, Theranostics 10 (2020) 2759–2772. https://doi.org/10.7150/thno.42006.

[153]   J. Sun, L. Li, F. Xing, Y. Yang, M. Gong, G. Liu, S. Wu, R. Luo, X. Duan, M. Liu, M. Zou, Z. Xiang, Graphene oxide-modified silk fibroin/nanohydroxyapatite scaffold loaded with urine-derived stem cells for immunomodulation and bone regeneration, Stem Cell Res Ther 12 (2021) 591. https://doi.org/10.1186/s13287-021-02634-w.

[154]   H. Belaid, S. Nagarajan, C. Teyssier, C. Barou, J. Barés, S. Balme, H. Garay, V. Huon, D. Cornu, V. Cavaillès, M. Bechelany, Development of new biocompatible 3D printed graphene oxide-

based scaffolds, Materials Science and Engineering: C 110 (2020) 110595. https://doi.org/10.1016/j.msec.2019.110595.

[155] X. Xie, K. Hu, D. Fang, L. Shang, S.D. Tran, M. Cerruti, Graphene and hydroxyapatite self-assemble into homogeneous, free standing nanocomposite hydrogels for bone tissue engineering, Nanoscale 7 (2015) 7992–8002. https://doi.org/10.1039/C5NR01107H.

[156] M.H. Norahan, M. Amroon, R. Ghahremanzadeh, N. Rabiee, N. Baheiraei, Reduced graphene oxide: osteogenic potential for bone tissue engineering, IET Nanobiotechnol. 13 (2019) 720–725. https://doi.org/10.1049/iet-nbt.2019.0125.

[157] M.S. Kang, S.J. Jeong, S.H. Lee, B. Kim, S.W. Hong, J.H. Lee, D.-W. Han, Reduced graphene oxide coating enhances osteogenic differentiation of human mesenchymal stem cells on Ti surfaces, Biomater Res 25 (2021) 4. https://doi.org/10.1186/s40824-021-00205-x.

[158] H. Golzar, D. Mohammadrezaei, A. Yadegari, M. Rasoulianboroujeni, M. Hashemi, M. Omidi, F. Yazdian, M. Shalbaf, L. Tayebi, Incorporation of functionalized reduced graphene oxide/magnesium nanohybrid to enhance the osteoinductivity capability of 3D printed calcium phosphate-based scaffolds, Composites Part B: Engineering 185 (2020) 107749. https://doi.org/10.1016/j.compositesb.2020.107749.

[159] W. Wu, W. Chen, D. Lin, K. Yang, Influence of Surface Oxidation of Multiwalled Carbon Nanotubes on the Adsorption Affinity and Capacity of Polar and Nonpolar Organic Compounds in Aqueous Phase, Environ. Sci. Technol. 46 (2012) 5446–5454. https://doi.org/10.1021/es3004848.

[160] Interaction of Graphene Oxide with Proteins and Applications of their Conjugates, JNMR 5 (2017). https://doi.org/10.15406/jnmr.2017.05.00109.

[161] R. Arambula-Maldonado, A. Geraili, M. Xing, K. Mequanint, Tissue engineering and regenerative therapeutics: The nexus of chemical engineering and translational medicine, Can J Chem Eng (2021) cjce.24094. https://doi.org/10.1002/cjce.24094.

[162] D. Xiao, W. Sun, H. Dai, Y. Zhang, X. Qin, L. Li, Z. Wei, X. Chen, Influence of Charge States on the π–π Interactions of Aromatic Side Chains with Surface of Graphene Sheet and Single-Walled Carbon Nanotubes in Bioelectrodes, J. Phys. Chem. C 118 (2014) 20694–20701. https://doi.org/10.1021/jp506336c.

[163] D. Li, W. Zhang, X. Yu, Z. Wang, Z. Su, G. Wei, When biomolecules meet graphene: from molecular level interactions to material design and applications, Nanoscale 8 (2016) 19491–19509. https://doi.org/10.1039/C6NR07249F.

[164] P. Hampitak, D. Melendrez, M. Iliut, M. Fresquet, N. Parsons, B. Spencer, T.A. Jowitt, A. Vijayaraghavan, Protein interactions and conformations on graphene-based materials mapped using a quartz-crystal microbalance with dissipation monitoring (QCM-D), Carbon 165 (2020) 317–327. https://doi.org/10.1016/j.carbon.2020.04.093.

[165] S. Namgung, K.Y. Baik, J. Park, S. Hong, Controlling the Growth and Differentiation of Human Mesenchymal Stem Cells by the Arrangement of Individual Carbon Nanotubes, ACS Nano 5 (2011) 7383–7390. https://doi.org/10.1021/nn2023057.

[166]   D.Y. Lee, Z. Khatun, J.-H. Lee, Y. Lee, I. In, Blood Compatible Graphene/Heparin Conjugate through Noncovalent Chemistry, Biomacromolecules 12 (2011) 336–341. https://doi.org/10.1021/bm101031a.

[167]   S. Wang, E.S. Humphreys, S.-Y. Chung, D.F. Delduco, S.R. Lustig, H. Wang, K.N. Parker, N.W. Rizzo, S. Subramoney, Y.-M. Chiang, A. Jagota, Peptides with selective affinity for carbon nanotubes, Nature Mater 2 (2003) 196–200. https://doi.org/10.1038/nmat833.

[168]   C. Rajesh, C. Majumder, H. Mizuseki, Y. Kawazoe, A theoretical study on the interaction of aromatic amino acids with graphene and single walled carbon nanotube, The Journal of Chemical Physics 130 (2009) 124911. https://doi.org/10.1063/1.3079096.

[169]   K. Iwashita, K. Shiraki, R. Ishii, T. Tanaka, A. Hirano, Liquid Chromatographic Analysis of the Interaction between Amino Acids and Aromatic Surfaces Using Single-Wall Carbon Nanotubes, Langmuir 31 (2015) 8923–8929. https://doi.org/10.1021/acs.langmuir.5b02500.

[170]   A. Hirano, T. Kameda, *Aromaphilicity Index* of Amino Acids: Molecular Dynamics Simulations of the Protein Binding Affinity for Carbon Nanomaterials, ACS Appl. Nano Mater. 4 (2021) 2486–2495. https://doi.org/10.1021/acsanm.0c03047.

[171]   Y. Chong, C. Ge, Z. Yang, J.A. Garate, Z. Gu, J.K. Weber, J. Liu, R. Zhou, Reduced Cytotoxicity of Graphene Nanosheets Mediated by Blood-Protein Coating, ACS Nano 9 (2015) 5713–5724. https://doi.org/10.1021/nn5066606.

[172]   M. Taale, F. Schütt, K. Zheng, Y.K. Mishra, A.R. Boccaccini, R. Adelung, C. Selhuber-Unkel, Bioactive Carbon-Based Hybrid 3D Scaffolds for Osteoblast Growth, ACS Appl. Mater. Interfaces 10 (2018) 43874–43886. https://doi.org/10.1021/acsami.8b13631.

[173]   C. Fu, H. Bai, J. Zhu, Z. Niu, Y. Wang, J. Li, X. Yang, Y. Bai, Enhanced cell proliferation and osteogenic differentiation in electrospun PLGA/hydroxyapatite nanofibre scaffolds incorporated with graphene oxide, PLoS ONE 12 (2017) e0188352. https://doi.org/10.1371/journal.pone.0188352.

[174]   Z. Du, X. Feng, G. Cao, Z. She, R. Tan, K.E. Aifantis, R. Zhang, X. Li, The effect of carbon nanotubes on osteogenic functions of adipose-derived mesenchymal stem cells in vitro and bone formation in vivo compared with that of nano-hydroxyapatite and the possible mechanism, Bioactive Materials 6 (2021) 333–345. https://doi.org/10.1016/j.bioactmat.2020.08.015.

[175]   H. Cindrič, B. Kos, G. Tedesco, M. Cadossi, A. Gasbarrini, D. Miklavčič, Electrochemotherapy of Spinal Metastases Using Transpedicular Approach—A Numerical Feasibility Study, Technol Cancer Res Treat 17 (2018) 153303461877025. https://doi.org/10.1177/1533034618770253.

[176]   S.A. Meguid, G.J. Weng, eds., Micromechanics and Nanomechanics of Composite Solids, Springer International Publishing, Cham, 2018. https://doi.org/10.1007/978-3-319-52794-9.

[177]   G. Yang, L. Li, W.B. Lee, M.C. Ng, Structure of graphene and its disorders: a review, Science and Technology of Advanced Materials 19 (2018) 613–648. https://doi.org/10.1080/14686996.2018.1494493.

[178] Y. Wang, G.J. Weng, Electrical Conductivity of Carbon Nanotube- and Graphene-Based Nanocomposites, in: S.A. Meguid, G.J. Weng (Eds.), Micromechanics and Nanomechanics of Composite Solids, Springer International Publishing, Cham, 2018: pp. 123–156. https://doi.org/10.1007/978-3-319-52794-9_4.

[179] W. Bauhofer, J.Z. Kovacs, A review and analysis of electrical percolation in carbon nanotube polymer composites, Composites Science and Technology 69 (2009) 1486–1498. https://doi.org/10.1016/j.compscitech.2008.06.018.

[180] H. Wei, J. Cui, K. Lin, J. Xie, X. Wang, Recent advances in smart stimuli-responsive biomaterials for bone therapeutics and regeneration, Bone Res 10 (2022) 17. https://doi.org/10.1038/s41413-021-00180-y.

[181] R. Balint, N.J. Cassidy, S.H. Cartmell, Electrical Stimulation: A Novel Tool for Tissue Engineering, Tissue Engineering Part B: Reviews 19 (2013) 48–57. https://doi.org/10.1089/ten.teb.2012.0183.

[182] M. Griffin, A. Bayat, Electrical Stimulation in Bone Healing: Critical Analysis by Evaluating Levels of Evidence, 11 (n.d.) 52.

[183] J. Kuan-Jung Li, J. Cheng-An Lin, H.-C. Liu, J.-S. Sun, R.-C. Ruaan, C. Shih, W. Hong-Shong Chang, Comparison of ultrasound and electromagnetic field effects on osteoblast growth, Ultrasound in Medicine & Biology 32 (2006) 769–775. https://doi.org/10.1016/j.ultrasmedbio.2006.01.017.

[184] H. Zhuang, W. Wang, R.M. Seldes, A.D. Tahernia, H. Fan, C.T. Brighton, Electrical Stimulation Induces the Level of TGF-β1 mRNA in Osteoblastic Cells by a Mechanism Involving Calcium/Calmodulin Pathway, Biochemical and Biophysical Research Communications 237 (1997) 225–229. https://doi.org/10.1006/bbrc.1997.7118.

[185] K. Srirussamee, S. Mobini, N.J. Cassidy, S.H. Cartmell, Direct electrical stimulation enhances osteogenesis by inducing Bmp2 and Spp1 expressions from macrophages and preosteoblasts, Biotechnology and Bioengineering 116 (2019) 3421–3432. https://doi.org/10.1002/bit.27142.

[186] S. Shokri, B. Movahedi, M. Rafieinia, H. Salehi, A new approach to fabrication of Cs/BG/CNT nanocomposite scaffold towards bone tissue engineering and evaluation of its properties, Applied Surface Science 357 (2015) 1758–1764. https://doi.org/10.1016/j.apsusc.2015.10.048.

[187] Y. Huang, W. Jing, Y. Li, Q. Cai, X. Yang, Composites made of polyorganophosphazene and carbon nanotube up-regulating osteogenic activity of BMSCs under electrical stimulation, Colloids and Surfaces B: Biointerfaces 204 (2021) 111785. https://doi.org/10.1016/j.colsurfb.2021.111785.

[188] D. Jamal, R.C. de Guzman, Silicone Substrate with Collagen and Carbon Nanotubes Exposed to Pulsed Current for MSC Osteodifferentiation, International Journal of Biomaterials 2017 (2017) 1–9. https://doi.org/10.1155/2017/3684812.

[189] J. Cao, Z. Liu, L. Zhang, J. Li, H. Wang, X. Li, Advance of Electroconductive Hydrogels for Biomedical Applications in Orthopedics, Advances in Materials Science and Engineering 2021 (2021) 1–13. https://doi.org/10.1155/2021/6668209.

[190]   N. Amiryaghoubi, N. Noroozi Pesyan, M. Fathi, Y. Omidi, Injectable thermosensitive hybrid hydrogel containing graphene oxide and chitosan as dental pulp stem cells scaffold for bone tissue engineering, International Journal of Biological Macromolecules 162 (2020) 1338–1357. https://doi.org/10.1016/j.ijbiomac.2020.06.138.

[191]   L. Wang, R. Lu, J. Hou, X. Nan, Y. Xia, Y. Guo, K. Meng, C. Xu, X. Wang, B. Zhao, Application of injectable silk fibroin/graphene oxide hydrogel combined with bone marrow mesenchymal stem cells in bone tissue engineering, Colloids and Surfaces A: Physicochemical and Engineering Aspects 604 (2020) 125318. https://doi.org/10.1016/j.colsurfa.2020.125318.

[192]   X. Liu, M.N. George, L. Li, D. Gamble, A.L. Miller II, B. Gaihre, B.E. Waletzki, L. Lu, Injectable Electrical Conductive and Phosphate Releasing Gel with Two-Dimensional Black Phosphorus and Carbon Nanotubes for Bone Tissue Engineering, ACS Biomater. Sci. Eng. 6 (2020) 4653–4665. https://doi.org/10.1021/acsbiomaterials.0c00612.

[193]   W. Wang, J.R.P. Junior, P.R.L. Nalesso, D. Musson, J. Cornish, F. Mendonça, G.F. Caetano, P. Bártolo, Engineered 3D printed poly(ε-caprolactone)/graphene scaffolds for bone tissue engineering, Materials Science and Engineering: C 100 (2019) 759–770. https://doi.org/10.1016/j.msec.2019.03.047.

[194]   H. Siddiqui, K. Pickering, M. Mucalo, A Review on the Use of Hydroxyapatite-Carbonaceous Structure Composites in Bone Replacement Materials for Strengthening Purposes, Materials 11 (2018) 1813. https://doi.org/10.3390/ma11101813.

[195]   J.W. Suk, R.D. Piner, J. An, R.S. Ruoff, Mechanical Properties of Monolayer Graphene Oxide, ACS Nano 4 (2010) 6557–6564. https://doi.org/10.1021/nn101781v.

[196]   C. Gómez-Navarro, M. Burghard, K. Kern, Elastic Properties of Chemically Derived Single Graphene Sheets, Nano Lett. 8 (2008) 2045–2049. https://doi.org/10.1021/nl801384y.

[197]   D.G. Papageorgiou, I.A. Kinloch, R.J. Young, Mechanical properties of graphene and graphene-based nanocomposites, Progress in Materials Science 90 (2017) 75–127. https://doi.org/10.1016/j.pmatsci.2017.07.004.

[198]   M. Tarfaoui, K. Lafdi, A. El Moumen, Mechanical properties of carbon nanotubes based polymer composites, Composites Part B: Engineering 103 (2016) 113–121. https://doi.org/10.1016/j.compositesb.2016.08.016.

[199]   J. Li, Z. Zhang, J. Fu, Z. Liang, K.R. Ramakrishnan, Mechanical properties and structural health monitoring performance of carbon nanotube-modified FRP composites: A review, Nanotechnology Reviews 10 (2021) 1438–1468. https://doi.org/10.1515/ntrev-2021-0104.

[200]   A. Takakura, K. Beppu, T. Nishihara, A. Fukui, T. Kozeki, T. Namazu, Y. Miyauchi, K. Itami, Strength of carbon nanotubes depends on their chemical structures, Nat Commun 10 (2019) 3040. https://doi.org/10.1038/s41467-019-10959-7.

[201]   M.G. Pastore Carbone, G. Tsoukleri, A.C. Manikas, E. Makarona, C. Tsamis, C. Galiotis, Production and Mechanical Characterization of Graphene Micro-Ribbons, J. Compos. Sci. 3 (2019) 42. https://doi.org/10.3390/jcs3020042.

[202]   M.-F. Yu, B.S. Files, S. Arepalli, R.S. Ruoff, Tensile Loading of Ropes of Single Wall Carbon Nanotubes and their Mechanical Properties, Phys. Rev. Lett. 84 (2000) 5552–5555. https://doi.org/10.1103/PhysRevLett.84.5552.

[203]   P. Zhang, L. Ma, F. Fan, Z. Zeng, C. Peng, P.E. Loya, Z. Liu, Y. Gong, J. Zhang, X. Zhang, P.M. Ajayan, T. Zhu, J. Lou, Fracture toughness of graphene, Nat Commun 5 (2014) 3782. https://doi.org/10.1038/ncomms4782.

[204]   M. Zu, W. Lu, Q.-W. Li, Y. Zhu, G. Wang, T.-W. Chou, Characterization of Carbon Nanotube Fiber Compressive Properties Using Tensile Recoil Measurement, ACS Nano 6 (2012) 4288–4297. https://doi.org/10.1021/nn300857d.

[205]   K. Cao, S. Feng, Y. Han, L. Gao, T. Hue Ly, Z. Xu, Y. Lu, Elastic straining of free-standing monolayer graphene, Nat Commun 11 (2020) 284. https://doi.org/10.1038/s41467-019-14130-0.

[206]   S. Zhang, Measuring the specific surface area of monolayer graphene oxide in water, Materials Letters (2020) 3.

[207]   J.B. Park, R.S. Lakes, Biomaterials: an introduction, 3rd ed, Springer, New York, 2007.

[208]   A. Aryaei, A.H. Jayatissa, A.C. Jayasuriya, Mechanical and biological properties of chitosan/carbon nanotube nanocomposite films: Chitosan/Carbon Nanotube Nanocomposite Films, J. Biomed. Mater. Res. 102 (2014) 2704–2712. https://doi.org/10.1002/jbm.a.34942.

[209]   P.E. Mikael, A.R. Amini, J. Basu, M. Josefina Arellano-Jimenez, C.T. Laurencin, M.M. Sanders, C. Barry Carter, S.P. Nukavarapu, Functionalized carbon nanotube reinforced scaffolds for bone regenerative engineering: fabrication, *in vitro* and *in vivo* evaluation, Biomed. Mater. 9 (2014) 035001. https://doi.org/10.1088/1748-6041/9/3/035001.

[210]   C. Gao, T. Liu, C. Shuai, S. Peng, Enhancement mechanisms of graphene in nano-58S bioactive glass scaffold: mechanical and biological performance, Sci Rep 4 (2015) 4712. https://doi.org/10.1038/srep04712.

[211]   R. Eivazzadeh-Keihan, A. Maleki, M. de la Guardia, M.S. Bani, K.K. Chenab, P. Pashazadeh-Panahi, B. Baradaran, A. Mokhtarzadeh, M.R. Hamblin, Carbon based nanomaterials for tissue engineering of bone: Building new bone on small black scaffolds: A review, Journal of Advanced Research 18 (2019) 185–201. https://doi.org/10.1016/j.jare.2019.03.011.

[212]   B.L. Allen, P.D. Kichambare, P. Gou, I.I. Vlasova, A.A. Kapralov, N. Konduru, V.E. Kagan, A. Star, Biodegradation of Single-Walled Carbon Nanotubes through Enzymatic Catalysis, Nano Lett. 8 (2008) 3899–3903. https://doi.org/10.1021/nl802315h.

[213]   E. Murray, B.C. Thompson, S. Sayyar, G.G. Wallace, Enzymatic degradation of graphene/polycaprolactone materials for tissue engineering, Polymer Degradation and Stability 111 (2015) 71–77. https://doi.org/10.1016/j.polymdegradstab.2014.10.010.

[214]   M. Yang, M. Zhang, H. Nakajima, M. Yudasaka, S. Iijima, T. Okazaki, Time-dependent degradation of carbon nanotubes correlates with decreased reactive oxygen species generation in macrophages, IJN Volume 14 (2019) 2797–2807. https://doi.org/10.2147/IJN.S199187.

[215]   V.E. Kagan, A.A. Kapralov, C.M. St. Croix, S.C. Watkins, E.R. Kisin, G.P. Kotchey, K. Balasubramanian, I.I. Vlasova, J. Yu, K. Kim, W. Seo, R.K. Mallampalli, A. Star, A.A. Shvedova, Lung Macrophages "Digest" Carbon Nanotubes Using a Superoxide/Peroxynitrite Oxidative Pathway, ACS Nano 8 (2014) 5610–5621. https://doi.org/10.1021/nn406484b.

[216]   R. Wang, R. Lohray, E. Chow, P. Gangupantula, L. Smith, R. Draper, Selective Uptake of Carboxylated Multi-Walled Carbon Nanotubes by Class A Type 1 Scavenger Receptors and Impaired Phagocytosis in Alveolar Macrophages, Nanomaterials 10 (2020) 2417. https://doi.org/10.3390/nano10122417.

[217]   M. Sano, M. Izumiya, H. Haniu, K. Ueda, K. Konishi, H. Ishida, C. Kuroda, T. Uemura, K. Aoki, Y. Matsuda, N. Saito, Cellular Responses of Human Lymphatic Endothelial Cells to Carbon Nanomaterials, Nanomaterials 10 (2020) 1374. https://doi.org/10.3390/nano10071374.

[218]   N.R. Jacobsen, P. Møller, P.A. Clausen, A.T. Saber, C. Micheletti, K.A. Jensen, H. Wallin, U. Vogel, Biodistribution of Carbon Nanotubes in Animal Models, Basic Clin Pharmacol Toxicol 121 (2017) 30–43. https://doi.org/10.1111/bcpt.12705.

[219]   P. Ruenraroengsak, S. Chen, S. Hu, J. Melbourne, S. Sweeney, A.J. Thorley, J.N. Skepper, M.S.P. Shaffer, T.D. Tetley, A.E. Porter, Translocation of Functionalized Multi-Walled Carbon Nanotubes across Human Pulmonary Alveolar Epithelium: Dominant Role of Epithelial Type 1 Cells, ACS Nano 10 (2016) 5070–5085. https://doi.org/10.1021/acsnano.5b08218.

[220]   M. Kucki, L. Diener, N. Bohmer, C. Hirsch, H.F. Krug, V. Palermo, P. Wick, Uptake of label-free graphene oxide by Caco-2 cells is dependent on the cell differentiation status, J Nanobiotechnol 15 (2017) 46. https://doi.org/10.1186/s12951-017-0280-7.

[221]   H. Kafa, J.T.-W. Wang, N. Rubio, K. Venner, G. Anderson, E. Pach, B. Ballesteros, J.E. Preston, N.J. Abbott, K.T. Al-Jamal, The interaction of carbon nanotubes with an in vitro blood-brain barrier model and mouse brain in vivo, Biomaterials 53 (2015) 437–452. https://doi.org/10.1016/j.biomaterials.2015.02.083.

[222]   D. Pantarotto, J.-P. Briand, M. Prato, A. Bianco, Translocation of bioactive peptides across cell membranes by carbon nanotubesElectronic supplementary information (ESI) available: details of the synthesis and characterization, cell culture, TEM, epifluorescence and confocal microscopy images of CNTs 1, 2 and fluorescein. See http://www.rsc.org/suppdata/cc/b3/b311254c/, Chem. Commun. (2004) 16. https://doi.org/10.1039/b311254c.

[223]   F. Zhao, Y. Zhao, Y. Liu, X. Chang, C. Chen, Y. Zhao, Cellular Uptake, Intracellular Trafficking, and Cytotoxicity of Nanomaterials, Small 7 (2011) 1322–1337. https://doi.org/10.1002/smll.201100001.

[224]   B. Huang, Carbon nanotubes and their polymeric composites: the applications in tissue engineering, Biomanuf Rev 5 (2020) 3. https://doi.org/10.1007/s40898-020-00009-x.

[225]   L. Lacerda, H. Ali-Boucetta, S. Kraszewski, M. Tarek, M. Prato, C. Ramseyer, K. Kostarelos, A. Bianco, How do functionalized carbon nanotubes land on, bind to and pierce through model and plasma membranes, Nanoscale 5 (2013) 10242. https://doi.org/10.1039/c3nr03184e.

[226]   N.W. Shi Kam, T.C. Jessop, P.A. Wender, H. Dai, Nanotube Molecular Transporters: Internalization of Carbon Nanotube−Protein Conjugates into Mammalian Cells, J. Am. Chem. Soc. 126 (2004) 6850–6851. https://doi.org/10.1021/ja0486059.

[227]   X. Shi, Cell entry of one-dimensional nanomaterials occurs by tip recognition and rotation, Nature Nanotechnology 6 (2011) 6.

[228]   L. Lacerda, J. Russier, G. Pastorin, M.A. Herrero, E. Venturelli, H. Dumortier, K.T. Al-Jamal, M. Prato, K. Kostarelos, A. Bianco, Translocation mechanisms of chemically functionalised carbon nanotubes across plasma membranes, Biomaterials 33 (2012) 3334–3343. https://doi.org/10.1016/j.biomaterials.2012.01.024.

[229]   Y. Sato, A. Yokoyama, Y. Nodasaka, T. Kohgo, K. Motomiya, H. Matsumoto, E. Nakazawa, T. Numata, M. Zhang, M. Yudasaka, H. Hara, R. Araki, O. Tsukamoto, H. Saito, T. Kamino, F. Watari, K. Tohji, Long-term biopersistence of tangled oxidized carbon nanotubes inside and outside macrophages in rat subcutaneous tissue, Sci Rep 3 (2013) 2516. https://doi.org/10.1038/srep02516.

[230]   D. Kersting, S. Fasbender, R. Pilch, J. Kurth, A. Franken, M. Ludescher, J. Naskou, A. Hallenberger, C. von Gall, C.J. Mohr, R. Lukowski, K. Raba, S. Jaschinski, I. Esposito, J.C. Fischer, T. Fehm, D. Niederacher, H. Neubauer, T. Heinzel, From *in vitro* to *ex vivo* : subcellular localization and uptake of graphene quantum dots into solid tumors, Nanotechnology 30 (2019) 395101. https://doi.org/10.1088/1361-6528/ab2cb4.

[231]   B. Kang, S. Chang, Y. Dai, D. Yu, D. Chen, Cell Response to Carbon Nanotubes: Size-Dependent Intracellular Uptake Mechanism and Subcellular Fate, Small 6 (2010) 2362–2366. https://doi.org/10.1002/smll.201001260.

[232]   V. Neves, E. Heister, S. Costa, C. Tîlmaciu, E. Borowiak-Palen, C.E. Giusca, E. Flahaut, B. Soula, H.M. Coley, J. McFadden, S.R.P. Silva, Uptake and Release of Double-Walled Carbon Nanotubes by Mammalian Cells, Adv. Funct. Mater. 20 (2010) 3272–3279. https://doi.org/10.1002/adfm.201000994.

[233]   A.E. Porter, M. Gass, K. Muller, J.N. Skepper, P.A. Midgley, M. Welland, Direct imaging of single-walled carbon nanotubes in cells, Nature Nanotech 2 (2007) 713–717. https://doi.org/10.1038/nnano.2007.347.

[234]   M. Jennifer, W. Maciej, Nanoparticle Technology as a Double-Edged Sword: Cytotoxic, Genotoxic and Epigenetic Effects on Living Cells, JBNB 04 (2013) 53–63. https://doi.org/10.4236/jbnb.2013.41008.

[235]   Q. Mu, D.L. Broughton, B. Yan, Endosomal Leakage and Nuclear Translocation of Multiwalled Carbon Nanotubes: Developing a Model for Cell Uptake, Nano Lett. 9 (2009) 4370–4375. https://doi.org/10.1021/nl902647x.

[236]   B. Rothen-Rutishauser, D.M. Brown, M. Piallier-Boyles, I.A. Kinloch, A.H. Windle, P. Gehr, V. Stone, Relating the physicochemical characteristics and dispersion of multiwalled carbon nanotubes in different suspension media to their oxidative reactivity *in vitro* and inflammation *in vivo*, Nanotoxicology 4 (2010) 331–342. https://doi.org/10.3109/17435390.2010.489161.

[237]   T.A. Tabish, C.J. Scotton, D.C. J Ferguson, L. Lin, A. van der Veen, S. Lowry, M. Ali, F. Jabeen, M. Ali, P.G. Winyard, S. Zhang, Biocompatibility and toxicity of graphene quantum dots for potential application in photodynamic therapy, Nanomedicine 13 (2018) 1923–1937. https://doi.org/10.2217/nnm-2018-0018.

[238]   C. Ge, Y. Li, J.-J. Yin, Y. Liu, L. Wang, Y. Zhao, C. Chen, The contributions of metal impurities and tube structure to the toxicity of carbon nanotube materials, NPG Asia Mater 4 (2012) e32–e32. https://doi.org/10.1038/am.2012.60.

[239]   K. Pulskamp, S. Diabate, H. Krug, Carbon nanotubes show no sign of acute toxicity but induce intracellular reactive oxygen species in dependence on contaminants, Toxicology Letters 168 (2007) 58–74. https://doi.org/10.1016/j.toxlet.2006.11.001.

[240]   P.-X. Hou, C. Liu, H.-M. Cheng, Purification of carbon nanotubes, Carbon 46 (2008) 2003–2025. https://doi.org/10.1016/j.carbon.2008.09.009.

[241]   O.J. Yoon, I. Kim, I.Y. Sohn, T.T. Kieu, N.-E. Lee, Toxicity of graphene nanoflakes evaluated by cell-based electrochemical impedance biosensing: Toxicity of Graphene Nanoflakes, J. Biomed. Mater. Res. 102 (2014) 2288–2294. https://doi.org/10.1002/jbm.a.34886.

[242]   V. Raffa, G. Ciofani, S. Nitodas, T. Karachalios, D. D'Alessandro, M. Masini, A. Cuschieri, Can the properties of carbon nanotubes influence their internalization by living cells?, Carbon 46 (2008) 1600–1610. https://doi.org/10.1016/j.carbon.2008.06.053.

[243]   Suresh H. Moolgavkar, Robert C. Bro, Biopersistence, Fiber Length, and Cancer Risk Assessment for Inhaled Fibers, Inhalation Toxicology 13 (2001) 755–772. https://doi.org/10.1080/08958370121106.

[244]   M. Zhang, M. Yang, T. Morimoto, N. Tajima, K. Ichiraku, K. Fujita, S. Iijima, M. Yudasaka, T. Okazaki, Size-dependent cell uptake of carbon nanotubes by macrophages: A comparative and quantitative study, Carbon 127 (2018) 93–101. https://doi.org/10.1016/j.carbon.2017.10.085.

[245]   C. Wei, Z. Liu, F. Jiang, B. Zeng, M. Huang, D. Yu, Cellular behaviours of bone marrow-derived mesenchymal stem cells towards pristine graphene oxide nanosheets, Cell Prolif 50 (2017) e12367. https://doi.org/10.1111/cpr.12367.

[246]   J.-W. Kim, Y. Shin, J.-J. Lee, E.-B. Bae, Y.-C. Jeon, C.-M. Jeong, M.-J. Yun, S.-H. Lee, D.-W. Han, J.-B. Huh, The Effect of Reduced Graphene Oxide-Coated Biphasic Calcium Phosphate Bone Graft Material on Osteogenesis, IJMS 18 (2017) 1725. https://doi.org/10.3390/ijms18081725.

[247]   M. van der Zande, R. Junker, X.F. Walboomers, J.A. Jansen, Carbon Nanotubes in Animal Models: A Systematic Review on Toxic Potential, Tissue Engineering Part B: Reviews 17 (2011) 57–69. https://doi.org/10.1089/ten.teb.2010.0472.

[248]   L. Newman, D.A. Jasim, E. Prestat, N. Lozano, I. de Lazaro, Y. Nam, B.M. Assas, J. Pennock, S.J. Haigh, C. Bussy, K. Kostarelos, Splenic Capture and *In Vivo* Intracellular Biodegradation of Biological-Grade Graphene Oxide Sheets, ACS Nano 14 (2020) 10168–10186. https://doi.org/10.1021/acsnano.0c03438.

[249]   L. Lacerda, M.A. Herrero, K. Venner, A. Bianco, M. Prato, K. Kostarelos, Carbon-Nanotube Shape and Individualization Critical for Renal Excretion, Small 4 (2008) 1130–1132. https://doi.org/10.1002/smll.200800323.

[250] D.A. Jasim, H. Boutin, M. Fairclough, C. Ménard-Moyon, C. Prenant, A. Bianco, K. Kostarelos, Thickness of functionalized graphene oxide sheets plays critical role in tissue accumulation and urinary excretion: A pilot PET/CT study, Applied Materials Today 4 (2016) 24–30. https://doi.org/10.1016/j.apmt.2016.04.003.

[251]   B. Sitharaman, X. Shi, X.F. Walboomers, H. Liao, V. Cuijpers, L.J. Wilson, A.G. Mikos, J.A. Jansen, In vivo biocompatibility of ultra-short single-walled carbon nanotube/biodegradable polymer nanocomposites for bone tissue engineering, Bone 43 (2008) 362–370. https://doi.org/10.1016/j.bone.2008.04.013.

[252]   N. Saito, H. Haniu, Y. Usui, K. Aoki, K. Hara, S. Takanashi, M. Shimizu, N. Narita, M. Okamoto, S. Kobayashi, H. Nomura, H. Kato, N. Nishimura, S. Taruta, M. Endo, Safe Clinical Use of Carbon Nanotubes as Innovative Biomaterials, Chem. Rev. 114 (2014) 6040–6079. https://doi.org/10.1021/cr400341h.

[253]   Y. Usui, K. Aoki, N. Narita, N. Murakami, I. Nakamura, K. Nakamura, N. Ishigaki, H. Yamazaki, H. Horiuchi, H. Kato, S. Taruta, Y.A. Kim, M. Endo, N. Saito, Carbon Nanotubes with High Bone-Tissue Compatibility and Bone-Formation Acceleration Effects, Small 4 (2008) 240–246. https://doi.org/10.1002/smll.200700670.

[254]   Y.C. Shin, J.H. Lee, O.S. Jin, S.H. Kang, S.W. Hong, B. Kim, J.-C. Park, D.-W. Han, Synergistic effects of reduced graphene oxide and hydroxyapatite on osteogenic differentiation of MC3T3-E1 preosteoblasts, Carbon 95 (2015) 1051–1060. https://doi.org/10.1016/j.carbon.2015.09.028.

Chapter 3

3. Sol-gel derived gelatin-bioactive glass nanocomposite biomaterials incorporating calcium chloride and calcium ethoxide*[3]

Overview: *The purpose of the study herein is to synthesize organic-inorganic hybrid biomaterials based on gelatin, tertiary bioactive glass and multiwall carbon nanotubes using either calcium chloride or calcium ethoxide as precursors in the sol-gel process. Characterizations of biomaterials were performed and the role of calcium sources in the nanocomposites were evaluated.*
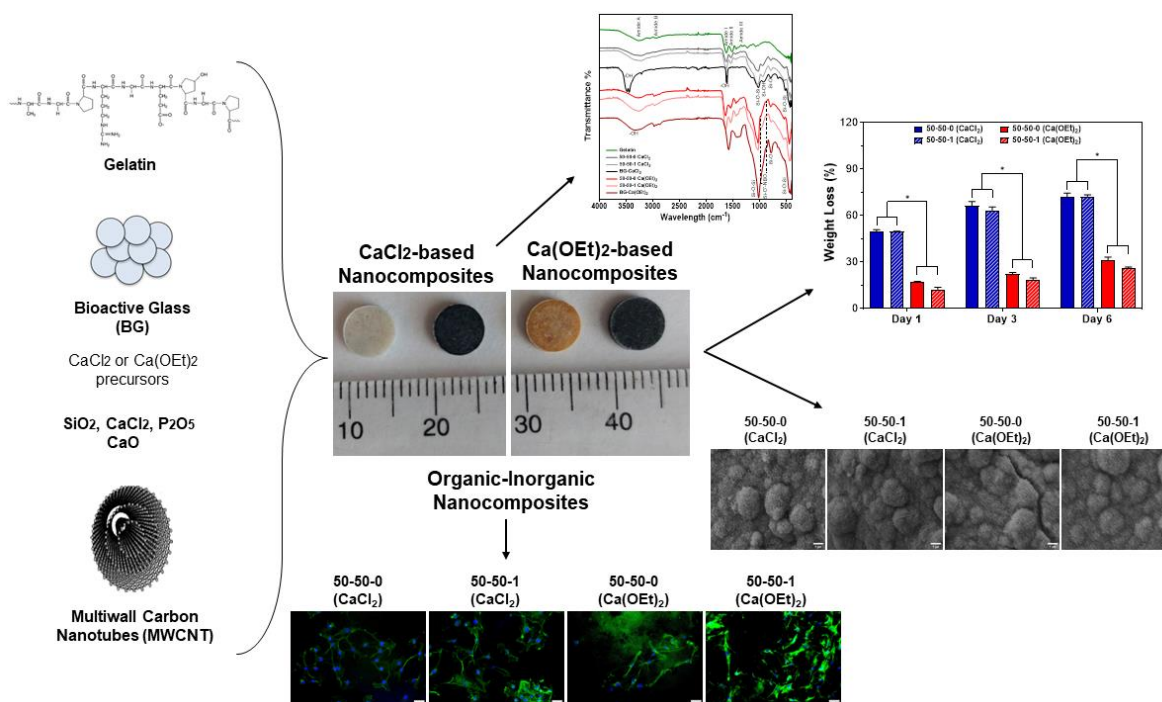
Scheme 3.1. Graphical abstract for Chapter 3.

3.1. Abstract

Calcium-containing organic-inorganic nanocomposites play an essential role in developing bioactive bone biomaterials. Ideally, bone substitute materials should mimic the organic-inorganic composition of bone. In this study, the roles of calcium chloride ($CaCl_2$) and calcium ethoxide ($Ca(OEt)_2$) were evaluated for the development of sol-gel derived organic-inorganic biomaterials composed of gelatin, bioactive glass (BG) and multiwall carbon nanotubes (MWCNTs) to create nanocomposites that mimic the elemental composition of bone. Nanocomposites composed of either $CaCl_2$ or $Ca(OEt)_2$ were chemically different but presented uniform elemental distribution. The role of calcium sources in the matrix of the nanocomposites played a major role in the swelling and degradation properties of biomaterials as a function of time, as well as the resulting porous properties of the nanocomposites. Regardless of the calcium source type, biomineralization in simulated body fluid and favorable cell attachment were promoted on the nanocomposites. 10T1/2 cell viability studies using standard media (DMEM with 5% FBS) and conditioned media showed that $Ca(OEt)_2$-based nanocomposites seemed more favorable biomaterials. Collectively, our study demonstrated that $CaCl_2$ and $Ca(OEt)_2$ could be used to prepare sol-gel-derived gelatin-BG-MWCNT nanocomposites, which have the potential to function as bone biomaterials.

Keywords: sol-gel, calcium, gelatin-bioactive glass-MWCNT biomaterials, nanocomposites, bioactivity, bone biomaterial

3.2. Introduction

Biomaterials that mimic the structural composition of bone tissue are desired for the repair or regeneration of fractures and defects. Native bone is composed of a complex hierarchical structure comprised of collagen as the main organic component and hydroxycarbonate apatite as the inorganic component.[1-3] The selection of appropriate materials for the preparation of organic-inorganic nanocomposites that simulate the composition of bone is crucial.

Bioactive glasses (BG) are ideal for use as an inorganic component for the preparation of bone biomaterials since they readily bond to bone and stimulate both osteoconduction and osteoinduction.[4,5] BGs are amorphous, silicate-based materials that are based on a covalent random network of corner-sharing silica tetrahedra containing Si-O-Si bridging bonds.[6] The original BG

(46.1%, SiO_2, 24.4%, Na_2O, 26.9% CaO, and 2.6% P_2O_5, in mol%), 45S5 Bioglass®, was developed by Hench and his colleagues.[7] Bioglass® was first produced through melt-quenching processing which involved melting the oxide components in platinum crucibles at a temperature of 1,370°C, followed by pouring into a preheated mold or pouring the melt into water to quench, creating a powder or frit.[7,8] One of the potential ways bone bonds to BG is through the formation of a hydroxycarbonate apatite (HCA) layer on the surface of the glasses in contact with body fluid, similar to the apatite in bone, that would facilitate the formation of a strong bond through the plausible interaction of collagen fibrils from the host bone and the HCA nodules forming on the glass.[7] This process occurs through the release of soluble ionic species from the glass to form a high-surface-area hydrated silica and polycrystalline HCA bilayer on the glass surface.[8]

BG can also be synthesized via the sol-gel process. Sol-gel-derived BGs are produced through the hydrolysis of alkoxide precursors to form a colloidal silica sol.[9] Metal alkoxides, such as tetraethyl orthosilicate (TEOS) are commonly used as silica precursors due to their ability to readily react with water.[10] In addition, triethyl phosphate (TEP) and calcium salts are used to incorporate phosphate and calcium into the sol-gel system, respectively.[10] A gel is formed by polycondensation of the silica species in the sol, forming a network of silica (Si-O-Si bridging bonds) that subsequently goes through a heat treatment to remove the condensation by-products and remove the nitrates in cases where calcium nitrate salt is used, due to the cytotoxic nature of nitrate.[6,9] In addition, different drying techniques of wet gels result in porous structured materials known as aerogels and xerogels.[9] Aerogels are low-density gels that are produced by the removal of liquid from the interconnected pore network as a gas phase under supercritical drying; whereas xerogels, generically called gels, are the resulting product from drying at or near ambient conditions by thermal evaporation.[9,11]

The advantage of sol-gel-derived over melt-quenching-derived BGs is the generation of different gel products, such as aerogels and gels that can be characterized for their applications as potential bioactive bone biomaterials.[12,13] In addition, the formation of HCA layer on the surfaces of glasses and bondage to bone can be achieved with compositions of 90 mol% silica, whereas osteoconduction and osteoinduction property is achieved at a silica content of 60 mol% or less in melt-derived BGs.[14] The increased bioactivity of sol-gel-derived BGs is due to its enhanced surface area as a result of its nanoporous network, compared to the dense melt-derived BGs, causing an increased rate of dissolution of the soluble ionic species of the BG composition.[15,16] In addition, the incorporation of

an organic component is more viable in the sol-gel process since it does not necessarily require high-temperature treatment, as would occur in the melt-derived BGs.

BGs are, however, brittle and require the incorporation of a polymer to induce toughness. The addition of biodegradable synthetic polymers, such as poly(ester amide) (PEA),[17] poly(caprolactone)(PCL),[2,18] poly(lactic-co-glycolic acid) (PLGA),[19] and polydimexylsiloxane (PDMS),[20] into BGs have been extensively studied for bone tissue engineering.[21] Preparation of monolithic silica/polydimexylsiloxane/calcium phosphate composites (70%Si20%PDMS10%CaP and 60%Si20%PDMS20%CaP) have been prepared via the sol-gel process combined with micro-molding technique at room temperature.[20] Evaluation of the bioactive properties of monolithic composites were assessed for their role as filling scaffolds in bone surgery with possible drug loading.[20] Results showed an increase in surface mineralization on 70%Si20%PDMS10%CaP composites which could potentially be used as a bone filling material, whereas 60%Si20%PDMS20%CaP composites showed delayed initial mineralization with potential use as a drug release material that bonds to bone.[20]

Among the polymers that can be incorporated into the BG system, synthetic polymers offer increased mechanical strength compared to natural polymers. However, natural polymers are preferred because they possess macromolecules that the biological environment recognizes and metabolizes.[22] Hybrid xerogels composed of silica (SiO_2)/chitosan (CS) and SiO_2/CS/tricalcium phosphate (TCP) have been developed to evaluate the effects of washing treatments using either ethanol or water on the textural and bioactive properties for their potential application in bone regeneration.[23] Gels washed in ethanol resulted in an increased surface area, pore volume, and pore size compared to gels washed in water. In addition, xerogels containing TCP presented a higher ability to form hydroxyapatite on hybrids, promoting the adhesion of cells and proliferation of osteoblasts.[23]

Selection of a natural polymer that better mimics the organic component of bone would, however, be beneficial for developing bone biomaterials. Due to the possible antigenic responses from collagen,[24] gelatin, the hydrolyzed form of type I collagen, could be a suitable polymer. The application of gelatin to develop bone biomaterials is relatively cheap, readily available, and can easily be dispersed in aqueous solutions.[25,26] Gelatins are polymers of a mixture of amino acid moieties joined by peptide bonds ranging from 15,000 and 400,000 Da in molecular weight.[27] The primary structure of gelatin is comprised of more than twenty amino acids in different proportions in such a way that their

molecules are composed of repeating sequences of glycine-X-Y triplets, where X and Y describe the positions of the proline and hydroxyproline, respectively.[27] Moreover, interactions between cells and the ECM are regulated by an arginine-glycine-aspartic acid (RGD) sequence present within the gelatin structure, which also functions as a specific integrin recognition site that promotes cell adhesion, preventing cells from apoptosis as well as accelerating tissue regeneration and therefore, functioning as a biomimetic peptide.[27,28] Furthermore, gelatin is able to molecularly interact with functional groups of organic and inorganic components that can be tailored to present specific physical properties necessary for the development of bioactive bone biomaterials. In the development of a tissue engineered biomaterial for bone repair via a sol-gel process, gelatin has been used as a toughening polymer since BGs are brittle and cannot be implanted in mechanically stressed bone sites.[29] Gelatin by itself would also be too weak to support a bone scaffold. Therefore, the development of a nanocomposite material where BG and gelatin act as the inorganic and organic components, respectively, would potentially improve the bioactivity while serving as a bone scaffold template for the body to repair and regenerate itself.[25] Therefore, combining both gelatin and BG would create a nanocomposite that mimics the hierarchical organic-inorganic structure of bone.

The development of organic-inorganic nanocomposites should possess bioactive features that would enhance their applications as bone biomaterials. Calcium is fundamental to the bioactivity of sol-gel tertiary BGs and a key component of osteogenesis.[30,31] Calcium nitrate has been conventionally used as a calcium source to prepare BGs; however, its use has some disadvantages. The heterogeneity caused by calcium-rich regions and thermal treatments (>400°C) to incorporate calcium ions into the silicate glass network are some of the drawbacks.[32-35] However, its major limitation comes from its incompatibility to incorporate a polymer component for the preparation of organic-inorganic nanocomposites at room temperature because of the high-temperature treatment needed to thermally decompose the nitrate.[1,36]

Different calcium sources that can be used at lower temperatures are required for the synthesis of sol-gel-derived organic-inorganic nanocomposites. The use of calcium chloride ($CaCl_2$), an alternative calcium salt, or calcium ethoxide ($Ca(OEt)_2$), a calcium alkoxide, have been previously reported for the development of nanocomposite bone biomaterials.[1,2,18] A study has also investigated the effects of various calcium sources, such as calcium methoxyethoxide (CME), calcium nitrate and $CaCl_2$, on the properties of sol-gel-derived two-component (SiO_2-CaO)-based BGs and found that CME was a

more suitable calcium source for its potential application in nanocomposite synthesis.[30] A separate research also evaluated the effects and properties of binary (SiO_2-CaO) BGs composed of the above-mentioned calcium sources, including $Ca(OEt)_2$, and assessed their biocompatibilities in a chitosan-BG composite model.[37] Their findings showed that $Ca(OEt)_2$ was the preferred calcium source, showing higher calcium incorporation into the silicate network, homogeneity, bioactivity and biocompatibility.[37] Another study has additionally compared the incorporation of calcium ions from $Ca(OEt)_2$, calcium hydroxide, $CaCl_2$, calcium citrate and calcium acetate into the silicate network of binary BGs.[31] Calcium hydroxide was selected as an alternative to calcium alkoxides for the synthesis and characterizations of polycaprolactone-BG nanocomposite scaffolds synthesized at room temperature.[31] These studies have made possible the understanding of the role and function of calcium sources in the silicate BG network and their application as a biomaterial that mimics the composition of bone.

Furthermore, the addition of carbon-based conductive materials has also been incorporated into organic-inorganic compositions as a new generation of biomaterials that provide additional functionality for bone substitutes, namely conductivity.[28,38] Bone possesses natural conductive properties,[39,40] and the addition of a conductive element into an organic-inorganic bone substitute could better mimic the natural electrical conductivity of bone, providing advantages at the physiological and mechanical levels.[41,42] Most importantly, carbon-based conductive materials could deliver electrical signals within a bone biomaterial through the application of electrical stimulation for the maturation of osteoblasts and to induce the repair and regeneration of bone defects.[43,44] Therefore, uniform distribution of a conductive component into organic-inorganic nanocomposites without affecting the overall properties of the synthesized bone biomaterials is beneficial for electrical stimulation future studies.

Herein, the effects of $CaCl_2$ and $Ca(OEt)_2$ as calcium sources to develop an efficient approach that incorporates gelatin, sol-gel-derived tertiary BG, and uniformly dispersed multiwall carbon nanotubes (MWCNTs) were reported to create bone nanocomposites that mimic the organic-inorganic composition of bone with an electrically conductive element. Incorporation of distributed MWCNT into gelatin-BG nanocomposites was possible and could allow the study of potential future exploration of exogenous electrical stimulation on the maturation of osteoblasts. The main objective of this study was to compare the physicochemical properties of $CaCl_2$- and $Ca(OEt)_2$-based nanocomposites, as well as their elemental distribution within the gelatin-BG-MWCNT biomaterials. In addition, the

swelling, degradation behavior and porosity of the nanocomposites were evaluated. Finally, the *in vitro* bioactive properties of nanocomposites and their suitability to support cell attachment and spreading were explored. Our data showed that gelatin-BG-MWCNT nanocomposites containing $CaCl_2$ or $Ca(OEt)_2$ possessed different physicochemical properties due to the fate of their calcium ions in the silicate glass network of the biomaterial. Although $Ca(OEt)_2$-based nanocomposites were most likely to have more advantageous properties in bone repairing applications, both $CaCl_2$- and $Ca(OEt)_2$-based gelatin-BG-MWCNT nanocomposites have the potential to function as bone repair biomaterials.

3.3. Materials and methods

3.3.1. Materials

Gelatin type A (porcine skin), pluronic F-127, multiwall carbon nanotube (MWCNT, >98% carbon basis, O.D. × L 6-13 nm × 2.5-20 μm), tetraethyl orthosilicate (TEOS, 98%), triethyl phosphate (TEP, 99.8 %), and anhydrous calcium chloride were purchased from Sigma-Aldrich (Milwaukee, WI, USA). Calcium ethoxide was obtained from Gelest Inc. (Morrisville, PA, USA). Dulbecco's Modified Eagle's Medium (DMEM), Hanks' Balanced Salt Solution (HBSS), Fetal Bovine Serum (FBS), penicillin/streptomycin (pen/strep) were acquired from Thermo Fisher. Alexa Fluor® 488 phalloidin and 4'6-diamidino-2-phenylindole (DAPI) were purchased from Life Technologies (Burlington, ON, Canada). Mouse embryo multipotent mesenchymal progenitor cells (C3H/10T1/2 cells) were obtained from ATCC (Manassas, VA, USA).

3.3.2. Preparation of sol-gel derived gelatin-BG-MWCNT nanocomposites using calcium chloride and calcium ethoxide

To prepare gelatin-BG-MWCNT nanocomposites based on calcium chloride ($CaCl_2$), 20 mg/ml of MWCNT was dispersed in Pluronic F-127 (PF-127) solution, which was previously dissolved in water at a high temperature to a concentration of 20 mg/ml, followed by sonication for 2 h at 50°C and stored at RT until further use. Gelatin type A (porcine skin) was dissolved in water at a concentration of 10% w/v. Meanwhile, BG was prepared by sol-gel process from TEOS, TEP, and $CaCl_2$ by adding water and a catalytic amount of 1M HCl for 30 min at room temperature. To prepare 100 mg of BG, 248 μl TEOS, 22 μl TEP and 49 mg of $CaCl_2$ were used. The mole ratio of water/TEOS was kept at 4:1, while 1M HCl was added at a volume ratio (water/HCl) of 3 to catalyze the TEOS hydrolysis.

Viscous gelatin solution was added dropwise to the tertiary glass precursors solution, followed by MWCNT (1 wt.%). Hydrolysis and polycondensation of TEOS were carried out *in situ* while the sol-gelatin-MWCNT mixture was vigorously stirred at 40°C until it became a gel. BG had a final molar composition of 70% SiO_2, 26% $CaCl_2$, and 4% P_2O_5, and the organic-inorganic ratio was maintained at 50 wt.%. Aging of gels was carried out at 55°C for one day, followed by drying under vacuum for one day at 60°C. The final product was then ground to a fine powder. **Table 3.1** presents the nomenclature of the samples.

To prepare gelatin-BG-MWCNT nanocomposites based on calcium ethoxide $(Ca(OEt)_2)$, PF-127 was used to prepare MWCNT stock dispersions (20 mg/ml PF-127 and 20 mg/ml MWCNT). Dispersions were sonicated for 1 h at 50°C and stored at RT until further use. Gelatin type A (porcine skin) was dissolved in water at a concentration of 10% w/v. 1 wt.% MWCNT was added to the gelatin solution, followed by sonication at 50°C for 30 min. BG (100 mg) was prepared by a sol-gel process,[1,45] which consisted of hydrolyzing TEOS (248 µl) and TEP (22 µl) with a catalytic amount of 1M HCl under vigorous stirring at RT. Calcium ethoxide was dissolved separately in 2-ethoxyethanol (54 mg/ml). The hydrolyzed BG precursors were added dropwise to the gelatin-MWCNT mix, followed by calcium ethoxide. BG had a final molar composition of 70% SiO_2, 26% CaO, and 4% P_2O_5, and the organic-inorganic ratio was maintained at 50 wt.%. Biomaterials were aged for one day at RT, followed by drying under vacuum at 40°C. Fine powder was obtained from the final product by grinding with a pestle and mortar. Sample nomenclatures are presented in **Table 3.1**.

Table 3.1. Nomenclature of gelatin-BG-MWCNT nanocomposites.

Gelatin-BG-MWCNT Nomenclature	Gelatin (wt.%)	BG (wt.%)	MWCNT (wt.%)*
50-50-0	50	50	0
50-50-1	50	50	1

*MWCNT was used as an additional filler and the weight percentage added was with respect to the total gelatin-BG composition, which is 100 wt.%.

3.4. Characterization of nanocomposites

3.4.1. Attenuated Total Reflectance Fourier Transform Infrared Spectroscopy (ATR-FTIR)

Dried and powdered nanocomposites were used for FTIR spectroscopy, which was conducted using a Thermo Scientific™ Nicolet™ Summit FTIR Spectrometer with the Everest ATR Accessory in the transmission mode at a resolution of 4 cm^{-1} and sample scans of 24 in the range of 4000 – 500 cm^{-1}.

3.4.2. Scanning Electron Microscopy (SEM) and Energy Dispersive X-ray Spectroscopy (EDX) analysis

Nanocomposite disks were prepared to visualize the surface morphology and elemental distribution of their chemical composition through SEM and EDX, respectively. Briefly, 70 mg of dried gelatin-BG-MWCNT were compress-molded at 121°C with a pressure of 145 psi for 50 min to obtain nanocomposite disk samples of 6 mm diameter and 1.5 mm height. Disks were sputter-coated with gold/palladium (K550X, sputter coater, Emitech Ltd., Ashford, UK), and SEM coupled to EDX was performed by using a Zeiss 1540XB FIB/SEM instrument with an accelerating voltage of 5 kV (Carl Zeiss: Oberkochen, Germany).

3.4.3. Swelling behavior of CaCl$_2$- and Ca(OEt)$_2$-based nanocomposites

Evaluation of the swelling behavior of nanocomposite disks (n=3) was performed in PBS for 6 days at 37°C. The weights of the samples were recorded before (W$_0$) and after incubation in PBS after 1, 3, and 6 days of incubation (W$_t$). The swelling ratio of samples was calculated according to Equation (3.1):

$$Swelling\ Ratio\ (\%) = \frac{W_t - W_0}{W_0} \times 100 \qquad (3.1)$$

3.4.4. *In vitro* biodegradability of CaCl$_2$- and Ca(OEt)$_2$-based nanocomposites

The weight loss percentage of nanocomposite disks (n=3) were determined by measuring the initial weight of the samples (W$_0$) and subsequently incubating in PBS at 37°C. At 1, 3, and 6 days of incubation, the samples were washed with deionized water and dried under vacuum at RT. The final weights of the dried samples were recorded (W$_f$) and were used to calculate the weight loss percentages of each sample, as presented in Equation (3.2).

$$Weight\ loss\ (\%) = \frac{W_0 - W_f}{W_0} \times 100 \qquad (3.2)$$

3.4.5. Micro-CT imaging of CaCl₂- and Ca(OEt)₂-based nanocomposites post-degradation

The morphology of nanocomposite disks after 6 days of degradation was imaged and studied using microcomputed tomography (microCT) (eXplore Locus SP, GE Healthcare, Canada). Nanocomposite disks were scanned at 20 μm voxel resolution, using an exposure time of 0.45 s, 5 frames per view, and a total of 900 views at an increment of 0.4°. Two-dimensional slice images were reassembled from the isotropic slice data and compiled to generate a 3D image. 3D images were analyzed using commercially available trabecular bone analysis software MicroView (GE Healthcare Biosciences). The threshold values distinguishing the nanocomposite biomaterials from air was selected by using air and water as control objects. Analyses of micro-CT images include porosity measurements, pore wall thickness, pore sizes, and surface area to volume ratio of the nanocomposites.

3.4.6. *In vitro* bioactivity of CaCl₂- and Ca(OEt)₂-based nanocomposites

Nanocomposite disks were incubated in simulated body fluid (SBF) solution at a concentration of 10 mg/ml at 37°C under constant shaking at 120 rpm for 7 days. SBF was refreshed every other day. After SBF incubation, nanocomposites were rinsed with water, dried under vacuum at RT, and their surfaces were visualized by SEM/EDX using Zeiss 1540XB FIB/SEM instrument with an accelerating voltage of 5 kV (Carl Zeiss: Oberkochen, Germany). FTIR and X-ray diffraction (XRD) data were acquired on dried samples. XRD data were obtained using an X-ray diffractometer Rigaku Ultima III operating on Cu Kα radiation with λ = 1.5418 Å at 30 kV and 15 mA in the 2θ range of 2–90° at a scanning speed of 2° /min and scanning width of 0.02°.

3.4.7. Cell adhesion and viability of CaCl₂- and Ca(OEt)₂-based nanocomposites

10T1/2 cells were used to investigate cell adhesion onto nanocomposites. Nanocomposite disks were disinfected under ultraviolet (UV) light and pretreated in HBSS (~10-15 min) to pre-wet the samples.[5] 10T1/2 cells (cultured in DMEM with 5% FBS and 1% pen/strep) were subsequently directly seeded onto nanocomposite disks that were placed in a 24 well plate. The nanocomposite disks have a surface area of 0.3 cm^2, thus the seeded cell density on nanocomposites was 98,956

cell/cm^2 and were incubated at 37°C in 5% CO_2. After 24 h incubation, cells were fixed using 4% paraformaldehyde (EMD Chemicals Inc. Gibbstown, NJ) and stained against DAPI (300 nmol in PBS) and phalloidin (1:100) to visualize cell nuclei and F-actin, respectively. Live/dead cell staining kit was used for 10T1/2 cells viability on standard media and conditioned media (extracts) after 24, 72, and 168 h according to manufacturer's protocol. Conditioned media was prepared by incubating nanocomposites in fresh DMEM (5% FBS, 1% pen/strep) for 24 h at 37°C. In a typical experiment, ~70 mg nanocomposite disks (6 mm diameter and 1.5 mm height) were incubated in 7 ml DMEM, corresponding to 10 mg/ml. After 24 h, the media which was conditioned with nanocomposite extracts, was used as cell culture media to perform viability studies in a 24-well plate (working volume was 1 ml conditioned media). The same number of cells that were plated onto nanocomposites were evenly plated into a 24-well plate, resulting in a cell density of 15,625 cells/cm^2. Standard culture media and conditioned media were changed every other day. Cells seeded on a tissue culture plate (TCP) were used as controls. Images were taken with a Leica DMi8 fluorescence microscope (Leica Microsystems CMS GmbH, Wetzlar, Germany). Experiments were done in triplicate.

3.4.8. Statistical analysis

Statistical analysis of the data was performed using GraphPad Prism. Differences were tested by one-way ANOVA, and a p-value of < 0.05 was used for statistical significance.

3.5. Results and discussion

3.5.1. Preparation of gelatin-BG-MWCNT nanocomposites from CaCl$_2$- and Ca(OEt)$_2$ calcium sources

Calcium is an important element in osseous tissue, and its presence in a nanocomposite biomaterial could mimic bone's natural inorganic composition. Evaluation of the effects of calcium sources on the synthesized tertiary BG could provide a better understanding of their role in the glass network and their function within nanocomposite bone biomaterials.

Figure 3.1 presents the FTIR spectra showing the different chemical groups of the PF-127 surfactant, sol-gel precursors (**Fig. 3.1A**) as well as of gelatin, tertiary BG using calcium chloride (CaCl$_2$) or calcium ethoxide (Ca(OEt)$_2$) as calcium sources, and their corresponding organic-inorganic

nanocomposites with their corresponding digital images (**Fig. 3.1B**). The bands associated for PF–127 spectrum are 2877 cm^{-1} (-C-H (aliphatic region)), 1473 cm^{-1} (C-C stretching), 1341 cm^{-1} (O–H plane) and 1101 cm^{-1} (region C-O) with three specific spots at 1061 cm^{-1}, 1106 cm^{-1} and 1145 cm^{-1} that also suggest C–O–C stretching.[46] Peaks at 1286 cm^{-1} and 1287 cm^{-1} correspond to CH$_2$ twisting, whereas bands at 956 cm^{-1} and 840 cm^{-1} are related to CH$_2$ wobbling.[46] The sol-gel precursors used were TEOS and TEP, and the calcium sources were CaCl$_2$ and Ca(OEt)$_2$ (**Fig. 3.1A**). TEOS, which was used as the silica precursor in the sol-gel process, possessed characteristics peaks at 2979, 2887, 1394, 1104, 1078 and 956 cm^{-1}. The band at around 2979 cm^{-1} is assigned to the stretching vibrations of -C-H bond, while the band observed at 2887 cm^{-1} corresponds to the absorption band of the methyl (CH$_3$) groups.[47] In addition, the peak at 1394 cm^{-1} is attributed to the asymmetric bending of -C-H bonds,[48] while the band presented at 1104 cm$^{-1,}$ corresponding to the ethoxy group bound to the silicon atom (Si-OCH$_2$CH$_3$), was observed. The peak at 1078 cm^{-1} is associated with the siloxane bonds (Si-O-Si), whereas the band at 956 cm^{-1} is characteristic of the -C-H rocking vibrations of TEOS.[48,49] Furthermore, the P$_2$O$_5$ precursor, TEP, also presented bands related to the symmetric stretching vibrations of -C-H bonds at 2987 and 2907 cm^{-1}, as well as peaks related to the asymmetric bending of the -C-H bonds at around 1500 and 1368 cm^{-1}.[50] The prominent peak observed at 1018 and 965 cm^{-1} corresponds to the -P-O valence vibrations, while the band at 1263 cm^{-1} is attributed to the -P=O stretching vibrations of TEP.[50] Moreover, CaCl$_2$ presented peaks observed at 3503 and 3393 cm^{-1} associated with the asymmetric -OH stretch, whereas the band at 1629 cm^{-1} corresponded to the H-O-H bending vibration of CaCl$_2$.[51,52] Although anhydrous calcium chloride was used, its hygroscopic nature during sample transfer is the likely source of the -OH stretch. The appearance of the bands corresponding to -OH and H-O-H indicate the existence of different hydrogen bonding environments resulting from interactions with chloride ions as well as water molecules.[51] Additional peaks at around 650 cm^{-1} are associated with the Ca-O stretching vibration.[53] Lastly, Ca(OEt)$_2$ presented peaks between 3000 and 2800 cm^{-1} due to the C-H stretching, as well as an alkane (-C-H) bending at 1400 cm^{-1}.[54] In addition, the bands observed between 1100 and 1050 cm^{-1} are characteristic of the primary alcohol (-C-O) stretching.[54]
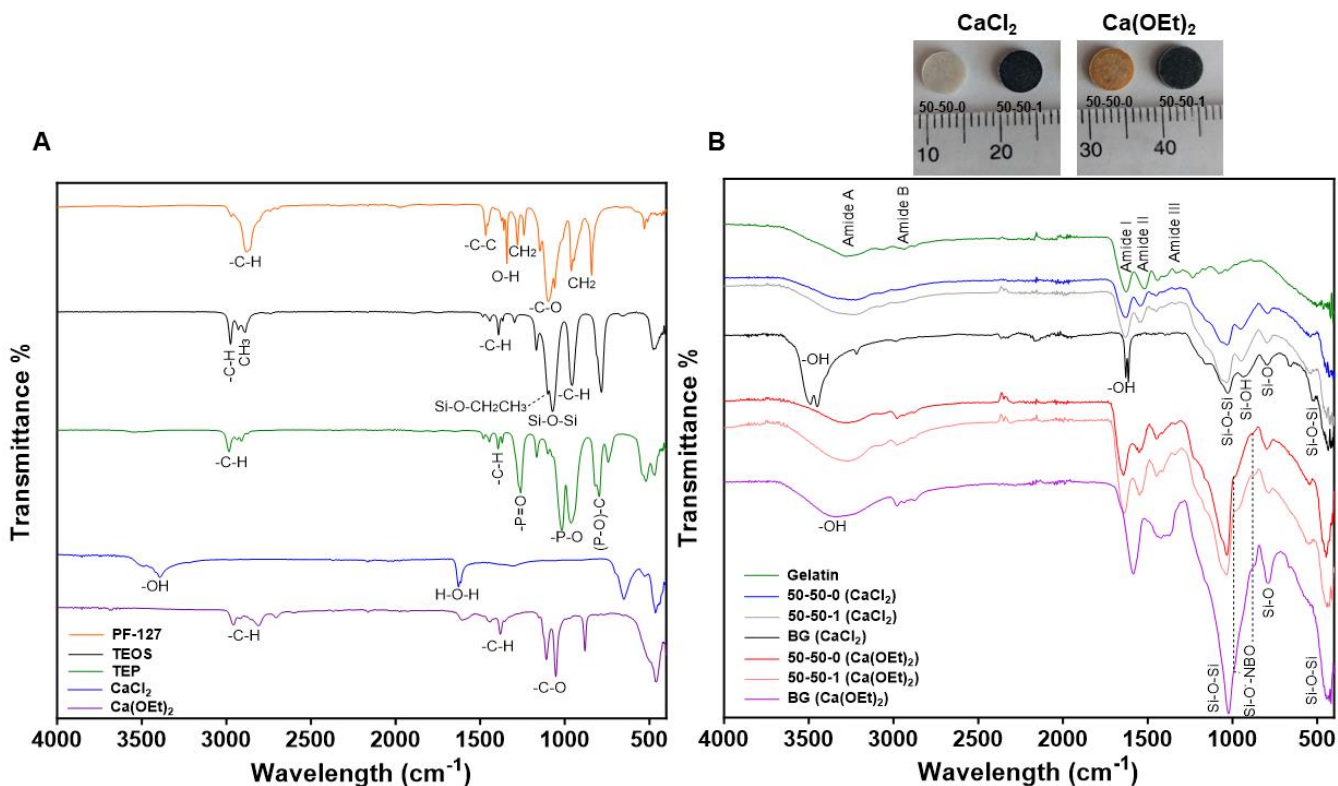
Figure 3.1. Chemical characterization of PF-127 surfactant, sol-gel precursors, organic, inorganic and nanocomposites using CaCl₂ and Ca(OEt)₂ as calcium sources. (**A**) FTIR spectra of PF-127 surfactant, sol-gel TEOS and TEP precursors, as well as CaCl₂ and Ca(OEt)₂ calcium sources. (**B**) Digital images of CaCl₂- and Ca(OEt)₂-based 50-50-0 and 50-50-1 nanocomposite disks. FTIR spectra of gelatin, BG containing CaCl₂ and Ca(OEt)₂, 50-50-0 and 50-50-1 nanocomposites composed of either CaCl₂ and Ca(OEt)₂.

The tertiary BG containing CaCl₂ presented characteristic peaks between 3496 and 3454 cm⁻¹ due to the -OH stretching and bending vibrations of the self-associated silanol (Si-OH) groups (**Fig. 3.1B**). In the Ca(OEt)₂-based tertiary BG, this peak is shifted slightly to 3370 cm⁻¹. However, the CaCl₂-based BG also presented an additional peak at 1630 cm⁻¹ due to the self-associated Si-OH groups[45] which overlapped with the peak associated with the residual water of CaCl₂.[51,52] In the BG containing Ca(OEt)₂, there were bands associated to C-H vibrational modes at around 2900 and 1400 cm⁻¹. While incomplete hydrolysis could be a suspect for these peaks, this cannot explain it fully, especially since the experiment was repeated with longer hydrolysis and drying times (96 h). Interestingly, the peak at around 2900 cm⁻¹ has been observed even in a melt-derived CaO-SiO₂ glass with no obvious source

of CH_2 groups and persisted even after SBF treatment.[55] This small peak was also observed in a previous study of SiO_2-P_2O_5 system after 72 h hydrolysis and 7 days of aging.[45] Therefore, the data indicates that these peaks are not necessarily associated with incomplete hydrolysis of the inorganic components. Furthermore, peaks at 1025 cm^{-1} due to the asymmetric stretching of the siloxane bond (Si-O-Si) as well as a band at around 800 cm^{-1} associated with the bending Si-O vibration of the ring structures of the glass for both $CaCl_2$- and $Ca(OEt)_2$-based BGs were observed (**Fig. 3.1B**).[56] Both $CaCl_2$- and $Ca(OEt)_2$-synthesized BGs presented a band at around 450 cm^{-1} corresponding to the rocking motion of oxygen bridging two adjacent silica atoms from the Si-O-Si groups of the glass network.[1] BG containing $CaCl_2$ as a calcium source presented a peak at 943 cm^{-1} related to the silanol (Si-OH) groups from the incomplete polycondensation of the TEOS (**Fig. 3.1B**).[45] In contrast, evidence of peaks showing the incorporation of calcium ions to the silicate glass network was observed in the $Ca(OEt)_2$-based BG as shown by the peaks at 984 cm^{-1} and 887 cm^{-1}, corresponding to the Si-O$^-$-non-bridging oxygen (NBO) (**Fig. 3.1B**).[57] Evidence showing the incorporation of calcium ions to the silicate glass network was observed by the broader Si-O-Si bands in the $Ca(OEt)_2$-based BG. The broader bands indicate increased disorganization and decreased polymerization within the silicate glass network due to the incorporation of network-modifying calcium ions.[37]

Furthermore, gelatin showed distinguishing bands at 3270 cm^{-1} and 2946 cm^{-1} associated with amide A and amide B, respectively. These bands corresponded to the stretching vibrations of the free N-H and O-H groups and the asymmetric stretching vibrations of =C-H and -NH_3^+ of the peptide fragments, respectively. Peaks corresponding to amide I at 1627 cm^{-1} as a result of the C=O stretching vibrations along the polypeptide backbone of gelatin was observed, as well as the presence of amide II at 1524 cm^{-1} corresponding to the N-H bending and C-N stretching vibrations.[57,58] An additional band at 1234 cm^{-1} was observed, indicating the presence of amide III which is associated to the wagging vibrations of CH_2 groups from the glycine backbone and proline side chains as well as the presence of the vibration of stretching C-N bonds and the vibration of bending N-H bonds.[59-61]

Gelatin-BG-MWCNT (50-50-1) nanocomposites composed of $CaCl_2$ and $Ca(OEt)_2$ showed peaks attributed to both the inorganic sol-gel derived silica phase as well as the organic gelatin component (**Fig. 3.1B**). In addition, **Figure 3.1B** shows the FTIR spectra of the 50-50-0 nanocomposites where the same peaks corresponding to the organic and inorganic elements of the 50-50-1 biomaterials, are observed. Therefore, no chemical shift is expected in the 50-50-0 nanocomposites. The presence of both organic-inorganic groups within the nanocomposites shows the existence of a physical bond

between these elements within the biomaterial. In addition, the band corresponding to amide III for both CaCl$_2$- and Ca(OEt)$_2$-based 50-50-0 and 50-50-1 nanocomposites was decreased (**Fig. 3.1B**). This characteristic feature has been observed before in another study and was reported to be due to the interaction between the silicon hydroxyl (Si-OH) groups of BG and the amino (-NH$_2$) groups of gelatin polymer by electrostatic and hydrogen bonding.[61] Finally, calcium ions from the Ca(OEt)$_2$-based 50-50-0 and 50-50-1 nanocomposites were also incorporated into the silicate glass network. This was observed from the peaks attributed to the NBO to form Si-O-Ca and the broader Si-O-Si bands in the Ca(OEt)$_2$-based nanocomposites.[37]

3.5.2. Surface morphological and elemental distribution of 50-50-1 nanocomposites prepared from CaCl$_2$- and Ca(OEt)$_2$ sources

Adequate dispersion of the elements of the nanocomposites is beneficial to ensure homogeneous incorporation of all components in the organic-inorganic system. Calcium is fundamental to the bioactivity of sol-gel BGs and a key component of osteogenesis.[30,31] The surface morphology and elemental distribution of nanocomposites using CaCl$_2$ (**Fig. 3.2A-F**) and Ca(OEt)$_2$ (**Fig. 3.2G-L**) as calcium sources for the preparation of 50-50-1 nanocomposites were visualized using SEM and EDX. The tables in **Figures 3.2B, H** show the atomic percentages of the elements in the specific region where the SEM was obtained. Although there is no elemental mapping for oxygen, its presence is characteristic due to the oxides in the tertiary BG (SiO$_2$, CaCl$_2$, P$_2$O$_5$ and SiO$_2$, CaO, P$_2$O$_5$). Both CaCl$_2$ and Ca(OEt)$_2$-based 50-50-1 nanocomposites showed uniform elemental distribution of their organic and inorganic components. Carbon atoms were uniformly dispersed within the nanocomposite, representing the presence of gelatin and MWCNT (**Fig. 3.2C, I**), whereas silicon, calcium, and phosphorous elements were attributed to the tertiary BG (**Fig. 3.2D-F, J-L**).

Chemically, CaCl$_2$ and Ca(OEt)$_2$-based 50-50-1 nanocomposites are different since the calcium ions from the Ca(OEt)$_2$ calcium source are incorporated within the nanocomposite network. Although evidence has shown that calcium chloride salts fail to enter the network even after applying any elevated temperatures,[30] both CaCl$_2$ and Ca(OEt)$_2$-based 50-50-1 nanocomposites showed uniform elemental distribution. The advantages of using CaCl$_2$ and Ca(OEt)$_2$ as calcium sources for the preparation of *in situ* sol-gel organic-inorganic nanocomposites are that they are synthesized at room temperature, and good surface homogeneity of their elements was obtained.
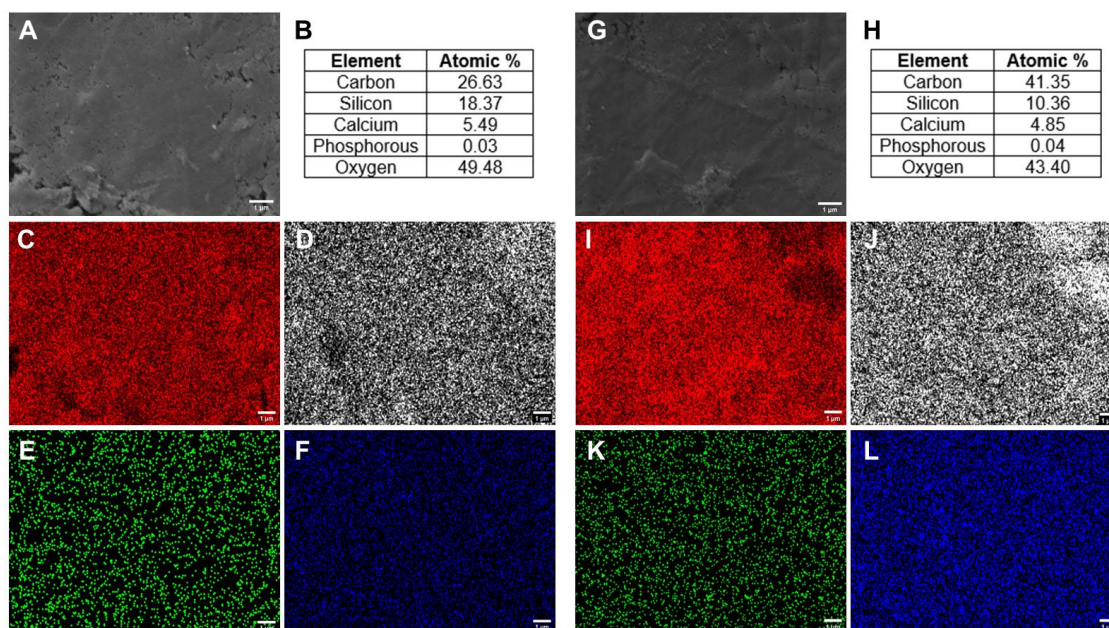
Figure 3.2. Surface elemental homogeneity in 50-50-1 nanocomposites using CaCl₂ and Ca(OEt)₂ as calcium sources. (**A**) SEM image, (**B**) atomic percentages of elements, and elemental mapping of (**C**) carbon, (**D**) silicon, (**E**) calcium, (**F**) phosphorous for the CaCl₂-based 50-50-1 nanocomposite. (**G**) SEM image, (**H**) atomic percentages of elements, and elemental mapping of (**I**) carbon, (**J**) silicon, (**K**) calcium, (**L**) phosphorus for the Ca(OEt)₂-based 50-50-1 nanocomposite. Scale bar = 1 µm.

3.5.3. Swelling behavior of nanocomposites composed of CaCl₂- and Ca(OEt)₂ calcium sources

The swelling of nanocomposites is an important property that ensures nutrient transport and removal of waste products for their application as bone biomaterials. Following the observation that CaCl₂ and Ca(OEt)₂-based nanocomposites are chemically different but show homogeneous incorporation of the organic-inorganic element system, an assessment of the swelling behavior as a function of calcium sources was conducted. Digital images of the swelling behavior of nanocomposite disks are shown before and after incubation in PBS for 6 days (**Fig. 3.3A&B**). The digital images demonstrate that Ca(OEt)₂-based nanocomposites swell and their diameters increased to 9 mm. However, CaCl₂-based nanocomposites did not swell after incubation in PBS; instead, their weight was reduced, and the diameter of the disks decreased by 1 mm. Therefore, the swelling ratio of the CaCl₂-based nanocomposites was not plotted in **Fig. 3.3C** since the water uptake of the biomaterials was not applicable. However, for Ca(OEt)₂-containing nanocomposites, swelling ratios of 130% (composition 50-50-0) and 226% (composition 50-50-1) were observed after 6 days of incubation. The increasing

swelling behavior observed in the 50-50-1 nanocomposite could be due to the addition of MWCNTs to the organic-inorganic system, leading to a higher surface area and increasing its water uptake.[62,63]

The difference in swelling behavior is explained by the sources of calcium used to prepare the nanocomposites and the fate of gelatin in the system. Calcium ions in the $Ca(OEt)_2$-based nanocomposites are incorporated into the matrix, therefore entrapping the gelatin into the nanocomposite network, which causes swelling. In addition, the presence of strong ionic interactions between the released calcium ions from the BG with the carboxylic groups in gelatin causes aggregation of the polymer chains within the nanocomposite system.[64,65] The calcium in $CaCl_2$-containing nanocomposites, however, are not bonded in the matrix which results in mass loss due to the diffusion of calcium salts. In addition, the existence of weaker interactions between the organic and inorganic components causes the gelatin to leach out faster and, therefore, limits the swelling of the nanocomposite. Thus, $Ca(OEt)_2$-based nanocomposites, especially the 50-50-1, could function better as a bone biomaterial and could likely lead to efficient nutrient transport and removal of waste products for its application for the repair and regeneration of bone.
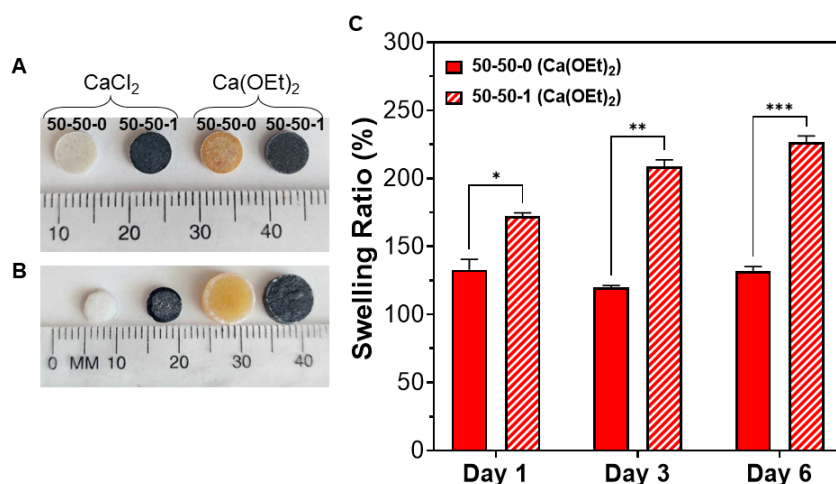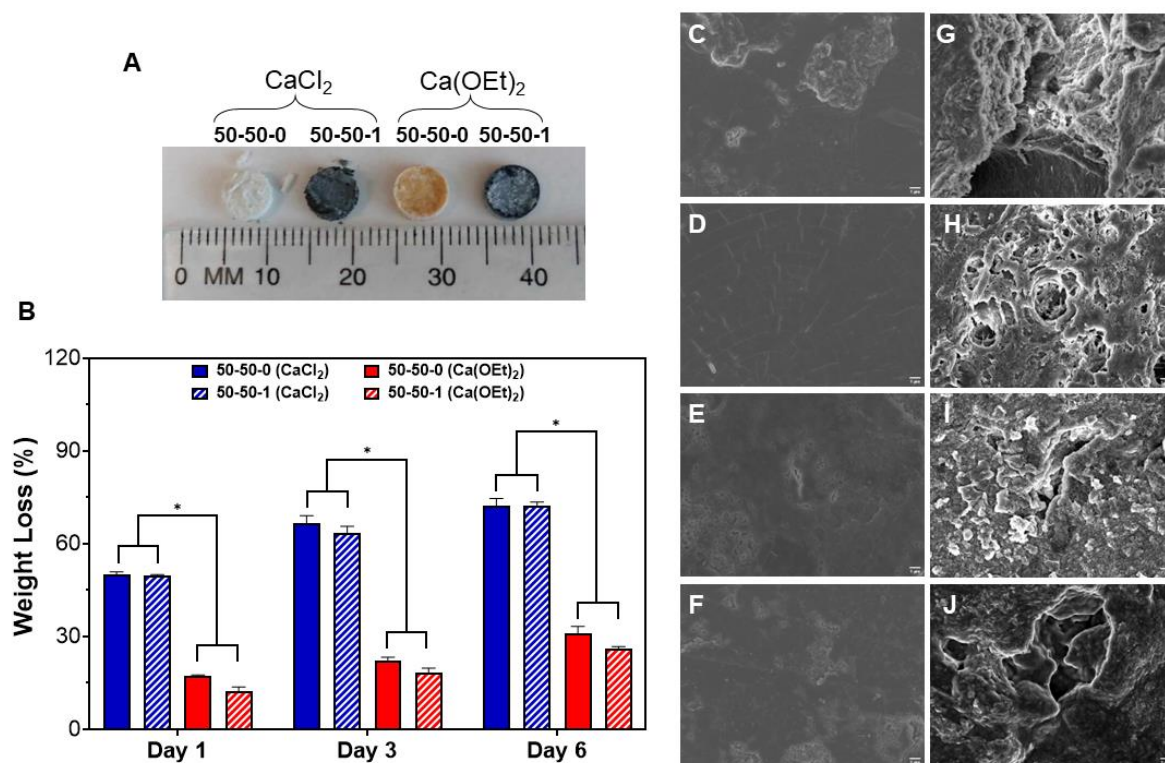

Figure 3.3. Swelling behavior of 50-50-0 and 50-50-1 nanocomposites composed of $CaCl_2$ and $Ca(OEt)_2$ calcium sources. Digital images of nanocomposites as-prepared in dry state (**A**) and after (**B**) incubation in PBS for 6 days in wet state. (**C**) Swelling ratio of $Ca(OEt)_2$-based nanocomposites throughout 6 days of incubation. *$p < 0.05$, **$p < 0.01$, ***$p < 0.001$.

3.5.4. *In vitro* biodegradation study of CaCl₂- and Ca(OEt)₂-based nanocomposites

The degradation behavior of 50-50-0 and 50-50-1 nanocomposites containing either $CaCl_2$ or $Ca(OEt)_2$ was performed for 6 days in PBS. Digital images were taken of the nanocomposite disks before (**Fig. 3.3A**) and after (**Fig. 3.4A**) degradation. Nanocomposites containing $CaCl_2$ as a calcium source were very brittle, as observed by the fragmented pieces after drying. In contrast, nanocomposites containing $Ca(OEt)_2$ as the calcium source were dimensionally stable (**Fig. 3.4A**).

The weight loss of 50-50-0 and 50-50-1 nanocomposites containing either $CaCl_2$ or $Ca(OEt)_2$ are shown in **Figure 3.4B**. Weight loss percentages of $CaCl_2$-based 50-50-0 and 50-50-1 nanocomposites were 50% after one day of degradation. However, $Ca(OEt)_2$-based nanocomposites showed significantly less weight loss percentages of 17% and 12% for the 50-50-0 and 50-50-1 nanocomposites, respectively. After 3 days of degradation, the 50-50-0 and 50-50-1 nanocomposites containing $CaCl_2$ continued degrading and presented weight loss percentages of 66% and 63%, respectively. In contrast, $Ca(OEt)_2$-based 50-50-0 and 50-50-1 nanocomposites showed a significantly decreased degradation of only 22% and 18%, respectively. This tendency was observed throughout the entire degradation period where at day 6 of degradation, $CaCl_2$-based nanocomposites showed a weight loss percent of 72%, but was low for the $Ca(OEt)_2$-containing biomaterials which were of 30% and 26% for the 50-50-0 and 50-50-1 nanocomposites, respectively. The significant difference in weight loss is due to the calcium sources used to prepare the sol-gel BG. The considerable mass loss of nanocomposites produced with $CaCl_2$ was due to the unsuccessful incorporation of the calcium ions derived from the chloride salt to enter the silicate network.[37] However, the $Ca(OEt)_2$ calcium source was involved in the *in situ* inorganic polymerization of the sol-gel BG during nanocomposite synthesis. This resulted in the incorporation of calcium ions into the silicate network,[30,66] as confirmed in **Figure 3.1B**, causing a decreased weight loss percentage. As stated in the methods section, 0.234g (0.001125mol) TEOS, 0.024 g (0.000132 mol) TEP and 0.049g (0.000441mol) $CaCl_2$ or 0.541g (0.000416mol) $Ca(OEt)_2$ were used to synthesize tertiary BG. After the stoichiometric reaction, 0.001125 mol of SiO_2, 0.0000659 mol P_2O_5 and 0.000441mol $CaCl_2$ or 0.000416 mol CaO will be produced. These correspond to a molar composition of ~70% SiO_2, ~4% P_2O_5 and ~26% $CaCl_2$ or CaO. Thus, the mass loss data for the $CaCl_2$-based system indicated that both gelatin and $CaCl_2$ were lost (the sum of gelatin + $CaCl_2$ in the formulation was ~69.5% on the basis of mass). Our results would, therefore, indicate that $Ca(OEt)_2$-based nanocomposites could become a better calcium source for synthesizing organic-inorganic bone biomaterials.

Figure 3.4. *In vitro* **biodegradation study of 50-50-0 and 50-50-1 nanocomposites composed of CaCl₂ and Ca(OEt)₂ calcium sources.** (**A**) Digital images of $CaCl_2$- and $Ca(OEt)_2$-based 50-50-0 and 50-50-1 nanocomposites after 6 days of degradation. (**B**) Biodegradation behavior of $CaCl_2$- and $Ca(OEt)_2$-based 50-50-0 and 50-50-1 nanocomposites within 6 days. SEM images of nanocomposites before (**C**) 50-50-0 ($CaCl_2$), (**D**) 50-50-1 ($CaCl_2$), (**E**) 50-50-0 ($Ca(OEt)_2$), (**F**) 50-50-1 ($Ca(OEt)_2$) and after (**G**) 50-50-0 ($CaCl_2$), (**H**) 50-50-1 ($CaCl_2$), (**I**) 50-50-0 ($Ca(OEt)_2$), (**J**) 50-50-1 ($Ca(OEt)_2$) 6 days of degradation. Scale bar = 1 µm. *$p < 0.05$.

The morphology of the nanocomposites before and after degradation was observed. **Figures 3.4C-F** show the SEM images of the surfaces of 50-50-0 (**Fig. 3.4C,E**) and 50-50-1 (**Fig. 3.4D, F**) before degradation where the calcium source used was either $CaCl_2$ (**Fig. 3.4C,D**) or $Ca(OEt)_2$ (**Fig. 3.4E,F**). A non-porous structure with some roughness due to the compression molding process of the nanocomposites were observed for all nanocomposites. However, nanocomposites presented a porous structure after the degradation period (**Fig.4G-J**). Formation of a porous structure post-degradation was most evident in nanocomposites containing $CaCl_2$ (**Fig. 3.4G,H**) than $Ca(OEt)_2$ (**Fig. 3.4I,J**). Degradation of BG occurs through hydrolysis of the Si-O-Si bonds of the glass structure, forming

Si(OH)$_4$ and silanol. The presence of calcium, as a network modifier, accelerates the degradation process since it disrupts the silicate network. This is the case for nanocomposites composed of Ca(OEt)$_2$. However, in the case of CaCl$_2$-based BG, the calcium ions are therefore entrapped physically in the glass network and can diffuse out easily upon contact with water or biological fluids. Pure BGs are inherently brittle regardless of the calcium sources that are being used, but toughness is conferred upon addition of gelatin.[29] Degradation of gelatin occurs hydrolytically and enzymatically,[67] and possesses a melting temperature of ~30°C. The gelatin component of the synthesized gelatin-BG-MWCNT nanocomposite would be leaching out of the biomaterial, creating a porous structure. For bone repair applications, the interconnected porous structure could potentially allow cells to infiltrate the pores of the nanocomposites and lay down their extracellular matrix (ECM) to remodel and regenerate bone.

3.5.5. Microstructure, pore size and porosity of CaCl$_2$- and Ca(OEt)$_2$-based nanocomposites

Micro-CT imaging was obtained to better visualize the morphology and investigate the porosity, pore wall thickness and pore size distribution of the nanocomposites after 6 days of degradation. **Figure 3.5** shows the micro-CT isosurface images of 50-50-0 and 50-50-1 nanocomposites containing either CaCl$_2$ or Ca(OEt)$_2$ calcium sources. The CaCl$_2$-based nanocomposites depict a more porous and brittle structure, where the biomaterial appears to have been disintegrating (lifted) as a result of the increased degradation. In contrast, Ca(OEt)$_2$-based nanocomposites have a more compact and tougher structure. The organic-inorganic nanocomposites post-degradation present reduced pore sizes and a decreased porous structure because the gelatin component was added as the polymer matrix and leached out throughout the whole nanocomposite.
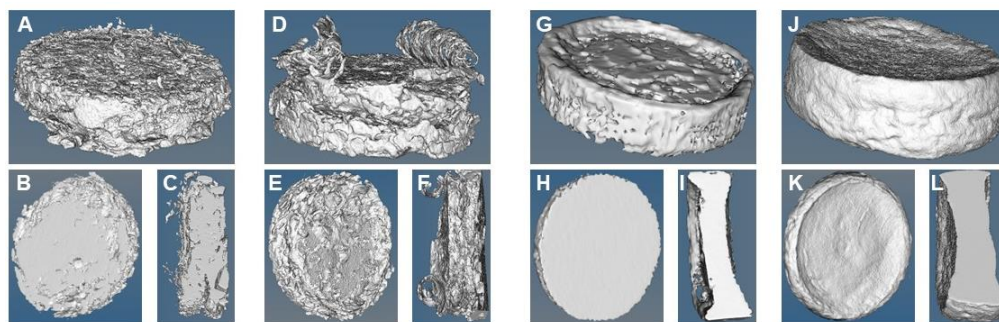
Figure 3.5. Micro-CT images of CaCl₂- and Ca(OEt)₂-containing 50-50-0 and 50-50-1 nanocomposites after 6 days of degradation. (**A-C**) 50-50-0 (CaCl₂), (**D-F**) 50-50-1 (CaCl₂), (**G-I**) 50-50-0 (Ca(OEt)₂), (**J-L**) 50-50-1 Ca(OEt)₂). (**B, E, H, K**) are horizontal cross sections of nanocomposites. (**C, F, I, L**) are vertical cross sections of the nanocomposites.

The average porosity of the 50-50-0 and 50-50-1 nanocomposites composed of $CaCl_2$ were 24.48% and 29.59%, respectively, whereas for the 50-50-0 and 50-50-1 nanocomposites composed of $Ca(OEt)_2$ were 5.03% and 5.84% (**Table 3.2**). The calcium in nanocomposites containing $CaCl_2$ was expected to leach out since the calcium ions are not bonded in the nanocomposite matrix, therefore resulting in more porosity after degradation. However, the low porosity found in $Ca(OEt)_2$-based nanocomposites would most likely come from the gelatin that had been leached during degradation since the calcium ions form part of the organic-inorganic matrix. Furthermore, pore wall thickness increased with the $Ca(OEt)_2$-based nanocomposites. 50-50-0 and 50-50-1 $CaCl_2$-based nanocomposites presented pore wall thickness values of 0.49 µm and 0.41 µm, respectively, while the values for $Ca(OEt)_2$-based nanocomposites were 1.64 µm and 1.92 µm. In addition, the pore sizes of nanocomposites containing $CaCl_2$ were 0.16 µm for both 50-50-0 and 50-50-1 nanocomposites. However, decreased pore size values were obtained for the 50-50-0 and 50-50-1 $Ca(OEt)_2$-containing nanocomposites which were 0.06 µm and 0.10 µm, respectively. Although the pore sizes of the nanocomposites are not large enough to allow cell infiltration into the porous structure, the generation of micropores (0.1-10 µm pore size) improves cell attachment by creating a rough surface allowing penetration of body fluids.[68,69] In addition, the generation of nanopores (<0.10 µm) creates a larger surface area that increases the bioactive properties of the materials and stimulates greater ion exchange and protein adsorption, which are favorable for bone repair applications.[69-71] The surface area to volume ratio was higher for $CaCl_2$-based nanocomposites, where the values for 50-50-0 and 50-50-1

nanocomposites were 4.08 mm^{-1} and 4.90 mm^{-1}, respectively, while the values for Ca(OEt)$_2$-based nanocomposites were 1.22 mm^{-1} and 1.04 mm^{-1}, respectively.

Table 3.2. Pore properties and porosity of CaCl$_2$- and Ca(OEt)$_2$-containing nanocomposites.

Sample	Porosity (%)	Pore wall thickness (μm)	Pore size (μm)	Surface area to volume ratio (mm^{-1})
50-50-0 (CaCl$_2$)	24.48	0.49	0.16	4.08
50-50-1 (CaCl$_2$)	29.59	0.41	0.16	4.90
50-50-0 Ca(OEt)$_2$	5.03	1.64	0.06	1.22
50-50-1 Ca(OEt)$_2$	5.84	1.92	0.10	1.04

3.5.6. *In vitro* bioactivity of CaCl$_2$- and Ca(OEt)$_2$-based 50-50-0 and 50-50-1 nanocomposites

Bone substitutes should be capable of possessing bioactive properties to promote the formation of bone. Due to the nature of BG, its presence within the organic-inorganic nanocomposites should provide bioactive features that induce the formation of hydroxycarbonate apatite (HCA) (Ca$_{10-x}$(PO$_4$)$_{6-x}$(CO$_3$)$_x$(OH)$_{2-x}$) which is normally found in bone. The formation of HCA layers occurs through the release of soluble ionic species from the tertiary BG component, such as Si, Ca^{2+}, and PO$_4$$^{3-}$ ions, into the simulated body fluid (SBF) solution. The release of these ions is followed by their re-deposition to form a high-surface-area hydrated silica and polycrystalline HCA bilayer on the glass surface, similar to that of bone.[18,28] Evaluation of the HCA formation on the surfaces of the organic-inorganic nanocomposite disks was performed by incubating in SBF. **Figure 3.6A** shows the SEM images of nanocomposites after incubation in SBF for 7 days. Although the formation of HCA can be evaluated at different time points ranging from day 0 to day 10,[18,72] day 7 represents a time point in which the HCA formation is comparable to that of further treatment periods in SBF. Regardless of the calcium sources used for the synthesis of the inorganic component within the organic-inorganic nanocomposite, characteristic spherical-shaped HCA crystallized particles were observed on the surfaces of 50-50-0 and 50-50-1 nanocomposite disks after incubation in SBF for 7 days. **Table 3.3** presents the atomic percentages of Ca and P before and after incubation in SBF, as well as the Ca/P ratio of CaCl$_2$- and Ca(OEt)$_2$-based nanocomposites after SBF treatment. The results show that the nanocomposites were enriched with Ca and P, the main components of HCA in bone, as observed in the increased atomic percentages of Ca and P on the nanocomposites after SBF incubation (**Table 3.3**). Additionally, the resulting Ca/P ratios after SBF treatment were higher than the stoichiometric Ca/P ratio of hydroxyapatite (Ca$_{10}$(PO$_4$)$_6$(OH)$_2$), a typical artificial bone,[73] which is between 1.67

and 1.50. The increased Ca/P ratio in the nanocomposite could be due to the carbonate ion substitution in the HCA structure.[74] In addition, the incorporation of 1 wt.% MWCNT did not interfere with the formation of HCA layer on the surfaces of nanocomposites. The increased atomic percentages of Ca and P in the Ca(OEt)$_2$-based nanocomposites depict enhanced bioactivity.

Table 3.3. Atomic percentages of Ca and P before and after SBF incubation including Ca/P ratio of CaCl$_2$- and Ca(OEt)$_2$-based nanocomposites after SBF treatment.

Sample	Atomic % Ca before SBF	Atomic % P before SBF	Atomic % Ca after SBF	Atomic % P after SBF	Ca/P ratio after SBF
50-50-0 CaCl$_2$	6.40	0.03	16.93	8.76	1.93
50-50-1 CaCl$_2$	5.49	0.03	17.93	9.62	1.86
50-50-0 Ca(OEt)$_2$	5.83	0.04	20.40	10.34	1.97
50-50-1 Ca(OEt)$_2$	4.85	0.04	20.20	10.53	1.91

Confirmation of the formation of HCA layer on the surfaces of the nanocomposites after SBF incubation was assessed using FTIR (**Fig. 3.6B**) and XRD (**Fig. 3.6C**). The FTIR spectra of nanocomposites presented peaks corresponding to the deformation vibration of PO$_4^{3-}$ ions at 567, 600 and 670 cm^{-1}.[28] The band at 600 cm^{-1} was mostly prominent to the CaCl$_2$-containing nanocomposites, whereas the peak at 670 cm^{-1} was slightly more noticeable to the Ca(OEt)$_2$-based nanocomposites. Some known bands overlapped with the peaks corresponding to the nanocomposites, but a distinguished peak was observed at around 960 relating to the deformation vibration of PO$_4^{3-}$ ions. Peaks corresponding to the CO$_3^{2-}$ group were observed at 1550 and 1460 cm^{-1} and were assigned to the A- and B-types carbonation (**Fig. 6B**). A-type carbonation occurs when the carbonate ions replace the hydroxyl ions, while the B-type carbonation appears when the carbonate ions enter the hydroxyapatite lattice replacing the phosphate ions.[74] In addition, a band at around 875 cm^{-1} was starting to form corresponding to the labile surface CO$_3^{2-}$ functional group.[75-77] The latter indicated the substitution of CO$_3^{2-}$ ions into the apatite, confirming the formation of HCA on the surface of nanocomposite hydrogels.[28,75,77] An increase in the peak intensity at around 800 cm^{-1}, corresponding to the Si−O−Si vibration, was observed for all nanocomposites. The increased band intensity suggests the existence of a silica-rich layer.[30] Similarly, the asymmetric stretching of the siloxane bond (Si-O-Si) at around 1025 cm^{-1} became broader in the CaCl$_2$-based 50-50-0 nanocomposite, which could also indicate the formation of a silica-rich layer. Moreover, a peak at 2980 cm^{-1} was observed due to the presence of H-C-O functional group.[77]
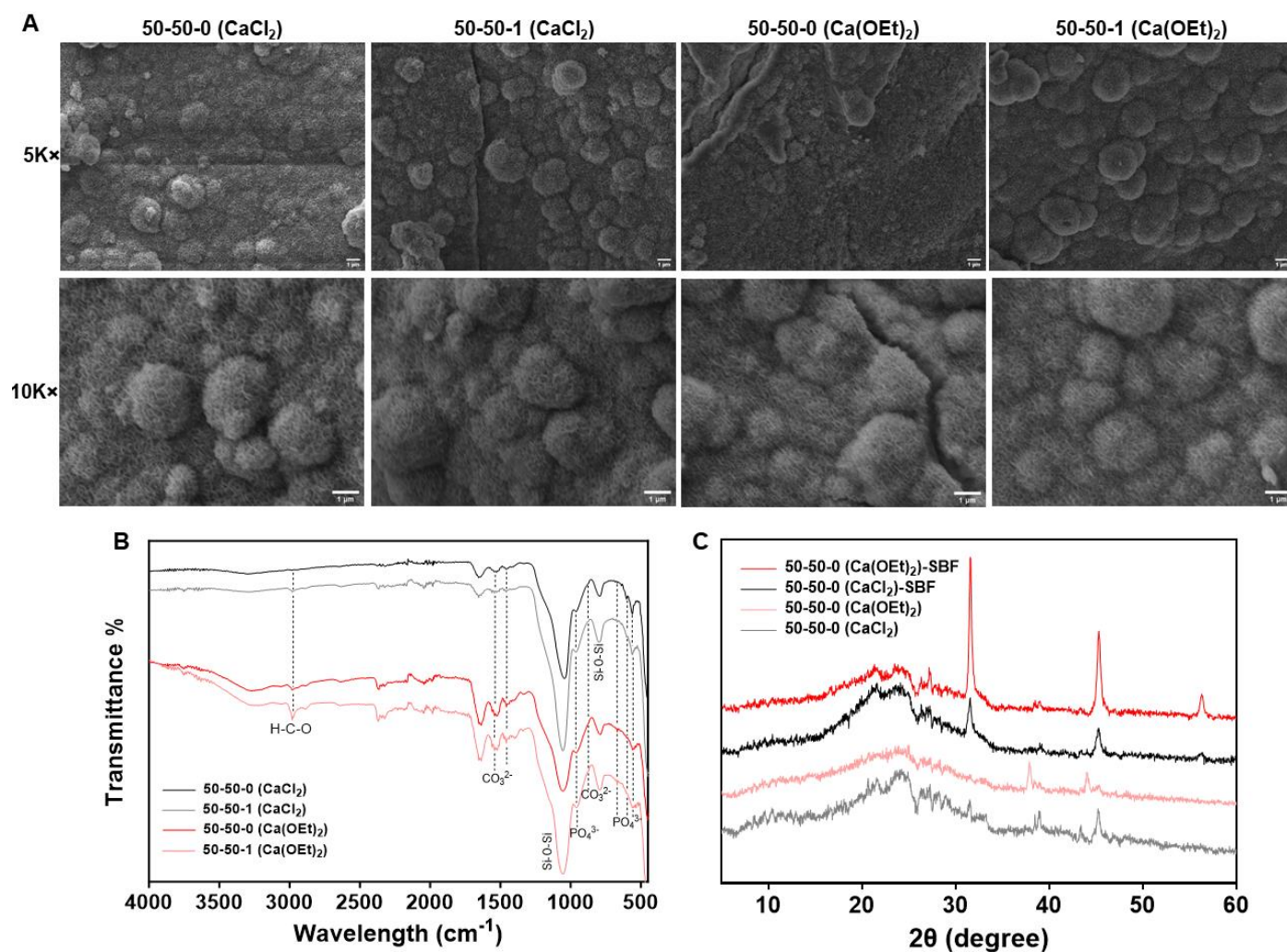
Figure 3.6. *In vitro* **bioactivity of CaCl₂- and Ca(OEt)₂-based 50-50-0 and 50-50-1 nanocomposites.** (**A**) SEM images of the surfaces of nanocomposites after SBF incubation for 7 days. Scale bar = 1 µm. (**B**) FTIR and (**C**) XRD spectra of CaCl₂- and Ca(OEt)₂-based 50-50-0 and 50-50-1 nanocomposites after SBF treatment for 7 days.

Further evaluation of the existence of mixed polycrystalline HCA layer on the surfaces of nanocomposites was assessed by XRD. The 50-50-1 nanocomposites were not evaluated since, according to **Figures 3.6A** and **B**, the bioactive properties of nanocomposites were not affected by the addition of MWCNTs in the gelatin-BG nanocomposites. Additionally, the 50-50-1 samples present the same chemical groups as their respective CaCl₂ or Ca(OEt)₂-containing 50-50-0 nanocomposites.

Figure 3.6C shows the XRD data of the 50-50-0 control and SBF-treated nanocomposites composed of CaCl$_2$ or Ca(OEt)$_2$. Compared to the controls, which depicted an amorphous structure,[45] nanocomposites treated in SBF presented diffraction peaks corresponding to the formation of HCA. These peaks were observed at $2\Theta = 27°$, $31°$, $45°$ and $56°$ which were associated with the diffraction planes (002), (211), (222) and (004) with reference to ICDD file #9-432.[18,28] The crystalline peaks of the 50-50-0 containing Ca(OEt)$_2$ were notably higher than the CaCl$_2$-based 50-50-0. This could imply that the formation of crystallinity obtained from Ca and P depositions after SBF incubation was higher in the Ca(OEt)$_2$-containing nanocomposites due to calcium ions in the silicate network. During incubation in SBF, the nanocomposites degrade through the exchange between Ca^{2+} ions from the glass component and the H$^+$ ions from the SBF solution, causing hydrolysis of the silica groups to form silanol (Si-OH) and Si(OH)$_4$.[8,37] Condensation of the Si-OH groups subsequently occur, leaving a silica-rich layer on the surfaces of the nanocomposites.[8] The Ca^{2+} and PO$_4^{3-}$ groups then migrate to the silica-rich layer surface where they form a film of CaO–P$_2$O$_5$ which further crystallizes as the OH$^-$ and CO$_3^{2-}$ anions from the SBF solution incorporate to form a mixed polycrystalline HCA layer on the surfaces of the nanocomposites.[8] Since the calcium ions in the 50-50-0 nanocomposite containing Ca(OEt)$_2$ are incorporated in the glass network, the initial ion exchange between the Ca^{2+} ions from the BG and the H$^+$ ions from the SBF is promoted leading to enhanced mineralization on the surfaces of Ca(OEt)$_2$-based nanocomposites. In the case of CaCl$_2$-containing nanocomposites, the calcium ions are leached out of the biomaterial and the rate of hydrolysis of the silica groups could potentially be reduced resulting in a decreased formation of mixed polycrystalline HCA layer and hence, lower intense crystalline peaks. Therefore, **Figure 3.6** confirms that nanocomposites containing either CaCl$_2$ or Ca(OEt)$_2$ as calcium sources present bioactive properties and was higher for those containing Ca(OEt)$_2$ due to the incorporation of calcium ions to the silicate glass network promoting hydrolysis by initial ion exchange. In addition, bioactivity of nanocomposites was not affected by the incorporation of MWCNTs since mineralization was contributed by the presence of BG. Collectively, the bioactivity present in the 50-50-0 and 50-50-1 nanocomposites is a favorable property in bone biomaterials which could contribute to the potential development of new bone tissue. As stated in the introduction, this study aimed to evaluate the role of calcium sources (calcium chloride vs. calcium ethoxide) in a gelatin-BG system in terms of their physicochemical properties. It was shown that the calcium ethoxide-based nanocomposites formed Si-O-NBO bridges as evidence for calcium incorporation to the silicate glass (**Fig. 3.1B**). Furthermore, it was demonstrated that the reduced mass loss is attributed due to the network stability and lower porosity attributed to minimal

leaching of the ions and gelatin (**Fig. 3.4B, Table 3.2**). Nanocomposites based on calcium ethoxide had enhanced bioactivity in SBF indicating hydroxycarbonate apatite formation compared with calcium chloride (**Fig. 3.6C, Table 3.3**). Taken together, our results collectively demonstrated the advantage of the calcium ethoxide-based nanocomposites compared to calcium chloride. However, calcium ion release studies which could have further strengthened the above-mentioned results, were not conducted. Future studies should include quantifying the released calcium ions. As a limitation of this study, further evaluations would have to be conducted to assess the thickness of HCA layer on the surfaces of the nanocomposites to compare and confirm the robustness of the bioactive of the different calcium-containing nanocomposites.

3.5.7. Mouse embryo multipotent mesenchymal progenitor 10T1/2 cell adhesion, spreading and viability on $CaCl_2$- and $Ca(OEt)_2$-based nanocomposites

Cell-materials interaction studies were performed on the 50-50-0 and 50-50-1 nanocomposites prepared with $CaCl_2$ and $Ca(OEt)_2$. **Figure 3.7A** shows the fluorescent images of 10T1/2 cells cultured on tissue culture plate (TCP) as control and on the surfaces of nanocomposites for 24 h. Cells had a favorable attachment and spreading to both $CaCl_2$ and $Ca(OEt)_2$-based nanocomposites by forming a uniform layer of elongated actin filaments onto the surfaces of the biomaterials. Entrapment of gelatin in the inorganic network could potentially act as an initial integrin recognition site for cells. This innate property of gelatin would be possible since it possesses an arginine-glycine-aspartic acid (RGD) sequence that could further favor the cell-ECM interactions, thus promoting cell adhesion.[78] Cells cultured on nanocomposites composed of $CaCl_2$ showed a more elongated morphology than those composed of $Ca(OEt)_2$. This could be due to the presence of micropores in the nanocomposites containing $CaCl_2$, as previously discussed in the micro-CT results, which could improve initial cell attachment. **Figures 3.7B-D** show the viability of 10T1/2 cells cultured on the surfaces of nanocomposites using standard and conditioned media for 24, 72, and 168 h accordingly. Cells cultured on TCP were used as control. The live/dead staining presented in **Figure 3.7B** shows that cells had good viability when cultured on the nanocomposites for different time points. Imaging cells cultured on $Ca(OEt)_2$-based nanocomposites was challenging most notably at 168 h of culture as the biomaterials seemed to have been stained. However, viable 10T1/2 cells were observed and are indicated in orange arrows in the $Ca(OEt)_2$-based 50-50-0 and 50-50-1 nanocomposites. In addition, it was observed that as the culture time increased, so did the viability of cells, which was comparable to that of TCP, especially by 168 h of culture. An analysis of the number of live cells was performed

using conditioned media containing the extracts of nanocomposites (**Figs. 3.7C,D**). 10T1/2 cells were not as viable at 24 h of culture with conditioned media, likely due to the calcium ions from the biomaterials. This was especially observed in the $CaCl_2$-based nanocomposites, since the calcium ions are physically bound to the matrix network, which can be easily diffused upon contact with the cell culture media during the conditioning process. The calcium ions released in the conditioned media could change the ionic strength, which can result in cell death.[79] The initial retained cells adapted to the conditioned media and started to grow between 72 and 168 h of culture. At 168 h of culture, 10T1/2 cells had adapted to the conditioned media containing extracts, and cell viability was favorable. Thus, cell density on cells cultured with conditioned media was higher at day 7. Although nanocomposites containing $Ca(OEt)_2$ showed a decreased number of live cells compared to TCP, the difference in viable cells at 168 h of culture was not significant (**Fig. 3.7D**). However, the number of viable cells on the $CaCl_2$-based nanocomposites was considerably lower ($p < 0.01$) than TCP control. In addition, the 50-50-0 $Ca(OEt)_2$ nanocomposite was significantly higher ($p < 0.05$) than the $CaCl_2$-containing biomaterials, whereas the 50-50-1 $Ca(OEt)_2$ was only substantially higher ($p < 0.05$) than the 50-50-0 $CaCl_2$ nanocomposite.

The addition of MWCNTs to the gelatin-BG nanocomposites did not hinder the adhesion and viability of cells, which could enable future studies aimed on their effects on osteogenic cells. The incorporation of MWCNTs to organic-inorganic bone nanocomposites could not only mimic the endogenous electrically conductive properties of bone, but could also potentially deliver electrical signals for the maturation of osseous tissue.[42-44] These results show that $CaCl_2$- and $Ca(OEt)_2$-based 50-50-0 and 50-50-1 nanocomposites could be used as potential bone biomaterials.
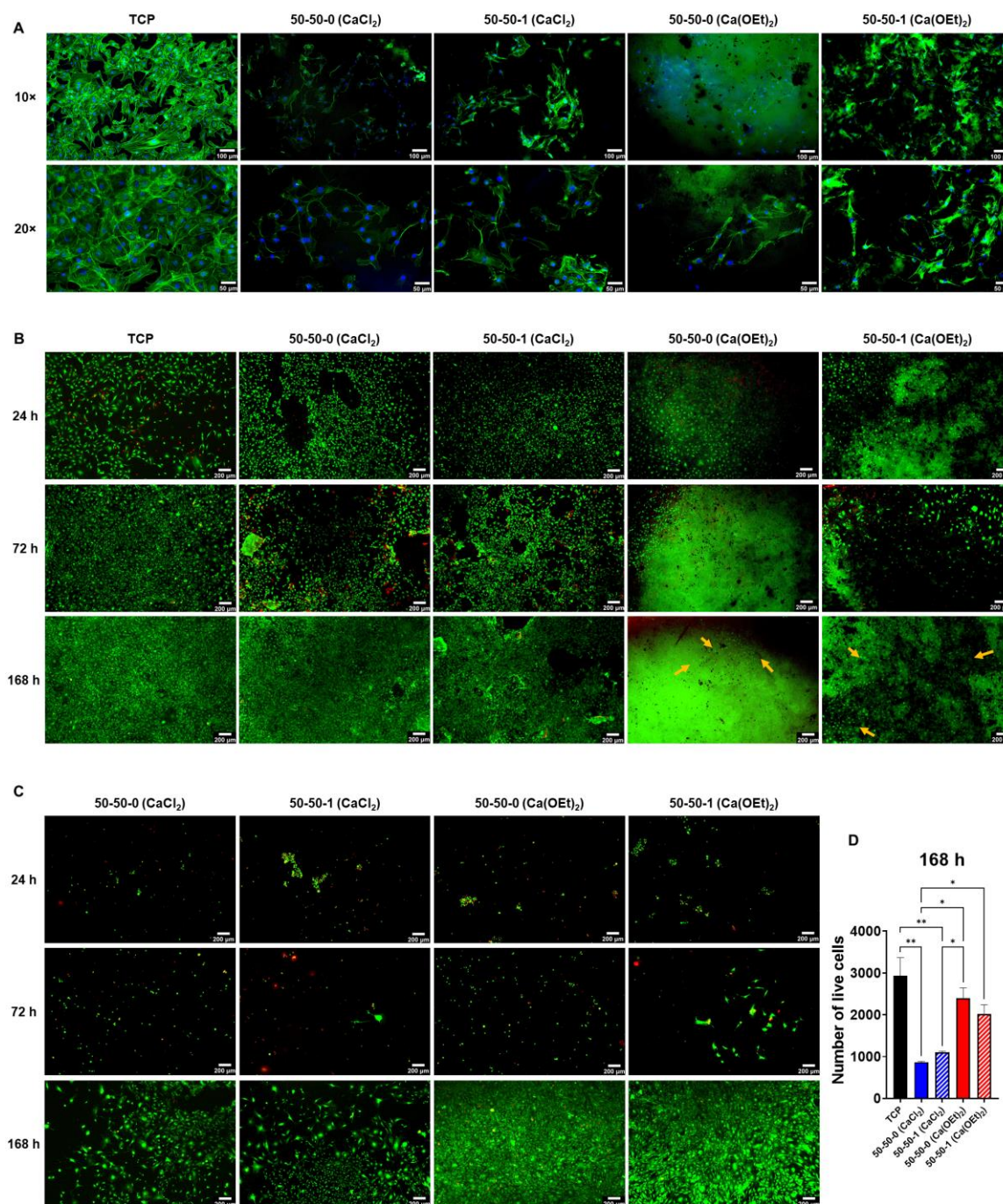
Figure 3.7. Attachment and viability of 10T1/2 cells on CaCl₂- and Ca(OEt)₂-based 50-50-0 and 50-50-1 nanocomposites. (**A**) Fluorescent images of 10T1/2 cells after 24 h of culture. Scale bar = 100 µm at 10× magnification and scale bar = 50 µm at 20× magnification. (**B**) Live/dead staining of 10T1/2 cells cultured on CaCl₂- and Ca(OEt)₂-based 50-50-0 and 50-50-1 nanocomposites. Scalebar

= 200 µm. (**C**) Live/dead staining on cells cultured with conditioned media (extracts). Scalebar = 200 µm. (**D**) Number of live cells at 168 h of conditioned media culture. $*p < 0.05$, $**p < 0.01$.

3.6. Conclusions

In this study, sol-gel derived gelatin-BG-MWCNT nanocomposites using $CaCl_2$ and $Ca(OEt)_2$ were prepared in an attempt to evaluate the different calcium sources for the development of bone biomaterials with an electrically conductive component. The nanocomposites varied chemically and were dependent on the calcium source used for their preparation. Calcium ions from the $Ca(OEt)_2$-based biomaterials were incorporated in the silicate glass nanocomposite network, whereas the calcium ions from $CaCl_2$-containing biomaterials were not. However, the surface elemental distribution was homogeneous for both $CaCl_2$- and $Ca(OEt)_2$-containing nanocomposites. Furthermore, swelling and degradation of nanocomposites occurred as a function of time and were significantly different due to the fate of the calcium ions within the organic-inorganic network. The calcium ions from the calcium sources used also influenced the resulting porosity of nanocomposites post-degradation. The bioactivity of $CaCl_2$- and $Ca(OEt)_2$-based nanocomposites was demonstrated through the formation of hydroxycarbonate apatite on their surfaces after incubation in SBF for 7 days. Finally, 10T1/2 cells showed favorable adhesion and spreading on nanocomposites composed of $CaCl_2$ and $Ca(OEt)_2$ at 24 h of incubation. Cell viability studies using standard and conditioned media showed that $Ca(OEt)_2$-based nanocomposites seemed more favorable biomaterials. Uniformly distributed MWCNTs did not hinder any of the properties of nanocomposites, which was a desired attribution to carry out future studies on their electrically conductive properties. Although $Ca(OEt)_2$-based nanocomposites are most likely to have more advantageous properties in bone repair applications, both $CaCl_2$- and $Ca(OEt)_2$-based nanocomposites have the potential to function as bone biomaterials to repair and regenerate osseous defects.

3.7. References

[1]   N. Aslankoohi, K. Mequanint, Poly(ester amide)–Bioactive Glass Hybrid Biomaterials for Bone Regeneration and Biomolecule Delivery, ACS Appl. Bio Mater. 3 (2020) 3621–3630. https://doi.org/10.1021/acsabm.0c00257.

[2]   D. Mondal, S. Lin, A.S. Rizkalla, K. Mequanint, Porous and biodegradable polycaprolactone-borophosphosilicate hybrid scaffolds for osteoblast infiltration and stem cell differentiation, Journal

of the Mechanical Behavior of Biomedical Materials 92 (2019) 162–171. https://doi.org/10.1016/j.jmbbm.2019.01.011.

[3]   F. Tallia, H.-K. Ting, S.J. Page, J.P. Clark, S. Li, T. Sang, L. Russo, M.M. Stevens, J.V. Hanna, J.R. Jones, Bioactive, Degradable and Tough Hybrids Through Calcium and Phosphate Incorporation, Front. Mater. 9 (2022) 901196. https://doi.org/10.3389/fmats.2022.901196.

[4]   L.L. Hench, Bioceramics, Journal of the American Ceramic Society 81 (2005) 1705–1728. https://doi.org/10.1111/j.1151-2916.1998.tb02540.x.

[5]   N. Aslankoohi, S. Lin, K. Mequanint, Bioactive fluorescent hybrid microparticles as a stand-alone osteogenic differentiation inducer, Materials Today Bio 13 (2022) 100187. https://doi.org/10.1016/j.mtbio.2021.100187.

[6]   J.R. Jones, S. Lin, S. Yue, P.D. Lee, J.V. Hanna, M.E. Smith, R.J. Newport, Bioactive glass scaffolds for bone regeneration and their hierarchical characterisation, Proc Inst Mech Eng H 224 (2010) 1373–1387. https://doi.org/10.1243/09544119JEIM836.

[7]   L.L. Hench, R.J. Splinter, W.C. Allen, T.K. Greenlee, Bonding mechanisms at the interface of ceramic prosthetic materials, J. Biomed. Mater. Res. 5 (1971) 117–141. https://doi.org/10.1002/jbm.820050611.

[8]   J.R. Jones, E. Gentleman, J. Polak, Bioactive Glass Scaffolds for Bone Regeneration, Elements 3 (2007) 393–399. https://doi.org/10.2113/GSELEMENTS.3.6.393.

[9]   L.L. Hench, J.K. West, The sol-gel process, Chem. Rev. 90 (1990) 33–72. https://doi.org/10.1021/cr00099a003.

[10]   N. Aslankoohi, D. Mondal, A.S. Rizkalla, K. Mequanint, Bone Repair and Regenerative Biomaterials: Towards Recapitulating the Microenvironment, Polymers 11 (2019) 1437. https://doi.org/10.3390/polym11091437.

[11]   W. Sakuma, S. Yamasaki, S. Fujisawa, T. Kodama, J. Shiomi, K. Kanamori, T. Saito, Mechanically Strong, Scalable, Mesoporous Xerogels of Nanocellulose Featuring Light Permeability, Thermal Insulation, and Flame Self-Extinction, ACS Nano 15 (2021) 1436–1444. https://doi.org/10.1021/acsnano.0c08769.

[12]   D. Ksouri, H. Khireddine, A. Aksas, T. Valente, F. Bir, N. Slimani, B. Cabal, R. Torrecillas, J.D. Santos, Synthesis of ternary bioactive glass derived aerogel and xerogel: study of their structure and bioactivity, Nova Biotechnologica et Chimica 17 (2018) 150–159. https://doi.org/10.2478/nbec-2018-0016.

[13]   A. Pérez-Moreno, M. Piñero, R. Fernández-Montesinos, G. Pinaglia-Tobaruela, M.V. Reyes-Peces, M.D.M. Mesa-Díaz, J.I. Vilches-Pérez, L. Esquivias, N. De La Rosa-Fox, M. Salido, Chitosan-Silica Hybrid Biomaterials for Bone Tissue Engineering: A Comparative Study of Xerogels and Aerogels, Gels 9 (2023) 383. https://doi.org/10.3390/gels9050383.

[14]   R. Li, A.E. Clark, L.L. Hench, An investigation of bioactive glass powders by sol-gel processing, J of Applied Biomaterials 2 (1991) 231–239. https://doi.org/10.1002/jab.770020403.

[15]   P. Sepulveda, J.R. Jones, L.L. Hench, Characterization of melt-derived 45S5 and sol-gel-derived 58S bioactive glasses, J. Biomed. Mater. Res. 58 (2001) 734–740. https://doi.org/10.1002/jbm.10026.

[16]   P. Sepulveda, J.R. Jones, L.L. Hench, *In vitro* dissolution of melt-derived 45S5 and sol-gel derived 58S bioactive glasses, J. Biomed. Mater. Res. 61 (2002) 301–311. https://doi.org/10.1002/jbm.10207.

[17]   N. Aslankoohi, K. Mequanint, Intrinsically fluorescent bioactive glass-poly(ester amide) hybrid microparticles for dual drug delivery and bone repair, Materials Science and Engineering: C 128 (2021) 112288. https://doi.org/10.1016/j.msec.2021.112288.

[18]   B.A. Allo, A.S. Rizkalla, K. Mequanint, Hydroxyapatite Formation on Sol–Gel Derived Poly(ε-Caprolactone)/Bioactive Glass Hybrid Biomaterials, ACS Appl. Mater. Interfaces 4 (2012) 3148–3156. https://doi.org/10.1021/am300487c.

[19]   J.-H. Ryu, J.-S. Kwon, K.-M. Kim, H.J. Hong, W.-G. Koh, J. Lee, H.-J. Lee, H.-J. Choi, S. Yi, H. Shin, M.-H. Hong, Synergistic Effect of Porous Hydroxyapatite Scaffolds Combined with Bioactive Glass/Poly(lactic- *co* -glycolic acid) Composite Fibers Promotes Osteogenic Activity and Bioactivity, ACS Omega 4 (2019) 2302–2310. https://doi.org/10.1021/acsomega.8b02898.

[20]   M. Prokopowicz, A. Szewczyk, W. Sawicki, Bioactive monolithic composites of silica/polydimethylsiloxane/calcium phosphate obtained at room temperature in sol–gel micromolding technique, Materials Letters 184 (2016) 239–242. https://doi.org/10.1016/j.matlet.2016.08.063.

[21]   T. Ghassemi, A. Shahroodi, M.H. Ebrahimzadeh, A. Mousavian, J. Movaffagh, A. Moradi, Current Concepts in Scaffolding for Bone Tissue Engineering, . . NUMBER 6 (2018) 10.

[22]   P.C. Pires, F. Mascarenhas-Melo, K. Pedrosa, D. Lopes, J. Lopes, A. Macário-Soares, D. Peixoto, P.S. Giram, F. Veiga, A.C. Paiva-Santos, Polymer-based biomaterials for pharmaceutical and biomedical applications: A focus on topical drug administration, European Polymer Journal 187 (2023) 111868. https://doi.org/10.1016/j.eurpolymj.2023.111868.

[23]   A. Pérez-Moreno, M.V. Reyes-Peces, J.I. Vilches-Pérez, R. Fernández-Montesinos, G. Pinaglia-Tobaruela, M. Salido, N. De La Rosa-Fox, M. Piñero, Effect of Washing Treatment on the Textural Properties and Bioactivity of Silica/Chitosan/TCP Xerogels for Bone Regeneration, IJMS 22 (2021) 8321. https://doi.org/10.3390/ijms22158321.

[24]   S. Gorgieva, V. Kokol, Collagen- vs. Gelatine-Based Biomaterials and Their Biocompatibility: Review and Perspectives, in: R. Pignatello (Ed.), Biomaterials Applications for Nanomedicine, InTech, 2011. https://doi.org/10.5772/24118.

[25]   C. Gao, Q. Gao, Y. Li, M.N. Rahaman, A. Teramoto, K. Abe, *In vitro* evaluation of electrospun gelatin-bioactive glass hybrid scaffolds for bone regeneration, J. Appl. Polym. Sci. 127 (2013) 2588–2599. https://doi.org/10.1002/app.37946.

[26]   A. Thomas, J. Bera, Preparation and characterization of gelatin-bioactive glass ceramic scaffolds for bone tissue engineering, Journal of Biomaterials Science, Polymer Edition 30 (2019) 561–579. https://doi.org/10.1080/09205063.2019.1587697.

[27]   M.C. Echave, P. Sánchez, J.L. Pedraz, G. Orive, Progress of gelatin-based 3D approaches for bone regeneration, Journal of Drug Delivery Science and Technology 42 (2017) 63–74. https://doi.org/10.1016/j.jddst.2017.04.012.

[28]   R. Arambula-Maldonado, Y. Liu, M. Xing, K. Mequanint, Bioactive and electrically conductive GelMA-BG-MWCNT nanocomposite hydrogel bone biomaterials, Biomaterials Advances 154 (2023) 213616. https://doi.org/10.1016/j.bioadv.2023.213616.

[29]   X. Dieudonné, V. Montouillout, É. Jallot, F. Fayon, J. Lao, Bioactive glass hybrids: a simple route towards the gelatin–SiO$_2$–CaO system, Chemical Communications 50 (2014) 8701. https://doi.org/10.1039/C3CC49113G.

[30]   B. Yu, C.A. Turdean-Ionescu, R.A. Martin, R.J. Newport, J.V. Hanna, M.E. Smith, J.R. Jones, Effect of Calcium Source on Structure and Properties of Sol–Gel Derived Bioactive Glasses, Langmuir 28 (2012) 17465–17476. https://doi.org/10.1021/la303768b.

[31]   C. Bossard, H. Granel, É. Jallot, V. Montouillout, F. Fayon, J. Soulié, C. Drouet, Y. Wittrant, J. Lao, Mechanism of Calcium Incorporation Inside Sol–Gel Silicate Bioactive Glass and the Advantage of Using Ca(OH)$_2$ over Other Calcium Sources, ACS Biomater. Sci. Eng. 5 (2019) 5906–5915. https://doi.org/10.1021/acsbiomaterials.9b01245.

[32]   B. Yu, G. Poologasundarampillai, C. Turdean-Ionescu, M.E. Smith, J.R. Jones, A New Calcium Source for Bioactive Sol-Gel Hybrids, Bioceram. Dev. Appl. 1 (2011) 1–3. https://doi.org/10.4303/bda/D110178.

[33]   B.A.E. Ben-Arfa, I.E. Palamá, I.M. Miranda Salvado, J.M.F. Ferreira, R.C. Pullar, The role of calcium (source & content) on the in vitro behaviour of sol–gel quaternary glass series, Ceramics International 46 (2020) 1065–1075. https://doi.org/10.1016/j.ceramint.2019.09.073.

[34]   S. Lin, C. Ionescu, S. Baker, M.E. Smith, J.R. Jones, Characterisation of the inhomogeneity of sol–gel-derived SiO2–CaO bioactive glass and a strategy for its improvement, J Sol-Gel Sci Technol 53 (2010) 255–262. https://doi.org/10.1007/s10971-009-2085-0.

[35]   A. Rámila, F. Balas, M. Vallet-Regí, Synthesis Routes for Bioactive Sol−Gel Glasses: Alkoxides versus Nitrates, Chem. Mater. 14 (2002) 542–548. https://doi.org/10.1021/cm0110876.

[36]   J.R. Jones, Review of bioactive glass: From Hench to hybrids, Acta Biomaterialia 9 (2013) 4457–4486. https://doi.org/10.1016/j.actbio.2012.08.023.

[37]   A. Ruiz-Clavijo, A. Hurt, A. Kotha, N. Coleman, Effect of Calcium Precursor on the Bioactivity and Biocompatibility of Sol-Gel-Derived Glasses, JFB 10 (2019) 13. https://doi.org/10.3390/jfb10010013.

[38]   S. Shokri, B. Movahedi, M. Rafieinia, H. Salehi, A new approach to fabrication of Cs/BG/CNT nanocomposite scaffold towards bone tissue engineering and evaluation of its properties, Applied Surface Science 357 (2015) 1758–1764. https://doi.org/10.1016/j.apsusc.2015.10.048.

[39]   E. Fukada, I. Yasuda, On the Piezoelectric Effect of Bone, J. Phys. Soc. Jpn. 12 (1957) 1158–1162. https://doi.org/10.1143/JPSJ.12.1158.

[40]   I. Yasuda, The classic: Fundamental aspects of fracture treatment, reprinted from J. Kyoto Med. Soc., 4:395-406, 1953, Clin Orthop Relat Res (1977) 5–8.

[41]   T.W. Balmer, S. Vesztergom, P. Broekmann, A. Stahel, P. Büchler, Characterization of the electrical conductivity of bone and its correlation to osseous structure, Sci Rep 8 (2018) 8601. https://doi.org/10.1038/s41598-018-26836-0.

[42]   R. Arambula-Maldonado, K. Mequanint, Carbon-based electrically conductive materials for bone repair and regeneration, Mater. Adv. (2022) 10.1039.D2MA00001F. https://doi.org/10.1039/D2MA00001F.

[43]   E.P. e Silva, B. Huang, J.V. Helaehil, P.R.L. Nalesso, L. Bagne, M.A. de Oliveira, G.C.C. Albiazetti, A. Aldalbahi, M. El-Newehy, M. Santamaria-Jr, F.A.S. Mendonça, P. Bártolo, G.F. Caetano, In vivo study of conductive 3D printed PCL/MWCNTs scaffolds with electrical stimulation for bone tissue engineering, Bio-Des. Manuf. 4 (2021) 190–202. https://doi.org/10.1007/s42242-020-00116-1.

[44]   X. Liu, M.N. George, L. Li, D. Gamble, A.L. Miller II, B. Gaihre, B.E. Waletzki, L. Lu, Injectable Electrical Conductive and Phosphate Releasing Gel with Two-Dimensional Black Phosphorus and Carbon Nanotubes for Bone Tissue Engineering, ACS Biomater. Sci. Eng. 6 (2020) 4653–4665. https://doi.org/10.1021/acsbiomaterials.0c00612.

[45]   B.A. Allo, A.S. Rizkalla, K. Mequanint, Synthesis and Electrospinning of ε-Polycaprolactone-Bioactive Glass Hybrid Biomaterials via a Sol−Gel Process, Langmuir 26 (2010) 18340–18348. https://doi.org/10.1021/la102845k.

[46]   K.M.N. Costa, R.M. Barros, E.O. Jorge, M.R. Sato, M. Chorilli, B.P.G. De Lima Damasceno, D. Nicholas, J.F. Callan, J.A. Oshiro Junior, Doxorubicin-loaded nanostructured lipid carriers functionalized with folic acid against MCF-7 breast cancer cell line, J Nanopart Res 25 (2023) 56. https://doi.org/10.1007/s11051-023-05704-7.

[47]   D. Acharya, P. Pandey, F. Nasiri, K.M. Singha, B. Mohanta, Synthesis, Characterization and Antibacterial Effects of Ag@SiO$_2$ Core–Shell Nanoparticles, J Bionanosci 11 (2017) 391–396. https://doi.org/10.1166/jbns.2017.1459.

[48]   A. Hadela, M. Lakić, M. Potočnik, A. Košak, A. Gutmaher, A. Lobnik, Novel reusable functionalized magnetic cobalt ferrite nanoparticles as oil adsorbents, Adsorption Science & Technology 38 (2020) 168–190. https://doi.org/10.1177/0263617420922014.

[49]   P. Tan, Y.-H. Li, X.-Q. Liu, Y. Jiang, L.-B. Sun, Core–Shell AgCl@SiO$_2$ Nanoparticles: Ag(I)-Based Antibacterial Materials with Enhanced Stability, ACS Sustainable Chem. Eng. 4 (2016) 3268–3275. https://doi.org/10.1021/acssuschemeng.6b00309.

[50]   C. Militzer, J. Buchsbaum, V. Dzhagan, D.R.T. Zahn, H. Wulff, C.A. Helm, W.A. Goedel, Atomic Layer Deposition of Titanium Phosphate from Titanium Tetrachloride and Triethyl Phosphate onto Carbon Fibers, Adv Materials Inter 5 (2018) 1800423. https://doi.org/10.1002/admi.201800423.

[51]   J.A. Araujo, Y.J. Cortese, M. Mojicevic, M. Brennan Fournet, Y. Chen, Composite Films of Thermoplastic Starch and CaCl$_2$ Extracted from Eggshells for Extending Food Shelf-Life, Polysaccharides 2 (2021) 677–690. https://doi.org/10.3390/polysaccharides2030041.

[52]   M.M. Pereira, J.R. Jones, L.L. Hench, Bioactive glass and hybrid scaffolds prepared by sol–gel method for bone tissue engineering, Advances in Applied Ceramics 104 (2005) 35–42. https://doi.org/10.1179/174367605225011034.

[53]   S. Jurić, E. Đermić, S. Topolovec-Pintarić, M. Bedek, M. Vinceković, Physicochemical properties and release characteristics of calcium alginate microspheres loaded with Trichoderma viride spores, Journal of Integrative Agriculture 18 (2019) 2534–2548. https://doi.org/10.1016/S2095-3119(19)62634-1.

[54]   X. Liu, X. Piao, Y. Wang, S. Zhu, Calcium Ethoxide as a Solid Base Catalyst for the Transesterification of Soybean Oil to Biodiesel, Energy Fuels 22 (2008) 1313–1317. https://doi.org/10.1021/ef700518h.

[55]   F. Branda, Bioactivity of 1.25CaO · SiO2 glass: an FTIR and X-ray study on powdered samples, Biomaterials 17 (1996) 2247–2251. https://doi.org/10.1016/0142-9612(95)00328-2.

[56]   J. Serra, P. González, S. Liste, C. Serra, S. Chiussi, B. León, M. Pérez-Amor, H.O. Ylänen, M. Hupa, FTIR and XPS studies of bioactive silica based glasses, Journal of Non-Crystalline Solids 332 (2003) 20–27. https://doi.org/10.1016/j.jnoncrysol.2003.09.013.

[57]   J. Lao, X. Dieudonné, M. Benbakkar, É. Jallot, Bioactive glass coating on gelatin scaffolds at ambient temperature: easy route to make polymer scaffolds become bioactive, J Mater Sci 52 (2017) 9129–9139. https://doi.org/10.1007/s10853-017-0781-7.

[58]   X.-R. Yang, Y.-Q. Zhao, Y.-T. Qiu, C.-F. Chi, B. Wang, Preparation and Characterization of Gelatin and Antioxidant Peptides from Gelatin Hydrolysate of Skipjack Tuna (Katsuwonus pelamis) Bone Stimulated by in vitro Gastrointestinal Digestion, Marine Drugs 17 (2019) 78. https://doi.org/10.3390/md17020078.

[59]   M. Jackson, L.-P. Choo, P.H. Watson, W.C. Halliday, H.H. Mantsch, Beware of connective tissue proteins: Assignment and implications of collagen absorptions in infrared spectra of human tissues, Biochimica et Biophysica Acta (BBA) - Molecular Basis of Disease 1270 (1995) 1–6. https://doi.org/10.1016/0925-4439(94)00056-V.

[60]   K. Sisson, C. Zhang, M.C. Farach-Carson, D.B. Chase, J.F. Rabolt, Evaluation of Cross-Linking Methods for Electrospun Gelatin on Cell Growth and Viability, Biomacromolecules 10 (2009) 1675–1680. https://doi.org/10.1021/bm900036s.

[61]   B. Lei, K.-H. Shin, D.-Y. Noh, I.-H. Jo, Y.-H. Koh, W.-Y. Choi, H.-E. Kim, Nanofibrous gelatin–silica hybrid scaffolds mimicking the native extracellular matrix (ECM) using thermally induced phase separation, J. Mater. Chem. 22 (2012) 14133. https://doi.org/10.1039/c2jm31290e.

[62] E. Tamahkar Irmak, Carbon nanotube based polyvinylalcohol-polyvinylpyrolidone nanocomposite hydrogels for controlled drug delivery applications, Anadolu University Journal of Science and Technology A - Applied Sciences and Engineering 18 (2017) 1–1. https://doi.org/10.18038/aubtda.322138.

[63] H. Ravanbakhsh, G. Bao, N. Latifi, L.G. Mongeau, Carbon nanotube composite hydrogels for vocal fold tissue engineering: Biocompatibility, rheology, and porosity, Materials Science and Engineering: C 103 (2019) 109861. https://doi.org/10.1016/j.msec.2019.109861.

[64] Q. Xing, K. Yates, C. Vogt, Z. Qian, M.C. Frost, F. Zhao, Increasing Mechanical Strength of Gelatin Hydrogels by Divalent Metal Ion Removal, Sci Rep 4 (2015) 4706. https://doi.org/10.1038/srep04706.

[65] J. Zheng, F. Zhao, W. Zhang, Y. Mo, L. Zeng, X. Li, X. Chen, Sequentially-crosslinked biomimetic bioactive glass/gelatin methacryloyl composites hydrogels for bone regeneration, Materials Science and Engineering: C 89 (2018) 119–127. https://doi.org/10.1016/j.msec.2018.03.029.

[66] C. Vichery, J.-M. Nedelec, Bioactive Glass Nanoparticles: From Synthesis to Materials Design for Biomedical Applications, Materials 9 (2016) 288. https://doi.org/10.3390/ma9040288.

[67] S. Suvarnapathaki, M.A. Nguyen, X. Wu, S.P. Nukavarapu, G. Camci-Unal, Synthesis and characterization of photocrosslinkable hydrogels from bovine skin gelatin, RSC Adv. 9 (2019) 13016–13025. https://doi.org/10.1039/C9RA00655A.

[68] Z. Tang, X. Li, Y. Tan, H. Fan, X. Zhang, The material and biological characteristics of osteoinductive calcium phosphate ceramics, Regenerative Biomaterials 5 (2018) 43–59. https://doi.org/10.1093/rb/rbx024.

[69] P. Diaz-Rodriguez, M. Sánchez, M. Landin, Drug-Loaded Biomimetic Ceramics for Tissue Engineering, Pharmaceutics 10 (2018) 272. https://doi.org/10.3390/pharmaceutics10040272.

[70] L. Morejón, J.A. Delgado, A. Antunes Ribeiro, M. Varella De Oliveira, E. Mendizábal, I. García, A. Alfonso, P. Poh, M. Van Griensven, E.R. Balmayor, Development, Characterization and In Vitro Biological Properties of Scaffolds Fabricated From Calcium Phosphate Nanoparticles, IJMS 20 (2019) 1790. https://doi.org/10.3390/ijms20071790.

[71] S. Wang, T.J. Kowal, M.K. Marei, M.M. Falk, H. Jain, Nanoporosity Significantly Enhances the Biological Performance of Engineered Glass Tissue Scaffolds, Tissue Engineering Part A 19 (2013) 1632–1640. https://doi.org/10.1089/ten.tea.2012.0585.

[72] D. Mondal, A.S. Rizkalla, K. Mequanint, Bioactive borophosphosilicate-polycaprolactone hybrid biomaterials via a non-aqueous sol gel process, RSC Adv. 6 (2016) 92824–92832. https://doi.org/10.1039/C6RA08339K.

[73] K. Deguchi, S. Nomura, A. Tsuchiya, I. Takahashi, K. Ishikawa, Effects of the carbonate content in carbonate apatite on bone replacement, J Tissue Eng Regen Med 16 (2022) 200–206. https://doi.org/10.1002/term.3270.

[74]   L. Russo, F. Taraballi, C. Lupo, A. Poveda, J. Jiménez-Barbero, M. Sandri, A. Tampieri, F. Nicotra, L. Cipolla, Carbonate hydroxyapatite functionalization: a comparative study towards (bio)molecules fixation, Interface Focus. 4 (2014) 20130040. https://doi.org/10.1098/rsfs.2013.0040.

[75]   A.L.B. Maçon, T.B. Kim, E.M. Valliant, K. Goetschius, R.K. Brow, D.E. Day, A. Hoppe, A.R. Boccaccini, I.Y. Kim, C. Ohtsuki, T. Kokubo, A. Osaka, M. Vallet-Regí, D. Arcos, L. Fraile, A.J. Salinas, A.V. Teixeira, Y. Vueva, R.M. Almeida, M. Miola, C. Vitale-Brovarone, E. Verné, W. Höland, J.R. Jones, A unified in vitro evaluation for apatite-forming ability of bioactive glasses and their variants, J Mater Sci: Mater Med 26 (2015) 115. https://doi.org/10.1007/s10856-015-5403-9.

[76]   J. Xu, Y. Yang, R. Wan, Y. Shen, W. Zhang, Hydrothermal Preparation and Characterization of Ultralong Strontium-Substituted Hydroxyapatite Whiskers Using Acetamide as Homogeneous Precipitation Reagent, The Scientific World Journal 2014 (2014) 1–6. https://doi.org/10.1155/2014/863137.

[77]   R. Murugan, S. Ramakrishna, K. Panduranga Rao, Nanoporous hydroxy-carbonate apatite scaffold made of natural bone, Materials Letters 60 (2006) 2844–2847. https://doi.org/10.1016/j.matlet.2006.01.104.

[78]   M. Kirsch, L. Birnstein, I. Pepelanova, W. Handke, J. Rach, A. Seltsam, T. Scheper, A. Lavrentieva, Gelatin-Methacryloyl (GelMA) Formulated with Human Platelet Lysate Supports Mesenchymal Stem Cell Proliferation and Differentiation and Enhances the Hydrogel's Mechanical Properties, Bioengineering 6 (2019) 76. https://doi.org/10.3390/bioengineering6030076.

[79]   S. Maeno, Y. Niki, H. Matsumoto, H. Morioka, T. Yatabe, A. Funayama, Y. Toyama, T. Taguchi, J. Tanaka, The effect of calcium ion concentration on osteoblast viability, proliferation and differentiation in monolayer and 3D culture, Biomaterials 26 (2005) 4847–4855. https://doi.org/10.1016/j.biomaterials.2005.01.006.

Chapter 4

4. Bioactive and electrically conductive GelMA-BG-MWCNT nanocomposite hydrogel bone biomaterials*[4]

Overview: The purpose of this study is to synthesize electrically conductive organic-inorganic nanocomposite hydrogels composed of gelatin methacryloyl, sol-gel-derived tertiary bioactive glass, and uniformly dispersed multiwall carbon nanotubes. The nanocomposite hydrogels were processed to develop hydrogels with enhanced electro-mechanical properties as a function of multiwall carbon nanotube loading.
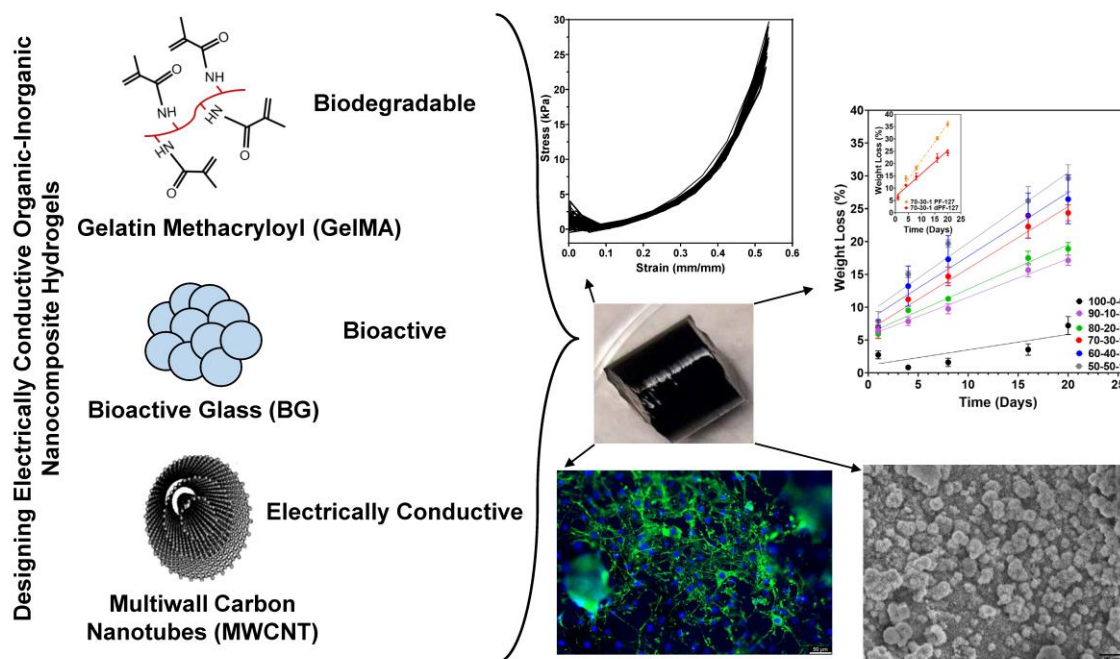
Scheme 4.1. Graphical abstract for Chapter 4.

4.1. Abstract

Natural bone is a complex organic-inorganic composite tissue that possesses endogenous electrically conductive properties in response to mechanical forces. Mimicking these unique properties collectively in a single synthetic biomaterial has so far remained a formidable task. In this study, a synthesis strategy that comprised gelatin methacryloyl (GelMA), sol-gel derived tertiary bioactive glass (BG), and uniformly dispersed multiwall carbon nanotubes (MWCNTs) was reported to create nanocomposite hydrogels that mimic the organic-inorganic composition of bone. Using this strategy, biomaterials that are electrically conductive and possess electro-mechanical properties similar to endogenous bone were prepared without affecting their biocompatibility. Nanocomposite hydrogel biomaterials were biodegradable and promoted biomineralization, and supported multipotent mesenchymal progenitor cell (10T1/2) cell interactions and differentiation into an osteogenic lineage. To the best of my knowledge, this work presents the first study to functionally characterize suitable electro-mechanical responses in nanocomposite hydrogels, a key process that occurs in the natural bone to drive its repair and regeneration. Overall, the results demonstrated GelMA-BG-MWCNT nanocomposite hydrogels have the potential to become promising bioactive biomaterials for use in bone repair and regeneration.

Keywords: electro-mechanical response, electrical conductivity, bioactivity, nanocomposite hydrogel, bone biomaterial

4.2. Introduction

The repair of bone fractures and critical-size bone defects that exceed the body's natural healing ability represents a significant challenge and imposes an ever-increasing financial burden on healthcare systems.[1,2] Natural bone is a complex organic-inorganic composite tissue with endogenous electrically conductive properties in response to mechanical forces. Electrical signals are generated by an applied mechanical load within bone tissue that is capable of supporting cell proliferation and osteogenic homeostasis.[3,4] Since the discovery of bone's electrically conductive properties, this feature has been clinically targeted to promote the healing of a wide range of bone injuries. However, most clinical applications have focused on augmenting the native bone with external electrical stimulation delivered through electrodes. Despite the promising clinical utility of electrical stimulation for bone healing, this application is limited to the reduction of pain and risk for radiographic nonunion but functional outcomes were limited.[5]

For bones that do not heal naturally, the development of synthetic bone substitutes is becoming increasingly important as the availability of donor bone sources, typically used to repair critical size defects, becomes more limited.[6] Incorporating electrically conductive components into a bone biomaterial has been proposed to accelerate the maturation and success of repaired bone or engineered bone tissue substitutes.[7-9] Conductive polymers have the advantage of being easily synthesized while possessing tunable electrical conductivity that can promote the differentiation of osteoblasts.[10,11] However, to achieve the electrical conductivity required to match the native bone, conducting polymers must undergo a doping process to form charge carriers.[12,13] Furthermore, conducting polymers have poor dispersibility and mechanical brittleness, which limits their application as biomaterials for bone regeneration.[14,15] Therefore, more suitable alternatives are required to develop electrically conductive biomaterials that can promote the repair of bone.

Recently, carbon-based electrically conductive materials, such as carbon nanotubes (CNTs), graphene, and reduced graphene oxide (rGO) have been described as potential candidates for bone tissue engineering solutions.[16-18] Unlike conducting polymers, carbon-based materials can be synthesized in various geometrical and morphological structures that can alter their physiological responses, potentially enhancing their capacity to treat bone defects.[19] CNT and graphene possess very high electrical conductivities of 10^4–10^5 S/cm and 10^6 S/cm, respectively,[20] suggesting that only low concentrations of carbon-based electrically conductive materials are required to achieve comparable electrical conductivity to bone. In addition, carbon-based electrically conductive materials possess excellent mechanical strength, further demonstrating their suitability for the development of bone biomaterials that repair and regenerate bone tissue.[1,21] However, from a biological perspective, bone substitutes composed solely of carbon-based electrically conductive materials do not resemble the structure and composition of native bone.

Composite material approaches offer a solution to mimicking the various physiological properties possessed by complex tissue systems.[22] Native bone possesses a complex hierarchical structure comprised of both organic components, predominantly collagen, and an inorganic component comprised of hydroxycarbonate apatite.[23-28] To mimic the nanocomposite and electrical properties of native bone, previous studies have mostly focused on carbon-based electrically conductive materials with either a polymeric[16,29] or an inorganic system.[30,31] Alternatively, other studies have developed biomaterials consisting of an organic-inorganic system predominantly comprised of crystalline ceramic hydroxyapatite and an electrically conductive component.[32-34] However, either

the failure to mimic the organic-inorganic biological composition of bone or the lack of reabsorption due to a high crystalline ceramic structure limits the application of these materials. Hence, there is a need for composite osteoconductive and osteoinductive biomaterials having tunable electrical conductivity.

Here, an efficient approach that incorporates gelatin methacryloyl (GelMA), tertiary bioactive glass (BG), and uniformly dispersed multiwall carbon nanotubes (MWCNTs)is reported to create nanocomposite hydrogels that mimic the organic-inorganic composition of bone as well as its electrically conductive and electro-mechanical properties (**Scheme 4.2**). The materials have a uniform distribution of the components within the nanocomposite hydrogels and possess increasing mechanical and electrically conductive properties as a function of MWCNT concentration while having bioactive, cytocompatible features and the ability to promote osteogenic differentiation of progenitor cells. Finally, the analyses show that nanocomposite hydrogels could be promising biomaterials for bone repair and regeneration.
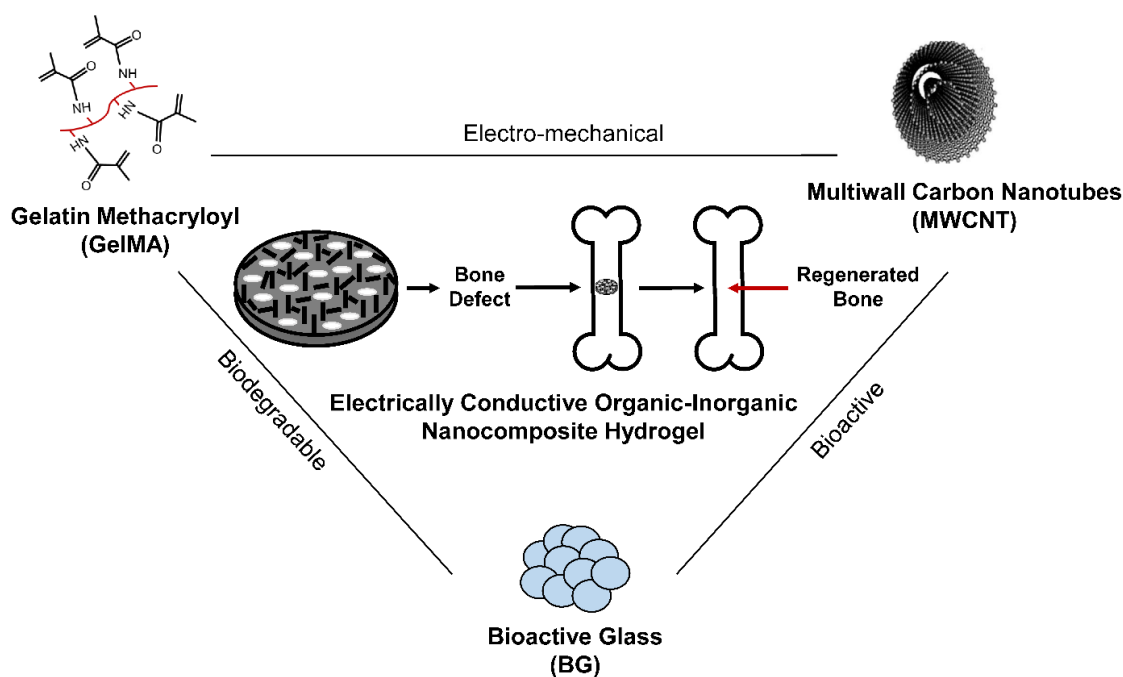
Scheme 4.2. Synthesis approach of GelMA-BG-MWCNT nanocomposite hydrogels.

4.3. Materials and methods

4.3.1. Materials

Gelatin type A (porcine skin) (G2500, gel strength (Bloom No.) 300 with viscosity average molecular weight of 100 kDa), methacrylic anhydride (containing 2000 ppm topanol A as an inhibitor, 94 %), potassium persulfate, pluronic F-127, diacrylated pluronic F-127, multiwall carbon nanotube (MWCNT, >98 % carbon basis, O.D. × L 6–13 nm × 2.5–20 μm), tetraethyl orthosilicate (TEOS, 98 %), and triethyl phosphate (TEP, 99.8 %) were purchased from Sigma-Aldrich (Milwaukee, WI, USA). Calcium ethoxide was obtained from Gelest Inc. (Morrisville, PA, USA). N,N,N′,N′-tetramethylethane-1,2-diamine (TEMED) was purchased from Merck KGaA (Darmstadt, Germany). Dulbecco's Modified Eagle's Medium (DMEM), Hanks' Balanced Salt Solution (HBSS), Fetal Bovine Serum (FBS), penicillin/streptomycin (pen/strep), and live/dead cell imaging kit were acquired from Thermo Fisher. Alexa Fluor® 488 phalloidin and 4′6-diamidino-2-phenylindole (DAPI) were purchased from Life Technologies (Burlington, ON, Canada). Mouse embryo multipotent mesenchymal progenitor cells (C3H/10T1/2 cells) were obtained from ATCC (Manassas, VA, USA).

4.3.2. Synthesis of gelatin methacryloyl (GelMA)

Gelatin type A (porcine skin) was mixed at 10 % w/v in phosphate-buffered saline (PBS) at 40 ℃ until fully dissolved. A 10 % v/v of methacrylic anhydride was added dropwise under stirring to the viscous gelatin solution and allowed to react for 1 h at 40 °C. To stop the reaction, a 5× dilution of warm PBS was added and dialyzed against distilled water using a 12–14 kDa cutoff dialysis tube for one week to remove unreacted components. The solution was vacuum dried at 40 °C, and GelMA prepolymer was stored at 4 ℃ until use.

4.3.3. Synthesis of tertiary bioactive glass (BG)

BG was prepared by a sol-gel process which consisted in hydrolyzing TEOS and TEP with a catalytic amount of 1 M HCl under vigorous stirring at room temperature (RT). Calcium ethoxide was dissolved separately in 2-ethoxyethanol and was added dropwise to the hydrolyzed TEOS until a gel was formed. The BG was aged for two days, followed by drying under vacuum at 50 ℃ to obtain a final molar composition of 70 % SiO_2, 26 % CaO, and 4 % P_2O_5. The final product was ground to a fine powder and stored at RT until further use.[23,35]

4.3.4. Preparation of GelMA-BG-MWCNT nanocomposite hydrogel biomaterials

Two surfactants, pluronic F-127 or diacrylated pluronic F-127, were used to prepare MWCNT stock dispersions. Surfactants were separately dissolved in water at high temperature to a concentration of 20 mg/ml followed by adding 20 mg/ml MWCNT. Dispersions were sonicated for 1 h at 50 ºC and stored at RT until further use for GelMA-BG-MWCNT biomaterial preparation. GelMA prepolymer was dissolved in water at a concentration of 10 % w/v. 1, 2, 3, and 5 wt.% MWCNT were added to the GelMA prepolymer solution, followed by sonication at 50 ºC for 30 min. BG powder was subsequently added to GelMA-MWCNT mix at different concentrations and was further sonicated for 30 min. KPS and TEMED were added separately as the thermal initiator and accelerator, respectively, at concentrations of 0.5 % w/v with respect to the total prepolymer concentration to crosslink GelMA at 60 ºC. Sample nomenclature is presented in **Table 4.1**.

Table 4.1. Nomenclature of GelMA-BG-MWCNT nanocomposite hydrogels.

GelMA-BG-MWCNT Nomenclature					GelMA (wt.%)	BG (wt.%)	MWCNT (wt.%)				
100-0-0					100	0	0				
100-0-1					100	0	1				
90-10-1					90	10	1				
80-20-1					80	20	1				
70-30-0	70-30-1	70-30-2	70-30-3	70-30-5	70	30	0	1	2	3	5
60-40-1					60	40	1				
50-50-1					50	50	1				

4.4. Characterization of biomaterials

4.4.1. ^{1}H Nuclear Magnetic Resonance (^{1}H NMR) spectroscopy

The degree of methacryloyl functionalization was determined by using ^{1}H NMR at a frequency of 400 MHz (Varian Inova Spectrometer; Varian, Palo Alto, CA, USA) at 50 ºC in deuterium oxide (D_2O) at a concentration of 2 % w/v. Solvent pre-saturation was applied solely to the H_2O/D_2O peak to reduce the intensity of the residual water, and the degree of methacryloylation was calculated by Eq. (4.1) where $Mol_{Val,Leu,Ile}$ and $Mol_{Lys,Hly}$ represent the total number of moles of valine, leucine, isoleucine, lysine, and hydroxylysine found in gelatin.[36,37] The integration peak corresponding to the hydrophobic alkyl side chains of valine (Val), leucine (Leu), and isoleucine (Ile) is represented by

$I_{1.06ppm}$, whereas the integration peak attributed to the acrylic proton of methacryloyl substituent groups is shown as $I_{5.8ppm}$.[36,37]

$$DM(\%) = Mol_{Val,Leu,Ile} \times \frac{I_{5.8ppm}}{I_{1.06ppm}} \times \frac{100}{Mol_{Lys,Hyl}} \quad (4.1)$$

4.4.2. Fourier Transform Infrared Spectroscopy (FTIR)

Dried and powdered biomaterials were used for FTIR spectroscopy which was conducted using a Perkin Elmer FTIR Spectrometer (Waltham, MA, USA) in the transmission mode at a resolution of 4 cm^{-1} and sample scans of 24.

4.4.3. Thermogravimetric Analysis (TGA)

TGA experiments were performed using a TA Instruments Q600 SDT TGA analyzer. 20 mg of dried BG and GelMA-BG were heated from 25 to 1000 ℃ under air at a heating rate of 10 ℃/min. The ratios of BG and GelMA-BG were calculated by recording the residual masses at 1000 ℃.

4.4.4. Scanning Electron Microscope (SEM) and Energy Dispersive X-ray Spectroscopy (EDX) analysis

Visualization of the surface morphology and elemental distribution of the chemical composition of the biomaterials were assessed through SEM and EDX, respectively. Disk-shaped samples were sputter-coated with gold/palladium (K550X, sputter coater, Emitech Ltd., Ashford, UK), and SEM coupled to EDX was performed by using a Zeiss 1540XB FIB/SEM instrument (Carl Zeiss: Oberkochen, Germany).

4.4.5. Swelling behavior of GelMA-BG-MWCNT nanocomposite hydrogels

Evaluation of the swelling behavior of nanocomposite hydrogels (n =6) was performed in PBS for 24 h at 37 ℃. The weights of the samples were recorded before (W_0) and after incubation in PBS at various time points (W_t). The swelling ratio of samples was calculated according to Eq. (4.2):

$$Swelling\ Ratio\ (\%) = \frac{W_t - W_0}{W_0} \times 100 \quad (4.2)$$

4.4.6. Biodegradability of GelMA-BG-MWCNT nanocomposite hydrogels

The weight loss percentage of nanocomposite hydrogels (n =6) was determined by measuring the initial weight of the samples (W_0) and subsequently incubating in PBS at 37 ℃. At various time points (1, 4, 8, 16 and 20 days), the samples were washed with deionized water and dried under vacuum at RT. The final weights of the dried samples were recorded (W_f) and were used to calculate the weight loss percentages of each sample.

$$Weight\ loss\ (\%) = \frac{W_0 - W_f}{W_0} \times 100 \qquad (4.3)$$

4.4.7. Rheological properties of GelMA-BG-MWCNT nanocomposite hydrogels

Dynamic rheological tests were performed on hydrogels using a HAAKE Mars 60 Rheometer (MARS, Germany). Hydrogels (10 mm diameter and 5 mm height) were loaded into 20 mm parallel plates with a gap of 2.5 mm between the plates to perform strain amplitude sweeps (0.001–100 %) at 37 ℃ to determine the linear viscoelastic region. Assessment of temperature dependence on the elastic modulus (G') and complex viscosity ($|\eta^*|$) of gelatin, un-crosslinked GelMA and crosslinked GelMA hydrogels were determined through oscillatory temperature sweep tests. Tests were performed at a constant angular velocity of 1 Hz at a fixed strain amplitude of 0.01 %, determined in the linear region, with temperature scanning ranging from 20 to 60 ℃. Oscillatory frequency sweep tests with constant deformation were performed at angular velocities ranging from 0.01 to 10 Hz at a fixed strain amplitude of 0.01 % at 37 ℃. Angular velocities of up to 100 Hz were also tested in oscillatory frequency sweep tests; however, a maximum frequency of 10 Hz was preferred since the data displayed clear moduli changes as a function of BG concentration and MWCNT loading. Time sweep tests for thermal crosslinking were performed at a constant angular velocity of 1 Hz with a fixed strain amplitude of 0.01 % at 60 ℃. Creep-recovery tests were done with applied shear stress of 40 Pa for 4 min followed by 4 min of recovery. All rheological measurements were performed in triplicate.

4.4.8. Electro-mechanical characterizations of GelMA-BG-MWCNT nanocomposite hydrogels

The electrical conductivities of GelMA-BG-MWCNT nanocomposite hydrogels were evaluated after incubating biomaterials in water for 10 min, 24 h, and in PBS for 24 h. For electrical impedance spectra (EIS), electrochemical tests were carried out using the electrochemical workstation (CS350, CorrTest Instruments Inc., China) at RT. The sample film was sandwiched between two copper tape electrodes with a frequency sweeping from 100,000 to 0.1 Hz. The surface resistivity of hydrogel samples was measured by a ST-2258C digital 4-probe tester (Suzhou Jingge Electrical Co., Ltd.) under a current range from 0.1 µA to 100 mA, with a linear probe head (2.0 mm space). Conductivity was calculated through the following formula: σ $\sigma\left(\frac{S}{cm}\right) = \frac{1}{\rho}$, where σ is the electrical conductivity and ρ is the resistivity in ohm·cm. Pressure-sensitive conductivity or strain/deformation-dependent conductivity (for sensor application) of GelMA-BG-MWCNT nanocomposite hydrogels were performed through cyclic durability tests conducted in an in-house built instrument via a combination of an MTS (MTS criterion model 43) tester and a 2-wire high-performance digital meter (Keithley). Resistance was obtained via two-probe measurement under a cyclic compression deformation of 50 % at a rate of 500 mm/min at RT.

4.4.9. *In vitro* bioactivity of GelMA-BG-MWCNT nanocomposite hydrogels

Nanocomposite hydrogels were incubated in simulated body fluid (SBF) solution at a concentration of 10 mg/ml at 37 ºC under constant shaking at 150 rpm for 7 days. SBF was refreshed every other day. After SBF incubation, hydrogels were rinsed with water, dried under vacuum at RT, and their surfaces were visualized by SEM/EDX using a Zeiss 1540XB FIB/SEM instrument (Carl Zeiss: Oberkochen, Germany). FTIR and X-ray diffraction (XRD) data were acquired on dried samples. XRD data were obtained using an X-ray diffractometer Rigaku Ultima III operating on Cu Kα radiation with λ = 1.5418 Å at 30 kV and 15 mA in the 2θ range of 2–90º at a scanning speed of 2º/min and scanning width of 0.02º.

4.4.10. Cell adhesion and cytotoxicity of GelMA-BG-MWCNT nanocomposite hydrogels

Mouse embryo multipotent mesenchymal progenitor 10T1/2 cells were used to investigate cell adhesion to the electrically conductive nanocomposite hydrogels. Hydrogels were disinfected under ultraviolet (UV) light and pretreated in HBSS. 10T1/2 cells (cultured in DMEM with 5 % FBS and 1

% pen/strep) were subsequently seeded with a density of approximately 10,500 cells/cm^2. After 1 and 3 days, cells were fixed using 4 % paraformaldehyde (EMD Chemicals Inc. Gibbstown, NJ) and stained against DAPI (300 nmol in PBS) and phalloidin (1:100) to visualize cell nuclei and F-actin, respectively. Live/dead cell staining kit was used to detect 10T1/2 cells' viability after 1, 3 and 7 days of culture and was used according to manufacturer's protocol. Tissue culture plate (TCP) was used as control. Images were taken with a Leica DMi8 fluorescence microscope (Leica Microsystems CMS GmbH, Wetzlar, Germany).

4.4.11. Osteogenic gene expression of mouse embryo multipotent mesenchymal progenitor 10T1/2 cells on GelMA-BG-MWCNT nanocomposite hydrogels

For osteogenic differentiation of 10T1/2 cells on nanocomposite hydrogels, samples were disinfected under UV light and pretreated in HBSS. 10T1/2 cells (cultured in DMEM with 5 % FBS and 1 % pen/strep) were seeded with a density of ~15,500 cells/cm^2. After reaching 70 % confluency, cell culture media was replaced with osteogenic induction media (100 nM dexamethasone, 50 μg/ml L-ascorbic acid, and 10 mM $Na_xH_{3-x}PO_4$) for 7 days of culture. Cells differentiated on pure GelMA (100-0-0) hydrogels were used as a control to evaluate the effects of BG and MWCNT on osteogenic differentiation induction. Total RNA was extracted from 10T1/2 cells using the Bio-Rad Aurum™ Total RNA Mini Kit (Mississauga, ON, Canada) according to the manufacturer's protocol. Complementary DNA (cDNA) template was prepared by using 1 μg of total RNA primed with random primers according to Promega™ Random Hexamers protocol (Thermo Fisher). Quantitative real-time PCR (qRT-PCR) was conducted in 10 μl of reaction volumes using a CFX96™ Real-Time System (C1000 Touch Thermal Cycler; Bio-Rad, Mississauga, ON, Canada), and measured with iQ™ SYBR® Green Supermix (Bio-Rad) according to the recommended procedures. The sequences of primers are presented in **Table 4.2**. The results were analyzed with the comparative threshold cycle method and normalized with mouse 18S as an endogenous reference and reported as relative values (ΔΔ CT) to the control.

Table 4.2. Primers for mouse-specific mRNA amplification.

Gene	Forward (5'→ 3')	Reverse (5'→ 3')
Sp7	GCCAGTAATCTTCAAGCCAGA	CCATAGTGAGCTTCTTCCTGG
Spp1	ATCTCACCATTCGGATGAGTCT	TGTAGGGACGATTGGAGTGAAA
BSP	GAGCCAGGACTGCCGAAAGGAA	CCGTTGTCTCCTCCGCTGCTGC
18S	GCGGTTCTATTTTGTTGGTTT	CTCCGACTTTCGTTCTTGATT

Sp7: Osterix; Spp1: Osteopontin; BSP: Bone sialoprotein.

4.4.12. Statistical analysis

Statistical analysis of the data was performed using GraphPad Prism and data are expressed as mean ± standard error of the mean. Differences were tested by one-way ANOVA and a p-value of <0.05 was used for statistical significance.

4.5. Results and discussion

**4.5.1. Synthesis of gelatin methacryloyl (GelMA) and tertiary bioactive glass (BG) biomaterials**

Since GelMA is a semi-synthetic polymer derived from gelatin, the hydrolyzed form of type I collagen found in bone, the application of this polymer for the synthesis of bone nanocomposite biomaterials could bring a great benefit in the field of bone repair and regeneration. Some advantages of synthesizing GelMA are that it allows control on the reproducibility, the degree of methacryloyl substitution, and thus the initial mechanical properties of GelMA hydrogel. The degree of methacryloylation (DM) is an important factor that influences the network density and stiffness of GelMA.[37] Using ^{1}H NMR spectra, the successful functionalization of gelatin with methacrylamide and methacrylate groups was assessed (**Fig. 4.1A**).[38] In the GelMA ^{1}H NMR spectra, five characteristic peaks associated with the formation of new functional groups were observed. Peaks at 5.56 and 5.8 ppm were attributed to the acrylic protons of methacrylamide substituent groups of lysine and hydroxylysine, while the third peak at 2 ppm was associated with the methyl protons of methacryloyl groups. An additional small peak at 5.85 ppm corresponded to the acrylic protons of methacrylate groups.[39] Finally, the peak at 3.1 ppm showed a decreased intensity compared to the unmodified gelatin which corresponded to the methylene protons of lysine groups, indicating a successful reaction of the lysine residues with methacrylic anhydride.[40] A DM of 53.65 % for GelMA was calculated from Eq. (4.1) by obtaining the integration of two reference peaks. The first integration reference peak was at 5.8 ppm, whereas the second was at 1.06, representing the hydrophobic alkyl side chain of valine (Val), leucine (Leu), and isoleucine (Ile), which are chemically inert amino acids that are not involved in the reaction with methacrylic anhydride.[37]

From FTIR spectra (**Fig. 4.2A**), GelMA prepolymer showed characteristic peaks at 3284 cm^{-1} and 2945 cm^{-1} corresponding to amide A and amide B, respectively, which were associated with the

stretching vibration of the free N-H and O-H groups, and the asymmetric stretching vibrations of $=$C-H and -NH_3^+ of the peptide fragments, respectively. In addition, peaks at 1632 cm^{-1} corresponding to amide I as a result of the C$=$O stretching vibrations along the polypeptide backbone of GelMA, and 1518 cm^{-1} corresponding to amide II from N-H bending and C-N stretching vibrations were observed.[41,42] Furthermore, an additional peak at 1236 cm^{-1} was present in GelMA, indicating the presence of amide III that corresponded to the wagging vibrations of CH_2 groups from the glycine backbone and proline side chains as well as the vibration stretching of C-N bonds and the vibration of bending N-H bonds.[43-45] The sol-gel derived tertiary bioactive glass (BG) showed bands at 450 cm^{-1} due to the rocking motion of oxygen bridging two adjacent silica atoms from the siloxane groups (Si-O-Si) of the BG, whereas the peak found at 800 cm^{-1} was associated with the bending Si-O vibration of the ring structures of the BG.[46] In addition, peaks at 1030 cm^{-1} and 1170 cm^{-1} showing the asymmetric Si-O-Si stretching of the oxygen atom moving back and forth along the Si atoms were observed. Finally, a broad peak at 3370 cm^{-1} due to OH stretching vibrations of self-associated silanol (Si-OH) groups was also observed.[35]

The temperature-dependent rheological properties of gelatin demonstrated that the storage modulus (G′) of gelatin gels decreased drastically to 0.135 Pa above its melting point of ~30 ℃ due to the weakening of the gelatin physical network (**Fig. 4.1B**).[47,48] Un-crosslinked GelMA hydrogels had a higher G′ of 0.322 Pa at 60 ℃ when compared with gelatin hydrogel due to the functionalization of gelatin with the methacryloyl groups. In contrast, crosslinked GelMA hydrogels maintained a constant storage modulus (G′) of 348 Pa as the temperature increased to 60 ℃ (**Fig. 4.1B**). Similarly, the effect of temperature on the complex viscosity of gelatin, un-crosslinked GelMA and crosslinked GelMA is shown in **Fig. 4.1C**. The complex viscosity of gelatin significantly decreased from 58.084 Pa·s to 0.033 Pa·s when the temperature reached 60 ℃, whereas the initial complex viscosity of un-crosslinked GelMA displayed a lower initial value of 36.498 Pa·s compared to gelatin gels due to the functionalization of gelatin with methacryloyl groups. Increased temperature caused a significant reduction in the complex viscosity of un-crosslinked GelMA, similar to that displayed by gelatin gels, until reaching a value of 0.068 Pa·s at 60 ℃. However, crosslinked GelMA hydrogels maintained a constant complex viscosity of around 55.376 Pa·s as the temperature increased to 60 ℃. Collectively, these results showed that the methacryloylation of gelatin and subsequent crosslinking resulted in increased stability of the hydrogel network and could be suitable for *in vitro* studies.

The composition of the organic-inorganic components in GelMA-BG hydrogels was demonstrated from TGA analysis (**Fig. 4.1D**). For pure BG, the first stage of degradation occurred below 275 ℃ due to the elimination of moisture and impurities from the incomplete condensation of hydrolyzed precursors, resulting in a 15 % weight loss. The second degradation stage was observed above 275 ℃ resulting in a final residual weight of 65 % at 1000 ℃. GelMA-BG nanocomposite (50 wt.% GelMA-50 wt.% BG) (50-50) also showed two main stages of degradation. The initial mass loss occurred below 145 ℃ due to moisture and impurities such as un-crosslinked GelMA. The second degradation phase was observed above 150 ℃ due to the degradation of GelMA. The residual weight at 1000 ℃ was 35 % of the initial GelMA-BG nanocomposite. The organic-inorganic weight percent ratio obtained from the TGA residual weight of GelMA-BG was 46-53, which was in good agreement with the 50-50 theoretical estimation of the weight percent ratio of GelMA-BG.
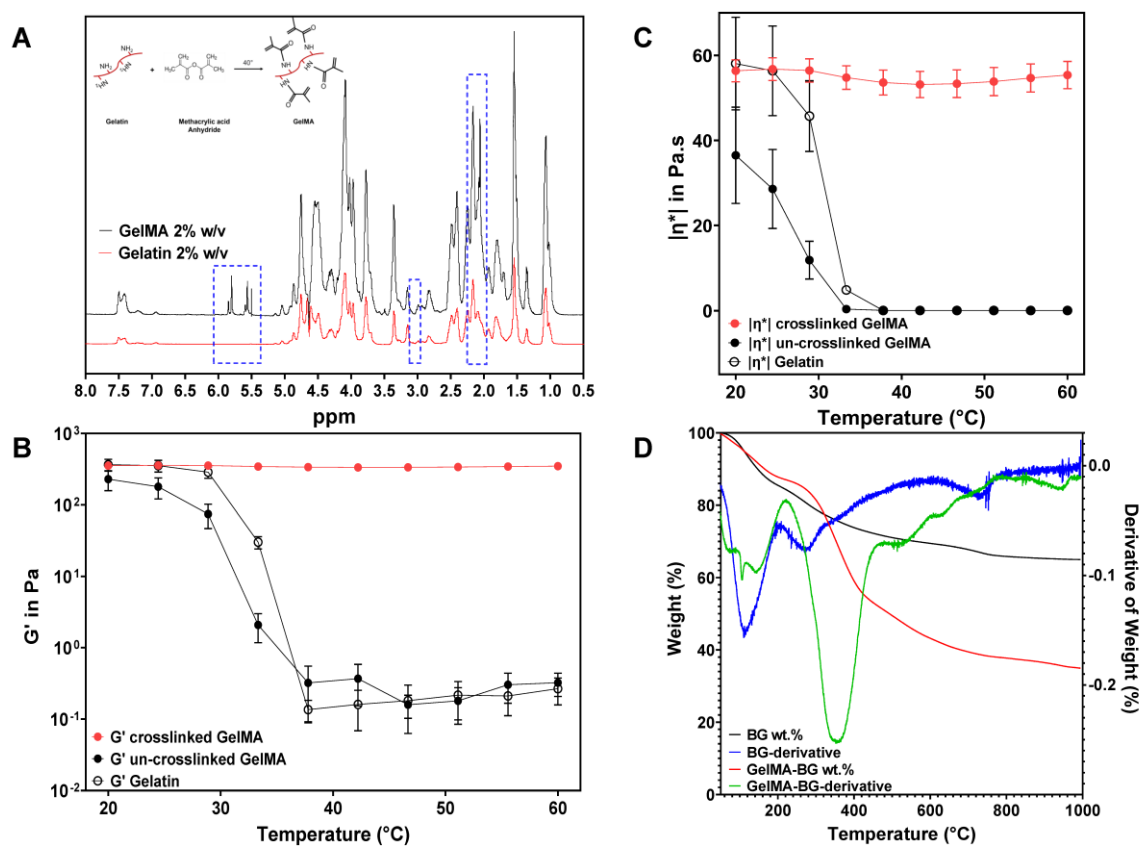
Figure 4.1. Characterization of GelMA and organic-inorganic biomaterials. (**A**) ^{1}H NMR spectra of gelatin and GelMA. (**B**) Temperature sweep test of gelatin, un-crosslinked GelMA and crosslinked GelMA. (**C**) Complex viscosity of gelatin, un-crosslinked GelMA and crosslinked GelMA as a function of temperature. (**D**) TGA curves and derivative of weight percent versus temperature curves for pure BG and GelMA-BG nanocomposite biomaterials.

4.5.2. Preparation of GelMA-BG-MWCNT biomaterials

Proper dispersion of MWCNT in GelMA solution is an important step in preparing uniform and mechanically acceptable nanocomposites. In this study, MWCNT dispersions were prepared using either Pluronic F- 127 (PF-127) or diacrylated Pluronic F-127 (dPF-127) surfactants. The resulting MWCNT dispersions were then added to the GelMA-BG composition and crosslinked. According to the FTIR spectra shown in **Fig. 4.2A**, 50-50-1 GelMA-BG-MWCNT nanocomposite presented characteristic peaks associated with the chemical groups of both GelMA and BG, showing the existence of a physical bond between the organic and inorganic elements of the biomaterial. The characteristic amide III band observed in GelMA disappeared in the 50-50-1 nanocomposite due to the plausible interaction between the silicon hydroxyl (-Si-OH) groups of BG and the amino ($-NH_2$) groups of GelMA polymer.[45] In addition, peaks that showed evidence of calcium incorporation into the silicate network at 970 cm^{-1} and 896 cm^{-1}, depicted as the Si-O-non- bridging oxygen (NBO) that resulted from the disruption of calcium ions to the siloxane bridges, were observed.[41] As shown from the frequency sweep experiments (**Fig. 4.2B**), the nanocomposite hydrogels prepared with MWCNT dispersed in dPF-127 had a higher storage (G′) and loss (G″) modulus of 226.7 and 13.8 Pa, respectively, than hydrogels prepared with PF-127. This strongly suggested that the dPF-127 surfactant allowed homogenization and further crosslinking of the GelMA prepolymer due to its diacrylate group, thus enhancing the elasticity and mechanical strength of the nanocomposite hydrogels. Furthermore, SEM and EDX were used to visualize the morphology and homogeneous elemental distribution of GelMA-BG-MWCNT nanocomposite hydrogels (**Fig. 4.2C, D**). Uniform elemental distribution of carbon, attributed to the organic GelMA polymer matrix and the MWCNT of the nanocomposite, was observed, while silicon (Si), calcium (Ca), and phosphorous (P) were associated with the presence of tertiary BG (SiO_2–CaO–P_2O_5) corresponding to the inorganic component of the hydrogel (**Fig. 4.2E-H**). Based on the data collectively presented in **Fig. 4.2**, dPF-127 was chosen as the surfactant to prepare MWCNT stock and for the preparation of nanocomposite hydrogels.
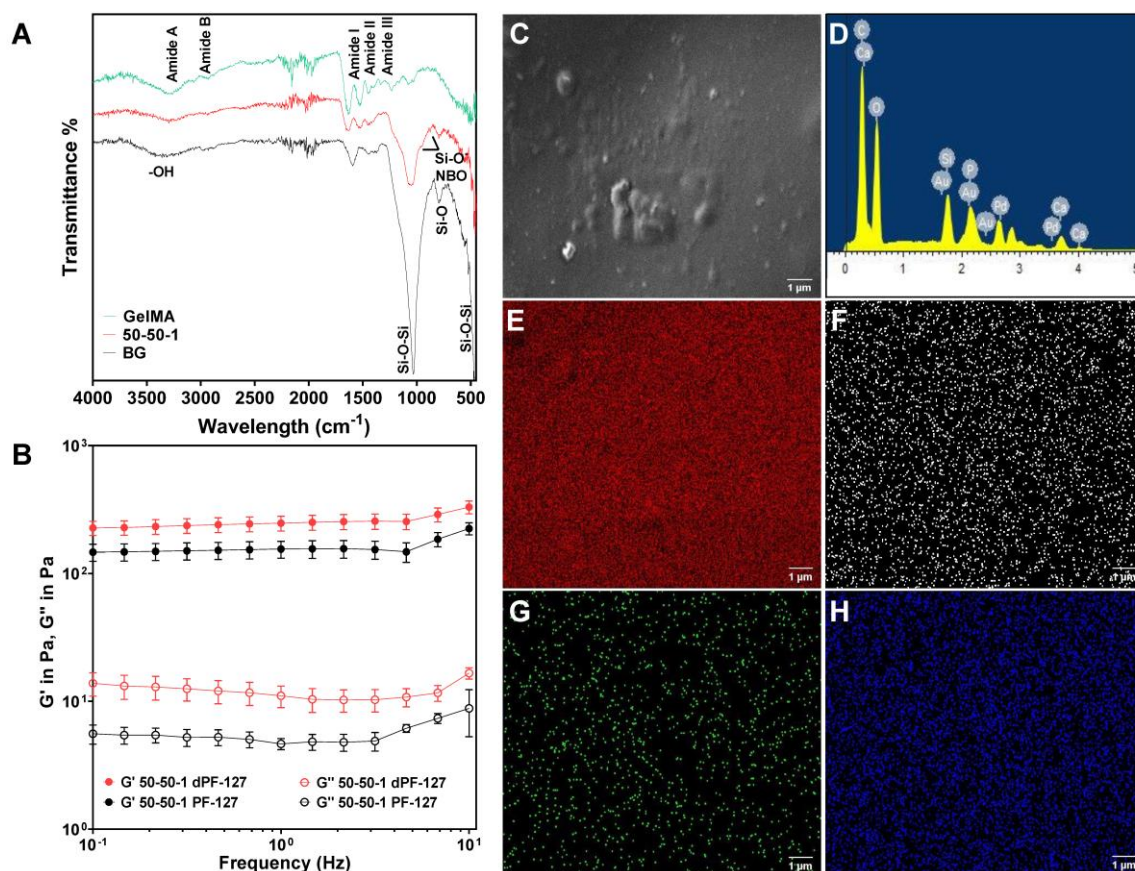
Figure 4.2. Chemical, mechanical, and elemental homogeneity in GelMA-BG-MWCNT nanocomposite biomaterials. (**A**) FTIR of GelMA, GelMA-BG-MWCNT (50-50-1) nanocomposite biomaterial and BG. (**B**) Comparison of frequency sweep test of 50-50-1 nanocomposite hydrogels using two types of surfactants for the preparation of MWCNT dispersion, PF-127 (black) or dPF-127 (red) surfactant. (**C**) SEM image, (**D**) EDX spectra, and elemental mapping of (**E**) carbon, (**F**) silicon, (**G**) calcium, (**H**) phosphorous for the 50-50-1 nanocomposite biomaterial. Scale bar = 1 μm.

4.5.3. Swelling and degradation behavior of GelMA-BG-MWCNT nanocomposite hydrogels

The swelling of hydrogels plays a crucial role in the healing and regeneration of bone tissue since it allows nutrient transport and removal of waste products through diffusion.[49] Nanocomposite hydrogels composed of different GelMA-BG percentages have different abilities to absorb water. **Fig. 4.3B** shows the percentage of swelling ratio behavior of hydrogels (digital pictures shown in **Fig. 4.3A**) after incubating in PBS for 24 h. All hydrogels reached their equilibrium swelling after 6 h of incubation. The crosslinked GelMA containing 1 wt % MWCNT (sample 100-0-1) had a decreased swelling ratio compared with the 100-0-0 control hydrogel due to the hydrophobic nature of MWCNT,

but both showed a significant increase in swelling ratio compared to those hydrogels containing BG due to the hydrophilic groups present in GelMA polymer chains. The swelling ratio of nanocomposite hydrogels decreased as the concentration of BG increased from 10 wt.% (90-10-1) to 50 wt.% (50-50-1) due to the strong interactions between the GelMA matrix network and the BG. These strong interactions included ionic interactions between the released calcium ions from the BG with the carboxylic groups in GelMA, causing aggregation of the polymer chains which resulted in a lower swelling ratio due to the decreased hydrophilicity of the nanocomposite hydrogels.[50,51] The lower swelling ratio of nanocomposite hydrogels with increased BG concentration could also be due to electrostatic interactions between the negatively charged silicon hydroxyl (-Si-OH) groups of the BG surface with the positively charged amino (-NH$_2$) groups of GelMA.[51] Therefore, these results show that nanocomposite hydrogels possess favorable swelling ratios that would correlate with the efficiency of absorption of nutrient diffusion if transplanted into the body to regenerate bone.

The degradation of nanocomposite hydrogels was evaluated over 20 days of incubation in PBS, which is the approximate time required for the bone to heal and remodel after fracture.[52] As shown in **Fig. 4.3C**, the degradation of all hydrogels increased as a function of time, whereby 100-0-0 hydrogel had the lowest degradation. However, the degradation of nanocomposite hydrogels depended on the BG content, since higher concentrations of BG resulted in increased weight loss. The plausible explanation for the increased degradation in hydrogels containing higher BG concentrations was due to the diffusion of water into the silica glass network, causing hydrolysis of the siloxane (Si-O-Si) bonds to form silanol (-Si-OH) groups. In addition, the presence of network modifiers, such as calcium, accelerated the degradation process by disrupting the silicate network. Therefore, hydrogels composed of 50-50-1 had the highest degradation rate since this composition contained the highest concentration of BG. One of the crucial steps when developing nanocomposite hydrogels for bone tissue engineering is the selection of a suitable organic-inorganic composition that resembles that of natural bone. Natural bone is composed of 30 wt.% collagen and 70 wt.% hydroxycarbonate apatite (HCA).[53] However, the development of nanocomposite hydrogels composed of 30 wt.% GelMA and 70 wt.% BG would not be viable for bone repair and regeneration applications since it would result in a hydrogel with an increased degradation rate than the 50-50-1 hydrogel, thus limiting its ability to support bone healing. Collagen fibers found in bone, however, provide a framework in which the HCA nucleates and grows.[54] Therefore, the selection of the GelMA-BG hydrogel composition of 70-30 could provide a similar framework to that of natural bone, where the 70 wt.% GelMA would

function as a template for the deposition of HCA *in vitro* formed from the release of soluble ionic species from the 30 wt.% BG, hence promoting biomineralization while acting as a support for bone regeneration. In addition, the 70-30 hydrogel composition possessed suitable degradation properties that could potentially be studied in *in vivo* models. Further studies would enable the assessment of the rate of degradation with the formation of new bone tissue until the biomaterial is completely remodeled and matches the original tissue mechanical strength.[1] Consistent with **Fig. 4.2B**, the use of dPF-127 to disperse MWCNT decreased the degradation for the hydrogel composition of 70-30-1, as shown in the inset of **Fig. 4.3C**, confirming higher crosslink density and hence hydrolytically stable hydrogels.

4.5.4. Rheological and creep-recovery properties of GelMA-BG-MWCNT nanocomposite hydrogels

Bone undergoes natural tension and compression forces, and it is, therefore, crucial for bone biomaterials to provide temporary mechanical support until tissue remodeling. For materials that undergo macro- or micro-structural rearrangement with time, dynamic moduli are dependent on frequency. The oscillatory frequency sweep test results for nanocomposite hydrogels containing various concentrations of GelMA- BG at a fixed 1 wt.% MWCNT loading is shown in **Fig. 4.3D**. As expected, the hydrogels showed an upward trend in their G' and G'' values with higher frequencies. Regardless of the BG content, all hydrogel compositions had higher storage modulus (G') than the counterpart loss modulus (G'') which meant that hydrogels possessed an elastic behavior and high resistance to deformation. As the percentage of BG increased, G'' increased compared to the control GelMA (100-0-0) hydrogel due to a decrease in viscosity as the BG increased and was more compact in the polymer matrix. However, an opposite effect was observed in the resulting G', where the addition of BG did not significantly increase the elasticity of nanocomposite hydrogels. This was evident for hydrogels composed of 70-30-1 and 60-40-1 where their G' values were 178 Pa and 248 Pa, respectively, compared to 274 Pa for pure 100-0-0 hydrogels. However, 80-20-1 and 50-50-1 nanocomposite hydrogels possessed a higher G' value of 375 Pa and 330 Pa, respectively, compared to 100-0- 0. The resulting decrease of G' could be explained by the fact that above 20 wt.% BG loading within the nanocomposite hydrogels disrupted the GelMA network, which is responsible for an elastic behavior, thus decreasing their G' value. However, nanocomposite hydrogels require at least a BG concentration of 50 wt.% to increase the G' and hence, its resistance to deformation.

The effect of MWCNT loading on G′ and G″ for the 70-30 GelMA-BG composition, the chosen hydrogel candidate for bone repair and regeneration applications, is shown in **Fig. 4.3E.** It was evident that more elastic hydrogels resistant to deformation were prepared with increased MWCNT loading. Nanocomposite hydrogels containing 5 wt.% MWCNT (70-30-5) therefore displayed the highest G′ of 632.2 Pa and G″ of 38 Pa. These results concluded that the incorporation of MWCNT improved the mechanical strength of the nanocomposite hydrogels, enhancing their moduli and their potential suitability to support bone repair and regeneration. The role of the reactive dPF-127 surfactant used to disperse MWCNT not only improved the homogeneity of the GelMA-BG- MWCNT nanocomposites and slowed degradation, but also increased the mechanical strength and resistance to deformation of nanocomposite hydrogels (**Fig. 4.3F**).
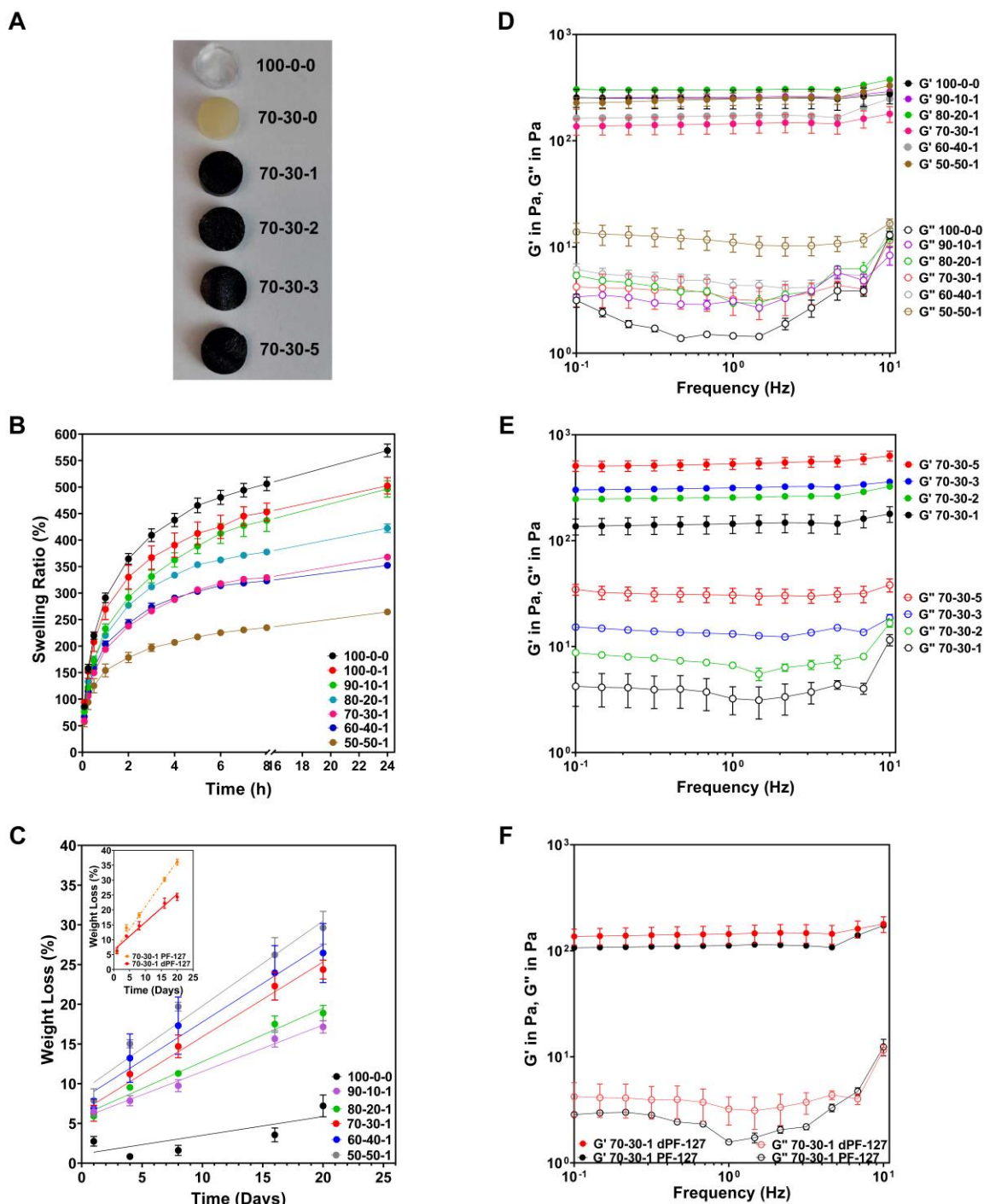
Figure 4.3. Swelling ratio, biodegradation, and rheological properties of GelMA-BG-MWCNT nanocomposite hydrogels. (**A**) Digital image of hydrogels containing different concentrations of MWCNT. (**B**) The swelling ratio of nanocomposite hydrogels reached their swelling equilibrium state within 6 h. (**C**) Biodegradation behavior of GelMA-BG-MWCNT nanocomposite hydrogels within 20 days. (**D**) Frequency sweep test of GelMA-BG-MWCNT nanocomposite hydrogels containing different concentrations of GelMA-BG. (**E**) Frequency sweep test of 70-30 nanocomposite hydrogels containing different concentrations (1, 2, 3, 5 wt.%) of MWCNT. (**F**) Comparison of frequency sweep

test of 70-30-1 nanocomposite hydrogels using two types of surfactants for the preparation of MWCNT dispersion, PF-127 (black) or dPF-127 (red) surfactant.

Notwithstanding the useful information obtained from oscillatory frequency sweep tests, time sweeps directly provide kinetic information about how a material changes with time. The kinetics of the crosslinking reaction in 70-30 hydrogels containing various concentrations of MWCNT was evaluated at 60 ℃. The pure crosslinked GelMA, 100-0-0 hydrogel, became stiffer as the thermal crosslinking time increased, reaching the gelation time (G′=G″) at 8 s (**Fig. 4.4A**). Similarly, GelMA-BG hydrogels without MWCNT (70-30-0), reached gelation time after 9 s, suggesting that the incorporation of BG into the GelMA matrix did not affect the crosslinking time (**Fig. 4.4B**). However, the 70-30-1 hydrogel displayed two crossover points, but only one of them was the gelation point of the nanocomposite hydrogel (**Fig. 4.4C**). The first crossover point occurred after 32 s, where the hydrogel behaved more as a viscous material since the G″ was higher than the G′. The second crossover point showed the gelation point at 71 s, where the G′ became higher than the G″, resulting in a crosslinked hydrogel with an elastic behavior. Therefore, the addition of 1 wt.% MWCNT into GelMA- BG hydrogels delayed the crosslinking time which could be due to the interruption of the polymeric crosslinked GelMA network after the addition of MWCNTs. However, hydrogels containing 2, 3, and 5 wt.% MWCNT (70-30-2, 70-30-3, 70-30-5) did not show a delayed gelation point since their G′ was always higher than their G″ (**Fig. 4.4D, E,F**). Two factors affect the gelation behavior in nanocomposite hydrogels containing MWCNT. The first one involves the entanglement of the MWCNTs themselves as a result of their large aspect ratios and their intrinsic random curvature, while the second factor involves the non-covalent interactions between the polymer chains and the MWCNTs.[55]   As the concentration of MWCNTs is increased within the nanocomposite hydrogels, the MWCNTs form a higher interconnected structure, similar to polymeric interpenetrating networks, that lead to a decreased crosslinking time. Therefore, the resulting interconnected network of MWCNTs formed a restrained structure that limited the relaxation of polymer chains.[55,56]   This implied that as the MWCNT concentration increased in the nanocomposite hydrogels beyond 1 wt.%, the hydrogels had faster thermal crosslinking kinetics showing a consistent elastic behavior throughout the curing process which resulted in hydrogels that possessed enhanced resistance to deformation that could potentially serve as suitable biomaterial for bone repair and regeneration.
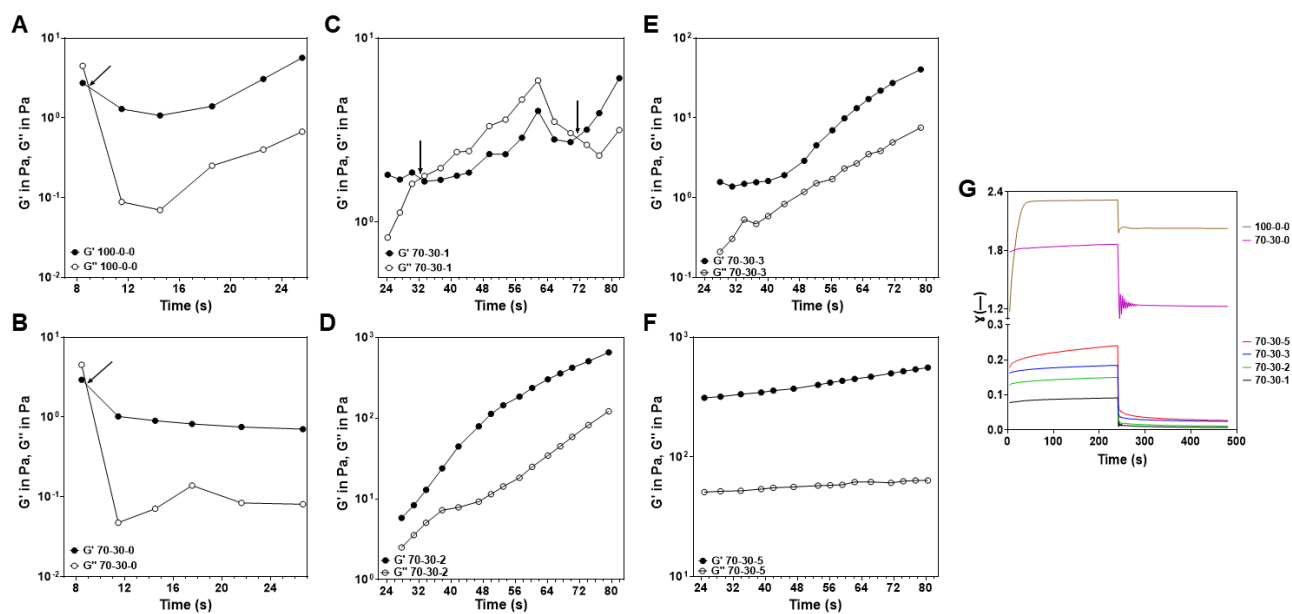
Figure 4.4. Rheological properties of 70-30 nanocomposite hydrogels as a function of MWCNT concentrations. Time sweep test for thermal crosslinking of (**A**) 100-0-0 hydrogel, (**B**) 70-30-0, (**C**) 70-30-1, (**D**) 70-30-2, (**E**) 70-30-3, and (**F**) 70-30-5 nanocomposite hydrogels, (**G**) creep and recovery test of 100-0-0 hydrogel, 70-30-0, and 70-30 nanocomposite hydrogels containing different concentrations (1, 2, 3, 5 wt.%) of MWCNT.

For viscoelastic materials, dimensional recovery after stress removal is essential for its functionality in cyclic loading.[1] From creep and recovery tests, it was found that all hydrogels had an instantaneous deformation upon the application of constant stress (**Fig. 4.4G**). However, differences in the creep strain profile were noted between hydrogels; with pure 100-0-0 hydrogel displaying an increase of strain in a time- dependent trend until 37 s, after which the deformation became constant resulting in a greater creep strain deformation than all other biomaterials. In contrast, 70-30 nanocomposite hydrogels had a time-independent behavior at all times throughout force application and recovery. The incorporation of MWCNT significantly improved the creep recovery of 70-30 nanocomposite hydrogels. At 1 wt.% MWCNT loading (70-30-1), nanocomposite hydrogels showed the lowest creep strain deformation and full recovery after the applied force was removed, likely related to the high degree of randomly dispersed MWCNTs in the form of single nanotube or small bundles.[57] However, nanocomposite hydrogels containing >1 wt.% MWCNT had a higher creep level and unrecoverable strain, especially for those hydrogels containing 3 wt.% (70-30-3) and 5 wt.% (70-30-5) MWCNT. The loss of recovery post-strain in materials possessing higher levels of MWCNT would be anticipated due to the strong hydrophobic and van der Waals interactions that exist between the

MWCNTs, which could limit their distribution within the GelMA matrix and was most strongly observed in 70-30-5 nanocomposite hydrogels.[57] Evidence of a heterogenous elemental distribution was observed, which shows the SEM/EDX of the surface of the 70-30-5 hydrogel (**Fig. 4.5**). It was observed that the organic-inorganic elemental distribution of the biomaterial was not uniform, where the carbon element displayed high aggregations due to the increased concentration of MWCNTs, resulting in an impaired recovery to deformation. Therefore, 70-30-1 and potentially 70-30-2 hydrogels could become more suitable bone biomaterial candidates since they possess a better recovery to deformation.
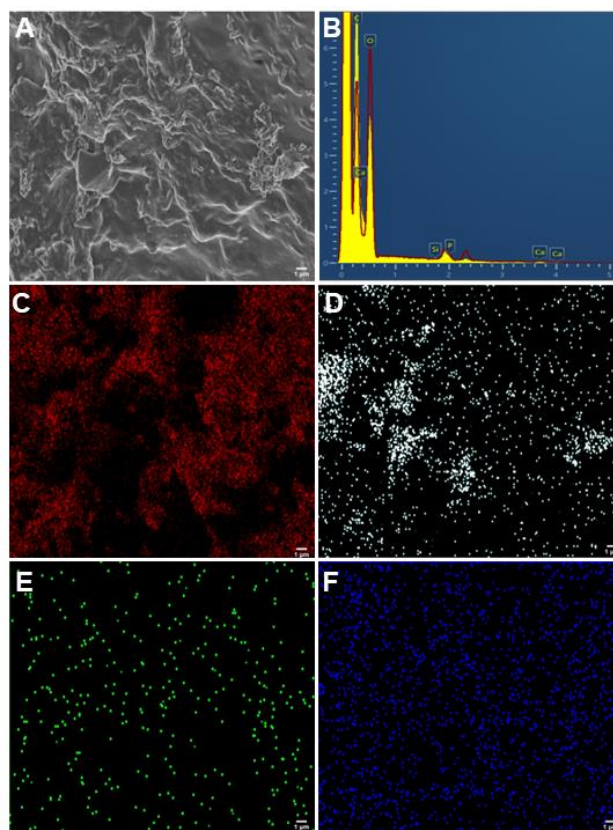
Figure 4.5. Elemental distribution of 70-30-5 nanocomposite biomaterial. (**A**) SEM image, (**B**) EDX spectra, and elemental mapping of (**C**) carbon, (**D**) silicon, (**E**) calcium, (**F**) phosphorous for the 70-30-5 nanocomposite biomaterial. Scale bar = 1 µm.

4.5.5. Electro-mechanical properties of GelMA-BG-MWCNT nanocomposite hydrogels

Since the 70-30 nanocomposite hydrogel composition was chosen to provide a similar biomineralization framework to that of natural bone,[54] its electrical properties as a function of MWCNT concentration were studied. Human cortical and cancellous bone have electrical conductivities of 0.0002 S/cm and 0.0007 S/cm, respectively,[58] and incorporating a low MWCNT concentration into the nanocomposite hydrogels could potentially result in a conductivity that mimics endogenous bone.[1] In addition, investigating the electrical properties of potential tissue-engineered bone by adding MWCNT would allow us to explore electrical stimulation in bone regeneration for future research. Since hydrogels would be tested *in vitro* in their hydrated form, electrical characterizations were performed in nanocomposite hydrogels after being incubated in either water or PBS. Fig. 5 shows the impedance and conductivity of nanocomposite hydrogels containing different MWCNT concentrations after incubation in water for 10 min (**Fig. 4.6A, B, C**) and 24 h (**Fig. 4.6D, E, F**), as well as in PBS for 24 h (**Fig. 4.6G, H, I**). The impedance of nanocomposite hydrogels was studied by electrochemical impedance spectroscopy (EIS) at different frequencies in an alternative current (AC) system. All hydrogel compositions incubated in either water or PBS showed a frequency-dependent behavior depicting that the hydrogels functioned as capacitors. This capacitive-like behavior of nanocomposite hydrogels could be explained by the incorporation of BG into the polymer matrix since the resulting graphs showed that impedance was higher in the 70-30-0 hydrogel than for pure 100-0-0 hydrogel (**Fig. 4.6A, D, G**).

The decreased conductivity in the presence of BG could be explained due to the amorphous structure of the tertiary glass network since the BG was not crystalline, which has been shown to increase conductivity.[59] However, the aim of incorporating BG into nanocomposite hydrogels was to promote a bioactive environment for bone regeneration, which is less likely to occur in crystallized BG since degradation occurs at a slower rate reducing its bioactivity.[60-62] Therefore, it was envisaged that the presence of MWCNTs would provide electrical properties, and not surprisingly, the electrical conductivities increased as a function of MWCNT concentration. The EIS data was consistent with the data generated with the 4-probe tester used to measure the conductivity of hydrogels in both positive (**Fig. 4.6B, E, H**) and negative (**Fig. 4.6C, F, I**) current directions to mimic the sinusoidal frequency in the EIS. Increased conductivity in both positive and negative current directions was observed for hydrogels containing 3 wt.% MWCNT (70-30-3) after incubation in water or PBS, and was further significantly enhanced in hydrogels with 5 wt.% MWCNT (70-30-5) (p <0.0001). The

initial increase of conductivity in 70-30-3 hydrogels could be explained by the percolation threshold, described as the critical volume fraction of MWCNT required to significantly increase the electrical conductivity of hydrogels through the formation of a continuous network of conductive particles within the polymer matrix.[63] In addition, the existence of strong hydrophobic and van der Waals interactions between the MWCNT particles increases with a higher MWCNT loading, resulting in a significant increase of electrical conductivity in 70-30-5 hydrogels.

Furthermore, the type of solution and the time of incubation were two variables that also played a crucial role in the resulting electrical conductivity of nanocomposite hydrogels. Incubation in water for 24 h led to the lowest conductivity due to the high swelling ratio of hydrogels, causing a limited interconnected network of MWCNTs within the GelMA matrix (**Fig. 4.6E, F**). However, hydrogels incubated in PBS for 24 h (**Fig. 4.6H, I**) had a significant increase in electrical conductivity since the salts present in PBS facilitated the electric conduction between the MWCNT particles in the polymer matrix. In addition, the electrical conductivity of nanocomposite hydrogels was not determined by the effect of the current direction. The electrical conductivity of 70-30-5 hydrogels incubated in PBS for 24 h displayed a higher conductive value of 9.21 S/cm measured in the positive current direction (**Fig. 4.6H**) than in the negative current direction with a conductivity of 4.09 S/cm (**Fig. 4.6I**). However, 70-30-5 hydrogels incubated in water for 10 min displayed a higher conductivity in the negative current direction with a value of 1.39 S/cm (**Fig. 4.6C**) than in the positive current direction with a conductivity of 0.72 S/cm (**Fig. 4.6B**).

The development of organic-inorganic hydrogels with electrically conductive properties has been explored to mimic the complex hierarchical nanocomposite structure and electrical properties of bone. Although previous studies have incorporated CNTs with either a polymeric or an inorganic system,[16,30] they fail to mimic the organic- inorganic biological composition of bone. Alternatively, other studies incorporated an electrically conductive component, specifically CNTs, into an organic-inorganic system,[33,34,64] but lacked characterizing the electrically conductive properties of the biomaterials. Furthermore, the present nanocomposite hydrogels possessed higher conductivities than other studies that also characterized the electrical properties of their bone biomaterials composed of an organic-inorganic system.[32,65] Although the hydrogels possessed higher electrically conductive properties than endogenous bone, nanocomposite hydrogels would function as an element to support the healing of bone defects by providing an environment in which a low amount of energy of electrical stimulation could potentially be delivered to promote the maturation of bone.
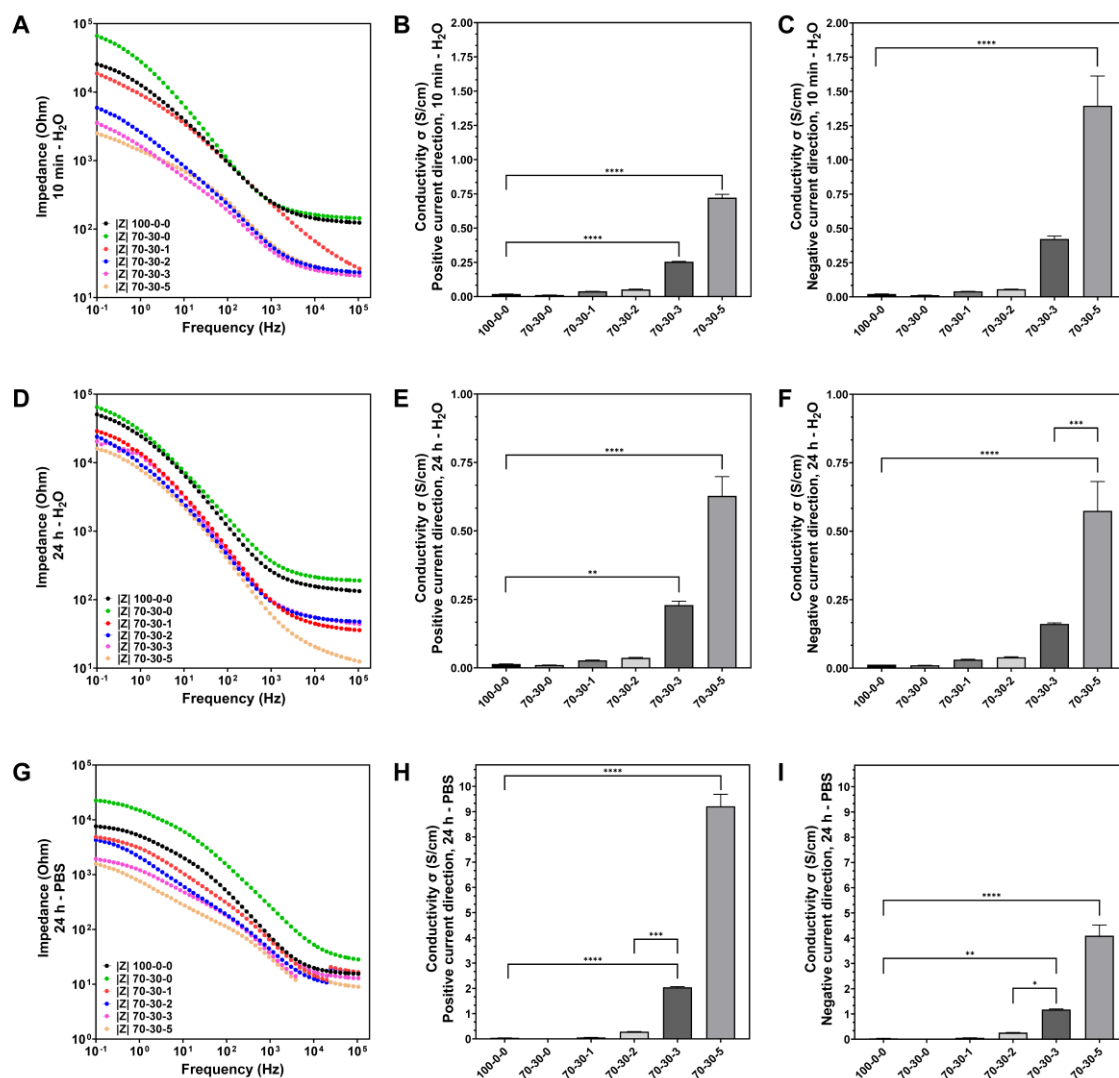
Figure 4.6. Electrically conductive properties of 70-30 nanocomposite hydrogels as a function of MWCNT concentrations. EIS spectra of electrically conductive hydrogels incubated in (**A**) water for 10 min, (**D**) water for 24 h, and (**G**) PBS for 24 h. The conductivity of electrically conductive hydrogels in positive current direction after incubating in (**B**) water for 10 min, (**E**) water for 24 h and (**H**) PBS for 24 h. The conductivity of electrically conductive hydrogels in negative current direction after incubating in (**C**) water for 10 min, (**F**) water for 24 h, and (**I**) PBS for 24 h. *p <0.05, **p <0.01, ***p <0.001, **** p <0.0001.

Endogenous bone generates electrical potentials through the application of mechanical strain generating electronegative potentials upon compression, producing bone formation, and electropositive potentials when a bone is under tension, causing bone resorption.[66] To the best of my knowledge, no other study has investigated this property in their biomaterials for bone tissue

engineering applications. The current nanocomposite hydrogels also possessed an electro-mechanical response, as shown in **Fig. 4.7**. The 100-0-0 hydrogels were not assessed for cyclic tests since they could not withstand the load during cyclic compression due to hydrogel breakage during testing. However, nanocomposite hydrogels underwent deformation of 50 % at a high compression rate of 500 mm/min. This high rate of deformation was required to obtain a good wave signal of resistance in the digital meter. The repeated cyclic strains observed showed fluctuations between high and low values in the resistance of all nanocomposite hydrogels. The resistance of hydrogels decreased as the concentration of MWCNTs increased in the GelMA-BG hydrogels, where 70-30-5 hydrogels had the lowest resistance of around 40,000 Ω (**Fig. 4.7I**) compared to 70-30-1 hydrogels which reached a higher resistance of approximately 70,000 Ω (**Fig. 4.7C**). 70-30-0 hydrogels had the highest resistance of approximately 80,000 Ω (**Fig. 4.7A**), which confirmed that nanocomposite hydrogels without MWCNT loading possessed the lowest electrical conductivity. These results were consistent with the impedance and the electrical conductivity measurements obtained in Fig. 5, confirming that an increase in electrical conductivity was dependent on the concentration of MWCNTs with 70-30-5 hydrogels achieving the highest conductivity.

The stress-strain curves of nanocomposite hydrogels obtained from cyclic compression tests, as well as the compressive modulus calculated from the stress-strain curves, also showed a similar relationship between the dependency of stiffness and MWCNT loading concentration (**Fig. 4.7B, D, F, H, J**). Since the compressive stress-strain curves were nonlinear, the compressive modulus was calculated by taking the derivative of the best fit equation and evaluating it at 30% strain. This strain was chosen since bone is likely not be deformed naturally beyond this point. A summary table showing the compressive modulus of each nanocomposite hydrogel is presented in **Table 4.3**. The compressive modulus of 70-30-0 was 24.8 kPa and subsequently increased as the concentration of MWCNTs was incorporated into the GelMA-BG hydrogels. 70-30-1 and 70-30-2 hydrogels possessed a compressive modulus of 32.5 kPa and 32.9 kPa, respectively, and further increased to 74.1 kPa in the 70-30-3 hydrogels. These results showed consistent behavior with the percolation threshold obtained in the electrical conductivity measurements. 70-30-3 hydrogels not only contained a critical volume fraction of MWCNT loading that significantly increased the electrical conductivity of hydrogels, but also enhanced the mechanical strength of GelMA-BG-MWCNT hydrogels.

Strong hydrophobic and van der Waals interactions that existed between the high MWCNT loading in the 70-30-5 hydrogels led to a significant increase in electrical conductivity values. However, this high MWCNTs concentration in the 70-30-5 hydrogels caused heterogeneity within the gel matrix,[57] and resulted in a decrease in the compressive modulus to 48.3 kPa compared to 70-30-3 hydrogels. Electro- mechanical properties of biomaterials are important to bone tissue engineering since they can be stimulated both mechanically and electrically to accelerate tissue formation and repair. Electrical responses in nanocomposite biomaterials would be beneficial since it has been shown in *in vitro* and in clinical studies that healing of bone defects can be induced by applying stimulation at the injured site at different currents and frequencies.[16,67-69] The application of mechanical stimulation in the form of loading frequencies has also been shown to promote the regeneration of bone.[70-72] Although electro-mechanical responses for bone repair and regeneration are yet to be explored, its application will be a step in the right direction for bone tissue engineering.
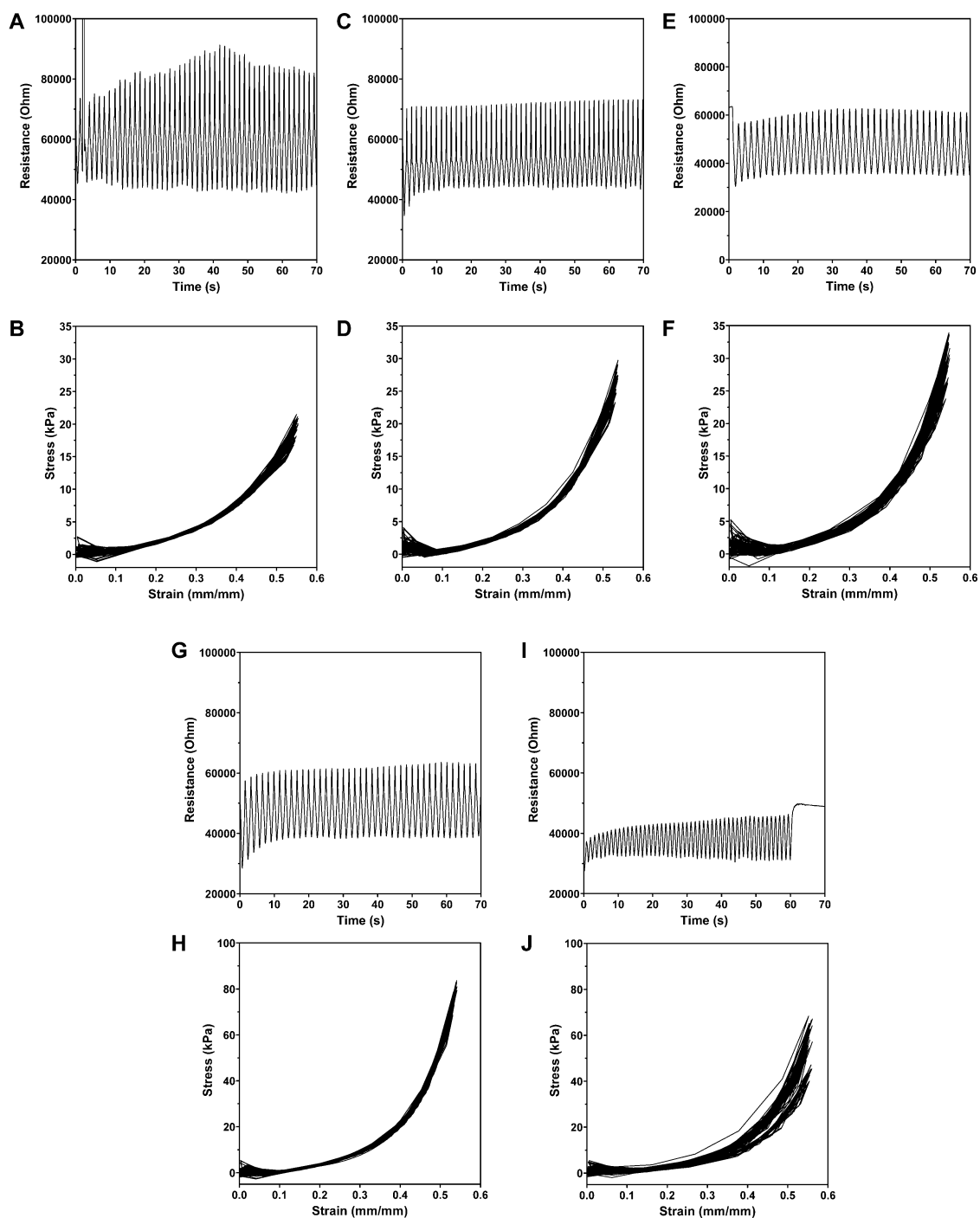
Figure 4.7. Cyclic durability tests of 70-30 nanocomposite hydrogels as a function of MWCNT concentrations. Cyclic electro-mechanical response of (**A, B**) 70-30-0, (**C, D**) 70-30-1, (**E, F**) 70-30-2, (**G, H**) 70-30-3, and (**I, J**) 70-30-5 hydrogels.

Table 4.3. Compressive modulus of nanocomposite hydrogels evaluated at 30% strain.

GelMA-BG-MWCNT Nomenclature	Compressive Modulus (kPa)
70-30-0	24.8
70-30-1	32.5
70-30-2	32.9
70-30-3	74.1
70-30-5	48.3

4.5.6. Bioactivity of GelMA-BG-MWCNT nanocomposite hydrogels

Ideal bone repair and bone scaffold materials should be capable of possessing bioactive features that would enhance bone formation. Formation of hydroxycarbonate apatite (HCA) ($Ca_{10-x}(PO_4)_{6-x}(CO_3)_x(OH)_{2-x}$) layers occurs through the release of soluble ionic species, such as Si, Ca and P ions, from the BG to form a high-surface-area hydrated silica and polycrystalline HCA bilayer on the glass surface, resulting in an apatite layer similar to that of bone, capable to stimulating the formation of bone tissue.[73,74] To assess the ability of HCA formation on the surfaces of nanocomposite hydrogels, samples were incubated in simulated body fluid (SBF). The 70-30-1 and 70-30-2 hydrogels were chosen for the evaluation of bioactivity since they showed less deformation as a function of applied force, and the effect of HCA formation as a function of MWCNT content could be assessed. Regardless of the MWCNT loading, spherical-shaped HCA particles were observed on the nanocomposite hydrogels following 7 days of incubation in SBF (**Fig. 4.8A**). The particles were enriched with Ca and P, the main components of HCA in bone, on their surfaces. In comparison, no enrichment of Ca and P was observed in the GelMA control 100-0-0 hydrogels, as depicted by the smooth surface and a high concentration of carbon as shown in the EDX spectra.

Quantitative EDX data showed a Ca/P ratio of 1.69 ± 0.09 for the 70-30-0 nanocomposite hydrogel after incubation in SBF for 7 days. The resulting Ca/P ratio was slightly higher than the stoichiometric Ca/P ratio of hydroxyapatite ($Ca_{10}(PO_4)_6(OH)_2$), a typical artificial bone,[75] which is between 1.67 and 1.50, which could be due to the carbonate ion substitution in the HCA structure.[23,76] The addition of 1 and 2 wt.% MWCNT did not interfere with the formation of HCA layer on the surfaces of the nanocomposite hydrogels. However, the Ca/P ratio decreased from 1.69 to 1.44 and 1.58 for the 70-30-1 and 70-30-2 biomaterials, respectively.

To confirm the formation of a mixed polycrystalline HCA layer on the surface of nanocomposite hydrogels after SBF incubation, XRD was used to assess crystallinity formation obtained from Ca and P depositions (**Fig. 4.8B**). In the nanocomposite hydrogels, diffraction peaks associated with the formation of HCA were observed at $2\theta = 27°$, $31.6°$, $45°$ and $56°$ which corresponded to diffraction planes (002), (211), (222) and (004) with reference to ICDD file #9-432.[77] However, 100-0-0 hydrogels did not display any diffraction peaks, indicating that no crystalline HCA was formed on their surface. From the FTIR spectra shown in **Fig. 4.8C**, nanocomposite hydrogels presented peaks at 601, 655, and 979 cm^{-1} corresponding to the deformation vibration of PO_4^{3-} ions; and bands at 1039, and 1051 cm^{-1} which were assigned to the stretching vibration of PO_4^{3-} ions.[78] Although some known peaks overlapped with the peaks of the material itself, distinguished bands at 906 and 1520 cm^{-1} pertaining to the CO_3^{2-} functional group were observed, indicating the substitution of CO_3^{2-} ions into the apatite confirming the formation of HCA on the surface of nanocomposite hydrogels.[78] Furthermore, a peak at 3203 cm^{-1} was observed due to the presence of surface hydroxyl groups. Collectively, the SEM/EDX, XRD, and FTIR data confirmed that the bioactive properties of nanocomposite hydrogels were not affected by the concentration of MWCNTs in the GelMA-BG biomaterials and was contributed by the presence of BG.

Previously, some studies that developed bone biomaterials comprised of an organic-inorganic system with an electrically conductive component, specifically CNTs, were mentioned. Their common main inorganic component was crystalline ceramic hydroxyapatite.[32-34,65] However, hydroxyapatite lacks reabsorption due to its high crystalline ceramic structure[79] which is not an ideal inorganic material to induce bone formation. BG, however, is reabsorbed and bonds to bone through the formation of an apatite layer on its surface after implantation into the damaged bone.[79] Although various polymers have been used to develop organic-inorganic bone biomaterials, opting for a polymer that mimics the natural bone's environment is crucial. Some studies have used synthetic or natural polymers, such as chitosan or gelatin,[33,64,65] for the development of an electrically conductive organic-inorganic bone biomaterial. However, since gelatin is the hydrolyzed form of type I collagen found in bone, the selection of this natural polymer would be ideal for creating an environment that mimics the main organic component of endogenous bone. Gelatin by itself melts at body temperature and cannot function as an ideal organic polymer to promote the healing of bone defects. Therefore, GelMA provides the main advantage of resisting higher temperatures, thus having a slower degradation rate compared to gelatin, as well as possessing higher mechanical strength. In addition, interactions

between cells and the extracellular matrix (ECM) is regulated by an arginine-glycine-aspartic acid (RGD) sequence present within the GelMA structure, functioning as an integrin recognition site which promotes cell adhesion.[80] Collectively, GelMA-BG nanocomposite hydrogels are ideal biomaterials that potentially mimic bone's natural biological environment while promoting the repair and regeneration of bone.
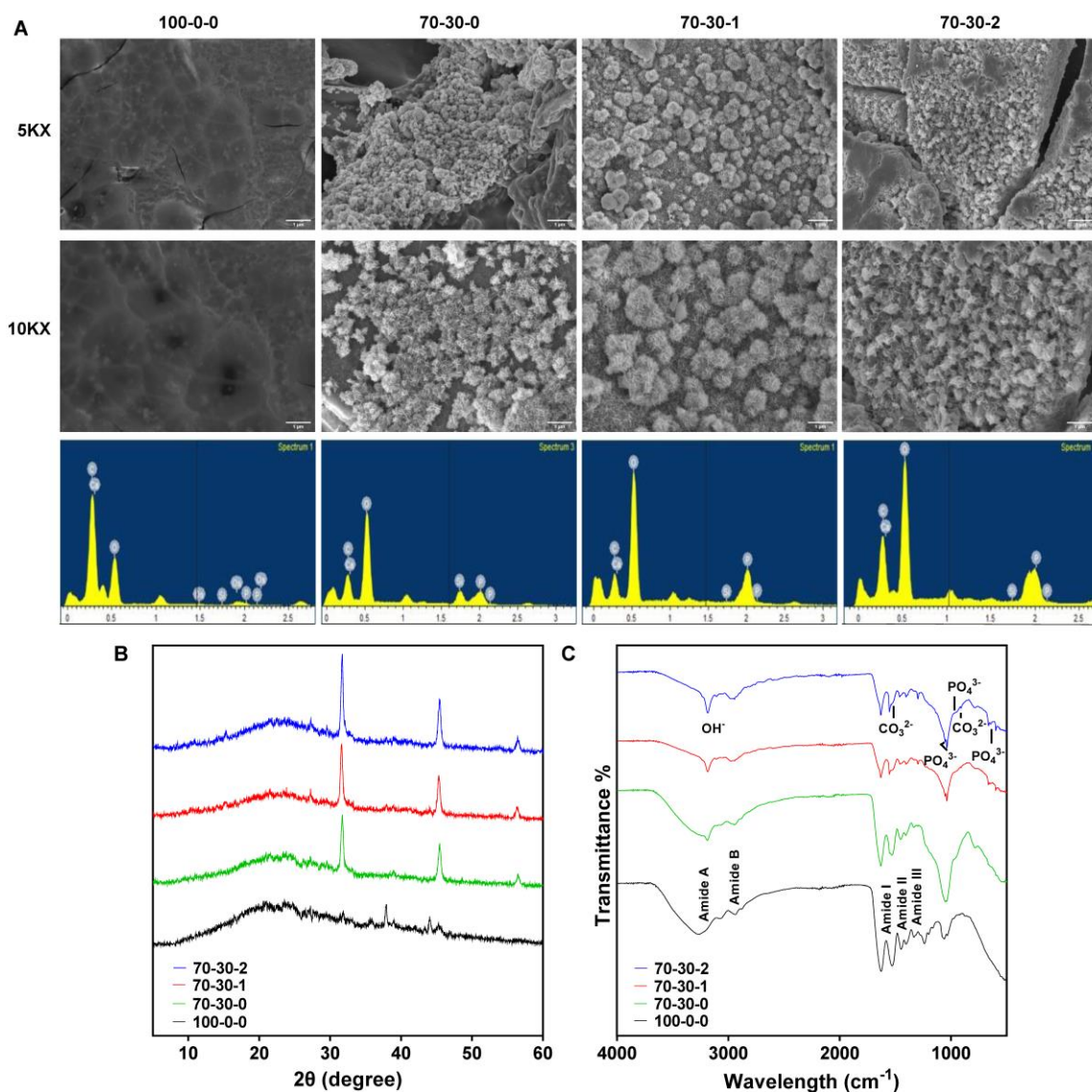
Figure 4.8. *In vitro* **bioactivity of 70-30 electrically conductive nanocomposite hydrogel biomaterials.** (**A**) SEM images and EDX elemental spectra of the surface of electrically conductive nanocomposite hydrogel biomaterials after incubation in SBF for 7 days. Scale bar = 1 μm. (**B**) XRD spectra and (**C**) FTIR spectra of electrically conductive nanocomposite hydrogel biomaterials after incubation in SBF for 7 days.

4.5.7. Mouse embryo multipotent mesenchymal progenitor 10T1/2 cell adhesion, spreading and viability on GelMA-BG-MWCNT nanocomposite hydrogels

Following the observation that the nanocomposite hydrogels possessed bioactive properties, cell interaction studies were conducted. **Fig. 4.9A** shows the fluorescent images of 10T1/2 cells cultured on the surface of 100-0-0 hydrogel and nanocomposite hydrogels for 24 and 72 h. Cells formed a uniform layer of actin filaments on the hydrogels, especially on nanocomposite hydrogels, with elongated morphology, suggesting favorable adhesion and spreading.[81]   **Fig. 4.9B** depicts the live/dead staining images of 10T1/2 cells cultured on the hydrogels for 24, 72, and 168 h. Of all the hydrogels tested, 70-30-1 hydrogel had the best viability after 24 h of culture, which was significantly higher to cells grown on a tissue culture plate (TCP) (p <0.01). This could be due to the hydrophobic nature of MWCNTs which can adsorb proteins owing to their highly delocalized π-bonds.[1] The protein adsorption property of MWCNTs promotes an initial cell attachment to the nanocomposite hydrogels, and, thus, an increase in cell growth. Similar studies have also shown this observation.[82,83] After three days of culture, the proliferation and viability of 10T1/2 cells on 100-0-0 and 70-30-2 hydrogels remained low but significantly increased for the 70-30- 0 hydrogels (p <0.01). In addition, cell proliferation on the 70-30-1 hydrogels continued to increase considerably (p <0.01) and cells remained viable after 72 h of culture (**Fig. 4.9C**). After 168 h of culture, 10T1/2 cells grew significantly on 100-0-0 hydrogels (p <0.01) compared to 24 and 72 h of culture, whereas cells grown on 70-30-0 and 70-30-1 hydrogels were maintained and did not present significant cell death (**Fig. 4.9D**). These results indicated that cells grown on pure GelMA hydrogels likely require more time to adapt to the substrate, while nanocomposite hydrogels required at least 72 h to adapt to the materials, after which cells were proliferating. Although hydrogels containing 2 wt.% MWCNT (70-30-2) possessed the lowest cell proliferation after 168 h of culture, there was no evidence of cytotoxic response due to the addition of MWCNT, thus speculating an increase of cell growth and viability as the cell culture time increases. The delayed cell proliferation observed in the 70-30-2 hydrogels was due to the initial low cell adhesion/retention at 24 h which affects the cell numbers after 168 h. Furthermore, cells struggle to adhere to higher concentrations of hydrophobic surfaces, such as MWCNTs, which was the reason why the cell attachment on the 2 wt.% MWCNT (70-30-2) hydrogels were not as favorable. In contrast, hydrogels containing 1 wt.% MWCNT (70-30-1) showed higher cell retention at 24 h, possessing a more favorable environment for cells to initially attach and

proliferate, thus resulting in an increased cell density after 168 h compared to the 70-30-2 hydrogels. Therefore, the 70-30-1 hydrogel could become a potential scaffold for bone tissue engineering.
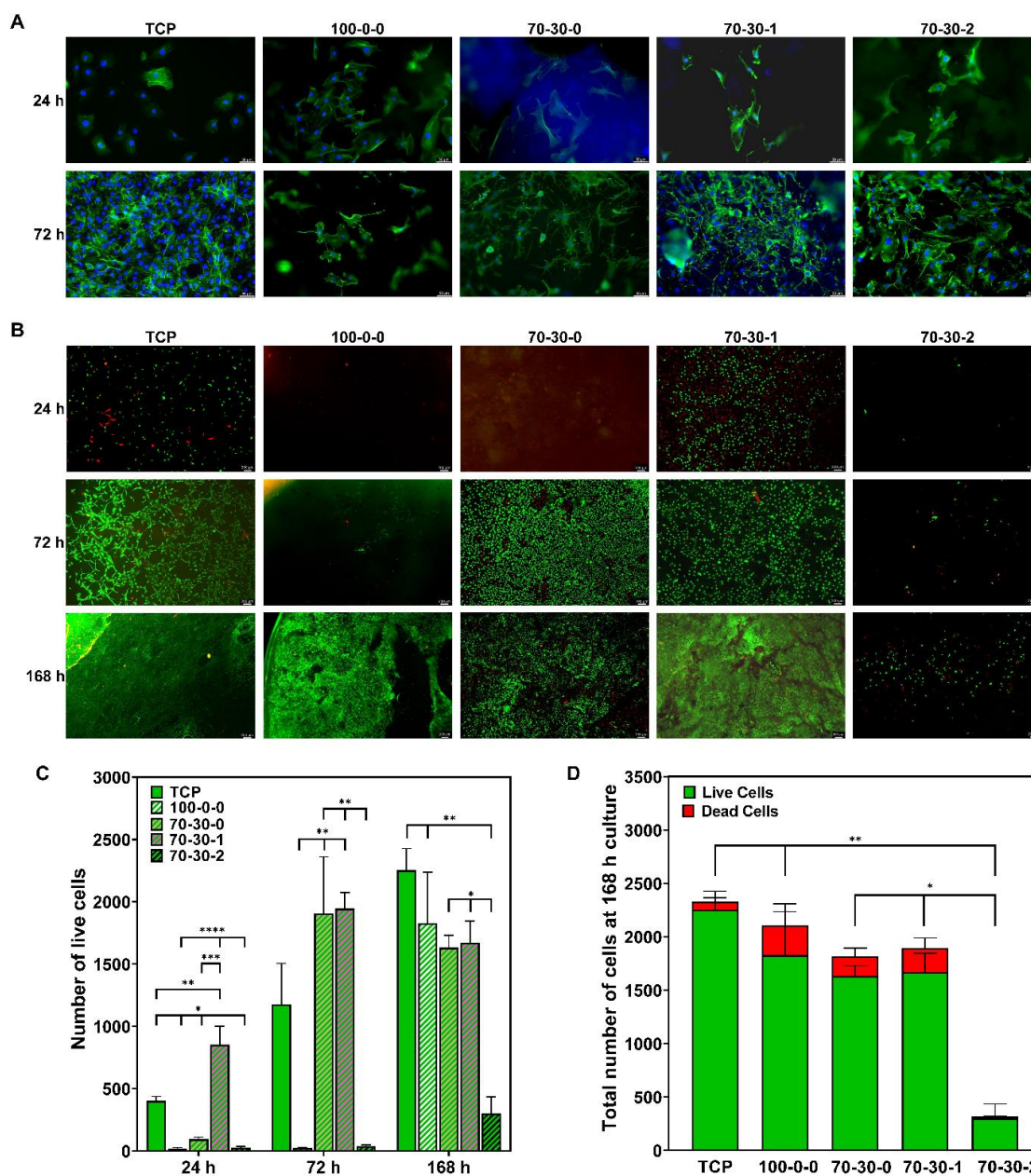
Figure 4.9. Attachment, spreading, and viability of 10T1/2 cells on GelMA-BG-MWCNT nanocomposite hydrogels. (**A**) Fluorescent images of 10T1/2 cells cultured on nanocomposite hydrogels after 24 and 72 h of culture. Scale bar = 50 μm. (**B**) Live/dead staining of 10T1/2 cells cultured on nanocomposite hydrogels after 24, 72, and 168 h. Scale bar = 200 μm. (**C**) Number of live cells at 24, 72 and 168 h of culture. (**D**) Total number of cells at 168 h of culture. *p <0.05, **p <0.01, ***p < 0.001, **** p <0.0001.

4.5.8. Osteogenic gene expression of mouse embryo multipotent mesenchymal progenitor 10T1/2 cells on GelMA-BG-MWCNT nanocomposite hydrogels

After establishing that 10T1/2 cells were able to attach and proliferate on nanocomposite hydrogels, their differentiation potential towards an osteogenic phenotype on GelMA-BG- MWCNT hydrogels was next investigated. **Fig. 4.10** shows the expression of three osteogenic genes in response to the differentiation induction on nanocomposite hydrogels. Osterix is a key transcription factor for bone differentiation and mineralization[81] and functions downstream of Runt-related transcription factor 2 (Runx2), a master regulator of osteoblast differentiation.[84] Studies have shown that endochondral and intramembranous bone formation does not occur in osterix-null mouse embryos.[85,86] After 7 days of culture, the osterix gene Sp7, was significantly upregulated in the nanocomposite hydrogels containing 1 wt.% MWCNT (70-30-1) compared to 100-0-0 (p <0.01) and 70-30-0 (p <0.05) hydrogels resulting in a 5.2-fold upregulation (**Fig. 4.10A**). However, no significant upregulation was observed between the 70-30-1 and 70-30-2 hydrogels (p >0.05). Another essential role osterix possesses is its attribution to induce the expression of different osteogenic genes, such as osteopontin and bone sialoprotein (BSP).[87,88]

Osteopontin, also known as secreted phosphoprotein-1 (Spp1), and bone sialoprotein (BSP) are two major members of the non-collagenous proteins in bone extracellular matrix that are secreted by osteoblasts and osteoclasts.[89,90] The distinguished feature of both osteopontin and BSP is the presence of an RGD motif that binds to integrins and allows bone cells to adhere to the mineralized matrix.[89] Although osteopontin has been shown to be an inhibitor of mineralization in a dose- dependent manner by binding to the HCA and inhibiting further growth,[91] its presence promotes intrafibrillar mineralization of collagen.[92] Furthermore, BSP promotes mineralization and is abundantly expressed at late stages of differentiation in mature osteoblasts.[93] The presence of both osteopontin and BSP is crucial for bone remodeling and mineralization. Significant upregulation of the expression of osteopontin gene Spp1 on cells differentiated on 70-30-1 nanocomposite hydrogels (p <0.01) was observed and resulted in a 2.2-fold upregulation compared to 100-0-0 control hydrogels (p <0.0001) (**Fig. 4.10B**). In addition, expression of BSP was significantly higher on 70- 30-0 and 70-30-1 hydrogels (p <0.05) with respect to pure GelMA (100-0-0) control hydrogels as shown in **Fig. 4.10C**. Collectively, these results show that the osteogenic gene expression levels are mostly increased in the nanocomposite hydrogels containing 1 wt.% MWCNT (70-30-1). This was mostly evident in the Sp7 and Spp1 genes. Sp7 is essential for osteoblast differentiation at early stages,[94] while the expression

of Spp1 increases concomitantly as osteogenic maturation progresses.[95] These results indicate that cells grown on nanocomposite hydrogels are at a pre-osteoblast stage. Expression of BSP is mostly present in mature osteoblasts, which is the reason its expression on the 70-30-1 hydrogels is not significantly upregulated. These results show that cells grown on GelMA-BG-MWCNT nanocomposite hydrogels have the ability to differentiate into an osteogenic lineage where the 70-30-1 hydrogel could become a plausible potential tissue-engineered bone that can be investigated for the promotion of *in vivo* bone healing and further explore the effects of bone repair and regeneration through the application of exogenous electro-mechanical stimulation.
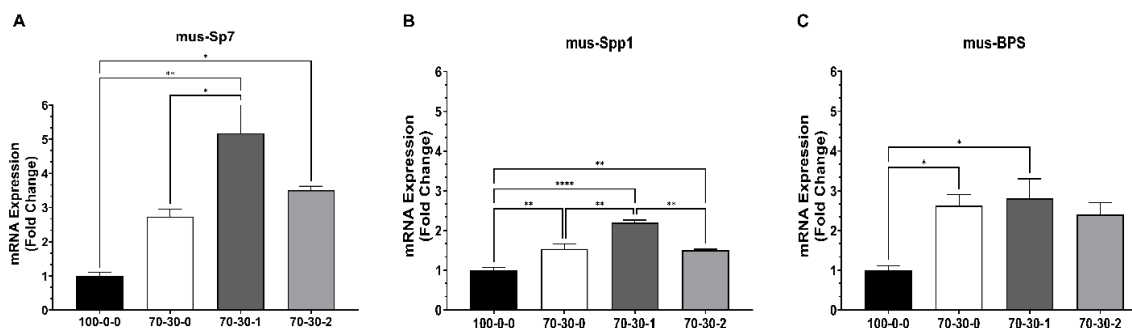
Figure 4.10. Osteogenic gene expression of 10T1/2 cells cultured on GelMA-BG-MWCNT nanocomposite hydrogels. (**A**) Sp7, (**B**) Spp1 and (**C**) BSP mRNA expressions of 10T1/2 cells cultured on nanocomposite hydrogels for 7 days. *p <0.05, **p <0.01, ***p <0.001, **** p <0.0001.

4.6. Conclusions

In this study, GelMA-BG-MWCNT biodegradable nanocomposite hydrogels were prepared in an attempt to mimic the organic-inorganic structural composition of bone with tunable electrical and electro- mechanical properties. The MWCNTs were uniformly distributed into the nanocomposite hydrogels using a reactive surfactant. Furthermore, the mechanical and electrically conductive effects of the organic-inorganic hydrogels as a function of MWCNT loading were assessed, which was related to the concentration of uniformly distributed MWCNTs added to the GelMA-BG biomaterials. To the best of my knowledge, this work is the first study investigating the electro-mechanical responses of nanocomposite hydrogels, which is an essential process that naturally occurs in the native bone during regeneration and healing. Furthermore, the bioactivity of nanocomposite hydrogels was demonstrated through the formation of hydroxycarbonate apatite on their surfaces after incubation in SBF for 7 days, which could become a promising bone biomaterial solution in *in vivo* applications. Cell

interaction studies were investigated, which showed good cytocompatibility properties allowing embryonic multipotent mesenchymal progenitor cells to attach, proliferate and further promote osteogenic differentiation upon induction onto the surfaces of the biomaterials for 7 days of culture. Based on the characterizations performed on various MWCNT-based hydrogels, this study shows that 70-30-1 nanocomposite hydrogel is the optimal composition to be evaluated for further studies. Electrically conductive GelMA-BG-MWCNT nanocomposite hydrogels could become a promising bone bioactive biomaterial to further investigate the repair and regeneration of bone defects through electro-mechanical stimulation.

4.7. References

[1]   R. Arambula-Maldonado, K. Mequanint, Carbon-based electrically conductive materials for bone repair and regeneration, Mater. Adv. (2022), https://doi.org/ 10.1039/D2MA00001F, 10.1039.D2MA00001F.

[2]   J.J. Chung, J. Yoo, B.S.T. Sum, S. Li, S. Lee, T.H. Kim, Z. Li, M.M. Stevens, T. K. Georgiou, Y. Jung, J.R. Jones, 3D printed porous methacrylate/silica hybrid scaffold for bone substitution, Adv. Healthc. Mater. 10 (2021) 2100117, https:// doi.org/10.1002/adhm.202100117.

[3]   E. Fukada, I. Yasuda, On the piezoelectric effect of bone, J. Phys. Soc. Jpn. 12 (1957) 1158–1162, https://doi.org/10.1143/JPSJ.12.1158 .

[4]   The classic: fundamental aspects of fracture treatment by Iwao Yasuda, reprinted from J. Kyoto Med. Soc., 4:395–406, 1953, Clin. Orthop. Relat. Res. (1977) 5–8.

[5]   I.S. Aleem, I. Aleem, N. Evaniew, J.W. Busse, M. Yaszemski, A. Agarwal, T. Einhorn, M. Bhandari, Efficacy of electrical stimulators for bone healing: a meta- analysis of randomized sham-controlled trials, Sci. Rep. 6 (2016) 31724, https:// doi.org/10.1038/srep31724.

[6]   H.-S. Sohn, J.-K. Oh, Review of bone graft and bone substitutes with an emphasis on fracture surgeries, Biomater. Res. 23 (2019) 9, https://doi.org/10.1186/ s40824-019-0157-y.

[7]   J. Chen, M. Yu, B. Guo, P.X. Ma, Z. Yin, Conductive nanofibrous composite scaffolds based on in-situ formed polyaniline nanoparticle and polylactide for bone regeneration, J. Colloid Interface Sci. 514 (2018) 517–527, https://doi.org/ 10.1016/j.jcis.2017.12.062.

[8]   I.A. Paun, A.M. Acasandrei, C.R. Luculescu, C.C. Mustaciosu, V. Ion, M. Mihailescu, E. Vasile, M. Dinescu, MAPLE deposition of polypyrrole-based composite layers for bone regeneration, Appl. Surf. Sci. 357 (2015) 975–984, https://doi.org/10.1016/ j.apsusc.2015.09.083.

[9]   A.G. Guex, J.L. Puetzer, A. Armgarth, E. Littmann, E. Stavrinidou, E.P. Giannelis, G. G. Malliaras, M.M. Stevens, Highly porous scaffolds of PEDOT:PSS for bone tissue engineering, Acta Biomater. 62 (2017) 91–101, https://doi.org/10.1016/j. actbio.2017.08.045.

[10]   M. Rahaman, A. Aldalbahi, M. Almoiqli, S. Alzahly, Chemical and electrochemical synthesis of polypyrrole using carrageenan as a dopant: polypyrrole/multi-walled carbon nanotube nanocomposites, Polymers. 10 (2018) 632, https://doi.org/ 10.3390/polym10060632.

[11]   J. Xu, Y. He, Y. Sun, X. Zhang, Y. Yi, W. Shi, D. Ge, Micropatterned polypyrrole/ hydroxyapatite composite coatings promoting osteoinductive activity by electrical stimulation, Coatings. 12 (2022) 849, https://doi.org/10.3390/coatings12060849.

[12]   V. Sethumadhavan, K. Zuber, C. Bassell, P.R. Teasdale, D. Evans, Hydrolysis of doped conducting polymers, Commun. Chem. 3 (2020) 153, https://doi.org/ 10.1038/s42004-020-00404-y.

[13]   T.-H. Le, Y. Kim, H. Yoon, Electrical and electrochemical properties of conducting polymers, Polymers. 9 (2017) 150, https://doi.org/10.3390/polym9040150.

[14]   N. Zanjanizadeh Ezazi, M.-A. Shahbazi, Y.V. Shatalin, E. Nadal, E. M¨akil¨a, J. Salonen, M. Kemell, A. Correia, J. Hirvonen, H.A. Santos, Conductive vancomycin-loaded mesoporous silica polypyrrole-based scaffolds for bone regeneration, Int. J. Pharm. 536 (2018) 241–250, https://doi.org/10.1016/j. ijpharm.2017.11.065.

[15]   B. Guo, P.X. Ma, Conducting polymers for tissue engineering, Biomacromolecules. 19 (2018) 1764–1782, https://doi.org/10.1021/acs.biomac.8b00276.

[16]   E.P. e Silva, B. Huang, J.V. Helaehil, P.R.L. Nalesso, L. Bagne, M.A. de Oliveira, G. C.C. Albiazetti, A. Aldalbahi, M. El-Newehy, M. Santamaria-Jr, F.A.S. Mendonça, P. B´artolo, G.F. Caetano, In vivo study of conductive 3D printed PCL/MWCNTs scaffolds with electrical stimulation for bone tissue engineering, Bio-Des. Manuf. 4 (2021) 190–202, https://doi.org/10.1007/s42242-020-00116-1.

[17]   X. Xie, K. Hu, D. Fang, L. Shang, S.D. Tran, M. Cerruti, Graphene and hydroxyapatite self-assemble into homogeneous, free standing nanocomposite hydrogels for bone tissue engineering, Nanoscale. 7 (2015) 7992–8002, https:// doi.org/10.1039/C5NR01107H.

[18]   Y. Li, J. He, J. Zhou, Z. Li, L. Liu, S. Hu, B. Guo, W. Wang, A conductive photothermal non-swelling nanocomposite hydrogel patch accelerating bone defect repair, Biomater. Sci. 10 (2022) 1326–1341, https://doi.org/10.1039/ D1BM01937F.

[19]   F. Vargas–Lara, A.M. Hassan, E.J. Garboczi, J.F. Douglas, Intrinsic conductivity of carbon nanotubes and graphene sheets having a realistic geometry, J. Chem. Phys. 143 (2015), 204902, https://doi.org/10.1063/1.4935970.

[20]   Y. Wang, G.J. Weng, Electrical conductivity of carbon nanotube- and graphene- based nanocomposites, in: S.A. Meguid, G.J. Weng (Eds.), Micromechanics and Nanomechanics of Composite Solids, Springer International Publishing, Cham, 2018, pp. 123–156, https://doi.org/10.1007/978-3-319-52794-9_4.

[21]   H. Lee, S. Jeong, S. Park, W. Chung, Enhanced mechanical and heating performance of multi-walled carbon nanotube-cement composites fabricated using different mixing methods, Compos. Struct. 225 (2019), 111072, https://doi.org/ 10.1016/j.compstruct.2019.111072.

[22]   N. Aslankoohi, K. Mequanint, Intrinsically fluorescent bioactive glass-poly(ester amide) hybrid microparticles for dual drug delivery and bone repair, Mater. Sci. Eng. C 128 (2021), 112288, https://doi.org/10.1016/j.msec.2021.112288.

[23]   N. Aslankoohi, K. Mequanint, Poly(ester amide)–bioactive glass hybrid biomaterials for bone regeneration and biomolecule delivery, ACS Appl. Bio Mater. 3 (2020) 3621–3630, https://doi.org/10.1021/acsabm.0c00257.

[24]   D. Mondal, S. Lin, A.S. Rizkalla, K. Mequanint, Porous and biodegradable polycaprolactone-borophosphosilicate hybrid scaffolds for osteoblast infiltration and stem cell differentiation, J. Mech. Behav. Biomed. Mater. 92 (2019) 162–171, https://doi.org/10.1016/j.jmbbm.2019.01.011.

[25]   B.A. Allo, S. Lin, K. Mequanint, A.S. Rizkalla, Role of bioactive 3D hybrid fibrous scaffolds on mechanical behavior and spatiotemporal osteoblast gene expression, ACS Appl. Mater. Interfaces 5 (2013) 7574–7583, https://doi.org/10.1021/ am401861w.

[26]   A. Svarca, A. Grava, A. Dubnika, A. Ramata-Stunda, R. Narnickis, K. Aunina, E. Rieksta, M. Boroduskis, I. Jurgelane, J. Locs, D. Loca, Calcium phosphate/ hyaluronic acid composite hydrogels for local antiosteoporotic drug delivery, Front. Bioeng. Biotechnol. 10 (2022), 917765, https://doi.org/10.3389/ fbioe.2022.917765.

[27]   F. Tallia, H.-K. Ting, S.J. Page, J.P. Clark, S. Li, T. Sang, L. Russo, M.M. Stevens, J. V. Hanna, J.R. Jones, Bioactive, degradable and tough hybrids through calcium and phosphate incorporation, Front. Mater. 9 (2022), 901196, https://doi.org/ 10.3389/fmats.2022.901196.

[28]   P. Song, M. Li, B. Zhang, X. Gui, Y. Han, L. Wang, W. Zhou, L. Guo, Z. Zhang, Z. Li, C. Zhou, Y. Fan, X. Zhang, DLP fabricating of precision GelMA/HAp porous composite scaffold for bone tissue engineering application, Compos. Part B Eng. 244 (2022), 110163, https://doi.org/10.1016/j.compositesb.2022.110163.

[29]   H. Belaid, S. Nagarajan, C. Teyssier, C. Barou, J. Bar´es, S. Balme, H. Garay, V. Huon, D. Cornu, V. Cavaill`es, M. Bechelany, Development of new biocompatible 3D printed graphene oxide-based scaffolds, Mater. Sci. Eng. C 110 (2020), 110595, https://doi.org/10.1016/j.msec.2019.110595.

[30]   K. Dixit, N. Sinha, Additive manufacturing of carbon nanotube reinforced bioactive glass scaffolds for bone tissue engineering, J. Eng. Sci. Med. Diagn. Ther. 4 (2021), 041004, https://doi.org/10.1115/1.4051801.

[31]   S. Constanda, M.S. Stan, C.S. Ciobanu, M. Motelica-Heino, R. Gu´egan, K. Lafdi, A. Dinischiotu, D. Predoi, Carbon nanotubes-hydroxyapatite nanocomposites for an improved osteoblast cell response, J. Nanomater. 2016 (2016) 1–10, https://doi. org/10.1155/2016/3941501.

[32]   A.G. Sanchez, E. Prokhorov, G. Luna-Barcenas, J. Hern´andez-Vargas, R. Rom´an- Doval, S. Mendoza, H. Rojas-Ch´avez, Chitosan-hydroxyapatite-MWCNTs nanocomposite patch for bone

tissue engineering applications, Mater. Today Commun. 28 (2021), 102615, https://doi.org/10.1016/j.mtcomm.2021.102615.

[33]   M. Aslani, M. Meskinfam, H. Reza Aghabozorg, In situ biomimetic synthesis of gelatin-carbon nanotube-hydroxyapatite biocomposites as bone filler, Orient. J. Chem. 33 (2017) 235–241, https://doi.org/10.13005/ojc/330127.

[34]   J. Venkatesan, Z.-J. Qian, B. Ryu, N. Ashok Kumar, S.-K. Kim, Preparation and characterization of carbon nanotube-grafted-chitosan – natural hydroxyapatite composite for bone tissue engineering, Carbohydr. Polym. 83 (2011) 569–577, https://doi.org/10.1016/j.carbpol.2010.08.019.

[35]   B.A. Allo, A.S. Rizkalla, K. Mequanint, Synthesis and electrospinning of ε-polycaprolactone-bioactive glass hybrid biomaterials via a sol gel process, Langmuir. 26 (2010) 18340–18348, https://doi.org/10.1021/la102845k.

[36]   A. Ovsianikov, A. Deiwick, S. Van Vlierberghe, P. Dubruel, L. M¨oller, G. Dr¨ager, B. Chichkov, Laser fabrication of three-dimensional CAD scaffolds from photosensitive gelatin for applications in tissue engineering, Biomacromolecules. 12 (2011) 851–858, https://doi.org/10.1021/bm1015305.

[37]   M. Costantini, S. Testa, E. Fornetti, A. Barbetta, M. Trombetta, S.M. Cannata, C. Gargioli, A. Rainer, Engineering muscle networks in 3D gelatin methacryloyl hydrogels: influence of mechanical stiffness and geometrical confinement, Front. Bioeng. Biotechnol. 5 (2017), https://doi.org/10.3389/fbioe.2017.00022.

[38]   D. Loessner, C. Meinert, E. Kaemmerer, L.C. Martine, K. Yue, P.A. Levett, T.J. Klein, F.P.W. Melchels, A. Khademhosseini, D.W. Hutmacher, Functionalization, preparation and use of cell-laden gelatin methacryloyl–based hydrogels as modular tissue culture platforms, Nat. Protoc. 11 (2016) 727–746, https://doi.org/ 10.1038/nprot.2016.037.

[39]   M. Zhu, Y. Wang, G. Ferracci, J. Zheng, N.-J. Cho, B.H. Lee, Gelatin methacryloyl and its hydrogels with an exceptional degree of controllability and batch-to-batch consistency, Sci. Rep. 9 (2019) 6863, https://doi.org/10.1038/s41598-019-42186-x.

[40]   H. Shirahama, B.H. Lee, L.P. Tan, N.-J. Cho, Precise tuning of facile one-pot gelatin methacryloyl (GelMA) synthesis, Sci. Rep. 6 (2016) 31036, https://doi.org/ 10.1038/srep31036.

[41]   J. Lao, X. Dieudonn´e, M. Benbakkar, ´E. Jallot, Bioactive glass coating on gelatin scaffolds at ambient temperature: easy route to make polymer scaffolds become bioactive, J. Mater. Sci. 52 (2017) 9129–9139, https://doi.org/10.1007/s10853- 017-0781-7.

[42]   X.-R. Yang, Y.-Q. Zhao, Y.-T. Qiu, C.-F. Chi, B. Wang, Preparation and characterization of gelatin and antioxidant peptides from gelatin hydrolysate of skipjack tuna (Katsuwonus pelamis) bone stimulated by in vitro gastrointestinal digestion, Mar. Drugs 17 (2019) 78, https://doi.org/10.3390/md17020078.

[43]   M. Jackson, L.-P. Choo, P.H. Watson, W.C. Halliday, H.H. Mantsch, Beware of connective tissue proteins: assignment and implications of collagen absorptions in infrared spectra of human

tissues, Biochim. Biophys. Acta (BBA) - Mol. Basis Dis. 1270 (1995) 1–6, https://doi.org/10.1016/0925-4439(94)00056-V.

[44]   K. Sisson, C. Zhang, M.C. Farach-Carson, D.B. Chase, J.F. Rabolt, Evaluation of cross-linking methods for electrospun gelatin on cell growth and viability, Biomacromolecules. 10 (2009) 1675–1680, https://doi.org/10.1021/bm900036s.

[45]   B. Lei, K.-H. Shin, D.-Y. Noh, I.-H. Jo, Y.-H. Koh, W.-Y. Choi, H.-E. Kim, Nanofibrous gelatin–silica hybrid scaffolds mimicking the native extracellular matrix (ECM) using thermally induced phase separation, J. Mater. Chem. 22 (2012) 14133, https://doi.org/10.1039/c2jm31290e.

[46]   J. Serra, P. Gonz´alez, S. Liste, C. Serra, S. Chiussi, B. Le´on, M. P´erez-Amor, H. O. Yl¨anen, M. Hupa, FTIR and XPS studies of bioactive silica based glasses, J. Non- Cryst. Solids 332 (2003) 20–27, https://doi.org/10.1016/j. jnoncrysol.2003.09.013.

[47]   L. Rebers, T. Granse, G. Tovar, A. Southan, K. Borchers, Physical interactions strengthen chemical gelatin methacryloyl gels, Gels. 5 (2019) 4, https://doi.org/ 10.3390/gels5010004.

[48]   M. Djabourov, J. Leblond, P. Papon, Gelation of aqueous gelatin solutions. I. Structural investigation, J. Phys. France 49 (1988) 319–332, https://doi.org/ 10.1051/jphys:01988004902031900.

[49]   B.V. Slaughter, S.S. Khurshid, O.Z. Fisher, A. Khademhosseini, N.A. Peppas, Hydrogels in regenerative medicine, Adv. Mater. 21 (2009) 3307–3329, https:// doi.org/10.1002/adma.200802106.

[50]   Q. Xing, K. Yates, C. Vogt, Z. Qian, M.C. Frost, F. Zhao, Increasing mechanical strength of gelatin hydrogels by divalent metal Ion removal, Sci. Rep. 4 (2015) 4706, https://doi.org/10.1038/srep04706.

[51]   J. Zheng, F. Zhao, W. Zhang, Y. Mo, L. Zeng, X. Li, X. Chen, Sequentially- crosslinked biomimetic bioactive glass/gelatin methacryloyl composites hydrogels for bone regeneration, Mater. Sci. Eng. C 89 (2018) 119–127, https://doi.org/ 10.1016/j.msec.2018.03.029.

[52]   O. Chaparro, I. Linero, Regenerative medicine: a new paradigm in bone regeneration, in: A.R. Zorzi, J.B. de Miranda (Eds.), Advanced Techniques in Bone Regeneration, InTech, 2016, https://doi.org/10.5772/62523.

[53]   T. Wang, X. Yang, X. Qi, C. Jiang, Osteoinduction and proliferation of bone-marrow stromal cells in three-dimensional poly (ε-caprolactone)/ hydroxyapatite/collagen scaffolds, J. Transl. Med. 13 (2015) 152, https://doi.org/10.1186/s12967-015- 0499-8.

[54]   M. Tavafoghi, M. Cerruti, The role of amino acids in hydroxyapatite mineralization, J. R. Soc. Interface 13 (2016) 20160462, https://doi.org/10.1098/ rsif.2016.0462.

[55]   C. Liu, J. Zhang, J. He, G. Hu, Gelation in carbon nanotube/polymer composites, Polymer. 44 (2003) 7529–7532, https://doi.org/10.1016/j.polymer.2003.09.013.

[56]   C. Zamora-Ledezma, L. Buisson, S.E. Moulton, G. Wallace, C. Zakri, C. Blanc, E. Anglaret, P. Poulin, Carbon nanotubes induced gelation of unmodified hyaluronic acid, Langmuir. 29 (2013) 10247–10253, https://doi.org/10.1021/ la4016492.

[57]   Z. Yao, D. Wu, C. Chen, M. Zhang, Creep behavior of polyurethane nanocomposites with carbon nanotubes, Compos. A: Appl. Sci. Manuf. 50 (2013) 65–72, https:// doi.org/10.1016/j.compositesa.2013.03.015.

[58]   H. Cindrič, B. Kos, G. Tedesco, M. Cadossi, A. Gasbarrini, D. Miklavčič, Electrochemotherapy of spinal metastases using transpedicular approach—a numerical feasibility study, Technol. Cancer Res. Treat. 17 (2018), https://doi.org/ 10.1177/1533034618770253, 153303461877025.

[59]   S.R. Gavinho, M.P.F. Graça, P.R. Prezas, J.S. Kumar, B.M.G. Melo, A.J.M. Sales, A. F. Almeida, M.A. Valente, Structural, thermal, morphological and dielectric investigations on 45S5 glass and glass-ceramics, J. Non-Cryst. Solids 562 (2021), 120780, https://doi.org/10.1016/j.jnoncrysol.2021.120780.

[60]   O.P. Filho, G.P. La Torre, L.L. Hench, Effect of crystallization on apatite-layer formation of bioactive glass 45S5, J. Biomed. Mater. Res. 30 (1996) 509–514, https://doi.org/10.1002/(SICI)1097-4636(199604)30:4<509::AID-JBM9>3.0.CO; 2-T.

[61]   J.R. Jones, Review of bioactive glass: from Hench to hybrids, Acta Biomater. 9 (2013) 4457–4486, https://doi.org/10.1016/j.actbio.2012.08.023.

[62]   D. Bellucci, V. Cannillo, A. Anesi, R. Salvatori, L. Chiarini, T. Manfredini, D. Zaffe, Bone regeneration by novel bioactive glasses containing strontium and/or magnesium: a preliminary in-vivo study, Materials. 11 (2018) 2223, https://doi. org/10.3390/ma11112223.

[63]   H. Li, Y. Zare, K.Y. Rhee, The percolation threshold for tensile strength of polymer/ CNT nanocomposites assuming filler network and interphase regions, Mater. Chem. Phys. 207 (2018) 76–83, https://doi.org/10.1016/j.matchemphys.2017.12.053.

[64]   N.K. de Moura, E.F. Martins, R.L.M.S. Oliveira, I.A.W. de Brito Siqueira, J.P. B. Machado, E. Esposito, S.S. Amaral, L.M.R. de Vasconcellos, F.R. Passador, E. de Sousa Trichˆes, Synergistic effect of adding bioglass and carbon nanotubes on poly (lactic acid) porous membranes for guided bone regeneration, Mater. Sci. Eng. C. 117 (2020), 111327, https://doi.org/10.1016/j.msec.2020.111327.

[65]   S. Shokri, B. Movahedi, M. Rafieinia, H. Salehi, A new approach to fabrication of Cs/BG/CNT nanocomposite scaffold towards bone tissue engineering and evaluation of its properties, Appl. Surf. Sci. 357 (2015) 1758–1764, https://doi. org/10.1016/j.apsusc.2015.10.048.

[66]   R.L. Duncan, C.H. Turner, Mechanotransduction and the functional response of bone to mechanical strain, Calcif. Tissue Int. 57 (1995) 344–358, https://doi.org/ 10.1007/BF00302070.

[67]   R.B. Heppenstall, Constant direct-current treatment for established nonunion of the tibia, Clin. Orthop. Relat. Res. (1983) 179–184, https://doi.org/10.1097/ 00003086-198309000-00020. NA.

[68]   F. Benazzo, M. Mosconi, G. Beccarisi, U. Galli, Use of capacitive coupled electric fields in stress fractures in athletes, Clin. Orthop. Relat. Res. (1995) 145–149, https://doi.org/10.1097/00003086-199501000-00023. NA.

[69]   S. Fornell, J. Ribera, M. Mella, A. Carranza, D. Serrano-Toledano, G. Domecq, Effects of electrical stimulation in the treatment of osteonecrosis of the femoral head, Hip Int. 28 (2018) 434–441, https://doi.org/10.5301/hipint.5000581.

[70]   P. Augat, M. Hollensteiner, C. Von Rüden, The role of mechanical stimulation in the enhancement of bone healing, Injury. 52 (2021) S78–S83, https://doi.org/10.1016/j.injury.2020.10.009.

[71]   C. Schwarz, D. Wulsten, A. Ellinghaus, J. Lienau, B.M. Willie, G.N. Duda, Mechanical load modulates the stimulatory effect of BMP2 in a rat nonunion model, Tissue Eng. Part A 19 (2013) 247–254, https://doi.org/10.1089/ten. tea.2012.0265.

[72]   E. Wehrle, G.R. Paul, D.C. Tourolle N´e Betts, G.A. Kuhn, R. Müller, Individualized cyclic mechanical loading improves callus properties during the remodelling phase of fracture healing in mice as assessed from time-lapsed in vivo imaging, Sci. Rep. 11 (2021) 23037, https://doi.org/10.1038/s41598-021-02368-y.

[73]   L.L. Hench, N. Roki, M.B. Fenn, Bioactive glasses: importance of structure and properties in bone regeneration, J. Mol. Struct. 1073 (2014) 24–30, https://doi.org/10.1016/j.molstruc.2014.03.066.

[74]   F. Baino, S. Yamaguchi, The use of simulated body fluid (SBF) for assessing materials bioactivity in the context of tissue engineering: review and challenges, Biomimetics. 5 (2020) 57, https://doi.org/10.3390/biomimetics5040057.

[75]   K. Deguchi, S. Nomura, A. Tsuchiya, I. Takahashi, K. Ishikawa, Effects of the carbonate content in carbonate apatite on bone replacement, J. Tissue Eng. Regen. Med. 16 (2022) 200–206, https://doi.org/10.1002/term.3270.

[76]   E. Landi, G. Celotti, G. Logroscino, A. Tampieri, Carbonated hydroxyapatite as bone substitute, J. Eur. Ceram. Soc. 23 (2003) 2931–2937, https://doi.org/ 10.1016/S0955-2219(03)00304-2.

[77]   B.A. Allo, A.S. Rizkalla, K. Mequanint, Hydroxyapatite formation on sol–gel derived poly(ε-caprolactone)/bioactive glass hybrid biomaterials, ACS Appl. Mater. Interfaces 4 (2012) 3148–3156, https://doi.org/10.1021/am300487c.

[78]   R. Murugan, S. Ramakrishna, K. Panduranga Rao, Nanoporous hydroxy-carbonate apatite scaffold made of natural bone, Mater. Lett. 60 (2006) 2844–2847, https://doi.org/10.1016/j.matlet.2006.01.104.

[79]   H. Oonishi, L.L. Hench, J. Wilson, F. Sugihara, E. Tsuji, M. Matsuura, S. Kin, T. Yamamoto, S. Mizokawa, Quantitative Comparison of Bone Growth Behavior in Granules of Bioglass®, A-W Glass-ceramic, and Hydroxyapatite, (n.d.) 10.

[80]   M. Kirsch, L. Birnstein, I. Pepelanova, W. Handke, J. Rach, A. Seltsam, T. Scheper, A. Lavrentieva, Gelatin-methacryloyl (GelMA) formulated with human platelet lysate supports mesenchymal stem cell proliferation and differentiation and enhances the hydrogel's mechanical properties, Bioengineering. 6 (2019) 76, https://doi.org/10.3390/bioengineering6030076.

[81]   N. Aslankoohi, S. Lin, K. Mequanint, Bioactive fluorescent hybrid microparticles as a stand-alone osteogenic differentiation inducer, Mater. Today Bio 13 (2022), 100187, https://doi.org/10.1016/j.mtbio.2021.100187.

[82]   L. Van Den Broeck, S. Piluso, A.H. Soultan, M. De Volder, J. Patterson, Cytocompatible carbon nanotube reinforced polyethylene glycol composite hydrogels for tissue engineering, Mater. Sci. Eng. C 98 (2019) 1133–1144, https:// doi.org/10.1016/j.msec.2019.01.020.

[83]   M. Imaninezhad, J. Schober, D. Griggs, P. Ruminski, I. Kuljanishvili, S.P. Zustiak, Cell attachment and spreading on carbon nanotubes is facilitated by integrin binding, Front. Bioeng. Biotechnol. 6 (2018) 129, https://doi.org/10.3389/ fbioe.2018.00129.

[84]   T. Komori, Runx2, an inducer of osteoblast and chondrocyte differentiation, Histochem. Cell Biol. 149 (2018) 313–323, https://doi.org/10.1007/s00418-018- 1640-6.

[85]   H. Fu, B. Doll, T. McNelis, J.O. Hollinger, Osteoblast differentiation in vitro and in vivo promoted by Osterix, J. Biomed. Mater. Res. 83A (2007) 770–778, https:// doi.org/10.1002/jbm.a.31356.

[86]   K. Nakashima, X. Zhou, G. Kunkel, Z. Zhang, J.M. Deng, R.R. Behringer, B. De Crombrugghe, The novel zinc finger-containing transcription factor osterix is required for osteoblast differentiation and bone formation, Cell. 108 (2002) 17–29, https://doi.org/10.1016/S0092-8674(01)00622-5.

[87]   Y. Yang, Y. Huang, L. Zhang, C. Zhang, Transcriptional regulation of bone sialoprotein gene expression by Osx, Biochem. Biophys. Res. Commun. 476 (2016) 574–579, https://doi.org/10.1016/j.bbrc.2016.05.164.

[88]   L. Wu, Y. Wu, Y. Lin, W. Jing, X. Nie, J. Qiao, L. Liu, W. Tang, W. Tian, Osteogenic differentiation of adipose derived stem cells promoted by overexpression of osterix, Mol. Cell. Biochem. 301 (2007) 83–92, https://doi.org/10.1007/s11010-006- 9399-9.

[89]   M. Morinobu, M. Ishijima, S.R. Rittling, K. Tsuji, H. Yamamoto, A. Nifuji, D. T. Denhardt, M. Noda, Osteopontin expression in osteoblasts and osteocytes during bone formation under mechanical stress in the calvarial suture in vivo, J. Bone Miner. Res. 18 (2003) 1706–1715, https://doi.org/10.1359/jbmr.2003.18.9.1706.

[90]   A. Bellahc`ene, K. Bonjean, B. Fohr, N.S. Fedarko, F.A. Robey, M.F. Young, L. W. Fisher, V. Castronovo, Bone sialoprotein mediates human endothelial cell attachment and migration and promotes angiogenesis, Circ. Res. 86 (2000) 885–891, https://doi.org/10.1161/01.RES.86.8.885.

[91]   G.K. Hunter, Role of osteopontin in modulation of hydroxyapatite formation, Calcif. Tissue Int. 93 (2013) 348–354, https://doi.org/10.1007/s00223-013-9698- 6.

[92]   D.E. Rodriguez, T. Thula-Mata, E.J. Toro, Y.-W. Yeh, C. Holt, L.S. Holliday, L. B. Gower, Multifunctional role of osteopontin in directing intrafibrillar mineralization of collagen and activation of osteoclasts, Acta Biomater. 10 (2014) 494–507, https://doi.org/10.1016/j.actbio.2013.10.010.

[93]   J.A.R. Gordon, C.E. Tye, A.V. Sampaio, T.M. Underhill, G.K. Hunter, H. A. Goldberg, Bone sialoprotein expression enhances osteoblast differentiation and matrix mineralization in vitro, Bone. 41 (2007) 462–473, https://doi.org/ 10.1016/j.bone.2007.04.191.

[94]   C.A. Yoshida, H. Komori, Z. Maruyama, T. Miyazaki, K. Kawasaki, T. Furuichi, R. Fukuyama, M. Mori, K. Yamana, K. Nakamura, W. Liu, S. Toyosawa, T. Moriishi, H. Kawaguchi, K. Takada, T. Komori, SP7 inhibits osteoblast differentiation at a late stage in mice, PLoS One 7 (2012), e32364, https://doi.org/10.1371/journal. pone.0032364.

[95]   L. Malaval, D. Modrowski, A.K. Gupta, J.E. Aubin, Cellular expression of bone- related proteins during in vitro osteogenesis in rat bone marrow stromal cell cultures, J. Cell. Physiol. 158 (1994) 555–572, https://doi.org/10.1002/ jcp.1041580322.

Chapter 5

5. Osteogenic Differentiation Potential of GelMA-BG-MWCNT Nanocomposite Hydrogels*[5]

Overview: This study describes the effects of GelMA-BG-MWCNT nanocomposite hydrogels as a bone biomaterial that promotes osteogenic differentiation. Mesenchymal stem cells derived from human-induced pluripotent stem cells (iMSCs) were cultured on nanocomposite hydrogels and cell interaction studies were evaluated, followed by the osteogenic differentiation ability of cells cultured on nanocomposite hydrogels by investigating their gene and protein expressions as well as the formation of mineralization.
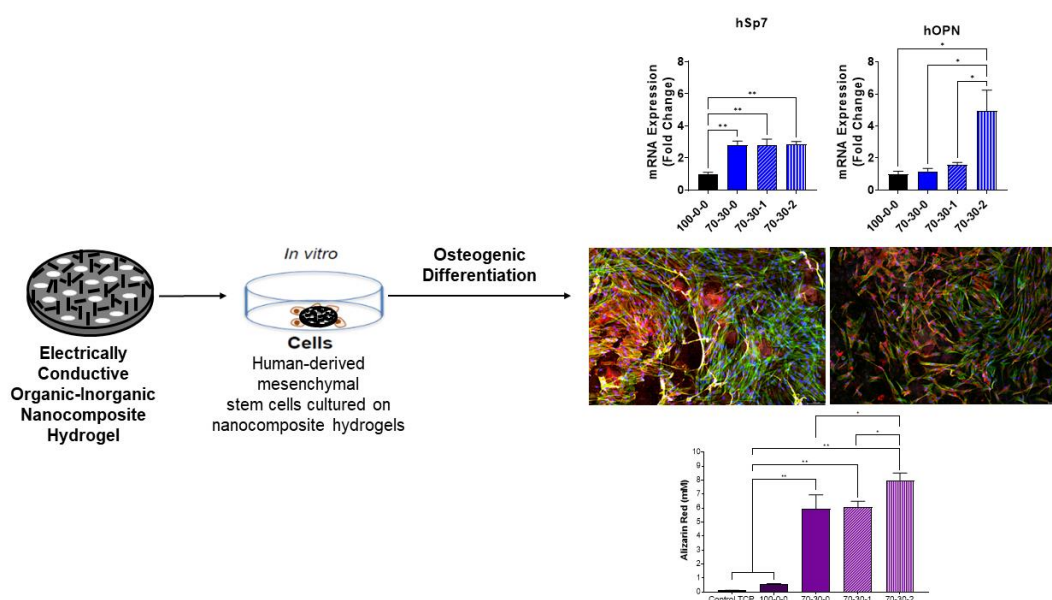
Scheme 5.1. Graphical abstract for Chapter 5.

5.1. Abstract

The ability of bone biomaterials to promote osteogenic differentiation is crucial for the repair and regeneration of osseous tissue. The development of a temporary bone substitute is of major importance in which the growth and differentiation of human-derived stem cells into an osteogenic lineage is enhanced. In this study, nanocomposite hydrogels composed of gelatin methacryloyl (GelMA), bioactive glass (BG), and multiwall carbon nanotubes (MWCNT) were developed to create a bone biomaterial that mimics the structural and electrically conductive nature of bone that can promote the differentiation of human-derived stem cells. GelMA-BG-MWCNT nanocomposite hydrogels supported mesenchymal stem cells derived from human induced pluripotent stem cells, hereinafter named iMSCs. Cell adhesion was improved upon coating nanocomposite hydrogels with fibronectin and was further enhanced when seeding pre-differentiated iMSCs. Osteogenic differentiation and mature mineralization were promoted in GelMA-BG-MWCNT hydrogels and were most evidently observed in the 70-30-2 hydrogels, which could be due to the stiff topography characteristic from the addition of MWCNTs. Overall, the results in this study showed that GelMA-BG-MWCNT hydrogels coated with fibronectin possess a favorable environment in which pre-differentiated iMSCs can better attach, proliferate, and further mature into an osteogenic lineage, which is crucial for the repair and regeneration of bone.

Keywords: osteogenic differentiation, electrically conductive, nanocomposite hydrogels, cell adhesion, mineralization

5.2. Introduction

The development of an electrically conductive composite is proposed as a promising biomaterial for bone tissue engineering. Natural bone is a complex organic-inorganic composite tissue composed of collagen-hydroxycarbonate apatite that possesses endogenous electrically conductive properties in response to mechanical forces.[1] Composite material approaches offer a solution to mimicking the various physiological properties possessed by complex tissue systems.[1,2] Since Fukada and Yasuda discovered the electrically conductive properties of bone,[3] the development of electrically conductive materials has been emerging for bone tissue engineering to mimic bone's natural structural and electrically conductive nature. The greatest attention, however, has been the incorporation of an electrically conductive component in bone biomaterials that can deliver electrical cues through the

application of electrical stimulation for the maturation of osteoblasts and the promotion of the repair and regeneration of bone defects.[4-6]

The design and fabrication of any bone biomaterial should entail several requirements. Successful bone reconstruction requires osteoproduction, osteoinduction, osteoconduction, and vascularization.[5,7] Bone biomaterials undergo different processes in which they can be implanted for clinical translation. In the first approach, cells are seeded to the biomaterial and are matured in a bioreactor with constant media flow and mechanical stimulation conditions.[8] In the second method, the bone biomaterials, with or without seeded cells, are implanted into the bone defect, in which the patient's body acts as a natural bioreactor to promote the regeneration of tissue.[8] In both approaches, the bone biomaterial serves as a temporary bone substitute in which the cells lay their extracellular matrix (ECM) on the surface of the implant, which is eventually resorbed and replaced over time in tune with the newly regenerated tissue.[1,8]

Biodegradable nanocomposite hydrogels composed of gelatin methacryloyl (GelMA), sol-gel derived tertiary bioactive glass (BG), and uniformly dispersed MWCNTs have been previously developed in an attempt to mimic the organic-inorganic structural composition of bone with tunable electrical and electro-mechanical properties.[1] GelMA is derived from gelatin, which is the hydrolyzed form of type I collagen found in bone. The application of GelMA as a polymer for developing a nanocomposite is, therefore, ideal for creating an environment that mimics the main organic component of endogenous bone. Its main advantage includes stability and possessing a slower degradation rate compared to gelatin. In addition, GelMA possesses an arginine-glycine-aspartic acid (RGD) that could further favor the cell-ECM interactions, thus promoting cell adhesion.[1,9] Furthermore, BGs have long been studied for their osteoconductive and osteoinductive potential stemming from the release of stimulatory ions, which promote bonding to bone.[10,11] One of the potential ways bone bonds to BG is through the formation of a hydroxycarbonate apatite (HCA) layer on the surface of the glasses in contact with body fluid, similar to the apatite in bone, that would facilitate the formation of a strong bond through the plausible interaction of collagen fibrils from the host bone and the HCA nodules forming on the glass.[12] This process occurs by releasing soluble ionic species from the glass to form a high-surface-area hydrated silica and polycrystalline HCA bilayer on the glass surface.[13] Finally, the incorporation of MWNCT into GelMA-BG nanocomposites is proposed as a promising bone biomaterial that can support cellular bioactivity, act as a reinforcement element, and promote the formation and maturation of bone through the application of exogenous electrical stimulation. Carbon-

based conductive materials, such as MWCNTs, have the advantage that they can be synthesized in various geometrical and morphological structures that can alter their physiological responses and hence, their ability to regenerate bone defects.[1]

Herein, GelMA-BG-MWCNT nanocomposite hydrogels were evaluated to assess their viability with mesenchymal stem cells derived from human induced pluripotent stem cells, termed as iMSCs. Since iMSCs are human-derived, their *in vitro* applications with GelMA-BG-MWCNT nanocomposite hydrogels could better resemble clinical translational outcomes. Good cytocompatibility properties were observed on nanocomposite hydrogels, presenting an increased initial cell adhesion of pre-differentiated cells after coating biomaterials with fibronectin, which was a crucial step to further evaluate their osteogenic ability and matrix mineralization. GelMA-BG-MWCNT nanocomposite hydrogels could become promising biomaterials for the repair and regeneration of bone that could potentially be applied for *in vivo* applications and further applications in clinical translation.

5.3. Materials and methods

5.3.1. Materials

Gelatin type A (porcine skin) (G2500, gel strength (Bloom No.) 300 with viscosity average molecular weight of 100 kDa), methacrylic anhydride (containing 2,000 ppm topanol A as an inhibitor, 94%), potassium persulfate, diacrylated pluronic F-127, multiwall carbon nanotube (MWCNT, >98% carbon basis, O.D. × L 6-13 nm × 2.5-20 μm), tetraethyl orthosilicate (TEOS, 98%), triethyl phosphate (TEP, 99.8 %), and Alizarin Red S were purchased from Sigma-Aldrich (Milwaukee, WI, USA). Calcium ethoxide was obtained from Gelest Inc. (Morrisville, PA, USA). N,N,N',N'-tetramethylethane-1,2-diamine (TEMED) was purchased from Merck KGaA (Darmstadt, Germany). Dulbecco's Modified Eagle's Medium (DMEM), Hanks' Balanced Salt Solution (HBSS), Fetal Bovine Serum (FBS), penicillin/streptomycin (pen/strep), and live/dead cell imaging kit were acquired from Thermo Fisher. Alexa Fluor® 488 phalloidin and 4'6-diamidino-2-phenylindole (DAPI) were purchased from Life Technologies (Burlington, ON, Canada).

5.3.2. Synthesis of gelatin methacryloyl (GelMA)

Gelatin type A (porcine skin) was mixed at 10% w/v in phosphate-buffered saline (PBS) at 40°C until fully dissolved. An 10% v/v of methacrylic anhydride was added dropwise under stirring to the viscous gelatin solution and allowed to react for 1 h at 40°C. To stop the reaction, a 5× dilution of warm PBS was added and dialyzed against distilled water using a 12-14 kDa cutoff dialysis tube for one week to remove unreacted components. The solution was vacuum dried at 40°C, and GelMA prepolymer was stored at 4°C until use.[1]

5.3.3. Synthesis of tertiary bioactive glass (BG)

BG was prepared by a sol-gel process which consisted in hydrolyzing TEOS and TEP with a catalytic amount of 1M HCl under vigorous stirring at room temperature (RT). Calcium ethoxide was dissolved separately in 2-ethoxyethanol and was added dropwise to the hydrolyzed TEOS until a gel was formed. The BG was aged for two days, followed by drying under vacuum at 50°C to obtain a final molar composition of 70% SiO_2, 26% CaO, and 4% P_2O_5. The final product was ground to a fine powder and stored at RT until further use.[1,14]

5.3.4. Preparation of GelMA-BG-MWCNT nanocomposite hydrogel biomaterials

Diacrylated pluronic F-127 surfactant was used to prepare MWCNT stock dispersions. Surfactant was dissolved in water at high temperature to a concentration of 20 mg/ml followed by adding 20 mg/ml MWCNT. Dispersion was sonicated for 1 h at 50°C and stored at RT until further use for GelMA-BG-MWCNT biomaterial preparation. GelMA prepolymer was dissolved in water at a concentration of 10% w/v. 1 and 2 wt.% of MWCNT were added to the GelMA prepolymer solution, followed by sonication at 50°C for 30 min. BG powder was subsequently added to GelMA-MWCNT mix at different concentrations and was further sonicated for 30 min. KPS and TEMED were added separately as the thermal initiator and accelerator, respectively at concentrations of 0.5% w/v with respect to the total prepolymer concentration to crosslink GelMA at 60°C. Sample nomenclature is presented in **Table 5.1**.

Table 5.1. Nomenclature of GelMA-BG-MWCNT nanocomposite hydrogels.

GelMA-BG-MWCNT Nomenclature			GelMA (wt.%)	BG (wt.%)	MWCNT (wt.%)		
100-0-0			100	0	0		
70-30-0	70-30-1	70-30-2	70	30	0	1	2

5.3.5. Cytotoxicity of iMSCs cultured on GelMA-BG-MWCNT nanocomposite hydrogels

Mesenchymal stem cells derived from human induced pluripotent stem cells, hereinafter named iMSCs (kindly donated by Dr. Dale Laird, Western University, Canada) were used for *in vitro* cell culture studies. Tissue culture plates (TCP) used for iMSCs maintenance were coated with gelatin diluted to 0.1% w/v in phosphate-buffered saline (PBS) and incubated at 37ºC for 1 h before aspirating gelatin solution and plating iMSCs. Cells were cultured in mesenchymal stem cell expansion media (MSCEM, Cedarlane Labs, Burlington, ON, Canada; HMSC.E.MEDIA-450) supplemented with 10% FBS and 1% pen/strep. Nanocomposite hydrogels were disinfected under ultraviolet (UV) light and pretreated in HBSS followed by coating in 0.1% w/v gelatin. iMSCs were seeded directly onto materials at a density of approximately 15,625 cells/cm^2. Live/dead cell staining kit was used to detect the viability of cells after 1, 3 and 7 days of culture and was used according to manufacturer's protocol. Tissue culture plate (TCP) was used as a control. Images were taken with a Leica DMi8 fluorescence microscope (Leica Microsystems CMS GmbH, Wetzlar, Germany). All *in vitro* experiments were done in triplicate. Unless specified, all experiments were carried out in a 24-well plate with nanocomposite hydrogel dimensions of 10 mm diameter and 5 mm height.

5.3.6. Adhesion of cells on gelatin- and fibronectin-coated GelMA-BG-MWCNT nanocomposite hydrogels

Nanocomposite hydrogels were disinfected under ultraviolet (UV) light and pretreated in HBSS followed by coating in either 0.1% w/v gelatin or 5 ug/ml fibronectin and incubated at 37ºC for 1 h. iMSCs were subsequently seeded directly onto coated materials at a density of approximately 15,625 cells/cm^2. Alternatively, iMSCs were pre-differentiated using osteogenic induction media (100 nM dexamethasone, 50 µg/ml L-ascorbic acid, and 10 mM Na$_x$H$_{3-x}$PO$_4$) for 5 days and then seeded at a density of ~15,625 cells/cm^2 onto fibronectin-coated nanocomposite hydrogels. After 1 day of culture, cells were fixed using 4% paraformaldehyde (EMD Chemicals Inc. Gibbstown, NJ) and were permeabilized for 10 min with 0.5% Triton X-100 in PBS followed by blocking cells with 1% BSA in PBS for 2 h at RT. Primary antibody incubation with anti-vinculin (1:100; MAB3574, clone VIIF9, EMD Millipore) was incubated overnight at 4ºC. After washing three times with PBS, Alexa Fluor 594 goat anti-mouse IgG secondary antibody (1:300; Thermo Fisher, Canada) was used to detect primary antibody binding. Cell cytoskeleton was stained with Alexa Fluor® 488 conjugated phalloidin (1:100) and counterstained with DAPI (300 nmol in PBS) to visualize cell nuclei.

5.3.7. Osteogenic gene expression of differentiated iMSCs cultured on GelMA-BG-MWCNT

Nanocomposite hydrogels were disinfected under UV light and pretreated in HBSS. iMSCs cultured in gelatin-coated dishes were differentiated for 5 days using osteogenic induction media (100 nM dexamethasone, 50 µg/ml L-ascorbic acid, and 10 mM $Na_xH_{3-x}PO_4$). Pre-differentiated cells were seeded at a density of ~15,625 cells/cm^2 onto fibronectin-coated nanocomposite hydrogels. After 15 days of further differentiation, total RNA was extracted from cells using the Bio-Rad Aurum™ Total RNA Mini Kit (Mississauga, ON, Canada) according to the manufacturer's protocol for osteogenic gene expression experiments. A complementary DNA (cDNA) template was prepared by using 1 µg of total RNA primed with random primers according to Promega™ Random Hexamers protocol (Thermo Fisher). Quantitative real-time PCR (qRT-PCR) was conducted in 10 µl of reaction volumes using a CFX96™ Real-Time System (C1000 Touch Thermal Cycler; Bio-Rad, Mississauga, ON, Canada), and measured with iQ™ SYBR® Green Supermix (Bio-Rad) according to the recommended procedures. **Table 5.2** presents the sequences of primers used. iMSCs differentiated on pure GelMA (100-0-0) hydrogels were used as a control to assess the effects of BG and MWCNT on the induction of osteogenic differentiation. The results were analyzed with the comparative threshold cycle method and normalized with mouse 18S as an endogenous reference and reported as relative values ($\Delta\Delta$ CT) to the control.

Table 5.2. Primers for human-specific mRNA amplification.

Gene	Forward (5′ ➔ 3′)	Reverse (5′ ➔ 3′)
Runx2	CCCAGTATGAGAGTAGGTGTCC	GGGTAAGACTGGTCATAGGACC
Sp7	TTCTGCGGCAAGAGGTTCACTC	GTGTTTGCTCAGGTGGTCGCTT
Col2A1	AGCCTGGTGATGATGGTGAA	ACTCTCACCCTTCACACCAG
OPN	TCACCTGTGCCATACCAGTT	TGTGGTCATGGCTTTCGTTG
18S	GCGGTTCTATTTGTTGGTTT	CTCCGACTTTCGTTCTTGATT

Runx2: Runt-related transcription factor 2; Sp7: Osterix; Col2A1: collagen type II alpha 1 chain, OPN: osteopontin.

5.3.8. Western blot analysis of differentiated iMSCs cultured on GelMA-BG-MWCNT

Evaluation of the levels of osteogenic proteins was performed through western blotting. Pre-differenitated cells were seeded onto fibronectin-coated nanocomposite hydrogels. In brief, after

further differentiating for 15 days, cells cultured on nanocomposite hydrogels were lysed in buffer containing 150 mM NaCl, 10 mM Tris-HCl (pH 7.4), 1 mM EDTA, 0.5% Nonidet P-40, and 1% Triton X-100 and supplemented with protease inhibitor (Roche Applied Science, Indianapolis, IN, USA). Protein concentrations were determined by Quick Start™ Bradford Protein Assay (Bio-Rad, Mississauga, ON, Canada), and 50 μg of total protein lysate was resolved on 10% SDS-PAGE and subsequently transferred to nitrocellulose membrane. The following primary antibodies were used for immunoblotting: anti-Osteopontin (rabbit, 1:2000; Abcam, ab8448) and anti-Osteocalcin (rabbit, 1:250; Abcam, ab133612). Primary antibody labeling was detected using HRP-conjugated goat anti-rabbit secondary antibody and the ECL detection system.

5.3.9. Immunofluorescence Microscopy

Assessment of osteogenic protein expression was evaluated on pre-differentated cells that had been further differentiated for 15 days. Cells were fixed using 4% paraformaldehyde (EMD Chemicals Inc. Gibbstown, NJ) and were permeabilized for 10 min with 0.5% Triton X-100 in PBS, followed by blocking cells with 1% BSA in PBS for 3 h at RT. Samples were labeled with the following antibodies overnight at 4°C: osteopontin (rabbit, 1:100; Abcam, ab8448), osteocalcin (rabbit, 1:100; Abcam, ab133612). Primary antibody binding was detected using Alexa Fluor® 555 goat anti-rabbit IgG. Counterstaining with Alexa Fluor® 488 conjugated phalloidin (1:100) and DAPI (300 nmol in PBS) were used to visualize phalloidin and cell nuclei.

5.3.10. Evaluation of mineralization of differentiated iMSCs on GelMA-BG-MWCNT

The mineralization ability of pre-differentiated iMSCs co-cultured with nanocomposite hydrogels was assessed by staining with Alizarin Red solution (pH = 4.2) for 5 min at RT. Glass coverslips were placed in TCP followed by the addition of nanocomposite hydrogels (6 mm diameter and 2 mm height). After 15 days of further differentiating cells co-cultured with GelMA-BG-MWCNT hydrogels, glass coverslips were dehydrated in acetone and immersed in an acetone-xylene (1:1) solution. Samples were cleared in 95% and 100% ethanol, followed by dipping in a xylene solution. Coverslips were subsequently tipped onto a synthetic mounting media for visualization. For quantification of Alizarin Red staining, pre-differentiated cells were cultured on the nanocomposite hydrogels (10 mm diameter and 5 mm height) and further differentiated for 15 days. After the differentiation period, samples were fixed with 70% ethanol at RT for 15 min followed by washing

with distilled water. 40 mM of Alizarin Red staining was added and incubated for 30 min at RT. Unincorporated dye was aspirated, followed by washing four times with distilled water under shaking for 5 min each time. 10% v/v acetic acid was added and incubated for 30 min under shaking at RT. The monolayer was scraped from the nanocomposite hydrogels and transferred to a microcentrifuge tube, followed by vortexing for 30 sec. The slurry was overlaid with mineral oil, heated to 85°C for 10 min and transferred to ice for 5 min. Samples were centrifuged and supernatants were transferred to a new tube followed by the addition of 10% v/v ammonium hydroxide to neutralize the acid. Samples were aliquoted in triplicate in a 96-well plate and absorbance was measured at 405 nm.[15]

5.3.11. Statistical Analysis

Statistical analysis of the data was performed using GraphPad Prism. Differences were tested by one-way ANOVA, and a p-value of <0.05 was used for statistical significance.

5.4. Results and Discussion

5.4.1. Cell viability of mesenchymal stem cells derived from human induced pluripotent stem cells (iMSCs) on GelMA-BG-MWCNT nanocomposite hydrogels

Attachment and proliferation of targeted cells to the biomaterial is a fundamental step in tissue engineering. To assess the viability of cells, the undifferentiated state of iMSCs need to be maintained by coating TCP surfaces with a biomimetic microenvironment in the form of adhesion or extracellular matrix (ECM) proteins for their attachment.[16-18] Gelatin was used as a substrate to coat nanocomposite hydrogels prior to seeding iMSCs. **Figure 5.1A** depicts the live/dead staining images of iMSCs cultured on nanocomposite hydrogels for 24, 72, and 168 h. After 24 h culture, pure GelMA (100-0-0) hydrogel and nanocomposite materials containing 1 and 2 wt.% MWCNT presented a significant decreased initial cell attachment ($p < 0.05$) compared to the 70-30-0 hydrogel (**Fig. 5.1A-B**). The initial cell viability after 24 h culture of the 70-30-0 hydrogel was comparable to that of the TCP control. Evaluation of the adhesion ability of human MSCs (hMSCs) has also been studied on methacrylated hyaluronic acid (MeHA) hydrogels and MeHA hydrogels conjugated with cell-adhesive ligands (RGD)-bearing silica nanoparticles (MeHA-SiO$_2$).[19] The findings of this study showed that hMSCs adhere better to the MeHA-SiO$_2$ hydrogels, but failed to adhere or spread well

on the MeHA hydrogels after only 24 h culture.[19] It also revealed that mature focal adhesion points, cell-ECM adhesion structures, were formed on the MeHA-SiO$_2$ hydrogels since the immobilization of SiO$_2$ nanoparticles conjugated with RGD was an important nanomaterial to incorporate in a soft polymeric matrix to regulate critical cellular responses.[19] Similar to the results from the study, pure 100-0-0 hydrogels presented a decreased initial cell adhesion compared to the 70-30-0 hydrogels. The BG in the 70-30-0 hydrogels plausibly function as anchorage points to enable cell attachment and spreading. The viability and proliferation of cells increased at 72 h of culture for all nanocomposite hydrogels, but it was significantly higher for the 70-30-0 and 70-30-1 hydrogels ($p < 0.05$) (**Fig. 5.1B**). Furthermore, at 168 h of culture, iMSCs continued to grow considerably on the hydrogels with minimal cell death, thus increasing their viability in function of culture time. These results indicate that iMSCs take up to three days to adapt to the 100-0-0, 70-30-1, and 70-30-2 hydrogels, after which, cell density and viability continue to increase. Although cell viability increased on the 70-30-2 hydrogel after 72 and 168 h culture, the rate in which cells proliferated was slower compared to the rest of the biomaterials and did not show evidence of cytotoxic response due to the addition of 2 wt.% MWCNT. The delayed cell proliferation observed in the 70-30-2 hydrogels was due to the initial low cell adhesion/retention at 24 h which affected the cell numbers by 168 h of culture.[1] In addition, it takes more effort for iMSCs to attach to higher concentrations of hydrophobic surfaces, such as MWCNTs, which was the reason why the initial cell adhesion on the 70-30-2 hydrogels was not as favorable.[1] Moreover, the initial cell attachment at 24 h on the 70-30-1 hydrogel was low, after which the cell density and viability considerably increased until reaching 168 h of culture. Although it has been known that stem cells attach and spread well to a rigid substrate, such as TCP or a glass coverslip,[19,20] MWCNT possesses a rough topography. It has been shown that the adhesion of hMSCs is regulated by interfacial roughness, in which cell adhesion and spreading decrease as the roughness of surfaces increases.[21] However, after 24 h of culture, the 70-30-1 hydrogel might adsorb proteins due to the highly delocalized π-bonds of the hydrophobic nature of MWCNT,[4] thus enhancing the spread of iMSCs on the nanocomposite hydrogel.[1]
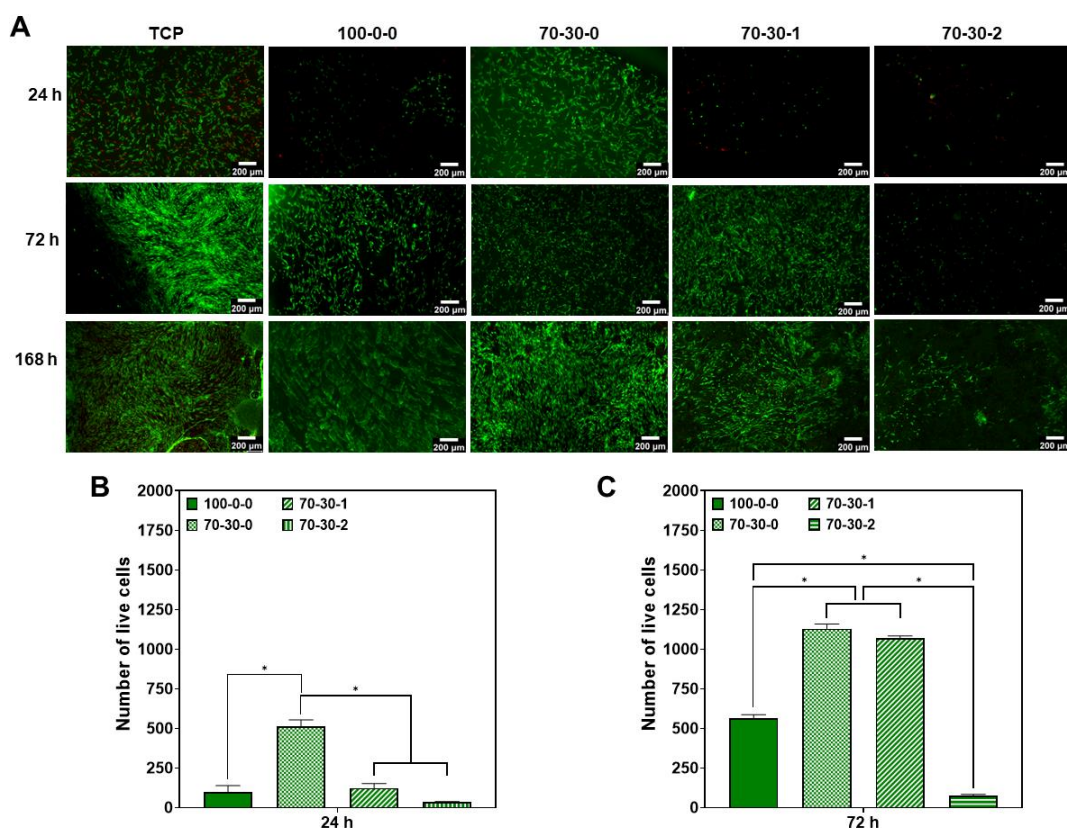
Figure 5.1. Viability of iMSCs on GelMA-BG-MWCNT nanocomposite hydrogels. (**A**) Live/dead staining of iMSCs cultured on nanocomposite hydrogels after 24, 72, and 168 h. Scale bar = 200 μm. Number of live iMSCs after (**B**) 24 h and (**C**) 72 h culture. *$p < 0.05$.

Differentiation of cells takes place at the expense of proliferation and would normally be initiated at a confluency of around 70%. However, according to the live/dead images, 70% confluency would be reached between days two and three for the cases of all hydrogels (**Fig. 5.1A**) except for the 70-30-2, which is significantly lower ($p < 0.05$) (**Fig. 5.1B-C**). In addition, cells growing on the 100-0-0 hydrogel are also low compared to the 70-30-0 and 70-30-1 hydrogels ($p < 0.05$) after 72 h culture (**Fig. 5.1C**). Therefore, the assessment of the osteogenic ability of cells cultured on nanocomposite hydrogels could not be evaluated since the initial cell density baseline is not even amongst the biomaterials, limiting the performance of appropriate comparisons.

Understanding the interfacial interactions between iMSCs and nanocomposite hydrogels allows to determine which culture condition requires modification to improve the initial cell adhesion until reaching an adequate and similar cell density amongst the biomaterials to induce osteogenic

differentiation. Formation of focal adhesions is the initial stage of cell adherence, with the substrates showing effective cell-biomaterial interactions necessary for cell migration, proliferation, and signal transduction.[22] Vinculin is a focal adhesion protein involved in anchoring actin filaments to integrin adhesive molecules.[22] Investigation of the presence of vinculin in cells cultured on nanocomposite hydrogels allows the evaluation of the degree of integrin-mediated communication between the iMSCs and the nanocomposite hydrogels. iMSCs were stained for vinculin (red) and nuclei (blue) at 24 h of culture to observe the cell-biomaterial interfacial interactions (**Fig 5.2**). It is observed that the number of cells attached to the hydrogels is less than that in the control glass coverslip. This is mostly evident for the 100-0-0, 70-30-1, and 70-30-2 hydrogels, which is similar to the results shown in the live/dead staining (**Fig. 5.1A**). Although the 70-30-0 hydrogel has more cells, the presence of vinculin is not as prominent as in the control. These results indicate that the plausible reason why there is a decreased initial number of iMSCs attached to the hydrogels at 24 h of culture could be due to the substrate used to coat the materials, namely gelatin. For this reason, a different substrate should be evaluated to assess whether the initial cell adherence to the nanocomposite hydrogels could be improved to enable the performance of differentiation studies.
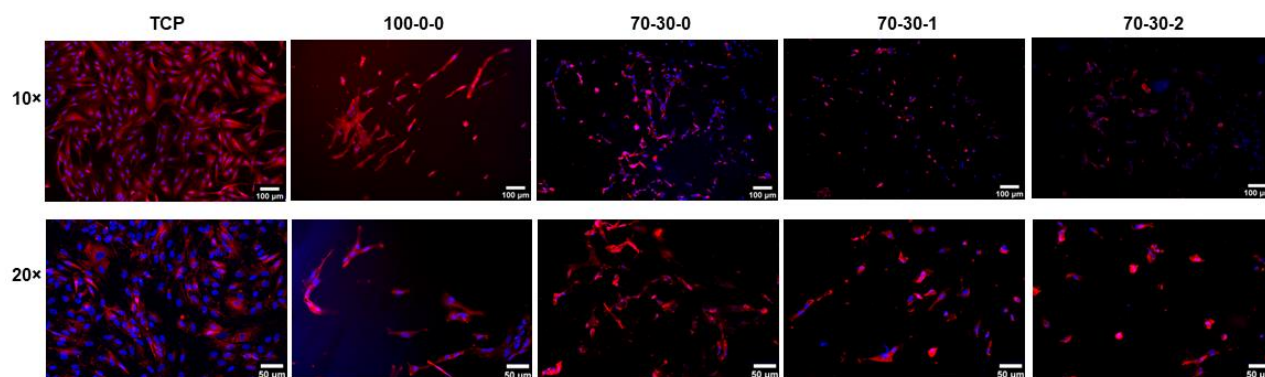
Figure 5.2. Immunofluorescence microscopy images of iMSCs cultured on gelatin-coated GelMA-BG-MWCNT nanocomposite hydrogels. Focal adhesions of iMSCs cultured on hydrogels (blue = nuclei, red = vinculin) at 24 h of culture. 10× scale bar = 100 µm. 20× scale bar = 50 µm.

5.4.2. Optimization of iMSC adhesion on GelMA-BG-MWCNT nanocomposite hydrogels

Although gelatin was used to coat TCP surfaces for the maintenance of iMSCs, its application as a coating substrate for nanocomposite hydrogels did not provide an adequate environment for the adhesion of cells. Therefore, a different protein substrate was used to evaluate whether the initial cell

adhesion on biomaterials would improve, especially for the nanocomposite hydrogels containing 1 and 2 wt.% MWCNT. Fibronectin was chosen as an alternative cell attachment substrate since it has been previously used for the proliferation and osteogenic differentiation of MSCs.[17,23] Cells cultured on fibronectin-coated hydrogels were stained for vinculin (red), F-actin (green), and nuclei (blue) after 24 h of culture (**Fig. 5.3**). A considerable increase of initial cell density was observed on the 100-0-0 hydrogel, which appeared similar to that of the control TCP. This indicates that iMSCs cultured on the fibronectin-coated 100-0-0 hydrogel presented a better cell-biomaterial interfacial interaction than the gelatin-coating substrate. This was also observed in the 70-30-0 hydrogel, which not only presented an increased cell adhesion but also an elongated cellular morphology and the formation of a uniform layer of actin filaments.
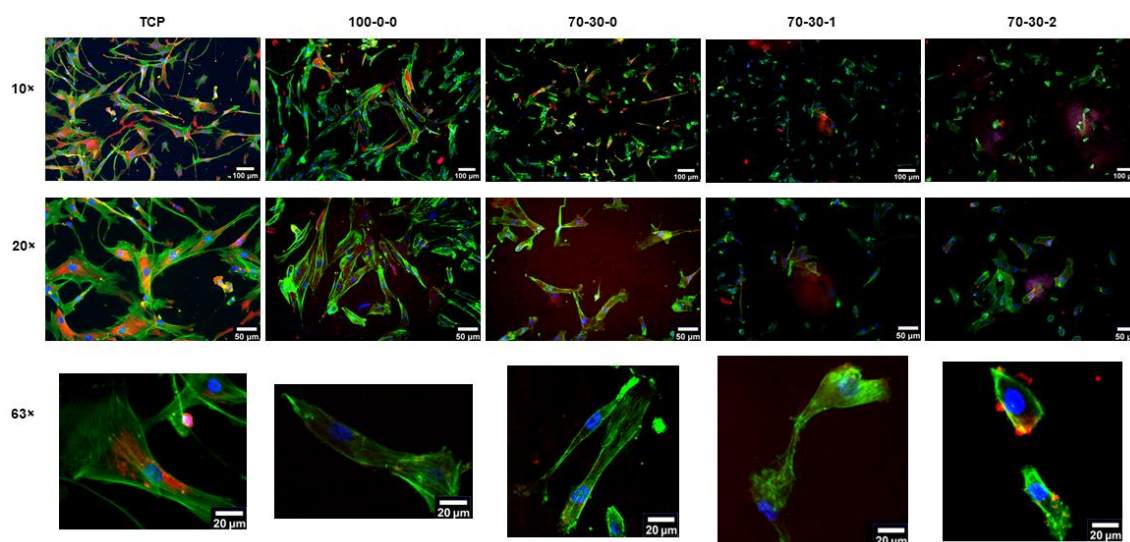
Figure 5.3. Immunofluorescence microscopy images of iMSCs cultured on fibronectin-coated GelMA-BG-MWCNT nanocomposite hydrogels. Focal adhesions of iMSCs cultured on hydrogels (blue = nuclei, green = F-actin, red = vinculin) after 24 h of culture. 10× scale bar = 100 µm. 20× scale bar = 50 µm. 63× scale bar = 20µm.

Cell attachment on the 70-30-1 and 70-30-2 hydrogels was not improved as observed in the 100-0-0 and 70-30-0 hydrogels. However, the expression of vinculin was showed at the periphery of cells cultured on all hydrogels. This observation depicts the presence of integrin-mediated communications between the iMSCs and the surfaces of the hydrogels. Collectively, these results indicate that the initial adherence of iMSCs on materials is better after coating with fibronectin, especially for the 100-

0-0 hydrogel, but could be further improved for the 70-30-1 and 70-3-2 nanocomposite hydrogels. Although surface roughness could direct differentiation towards an osteogenic cell lineage,[21,24] iMSCs cultured onto the 1 and 2 wt.% MWCNT containing hydrogels could delay this process due to the decreased attachment. The reduced cell adhesion could plausibly be due to the extended period that the iMSCs require to adapt to stiffer surfaces. Bone cells, however, are adapted to proliferate and differentiate on a stiff environment.[24] For this reason, initial cell attachment was further evaluated on pre-differentiated iMSCs to assess whether cell adhesion was enhanced on the 70-30-1 and 70-30-2 hydrogels (**Fig. 5.4**). Osteogenic differentiation of iMSCs was induced for five days followed by subsequent seeding onto hydrogels. **Figure 5.4** shows the fluorescent images of pre-differentiated iMSCs cultured on the surfaces of 100-0-0 hydrogel and nanocomposite hydrogels for 24 h. Favorable pre-differentiated cell adhesion was observed on the 100-0-0 and 70-30-0 hydrogels, but was improved in the nanocomposite hydrogels containing 1 and 2 wt.% MWCNT (**Fig. 5.4**) compared to that of the undifferentiated iMSCs (**Fig. 5.3**). In addition, cells formed an increased layer of elongated actin filaments on the hydrogels, suggesting favorable adhesion and spreading. Based on the results collectively presented in **Figures 5.3-5.4**, initial cell adherence on nanocomposite hydrogels was improved and more favorable after coating materials with fibronectin and seeding pre-differentiated iMSCs. The determination of these conditions was crucial to obtain a similar cell density baseline between each biomaterial to further investigate the osteogenic ability of cells cultured on nanocomposite hydrogels.
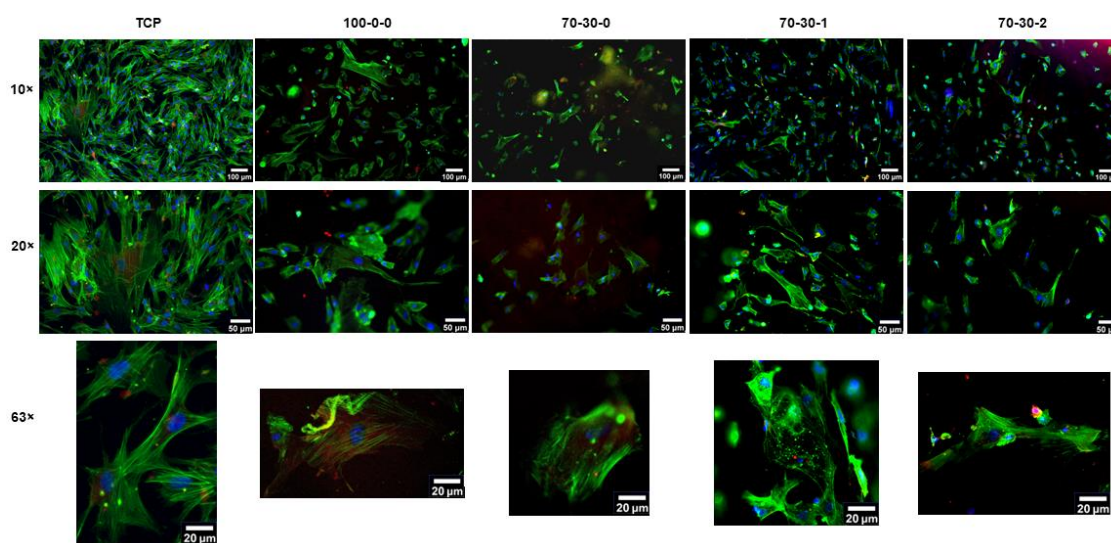
Figure 5.4. Immunofluorescence microscopy images of pre-differentiated iMSCs cultured on fibronectin-coated GelMA-BG-MWCNT nanocomposite hydrogels. Focal adhesions of iMSCs

cultured on hydrogels (blue = nuclei, green = F-actin, red = vinculin) after 24 h of culture. 10× scale bar = 100 µm. 20× scale bar = 50 µm. 63× scale bar = 20µm.

5.4.3. Osteogenic gene expression of differentiated iMSCs cultured on GelMA-BG-MWCNT nanocomposite hydrogels

Following the observation that pre-differentiated cells attach better to fibronectin-coated materials, their differentiation potential towards an osteogenic phenotype on GelMA-BG-MWCNT hydrogels was subsequently investigated. **Figure 5.5** shows the osteogenic expression of early and late osteogenic genes in response to differentiation induction on nanocomposite hydrogels. Osteogenic differentiation of iMSCs is a regulated process in which master transcription factors and their target genes control the expression of numerous downstream target genes that code for proteins that determine the osteoblast phenotype, which are necessary for the repair and regeneration of bone.[25,26] There are two master transcription factors that regulate the expression of osteogenic target genes: runt-related transcription factor 2 (Runx2) and transcription factor Sp7, also known as osterix. Runx2 initiates osteogenesis upstream of Sp7 early in the regulatory hierarchy of osteoblast development.[27] Targeted deletion of either gene results in loss of osteoblast differentiation and bone formation.[26] The differentiation of iMSCs cultured on pure GelMA (100-0-0) hydrogels was used as a control to evaluate the effects of BG and MWCNT on the induction of osteogenic differentiation. After 15 days of differentiation, the expression of Runx2 in the 70-30-1 and 70-30-2 nanocomposite hydrogels resulted in a 0.2-fold downregulation with respect to the pure GelMA hydrogel control showing no significance ($p > 0.05$) (**Fig. 5.5A**). However, Runx2 expression in 100-0-0 hydrogel and nanocomposite hydrogels containing 1 and 2 wt.% MWCNT was significantly higher ($p < 0.05$) than in the 70-30-0 hydrogel. Furthermore, Sp7 gene expression was significantly higher ($p < 0.05$) in the 70-30-0 hydrogel and in the hydrogels containing 1 and 2 wt.% MWCNT resulting in a 2.8-fold upregulation (**Fig. 5.5B**). The expressions of Runx2 and Sp7 induce the expression of downstream target genes, such as osteopontin and collagen, which are necessary for mineralization and endochondral ossification for the repair and regeneration of bone.[28]

Osteopontin (OPN) presents an RGD motif that binds to integrins and allows bone cells to adhere to the mineralized matrix.[29] Although OPN has been shown to be an inhibitor of mineralization in a dose-dependent manner by binding to the HCA and inhibiting further growth,[30] its presence promotes

intrafibrillar mineralization of collagen.[31,32] The major collagenous component of bone ECM is type I collagen. Type 1 collagen has been shown to promote proliferation, survival, adhesion, and osteogenesis in MSCs mediated by α2β1 integrin interaction.[33-35] Another form of collagen found in bone is type II. Type II collagen has been linked to the preformation of cartilaginous tissue during bone fracture healing process.[36] It has been shown that chondrogenic pre-induction of β-TCP/MSC composites presented a significant production of type II collagen and enhanced full bone formation, including marrow organization.[37] Therefore, type II collagen (Col2A1) serves as a modulator during osteogenic differentiation of MSCs via the activation of Runx2 through α2β1 integrin-related FAK signaling pathway and promotes healing of bone defects through endochondral ossification-like process.[36] Significant upregulation of the OPN gene expression on iMSCs differentiated on 70-30-2 nanocomposite hydrogels ($p < 0.05$) was obtained, resulting in a 5-fold upregulation (**Fig. 5.5C**). Furthermore, the expression of Col2A1 was higher in the 70-30-2 hydrogel compared to the 70-30-0 hydrogel ($p < 0.05$). However, Col2A1 expression significantly decreased in the 70-30-0 ($p < 0.001$) and nanocomposite hydrogels containing 1 ($p < 0.001$) and 2 ($p < 0.01$) wt.% MWCNT, resulting in a 0.73-, 0.6-, and 0.46-fold downregulation, respectively, compared to pure GelMA control (**Fig. 5.5D**). The smooth surface of 100-0-0 hydrogel could potentially facilitate the increased expression of Col2A1, which is present in cartilage ECM and in the terminal process of endochondral ossification in chondrocyte hypertrophic differentiation.[38] The expression of Col2A1 in nanocomposite hydrogels could plausibly increase if there is a longer period of differentiation. In addition, the incorporation of BG and MWNCT leads to a rougher and stiffer surface in which bone cells, or in this case, pre-differentiated iMSCs, are prone to proliferate which resulted in the increased expression of early and late osteogenic differentiation markers, as mainly observed in the cases of Sp7 (**Fig. 5.5B**) and OPN (**Fig. 5.5C**) genes. The 70-30-1 and 70-30-2 hydrogels presented good early osteogenic expressions (**Fig. 5.5A,B**) but was mostly enhanced in the 70-30-2 hydrogel for the expression of OPN as a late osteogenic differentiation marker (**Fig. 5C**), which could be due to the possible rough topography of the MWCNTs which could further enhance maturation. These results collectively show that GelMA-BG-MWCNT nanocomposite hydrogels possess a favorable environment and ability to further differentiate iMSCs into an osteogenic lineage that could potentially drive bone healing through the process of endochondral ossification.
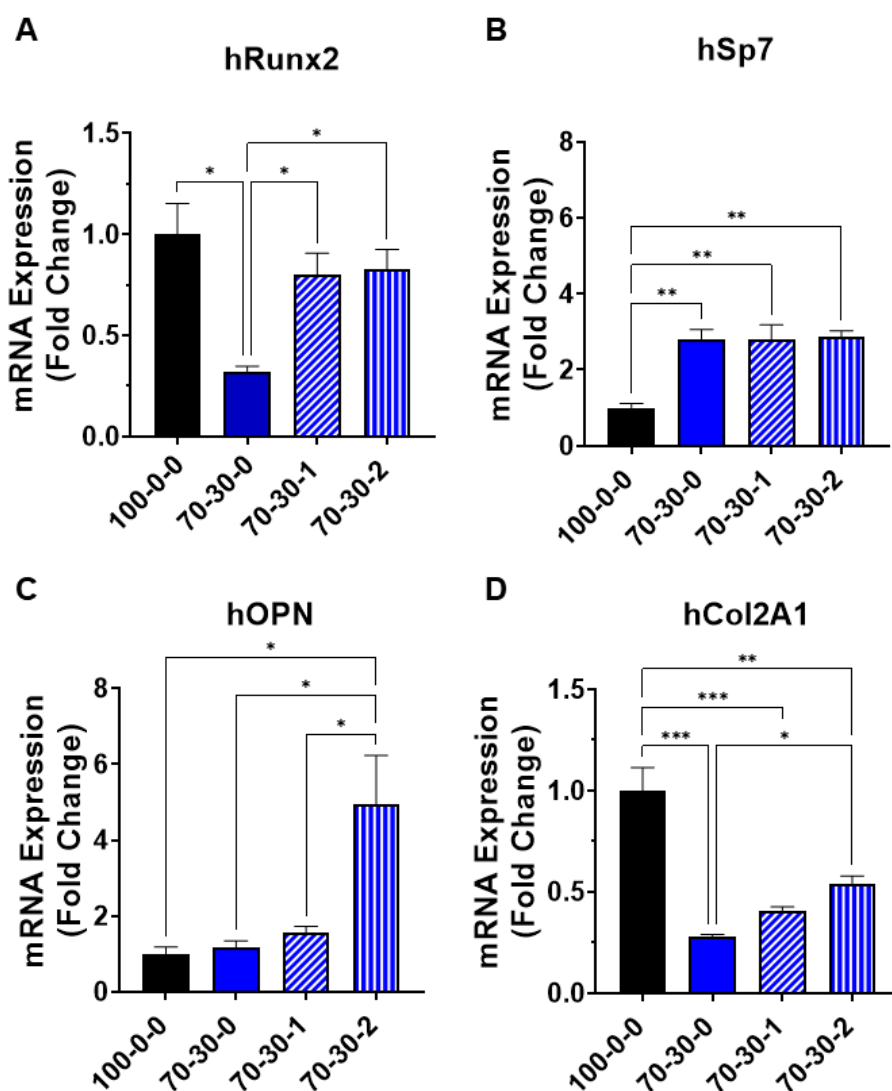
Figure 5.5. Osteogenic gene expression of differentiated iMSCs cultured on GelMA-BG-MWCNT nanocomposite hydrogels. (**A**) Runx2, (**B**) Sp7, (**C**) OPN and (**D**) Col2A1 mRNA expressions of differentiated iMSCs cultured on nanocomposite hydrogels for 15 days. $*p < 0.05$, $**p < 0.01$, $***p < 0.001$.

5.4.4. Osteogenic protein expression of differentiated iMSCs cultured on GelMA-BG-MWCNT nanocomposite hydrogels

After determining that iMSCs were able to further differentiate towards an osteogenic phenotype on GelMA-BG-MWCNT hydrogels, western blot analysis was conducted to investigate the expression of two non-collagenous proteins in differentiated cells cultured on nanocomposite hydrogels for 15 days. One of the characteristic properties to evaluate the transition towards a mature phenotype is the

increase in expression of bone matrix proteins, OPN and osteocalcin (OCN).[1,39] The secretion of OPN and OCN should progressively increase as the mineralization process advances for the formation of bone during its repair and regeneration.[11,40] TCP was used as a control. **Figure 5.6A** shows that the full-length (60 kDa) OPN protein was detected in all cultures, but was mostly expressed in the 70-30-2 hydrogel. OPN is known to be cleaved by matrix metalloproteinases (MMPs) that break down ECM proteins necessary for bone remodeling and regeneration.[41,42] The cleaved 32 kDa OPN fragment protein was also detected and was mostly observed in the 70-30-1 and 70-30-2 hydrogels, but was not noticeable in the 100-0-0 hydrogel. Furthermore, OCN protein was only identified in cells cultured on 70-30-0 hydrogels and nanocomposite hydrogels containing 1 and 2 wt.% MWCNT. Furthermore, immunofluorescence staining was performed on differenitaited cells to confirm the presence of OPN (**Fig. 5.6B**) and OCN (**Fig. 5.6C**) proteins. OPN protein was most prominently expressed in differentiated iMSCs cultured on nanocomposite hydrogels, specifically on the 70-30-2 hydrogel. In addition, the OCN protein was not as strongly expressed as compared to the OPN expression. These results are consistent with the western blot analysis. Collectively, the effects of BG and MWCNT in nanocomposite hydrogels reveal that these components enhance the expression of mature osteogenic phenotype marker proteins and have the ability to further drive differentiated cells towards a mature osteogenic lineage. The applications of GelMA-BG-MWCNT hydrogels, specifically the 70-30-1 and 70-30-2 hydrogels, could potentially be translated into *in vivo* models to explore the augmentation of bone regeneration.
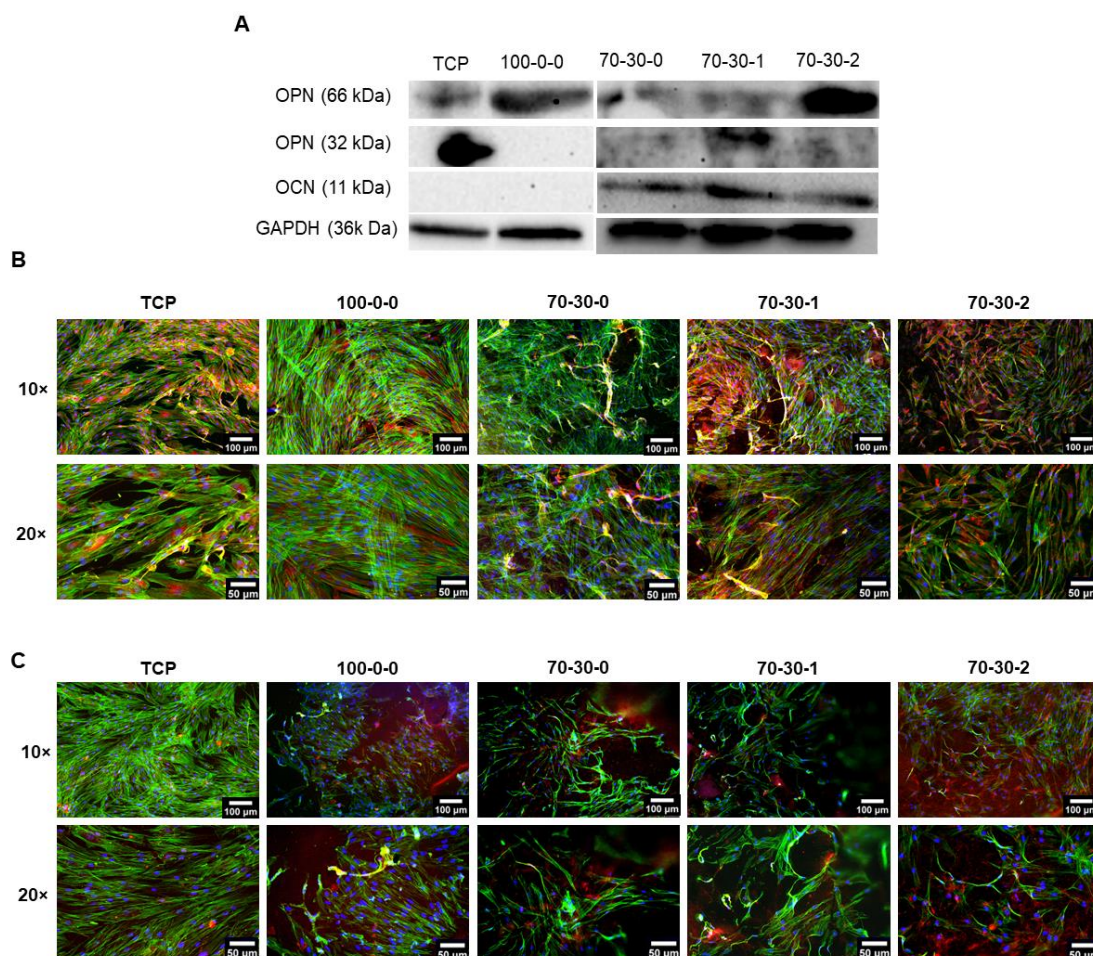
Figure 5.6. Osteogenic protein expression of differentiated iMSCs cultured on GelMA-BG-MWCNT nanocomposite hydrogels. (**A**) Representative western blot analysis of the osteogenic proteins OPN and OCN after 15 days of further differentiation of pre-differentiated iMSCs on nanocomposite hydrogels. Immunofluorescence staining of (**B**) osteopontin (OPN) and (**C**) osteocalcin (OCN) in differentiated cells cultured on GelMA-BG-MWCNT nanocomposite hydrogels after 15 days of further differentiation. Cells were stained for nuclei (blue), F-actin (green), and OPN or OCN (red). 10× scale bar = 100 µm. 20× scale bar = 50 µm.

5.4.5. Mineralization of differentiated iMSCs cultured on GelMA-BG-MWCNT nanocomposite hydrogels

Matrix mineralization is a definitive hallmark of osteoblast differentiation and the last phenotypic stage of osteogenic tissue.[11,43] Bioactive properties of GelMA-BG-MWCNT were previously shown when incubated in simulated body fluid (SBF).[1] The formation of hydroxycarbonate apatite (HCA) $(Ca_{10-x}(PO_4)_{6-x}(CO_3)_x(OH)_{2-x})$ layers occurs through the release of soluble ionic species, such as Si,

Ca, and P ions, from the BG to form a high-surface-area hydrated silica and polycrystalline HCA bilayer on the glass surface, resulting in an apatite layer similar to that of bone, capable to stimulating the formation of bone tissue.[1] The addition of osteogenic media also provides an exogenous source of phosphate that assists mineralization. Alizarin Red staining was used to visualize and quantify the mineral formation. Since the nanocomposite hydrogels are black due to MWCNTs, visualization of the mineralized tissue onto the materials was challenging. Instead, cells were co-cultured with nanocomposite hydrogels to observe the mineral depositions as a function of hydrogel composition. Glass coverslips were placed in TCP before seeding pre-differentiated iMSCs to ease visualization. **Figure 5.7A** shows the optical images of mineral depositions of differentiated cells cultured in TCP control and co-cultured with GelMA-BG-MWNCTs after 15 days of further differentiation. A slight increase of stained mineral deposition was depicted in cells co-cultured with 70-30-0 hydrogel and with the nanocomposites containing 1 and 2 wt.% MWCNT, which was observed as dark red to brown spots, evidencing the mineralized nodules. Quantification of the Alizarin staining of the iMSCs cultured on the surfaces of GelMA-BG-MWCNT nanocomposite hydrogels was subsequently performed, and their results are shown in **Figure 5.7B**. The 70-30-2 hydrogel had the highest mineral deposition after 15 days of further differentiating iMSCs. Mineralization of 70-30-2 hydrogels was significantly higher than 70-30-1 and 70-30-0 ($p < 0.05$) hydrogels and was even more noticeably higher than the 100-0-0 and TCP control ($p < 0.01$). The 70-30-1 and 70-30-0 hydrogels presented similar mineral deposition but were significantly higher than the 100-0-0 and TCP control ($p < 0.01$).

These results show that cells cultured on pure 100-0-0 hydrogel presented a similar mineralization to TCP control after 15 days of further differentiation, but could be insufficient to further enhance its promotion if pure GelMA were to be used as a bone biomaterial. A significant increase in mineral deposition was, however, observed upon the addition of BG and MWCNT. It could be assumed that the release of soluble ionic species from the BG considerably facilitates the formation of calcium and phosphorous depositions on the surfaces of the nanocomposite hydrogels. In addition, differentiated cells proliferate more on a stiffer and rougher surface that would mimic that of an osseous environment, such as those hydrogels containing BG and MWCNT. This was mostly evident for differentiated iMSCs cultured on 70-30-2 hydrogels which presented the highest mineralization. The increased mineral deposition in the 70-30-2 hydrogels was also in accordance with the OPN protein expression (**Fig. 5.6B**), which could plausibly significantly promote the repair and regeneration of bone defects *in vivo*.
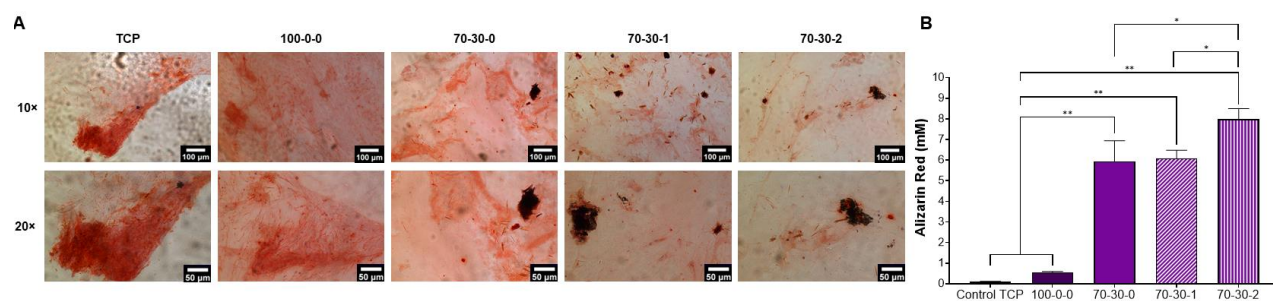
Figure 5.7. Mineralization of differentiated iMSCs. (**A**) Optical images of Alizarin Red staining of pre-differentiated iMSCs co-cultured with GelMA-BG-MWCNT nanocomposite hydrogels after 15 days of further differentiation. Mineral deposition is stained red. 10× scale bar = 100 µm. 20× scale bar = 50 µm. (**B**) Quantification of mineralization by extraction of Alizarin Red from pre-differentiated iMSCs cultured onto the surfaces of GelMA-BG-MWCNT nanocomposite hydrogels after 15 days of further differentiation. $*p < 0.05$, $**p < 0.01$.

5.5. Conclusions

In this study, GelMA-BG-MWCNT hydrogels were prepared to evaluate the viability and osteogenic ability of iMSCs cultured on the surfaces of nanocomposite hydrogels. iMSCs were chosen for the *in vitro* studies since they are human-derived and could potentially resemble clinically driven outcomes. Cell interaction studies showed good cytocompatibility properties when culturing iMSCs onto the surfaces of gelatin-coated nanocomposite hydrogels for 7 days. However, the initial cell density was not even amongst cells cultured on hydrogels and required further optimization to investigate the osteogenic ability of iMSCs on GelMA-BG-MWCNT hydrogels. Fibronectin was found to promote cell adhesion and, hence, increase the proliferation of cells. This was further enhanced upon seeding pre-differentiated iMSCs for 5 days onto nanocomposite hydrogels, especially for those materials containing 1 and 2 wt.% MWCNT, possibly due to the rough and stiff surface topography in which pre-differentiated cells are more favorable to mature. Further pre-differentiation of iMSCs on nanocomposites showed that GelMA-BG-MWCNT hydrogels possess a favorable environment in which the differentiation towards an osteogenic lineage is promoted. In addition, nanocomposite hydrogels have the ability to promote mature matrix mineralization, which was most evidently observed on differentiated cells cultured on 70-30-2 hydrogels. Although exogenous electrical stimulation was not assessed on cells cultured on nanocomposite hydrogels, it is suggested that its application could further enhance *in vitro* osteogenic maturation and *in vivo* bone healing. GelMA-

BG-MWCNT hydrogels could become a promising bone biomaterial that can promote the repair and regeneration of bone defects.

5.6. References

[1]   R. Arambula-Maldonado, Y. Liu, M. Xing, K. Mequanint, Bioactive and electrically conductive GelMA-BG-MWCNT nanocomposite hydrogel bone biomaterials, Biomaterials Advances. 154 (2023) 213616. https://doi.org/10.1016/j.bioadv.2023.213616.

[2]   N. Aslankoohi, K. Mequanint, Intrinsically fluorescent bioactive glass-poly(ester amide) hybrid microparticles for dual drug delivery and bone repair, Materials Science and Engineering: C. 128 (2021) 112288. https://doi.org/10.1016/j.msec.2021.112288.

[3]   E. Fukada, I. Yasuda, On the Piezoelectric Effect of Bone, J. Phys. Soc. Jpn. 12 (1957) 1158–1162. https://doi.org/10.1143/JPSJ.12.1158.

[4]   R. Arambula-Maldonado, K. Mequanint, Carbon-based electrically conductive materials for bone repair and regeneration, Mater. Adv. (2022) 10.1039.D2MA00001F. https://doi.org/10.1039/D2MA00001F.

[5]   E.P. e Silva, B. Huang, J.V. Helaehil, P.R.L. Nalesso, L. Bagne, M.A. de Oliveira, G.C.C. Albiazetti, A. Aldalbahi, M. El-Newehy, M. Santamaria-Jr, F.A.S. Mendonça, P. Bártolo, G.F. Caetano, In vivo study of conductive 3D printed PCL/MWCNTs scaffolds with electrical stimulation for bone tissue engineering, Bio-Des. Manuf. 4 (2021) 190–202. https://doi.org/10.1007/s42242-020-00116-1.

[6]   X. Liu, M.N. George, L. Li, D. Gamble, A.L. Miller II, B. Gaihre, B.E. Waletzki, L. Lu, Injectable Electrical Conductive and Phosphate Releasing Gel with Two-Dimensional Black Phosphorus and Carbon Nanotubes for Bone Tissue Engineering, ACS Biomater. Sci. Eng. 6 (2020) 4653–4665. https://doi.org/10.1021/acsbiomaterials.0c00612.

[7]   T. Minagawa, Y. Tabata, A. Oyama, H. Furukawa, T. Yamao, Y. Yamamoto, Controlled Release of Granulocyte Colony-Stimulating Factor Enhances Osteoconductive and Biodegradable Properties of Beta-Tricalcium Phosphate in a Rat Calvarial Defect Model, International Journal of Biomaterials. 2014 (2014) 1–11. https://doi.org/10.1155/2014/134521.

[8]   R. Arambula-Maldonado, A. Geraili, M. Xing, K. Mequanint, Tissue engineering and regenerative therapeutics: The nexus of chemical engineering and translational medicine, Can J Chem Eng. (2021) cjce.24094. https://doi.org/10.1002/cjce.24094.

[9]   M. Kirsch, L. Birnstein, I. Pepelanova, W. Handke, J. Rach, A. Seltsam, T. Scheper, A. Lavrentieva, Gelatin-Methacryloyl (GelMA) Formulated with Human Platelet Lysate Supports Mesenchymal Stem Cell Proliferation and Differentiation and Enhances the Hydrogel's Mechanical Properties, Bioengineering. 6 (2019) 76. https://doi.org/10.3390/bioengineering6030076.

[10]   L.L. Hench, Bioceramics, Journal of the American Ceramic Society. 81 (2005) 1705–1728. https://doi.org/10.1111/j.1151-2916.1998.tb02540.x.

[11]   N. Aslankoohi, S. Lin, K. Mequanint, Bioactive fluorescent hybrid microparticles as a stand-alone osteogenic differentiation inducer, Materials Today Bio. 13 (2022) 100187. https://doi.org/10.1016/j.mtbio.2021.100187.

[12]   L.L. Hench, R.J. Splinter, W.C. Allen, T.K. Greenlee, Bonding mechanisms at the interface of ceramic prosthetic materials, J. Biomed. Mater. Res. 5 (1971) 117–141. https://doi.org/10.1002/jbm.820050611.

[13]   J.R. Jones, E. Gentleman, J. Polak, Bioactive Glass Scaffolds for Bone Regeneration, Elements. 3 (2007) 393–399. https://doi.org/10.2113/GSELEMENTS.3.6.393.

[14]   N. Aslankoohi, K. Mequanint, Poly(ester amide)–Bioactive Glass Hybrid Biomaterials for Bone Regeneration and Biomolecule Delivery, ACS Appl. Bio Mater. 3 (2020) 3621–3630. https://doi.org/10.1021/acsabm.0c00257.

[15]   C.A. Gregory, W. Grady Gunn, A. Peister, D.J. Prockop, An Alizarin red-based assay of mineralization by adherent cells in culture: comparison with cetylpyridinium chloride extraction, Analytical Biochemistry. 329 (2004) 77–84. https://doi.org/10.1016/j.ab.2004.02.002.

[16]   B. Joddar, T. Hoshiba, G. Chen, Y. Ito, Stem cell culture using cell-derived substrates, Biomater. Sci. 2 (2014) 1595–1603. https://doi.org/10.1039/C4BM00126E.

[17]   A.B. Faia-Torres, T. Goren, T.O. Ihalainen, S. Guimond-Lischer, M. Charnley, M. Rottmar, K. Maniura-Weber, N.D. Spencer, R.L. Reis, M. Textor, N.M. Neves, Regulation of Human Mesenchymal Stem Cell Osteogenesis by Specific Surface Density of Fibronectin: a Gradient Study, ACS Appl. Mater. Interfaces. 7 (2015) 2367–2375. https://doi.org/10.1021/am506951c.

[18]   P. Mogha, S. Iyer, A. Majumder, Extracellular matrix protein gelatin provides higher expansion, reduces size heterogeneity, and maintains cell stiffness in a long-term culture of mesenchymal stem cells, Tissue and Cell. 80 (2023) 101969. https://doi.org/10.1016/j.tice.2022.101969.

[19]   B. Yin, H. Yang, M. Yang, Integrating Soft Hydrogel with Nanostructures Reinforces Stem Cell Adhesion and Differentiation, J. Compos. Sci. 6 (2022) 19. https://doi.org/10.3390/jcs6010019.

[20]   X. Li, L.H. Klausen, W. Zhang, Z. Jahed, C.-T. Tsai, T.L. Li, B. Cui, Nanoscale Surface Topography Reduces Focal Adhesions and Cell Stiffness by Enhancing Integrin Endocytosis, Nano Lett. 21 (2021) 8518–8526. https://doi.org/10.1021/acs.nanolett.1c01934.

[21]   Y. Hou, W. Xie, L. Yu, L.C. Camacho, C. Nie, M. Zhang, R. Haag, Q. Wei, Surface Roughness Gradients Reveal Topography-Specific Mechanosensitive Responses in Human Mesenchymal Stem Cells, Small. 16 (2020) 1905422. https://doi.org/10.1002/smll.201905422.

[22]   D.K. Knight, E.R. Gillies, K. Mequanint, Biomimetic l-aspartic acid-derived functional poly(ester amide)s for vascular tissue engineering, Acta Biomaterialia. 10 (2014) 3484–3496. https://doi.org/10.1016/j.actbio.2014.04.014.

[23]   R. Arredondo, F. Poggioli, S. Martínez-Díaz, M. Piera-Trilla, R. Torres-Claramunt, L. Tío, J.C. Monllau, Fibronectin-coating enhances attachment and proliferation of mesenchymal stem cells on a polyurethane meniscal scaffold, Regenerative Therapy. 18 (2021) 480–486. https://doi.org/10.1016/j.reth.2021.11.001.

[24]   S. Gao, B. Chen, M. Gao, Y. Xu, X. Yang, C. Yang, S. Pan, Substrate Stiffness of Bone Microenvironment Controls Functions of Pre-Osteoblasts and Fibroblasts In Vitro, Biomimetics. 8 (2023) 344. https://doi.org/10.3390/biomimetics8040344.

[25]   H. Hojo, S. Ohba, Sp7 Action in the Skeleton: Its Mode of Action, Functions, and Relevance to Skeletal Diseases, IJMS. 23 (2022) 5647. https://doi.org/10.3390/ijms23105647.

[26]   H. Rashid, C. Ma, H. Chen, H. Wang, M.Q. Hassan, K. Sinha, B. De Crombrugghe, A. Javed, Sp7 and Runx2 molecular complex synergistically regulate expression of target genes, Connective Tissue Research. 55 (2014) 83–87. https://doi.org/10.3109/03008207.2014.923872.

[27]   H. Hojo, T. Saito, X. He, Q. Guo, S. Onodera, T. Azuma, M. Koebis, K. Nakao, A. Aiba, M. Seki, Y. Suzuki, H. Okada, S. Tanaka, U. Chung, A.P. McMahon, S. Ohba, Runx2 regulates chromatin accessibility to direct the osteoblast program at neonatal stages, Cell Reports. 40 (2022) 111315. https://doi.org/10.1016/j.celrep.2022.111315.

[28]   N. Artigas, C. Ureña, E. Rodríguez-Carballo, J.L. Rosa, F. Ventura, Mitogen-activated Protein Kinase (MAPK)-regulated Interactions between Osterix and Runx2 Are Critical for the Transcriptional Osteogenic Program, Journal of Biological Chemistry. 289 (2014) 27105–27117. https://doi.org/10.1074/jbc.M114.576793.

[29]   M. Morinobu, M. Ishijima, S.R. Rittling, K. Tsuji, H. Yamamoto, A. Nifuji, D.T. Denhardt, M. Noda, Osteopontin Expression in Osteoblasts and Osteocytes During Bone Formation Under Mechanical Stress in the Calvarial Suture In Vivo, J Bone Miner Res. 18 (2003) 1706–1715. https://doi.org/10.1359/jbmr.2003.18.9.1706.

[30]   G.K. Hunter, Role of Osteopontin in Modulation of Hydroxyapatite Formation, Calcif Tissue Int. 93 (2013) 348–354. https://doi.org/10.1007/s00223-013-9698-6.

[31]   D.E. Rodriguez, T. Thula-Mata, E.J. Toro, Y.-W. Yeh, C. Holt, L.S. Holliday, L.B. Gower, Multifunctional role of osteopontin in directing intrafibrillar mineralization of collagen and activation of osteoclasts, Acta Biomaterialia. 10 (2014) 494–507. https://doi.org/10.1016/j.actbio.2013.10.010.

[32]   B. Depalle, C.M. McGilvery, S. Nobakhti, N. Aldegaither, S.J. Shefelbine, A.E. Porter, Osteopontin regulates type I collagen fibril formation in bone tissue, Acta Biomaterialia. 120 (2021) 194–202. https://doi.org/10.1016/j.actbio.2020.04.040.

[33]   C. Somaiah, A. Kumar, D. Mawrie, A. Sharma, S.D. Patil, J. Bhattacharyya, R. Swaminathan, B.G. Jaganathan, Collagen Promotes Higher Adhesion, Survival and Proliferation of Mesenchymal Stem Cells, PLoS ONE. 10 (2015) e0145068. https://doi.org/10.1371/journal.pone.0145068.

[34]   H.M. Akhir, P.L. Teoh, Collagen type I promotes osteogenic differentiation of amniotic membrane-derived mesenchymal stromal cells in basal and induction media, Bioscience Reports. 40 (2020) BSR20201325. https://doi.org/10.1042/BSR20201325.

[35]   M. Mizuno, R. Fujisawa, Y. Kuboki, Type I collagen-induced osteoblastic differentiation of bone-marrow cells mediated by collagen-?2?1 integrin interaction, J. Cell. Physiol. 184 (2000) 207–213. https://doi.org/10.1002/1097-4652(200008)184:2<207::AID-JCP8>3.0.CO;2-U.

[36]   L.-H. Chiu, W.-F.T. Lai, S.-F. Chang, C.-C. Wong, C.-Y. Fan, C.-L. Fang, Y.-H. Tsai, The effect of type II collagen on MSC osteogenic differentiation and bone defect repair, Biomaterials. 35 (2014) 2680–2691. https://doi.org/10.1016/j.biomaterials.2013.12.005.

[37]   P. Janicki, P. Kasten, K. Kleinschmidt, R. Luginbuehl, W. Richter, Chondrogenic pre-induction of human mesenchymal stem cells on β-TCP: Enhanced bone quality by endochondral heterotopic bone formation, Acta Biomaterialia. 6 (2010) 3292–3301. https://doi.org/10.1016/j.actbio.2010.01.037.

[38]   C. Lian, X. Wang, X. Qiu, Z. Wu, B. Gao, L. Liu, G. Liang, H. Zhou, X. Yang, Y. Peng, A. Liang, C. Xu, D. Huang, P. Su, Collagen type II suppresses articular chondrocyte hypertrophy and osteoarthritis progression by promoting integrin β1−SMAD1 interaction, Bone Res. 7 (2019) 8. https://doi.org/10.1038/s41413-019-0046-y.

[39]   R. Florencio-Silva, G.R. da S. Sasso, E. Sasso-Cerri, M.J. Simões, P.S. Cerri, Biology of Bone Tissue: Structure, Function, and Factors That Influence Bone Cells, BioMed Research International. 2015 (2015) 1–17. https://doi.org/10.1155/2015/421746.

[40]   L. Malaval, D. Modrowski, A.K. Gupta, J.E. Aubin, Cellular expression of bone-related proteins during in vitro osteogenesis in rat bone marrow stromal cell cultures, J. Cell. Physiol. 158 (1994) 555–572. https://doi.org/10.1002/jcp.1041580322.

[41]   C. Khoswanto, Role of matrix metalloproteinases in bone regeneration: Narrative review, Journal of Oral Biology and Craniofacial Research. 13 (2023) 539–543. https://doi.org/10.1016/j.jobcr.2023.06.002.

[42]   R. Agnihotri, H.C. Crawford, H. Haro, L.M. Matrisian, M.C. Havrda, L. Liaw, Osteopontin, a Novel Substrate for Matrix Metalloproteinase-3 (Stromelysin-1) and Matrix Metalloproteinase-7 (Matrilysin), Journal of Biological Chemistry. 276 (2001) 28261–28267. https://doi.org/10.1074/jbc.M103608200.

[43]   J.A.R. Gordon, C.E. Tye, A.V. Sampaio, T.M. Underhill, G.K. Hunter, H.A. Goldberg, Bone sialoprotein expression enhances osteoblast differentiation and matrix mineralization in vitro, Bone. 41 (2007) 462–473. https://doi.org/10.1016/j.bone.2007.04.191.

Chapter 6

6. General Discussion and Conclusions

Overview: *This chapter summarizes the research of the overall work, discusses the strengths and limitations of the thesis, and addresses some recommended future directions to this research.*

6.1. Summary

The focus of the research was to develop organic-inorganic nanocomposites composed of a gelatin-based polymer, tertiary bioactive glass, and multiwall carbon nanotubes (gelatin-BG-MWCNT and GelMA-BG-MWCNT) as potential bone biomaterials for bone tissue engineering solutions. Bioactive glasses (BG) have gained significant attention for bone healing applications due to their bioactive nature promoting the formation of hydroxycarbonate apatite bilayer on the glass surface, similar to that found in natural bone.[1,2]   The formation of hydroxycarbonate apatite occurs through the interaction of the released soluble ionic species from the tertiary BG component, such as Si, Ca^{2+}, and PO_4^{3-} ions, with the physiological environment which promotes bonding to bone tissue. BGs are ideal for use as an inorganic component for the preparation of bone biomaterials since they readily bond to bone and stimulate both osteoconduction and osteoinduction.[3,4]   Calcium is fundamental to the bioactivity of sol-gel tertiary BGs and a key component of osteogenesis.[5,6]   Different calcium precursors have been used for the synthesis of sol-gel-derived BGs. These include calcium chloride and calcium ethoxide. The main advantage of using these calcium sources is its compatibility to incorporate a polymer component for the preparation of organic-inorganic nanocomposites at room temperature.[7-9]

Due to the brittle nature of BGs, a polymer component is necessary to induce toughness and provide additional functionalities. In addition, the preparation of an organic-inorganic nanocomposite would create a bone biomaterial that mimics the hierarchical structural composition of bone. Gelatin, the hydrolyzed form of type I collagen found in natural bone, would work as an ideal polymer for creating an environment that mimics the main organic component of endogenous bone. One of the drawbacks of using gelatin, however, is that it melts at physiologic temperature and cannot function as an organic polymer for the preparation of bone biomaterials. Therefore, gelatin methacryloyl (GelMA) provides

the main advantage of stability at physiologic temperature and has a slower degradation rate compared to gelatin, as well as possessing higher mechanical strength.

Moreover, native bone possesses endogenous conductive properties[10] and the incorporation of a conductive element into a bone biomaterial could better mimic the bone's natural electrical conductivity, providing significant advantages at a physiological level.[11] Multiwall carbon nanotubes (MWCNT) have been incorporated into organic-inorganic bone biomaterials as an element that can mimic the natural electrically conductive properties of bone as well as a component that can deliver electrical cues through the application of electrical stimulation for the maturation of osteoblasts and promotion of the repair and regeneration of bone defects.[12]

Chapter 3 presented the preparation of sol-gel-derived gelatin-BG nanocomposites containing either calcium chloride ($CaCl_2$) or calcium ethoxide ($Ca(OEt)_2$) as calcium precursor sources for the sol-gel synthesis. MWCNTs were also added to the organic-inorganic nanocomposites and did not hinder any of the properties of the biomaterials, which was a desired attribution to carry out future studies on their electrically conductive properties. The surface elemental distribution was homogeneous for both $CaCl_2$- and $Ca(OEt)_2$-containing nanocomposites. However, the calcium ions from the $Ca(OEt)_2$-based nanocomposites were incorporated in the silicate glass nanocomposite network, whereas the calcium ions from $CaCl_2$-containing nanocomposites were not. The fate of the calcium ions influenced the swelling, degradation, and the resulting porous properties after degradation of the organic-inorganic nanocomposites. Both $CaCl_2$- and $Ca(OEt)_2$-containing nanocomposites presented bioactive properties through the formation of hydroxycarbonate apatite on their surfaces after incubation in simulated body fluid. Favorable cell adhesion and spreading were observed in 10T1/2 cells cultured on $CaCl_2$- and $Ca(OEt)_2$-containing nanocomposites. Nanocomposites composed of $Ca(OEt)_2$ presented more advantages than $CaCl_2$-based nanocomposites in terms of degradation, bioactivity, and cell interaction properties.

Since GelMA could function better as an organic component due to its decreased biodegradation rate, and calcium ethoxide presented more advantages for the synthesis of sol-gel-derived BGs compared to calcium chloride, chapter 4 discusses the preparation of organic-inorganic nanocomposite hydrogels using GelMA, tertiary BG and MWCNT. GelMA-BG-MWCNT hydrogels were prepared in an attempt to mimic the organic-inorganic structural composition of bone with tunable electrical and electro-mechanical properties. The mechanical and electrically conductive effects of the organic-

inorganic hydrogels were evaluated as a function of MWCNT loading, which was related to the concentration of uniformly distributed MWCNTs added to the GelMA-BG biomaterials. GelMA-BG-MWCNT nanocomposite hydrogels presented bioactive properties and showed good cytocompatibility properties that could further promote osteogenic differentiation.

The viability and osteogenic ability of human-induced pluripotent stem cells (iMSCs) were further evaluated on GelMA-BG-MWCNT nanocomposite hydrogels which is discussed in chapter 5. Cells presented good cytocompatibility properties on gelatin-coated nanocomposite hydrogels. However, optimization of the initial cell density baseline cultured on hydrogels was required for the induction of osteogenic differentiation. Fibronectin-coated nanocomposite hydrogels improved iMSC adhesion, but was further enhanced in the 70-30-1 and 70-30-2 hydrogels by culturing pre-differentiated iMSCs. GelMA-BG-MWCNT hydrogels presented a favorable environment for the upregulation of osteogenic differentiation and enhanced mineralization, especially on the 70-30-2 hydrogel.

6.2. Strengths and limitations

The preparation of sol-gel-derived gelatin-BG-MWCNT containing calcium chloride or calcium ethoxide allowed understanding the role of calcium ions in the organic-inorganic network. In addition, the chemical and physical characterizations of nanocomposites allowed a better understanding of the resulting compositions of biomaterials. An improved strategy was further developed to obtain nanocomposite hydrogels composed of GelMA, tertiary BG containing calcium ethoxide as a calcium precursor, and MWCNT with tunable electrical and mechanical properties.

To the best of my knowledge, this is the first work that has evaluated the electro-mechanical responses of GelMA-BG-MWCNT nanocomposite hydrogels, which is a fundamental process that naturally occurs in bone especially during its regeneration and healing. In addition, the nanocomposite hydrogels presented higher conductivities than other studies that also characterized the electrical properties of organic-inorganic systems in bone biomaterials.[13,14] A similar compositional framework to that of natural bone was developed, composed of 70 wt.% GelMA and 30 wt.% BG. Here, the GelMA would act as a template for the deposition of hydroxycarbonate apatite formed from the release of soluble ionic species from the BG composition, promoting biomineralization while acting as a support for bone repair and regeneration. Furthermore, the use of diacrylated Pluronic F-127 as a reactive surfactant allowed homogenization and further crosslinking of the GelMA

prepolymer due to its diacrylate group and enhanced the elasticity and mechanical strength of the GelMA-BG-MWCNT hydrogels.

GelMA-BG-MWCNT nanocomposite hydrogels showed that they have the ability to promote osteogenic differentiation in mouse embryo multipotent mesenchymal progenitor cells (10T1/2 cells) and mesenchymal stem cells derived from human induced pluripotent stem cells (iMSCs). Enhanced protein expression and mineralization of iMSCs was observed in nanocomposite hydrogels containing MWCNT.

Although GelMA-BG-MWCNT hydrogels increased the osteogenic ability of mouse- and human-derived cells, the application of exogenous electrical stimulation on cells cultured on nanocomposite hydrogels was not performed due to time constraints. The selection of human-derived iMSCs was to perform *in vitro* studies since they could potentially resemble clinically driven outcomes. However, *in vivo* studies on the potential repair and regeneration of bone are necessary to investigate whether GelMA-BG-MWCNT nanocomposite hydrogels augment the healing of bone defects and whether bone regeneration is accelerated through the application of exogenous electrical stimulation.

6.3. Future directions

The current thesis work reported an approach to develop sol-gel-derived gelatin-BG-MWCNT nanocomposites containing calcium chloride and calcium ethoxide as calcium precursors. This approach allowed us to improve the synthesis strategy to develop nanocomposite hydrogels comprised of GelMA, sol-gel-derived tertiary BG, and uniformly dispersed MWCNT to create nanocomposite hydrogels that mimic the organic-inorganic composition as well as the electro-mechanical properties similar to endogenous bone. Future studies can broaden the potential applications of nanocomposite hydrogels for bone tissue engineering solutions.

1. Investigating the effects of exogenous electrical stimulation. The application of exogenous electrical stimulation is suggested to further enhance the differentiation of bone tissue *in vitro*[15] and accelerate the healing of bone defects *in vivo*[12] in bone biomaterials containing a carbon-based electrically conductive material. The evaluation of osteogenic differentiation, maturation, and regeneration of bone tissue could be assessed in GelMA-BG-MWCNT nanocomposite hydrogels.

2. Evaluation of the effects of additional inorganic components. The composition of tertiary BG in the first study was of SiO_2, P_2O_5, and $CaCl_2$ or CaO, which showed that calcium ethoxide precursor was the best source of calcium used for the synthesis of sol-gel-derived tertiary BG. The use of additional ions, such as boron,[8] magnesium,[16] and strontium[17] have been incorporated into sol-gel-derived BGs to promote osteo-stimulative effects. It would be insightful to investigate the addition of different elements to evaluate their potential biological effects.

3. Investigating the cellular processing mechanisms of MWCNTs. The complete degradation and fate of MWCNTs in the body are still relatively unknown. However, *in vitro* and *in vivo* studies have shown that a variety of cell types such as macrophages,[18–20] endothelial cells,[21] pulmonary epithelia,[22,23] intestinal epithelia,[24] and neuronal cells[25] can degrade and uptake carbon-based conductive materials. Therefore, understanding how the MWCNT component in nanocomposite hydrogels is processed and degraded by the specialized bone cells they interact with will be important for establishing and ensuring safety in clinical translations.

6.4. References

[1]   R. Arambula-Maldonado, Y. Liu, M. Xing, K. Mequanint, Bioactive and electrically conductive GelMA-BG-MWCNT nanocomposite hydrogel bone biomaterials, Biomaterials Advances 154 (2023) 213616. https://doi.org/10.1016/j.bioadv.2023.213616.

[2]   J.R. Jones, E. Gentleman, J. Polak, Bioactive Glass Scaffolds for Bone Regeneration, Elements 3 (2007) 393–399. https://doi.org/10.2113/GSELEMENTS.3.6.393.

[3]   L.L. Hench, Bioceramics, Journal of the American Ceramic Society 81 (2005) 1705–1728. https://doi.org/10.1111/j.1151-2916.1998.tb02540.x.

[4]   N. Aslankoohi, S. Lin, K. Mequanint, Bioactive fluorescent hybrid microparticles as a stand-alone osteogenic differentiation inducer, Materials Today Bio 13 (2022) 100187. https://doi.org/10.1016/j.mtbio.2021.100187.

[5]   B. Yu, C.A. Turdean-Ionescu, R.A. Martin, R.J. Newport, J.V. Hanna, M.E. Smith, J.R. Jones, Effect of Calcium Source on Structure and Properties of Sol–Gel Derived Bioactive Glasses, Langmuir 28 (2012) 17465–17476. https://doi.org/10.1021/la303768b.

[6]   C. Bossard, H. Granel, É. Jallot, V. Montouillout, F. Fayon, J. Soulié, C. Drouet, Y. Wittrant, J. Lao, Mechanism of Calcium Incorporation Inside Sol–Gel Silicate Bioactive Glass and the

Advantage of Using Ca(OH) $_2$ over Other Calcium Sources, ACS Biomater. Sci. Eng. 5 (2019) 5906–5915. https://doi.org/10.1021/acsbiomaterials.9b01245.

[7]   N. Aslankoohi, K. Mequanint, Poly(ester amide)–Bioactive Glass Hybrid Biomaterials for Bone Regeneration and Biomolecule Delivery, ACS Appl. Bio Mater. 3 (2020) 3621–3630. https://doi.org/10.1021/acsabm.0c00257.

[8]   D. Mondal, S. Lin, A.S. Rizkalla, K. Mequanint, Porous and biodegradable polycaprolactone-borophosphosilicate hybrid scaffolds for osteoblast infiltration and stem cell differentiation, Journal of the Mechanical Behavior of Biomedical Materials 92 (2019) 162–171. https://doi.org/10.1016/j.jmbbm.2019.01.011.

[9]   B.A. Allo, A.S. Rizkalla, K. Mequanint, Hydroxyapatite Formation on Sol–Gel Derived Poly(ε-Caprolactone)/Bioactive Glass Hybrid Biomaterials, ACS Appl. Mater. Interfaces 4 (2012) 3148–3156. https://doi.org/10.1021/am300487c.

[10]   E. Fukada, I. Yasuda, On the Piezoelectric Effect of Bone, J. Phys. Soc. Jpn. 12 (1957) 1158–1162. https://doi.org/10.1143/JPSJ.12.1158.

[11]   T.W. Balmer, S. Vesztergom, P. Broekmann, A. Stahel, P. Büchler, Characterization of the electrical conductivity of bone and its correlation to osseous structure, Sci Rep 8 (2018) 8601. https://doi.org/10.1038/s41598-018-26836-0.

[12]   E.P. e Silva, B. Huang, J.V. Helaehil, P.R.L. Nalesso, L. Bagne, M.A. de Oliveira, G.C.C. Albiazetti, A. Aldalbahi, M. El-Newehy, M. Santamaria-Jr, F.A.S. Mendonça, P. Bártolo, G.F. Caetano, In vivo study of conductive 3D printed PCL/MWCNTs scaffolds with electrical stimulation for bone tissue engineering, Bio-Des. Manuf. 4 (2021) 190–202. https://doi.org/10.1007/s42242-020-00116-1.

[13]   A.G. Sanchez, E. Prokhorov, G. Luna-Barcenas, J. Hernández-Vargas, R. Román-Doval, S. Mendoza, H. Rojas-Chávez, Chitosan-hydroxyapatite-MWCNTs nanocomposite patch for bone tissue engineering applications, Materials Today Communications 28 (2021) 102615. https://doi.org/10.1016/j.mtcomm.2021.102615.

[14]   S. Shokri, B. Movahedi, M. Rafieinia, H. Salehi, A new approach to fabrication of Cs/BG/CNT nanocomposite scaffold towards bone tissue engineering and evaluation of its properties, Applied Surface Science 357 (2015) 1758–1764. https://doi.org/10.1016/j.apsusc.2015.10.048.

[15]   X. Liu, M.N. George, L. Li, D. Gamble, A.L. Miller II, B. Gaihre, B.E. Waletzki, L. Lu, Injectable Electrical Conductive and Phosphate Releasing Gel with Two-Dimensional Black Phosphorus and Carbon Nanotubes for Bone Tissue Engineering, ACS Biomater. Sci. Eng. 6 (2020) 4653–4665. https://doi.org/10.1021/acsbiomaterials.0c00612.

[16]   A. Moghanian, A. Sedghi, A. Ghorbanoghli, E. Salari, The effect of magnesium content on in vitro bioactivity, biological behavior and antibacterial activity of sol–gel derived 58S bioactive glass, Ceramics International 44 (2018) 9422–9432. https://doi.org/10.1016/j.ceramint.2018.02.159.

[17]   D. Bellucci, V. Cannillo, A. Anesi, R. Salvatori, L. Chiarini, T. Manfredini, D. Zaffe, Bone Regeneration by Novel Bioactive Glasses Containing Strontium and/or Magnesium: A Preliminary In-Vivo Study, Materials 11 (2018) 2223. https://doi.org/10.3390/ma11112223.

[18]   M. Yang, M. Zhang, H. Nakajima, M. Yudasaka, S. Iijima, T. Okazaki, Time-dependent degradation of carbon nanotubes correlates with decreased reactive oxygen species generation in macrophages, IJN Volume 14 (2019) 2797–2807. https://doi.org/10.2147/IJN.S199187.

[19]   V.E. Kagan, A.A. Kapralov, C.M. St. Croix, S.C. Watkins, E.R. Kisin, G.P. Kotchey, K. Balasubramanian, I.I. Vlasova, J. Yu, K. Kim, W. Seo, R.K. Mallampalli, A. Star, A.A. Shvedova, Lung Macrophages "Digest" Carbon Nanotubes Using a Superoxide/Peroxynitrite Oxidative Pathway, ACS Nano 8 (2014) 5610–5621. https://doi.org/10.1021/nn406484b.

[20]   R. Wang, R. Lohray, E. Chow, P. Gangupantula, L. Smith, R. Draper, Selective Uptake of Carboxylated Multi-Walled Carbon Nanotubes by Class A Type 1 Scavenger Receptors and Impaired Phagocytosis in Alveolar Macrophages, Nanomaterials 10 (2020) 2417. https://doi.org/10.3390/nano10122417.

[21]   M. Sano, M. Izumiya, H. Haniu, K. Ueda, K. Konishi, H. Ishida, C. Kuroda, T. Uemura, K. Aoki, Y. Matsuda, N. Saito, Cellular Responses of Human Lymphatic Endothelial Cells to Carbon Nanomaterials, Nanomaterials 10 (2020) 1374. https://doi.org/10.3390/nano10071374.

[22]   N.R. Jacobsen, P. Møller, P.A. Clausen, A.T. Saber, C. Micheletti, K.A. Jensen, H. Wallin, U. Vogel, Biodistribution of Carbon Nanotubes in Animal Models, Basic Clin Pharmacol Toxicol 121 (2017) 30–43. https://doi.org/10.1111/bcpt.12705.

[23]   P. Ruenraroengsak, S. Chen, S. Hu, J. Melbourne, S. Sweeney, A.J. Thorley, J.N. Skepper, M.S.P. Shaffer, T.D. Tetley, A.E. Porter, Translocation of Functionalized Multi-Walled Carbon Nanotubes across Human Pulmonary Alveolar Epithelium: Dominant Role of Epithelial Type 1 Cells, ACS Nano 10 (2016) 5070–5085. https://doi.org/10.1021/acsnano.5b08218.

[24]   M. Kucki, L. Diener, N. Bohmer, C. Hirsch, H.F. Krug, V. Palermo, P. Wick, Uptake of label-free graphene oxide by Caco-2 cells is dependent on the cell differentiation status, J Nanobiotechnol 15 (2017) 46. https://doi.org/10.1186/s12951-017-0280-7.

[25]   H. Kafa, J.T.-W. Wang, N. Rubio, K. Venner, G. Anderson, E. Pach, B. Ballesteros, J.E. Preston, N.J. Abbott, K.T. Al-Jamal, The interaction of carbon nanotubes with an in vitro blood-brain barrier model and mouse brain in vivo, Biomaterials 53 (2015) 437–452. https://doi.org/10.1016/j.biomaterials.2015.02.083.

Appendix

Appendix 1. Copyright permissions

1. R. Arambula-Maldonado, K. Mequanint, Carbon-based electrically conductive materials for bone repair and regeneration, Mater. Adv. (2022) 10.1039.D2MA00001F. https://doi.org/10.1039/D2MA00001F.

2. R.L. Duncan, C.H. Turner, Mechanotransduction and the functional response of bone to mechanical strain, Calcif Tissue Int 57 (1995) 344–358. https://doi.org/10.1007/BF00302070.

3. C. Fu, H. Bai, J. Zhu, Z. Niu, Y. Wang, J. Li, X. Yang, Y. Bai, Enhanced cell proliferation and osteogenic differentiation in electrospun PLGA/hydroxyapatite nanofibre scaffolds incorporated with graphene oxide, PLoS ONE 12 (2017) e0188352. https://doi.org/10.1371/journal.pone.0188352.

4. Z. Du, X. Feng, G. Cao, Z. She, R. Tan, K.E. Aifantis, R. Zhang, X. Li, The effect of carbon nanotubes on osteogenic functions of adipose-derived mesenchymal stem cells in vitro and bone formation in vivo compared with that of nano-hydroxyapatite and the possible mechanism, Bioactive Materials 6 (2021) 333–345. https://doi.org/10.1016/j.bioactmat.2020.08.015.

The effect of carbon nanotubes on osteogenic functions of adipose-derived mesenchymal stem cells *in vitro* and bone formation *in vivo* compared with that of nano-hydroxyapatite and the possible mechanism

Zhipo Du,[a,1] Xinxing Feng,[b,1] Guangxiu Cao,[c,d,1] Zhending She,[e] Rongwei Tan,[e] Katerina E. Aifantis,[f] Ruihong Zhang,[g,**] and Xiaoming Li[c,d,*]

▸ Author information ▸ Article notes ▾ Copyright and License information   PMC Disclaimer

5. X. Liu, M.N. George, S. Park, A.L. Miller II, B. Gaihre, L. Li, B.E. Waletzki, A. Terzic, M.J. Yaszemski, L. Lu, 3D-printed scaffolds with carbon nanotubes for bone tissue engineering: Fast and homogeneous one-step functionalization, Acta Biomaterialia 111 (2020) 129–140. https://doi.org/10.1016/j.actbio.2020.04.047.

3D-printed scaffolds with carbon nanotubes for bone tissue engineering: Fast and homogeneous one-step functionalization
Author: Xifeng Liu,Matthew N. George,Sungjo Park,A. Lee Miller II,Bipin Gaihre,Linli Li,Brian E. Waletzki,Andre Terzic,Michael J. Yaszemski,Lichun Lu
Publication: Acta Biomaterialia
Publisher: Elsevier
Date: 15 July 2020

Order Completed

Thank you for your order.

This Agreement between University of Western Ontario -- Rebeca Arambula Maldonado ("You") and Elsevier ("Elsevier") consists of your license details and the terms and conditions provided by Elsevier and Copyright Clearance Center.

Your confirmation email will contain your order number for future reference.

License Number: 5732660045388

License date: Feb 19, 2024

Printable Details

Licensed Content

Licensed Content Publisher	Elsevier
Licensed Content Publication	Acta Biomaterialia
Licensed Content Title	3D-printed scaffolds with carbon nanotubes for bone tissue engineering: Fast and homogeneous one-step functionalization
Licensed Content Author	Xifeng Liu,Matthew N. George,Sungjo Park,A. Lee Miller II,Bipin Gaihre,Linli Li,Brian E. Waletzki,Andre Terzic,Michael J. Yaszemski,Lichun Lu
Licensed Content Date	Jul 15, 2020
Licensed Content Volume	111
Licensed Content Issue	n/a
Licensed Content Pages	12

Order Details

Type of Use	reuse in a thesis/dissertation
Portion	figures/tables/illustrations
Number of figures/tables/illustrations	1
Format	both print and electronic
Are you the author of this Elsevier article?	No
Will you be translating?	No

About Your Work

Title of new work	Bioactive and Electrically Conductive Biomaterials for Bone Repair
Institution name	University of Western Ontario
Expected presentation date	May 2024

Additional Data

Portions	Figure 2i,j

Requestor Location

Requestor Location	University of Western Ontario 1151 Richmond Street School of Biomedical Engineering University of Western Ontario London, ON N6A 5B9 Canada Attn: University of Western Ontario

Tax Details

Publisher Tax ID	GB 494 6272 12

Total: 0.00 CAD

CLOSE WINDOW   ORDER MORE

6. S. Shokri, B. Movahedi, M. Rafieinia, H. Salehi, A new approach to fabrication of Cs/BG/CNT nanocomposite scaffold towards bone tissue engineering and evaluation of its properties, Applied Surface Science 357 (2015) 1758–1764. https://doi.org/10.1016/j.apsusc.2015.10.048.

7. R. Balint, N.J. Cassidy, S.H. Cartmell, Electrical Stimulation: A Novel Tool for Tissue Engineering, Tissue Engineering Part B: Reviews 19 (2013) 48–57. https://doi.org/10.1089/ten.teb.2012.0183.

8. X. Liu, M.N. George, L. Li, D. Gamble, A.L. Miller II, B. Gaihre, B.E. Waletzki, L. Lu, Injectable Electrical Conductive and Phosphate Releasing Gel with Two-Dimensional Black Phosphorus and Carbon Nanotubes for Bone Tissue Engineering, ACS Biomater. Sci. Eng. 6 (2020) 4653–4665. https://doi.org/10.1021/acsbiomaterials.0c00612.

9. E.P. e Silva, B. Huang, J.V. Helaehil, P.R.L. Nalesso, L. Bagne, M.A. de Oliveira, G.C.C. Albiazetti, A. Aldalbahi, M. El-Newehy, M. Santamaria-Jr, F.A.S. Mendonça, P. Bártolo, G.F. Caetano, In vivo study of conductive 3D printed PCL/MWCNTs scaffolds with electrical stimulation for bone tissue engineering, Bio-Des. Manuf. 4 (2021) 190–202. https://doi.org/10.1007/s42242-020-00116-1.

10. H. Belaid, S. Nagarajan, C. Teyssier, C. Barou, J. Barés, S. Balme, H. Garay, V. Huon, D. Cornu, V. Cavaillès, M. Bechelany, Development of new biocompatible 3D printed graphene oxide-based scaffolds, Materials Science and Engineering: C 110 (2020) 110595. https://doi.org/10.1016/j.msec.2019.110595.

11. S. Qian, Z. Yan, Y. Xu, H. Tan, Y. Chen, Z. Ling, X. Niu, Carbon nanotubes as electrophysiological building blocks for a bioactive cell scaffold through biological assembly to induce osteogenesis, RSC Adv. 9 (2019) 12001–12009. https://doi.org/10.1039/C9RA00370C.

12. R. Arambula-Maldonado, K. Mequanint, Sol-Gel Derived Gelatin–Bioactive Glass Nanocomposite Biomaterials Incorporating Calcium Chloride and Calcium Ethoxide, Polymers 16(6) (2024) 747. https://doi.org/10.3390/polym16060747.

13. R. Arambula-Maldonado, Y. Liu, M. Xing, K. Mequanint, Bioactive and electrically conductive GelMA-BG-MWCNT nanocomposite hydrogel bone biomaterials, Biomaterials Advances 154 (2023) 213616. https://doi.org/10.1016/j.bioadv.2023.213616.

Permissions form [240220-008935]

ⓘ Some content in this message has been blocked because the sender isn't in your Safe senders list. I trust content from permissions@elsevier.com. | Show blocked content

RP Rights and Permissions (ELS) <Permissions@elsevier.com>
To: Rebeca Arambula Maldonado   Tue 20/02/2024 01:43

You don't often get email from permissions@elsevier.com. Learn why this is important

Dear Rebeca Arambula-Maldonado

We hereby grant you permission to reprint the material below at no charge in your thesis subject to the following conditions:

RE: Bioactive and electrically conductive GelMA-BG-MWCNT nanocomposite hydrogel bone biomaterials, Biomaterials Advances, Volume 154, 2023, Arambula-Maldonado et al.

1. If any part of the material to be used (for example, figures) has appeared in our publication with credit or acknowledgment to another source, permission must also be sought from that source. If such permission is not obtained then that material may not be included in your publication/copies.

2. Suitable acknowledgment to the source must be made, either as a footnote or in a reference list at the end of your publication, as follows:

"This article was published in Publication title, Vol number, Author(s), Title of article, Page Nos, Copyright Elsevier (or appropriate Society name) (Year)."

3. Your thesis may be submitted to your institution in either print or electronic form.

4. Reproduction of this material is confined to the purpose for which permission is hereby given.

5. This permission is granted for non-exclusive world English rights only. For other languages please reapply separately for each one required. Permission excludes use in an electronic form other than submission. Should you have a specific electronic project in mind please reapply for permission.

6. As long as the article is embedded in your thesis, you can post/share your thesis in the University repository.

7. Should your thesis be published commercially, please reapply for permission.

8. Posting of the full article/ chapter online is not permitted. You may post an abstract with a link to the Elsevier website [http://www.elsevier.com./]www.elsevier.com, or to the article on ScienceDirect if it is available on that platform.

Kind regards,

Roopa Lingayath
Senior Copyrights Specialist
ELSEVIER | HCM - Health Content Management

Visit Elsevier Permissions

Curriculum Vitae

Name:	Rebeca Alejandra Arámbula Maldonado

Post-secondary Education and Degrees:

2010-2015: B.S. Biotechnology Engineering
Instituto Tecnológico de Estudios Superiores de Monterrey
Monterrey, Mexico

Technische Universität Braunschweig
Braunschweig, Germany
University Exchange with "Deutsche Akademische Austausch Dienst"
(DAAD)
B.S. Biotechnology Engineering
2013-2014

2016-2017: MSc (Stem Cell and Regenerative Medicine)
University of Sheffield
Sheffield, United Kingdom

2019-2024: PhD Biomedical Engineering
University of Western Ontario
London, Ontario Canada

Honours and Awards

Deutsche Akademischer Austausch Dienst (DAAD)
Received a scholarship for an exchange year during my undergraduate degree in Biotechnology Engineering, where I completed a semester at Technische Universität Braunschweig and an industrial placement at Helmholtz Centre for Infection Research, Germany. Courses and placement were in German language and accredited.
2013-2014

Member of the First Advisory Council Meeting Award
Obtained an award from the Biotechnology School and Health Science from my undergraduate university for having contributed as a Member of the First Advisory Council Meeting where my skills and working experiences helped enrich and redesign the study plan structure of the Bachelor's Degree in Biotechnology Engineering (2016-2017) for new coming students.

National Council of Science and Technology (CONACYT)
Received a full scholarship to study my Master's Degree in Stem Cells and Regenerative Medicine at the University of Sheffield, UK.
2016-2017

CAMBR Day Poster Presentation Award
University of Western Ontario
London, Ontario
2021

Related Work Experience	Teaching Assistant The University of Western Ontario 2020-2021

Publications and Conferences:

1. Rebeca Arambula-Maldonado, Armin Geraili, Malcolm Xing, Kibret Mequanint. Tissue engineering and regenerative therapeutics: The nexus of chemical engineering and translational medicine. Canadian Journal of Chemical Engineering; 99(10), 2069–2086; **2021**. https://doi.org/10.1002/cjce.24094. Selected as a featured article in the Issue Highlights.

2. Rebeca Arambula-Maldonado and Kibret Mequanint. Electrically Conductive and Bioactive Scaffolds for Bone Repair and Regeneration. 36th Annual Meeting of the Canadian Biomaterials Society, May 13-15, **2021**, Waterloo, ON.

3. Rebeca Arambula-Maldonado and Kibret Mequanint. Electrically Conductive and Bioactive Scaffolds for Bone Repair and Regeneration. Centre for Advanced Materials and Biomaterials Research (CAMBR) Day, June 17, **2021**, University of Western Ontario, London, ON.

4. Rebeca Arambula-Maldonado and Kibret Mequanint. Electrically Conductive GelMA-Bioglass Biomaterials for Bone Repair and Regeneration. 37th Annual Meeting of the Canadian Biomaterials Society, May 25-27, **2022**, Banff Center for the Arts and Creativity, AB.

5. Rebeca Arambula-Maldonado and Kibret Mequanint. Carbon-based electrically conductive materials for bone repair and regeneration. Materials Advances; 3(13), 5186–5526; **2022**. https://doi.org/10.1039/d2ma00001f. Selected for inclusion in the 2022 Popular Advances collection, highlighted as a "Popular Advance".

6. Rebeca Arambula-Maldonado, Yuqing Liu, Malcolm Xing, Kibret Mequanint. Bioactive and electrically conductive GelMA-BG-MWCNT nanocomposite hydrogel bone biomaterials. Biomaterials Advances; 154, 213616; **2023**. https://doi.org/10.1016/j.bioadv.2023.213616.

7. Rebeca Arambula-Maldonado and Kibret Mequanint. Sol-gel derived gelatin-bioactive glass nanocomposite biomaterials incorporating calcium chloride and calcium ethoxide. Polymers; 16(6), 747; **2024**. https://doi.org/10.3390/polym16060747. This article belongs to the Special Issue Biomaterials in Medical Applications II.

8. Rebeca Arambula-Maldonado and Kibret Mequanint. Osteogenic differentiation potential of GelMA-BG-MWCNT nanocomposite hydrogels. To be submitted for publication.